State of Oregon
Oregon Department of Geology and Mineral Industries
Brad Avy, State Geologist

**OPEN-FILE REPORT O-17-05**

# COASTAL FLOOD HAZARD STUDY, LANE AND DOUGLAS COUNTIES, OREGON

By Jonathan C. Allan[1], Peter Ruggiero[2], Nick Cohn[2], Fletcher O'Brien[3], Katherine Serafin[2], Jed T. Roberts[3], and Laura L. S. Gabel[1]

2017

[1]Oregon Department of Geology and Mineral Industries, Coastal Field Office, P.O. Box 1033, Newport, OR 97365
[2]College of Earth, Ocean and Atmospheric Sciences, Oregon State University, Corvallis, OR 97331
[3]Oregon Department of Geology and Mineral Industries, 800 NE Oregon St., Ste. 965, Portland, OR 97232

## DISCLAIMER

This product is for informational purposes and may not have been prepared for or be suitable for legal, engineering, or surveying purposes. Users of this information should review or consult the primary data and information sources to ascertain the usability of the information. This publication cannot substitute for site-specific investigations by qualified practitioners. Site-specific data may give results that differ from the results shown in the publication.

*Cover photograph: View looking south along Stonefield Beach, located at the north end of Lane County. Photo taken by J. Allan, March 30, 2014.*

Oregon Department of Geology and Mineral Industries Open-File Report O-17-05
Published in conformance with ORS 516.030

For additional information:
Administrative Offices
800 NE Oregon Street, Suite 965
Portland, OR 97232
Telephone (971) 673-1555
Fax (971) 673-1562
http://www.oregongeology.org
http://oregon.gov/DOGAMI/

# TABLE OF CONTENTS

## LIST OF FIGURES

## LIST OF TABLES

# 1.0 INTRODUCTION

The objective of this project is to develop updated Digital Flood Insurance Rate Maps (DFIRM) and a Flood Insurance Study (FIS) report for Lane and Douglas counties, Oregon (**Figure 1-1**). For this effort, the Oregon Department of Geology and Mineral Industries (DOGAMI) used lidar data to redelineate coastal and riverine flood hazards within the counties, to produce revised DFIRMs and a revised FIS report, and to produce other mapping products useful at local, state, and federal levels for mitigation planning, risk analysis, and disaster response.

As part of the redelineation, DOGAMI was contracted to perform detailed coastal flood hazard studies for several stretches of beach along the Lane and Douglas counties Pacific coast shoreline. These analyses included assessments of the 1% annual probability, or 100-year extreme storm wave event and the associated calculated wave setup, runup, and total water level (i.e., the wave runup superimposed on the tidal level). These studies help guide the determination of Special Flood Hazard Areas (SFHAs), the most significant being regions subject to high coastal flood risk (Zone VE), characterized with base flood elevations (BFEs) that are used to guide building practices. Additional modeling of the 0.2%, or 500-year, event was also undertaken.

Detailed coastal flood analysis is limited to the Siuslaw River mouth, north to the Lane–Lincoln County border. Aside from this area, DOGAMI developed revised V zones for the remainder of the Lane and Douglas counties shoreline. Although a few sections of the coastline had previously been mapped as VE, most of the coastline either had not been mapped or had been mapped as approximate ("A"). After consultation with FEMA and state government representatives, the decision was made to revise these latter zones to better reflect the geomorphology of the coast and, in addition, to redefine these zones as V zones.

Developing coastal flood maps is complicated due to dependence on the many data sources required to perform wave transformation, runup, and overtopping calculations. This challenge is further compounded by an equally wide range of physical settings in which the data and methods can be applied: dune- to bluff-backed beaches; sites that may be backed by coastal engineering structures such as sea walls, riprap revetments, or wooden bulkheads; and gravel and hard rock shorelines. **Figure 1-2** broadly summarizes the steps described in the next sections to help the reader understand conceptually the process that leads to coastal flood hazard zone maps.

**SECTION 2** of this report examines the coastal geology and geomorphology of the Lane-Douglas shoreline, including a discussion of the erosion history of the coast. The results form the basis for defining flood zones along the Lane-Douglas coastline.

**SECTION 3** presents the results of Real-Time Kinematic Differential Global Positioning Surveys (RTK-DGPS) of the detailed study sites established along the length of Lane-Douglas shoreline, undertaken at the peak of the 2013-2014 winter. These surveys are compared with recent historical data derived from lidar, which are used to help define the most eroded winter profile used in runup calculations described in SECTION 6. SECTION 3 also documents the parameters associated with the measured beach profile data, including beach-dune junction elevation, beach slope, and dune/bluff crest/top elevations.

**SECTION 4** examines tide data measured by the National Ocean Service (NOS) at multiple stations, including South Beach (Yaquina Bay), Charleston (Coos Bay), and Port Orford, and includes an analysis of the 1% and 0.2% still water levels (SWL).

**SECTION 5** describes the steps to create a synthesized wave climate, critical for developing the input wave statistics used in calculating wave runup. SECTION 5 also examines the procedures used to refract the waves from deepwater into the nearshore using the SWAN (Simulating Waves Nearshore) wave model.

**Figure 1-1. Location map of coastline along Lane and Douglas counties, Oregon.**

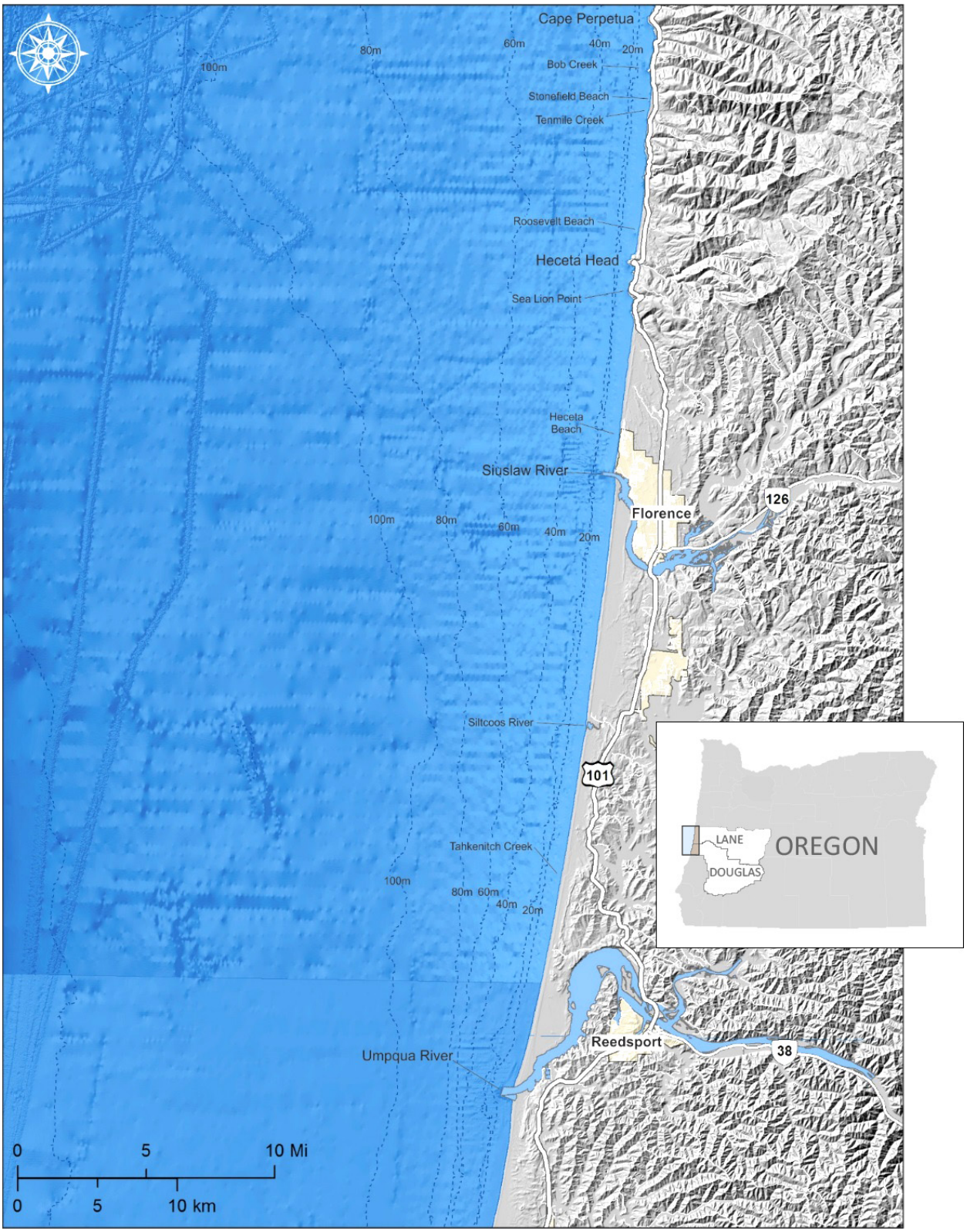

**SECTION 6** presents and discusses analyses of wave runup, including calculation of the 1% and 0.2% total water levels (TWL) as well as any overtopping calculations.

**SECTION 7** discusses the steps used to determine the degree of erosion that might occur on the dune-backed beaches, including the approach used to define the duration reduced erosion factor, important for further establishing the initial conditions on which the runup and overtopping calculations are ultimately performed. Similar discussions describe observations of bluff erosion, characteristic of a few discrete sections of the Lane-Douglas shoreline.

**SECTION 8** synthesizes all of the information and describes the steps taken to draft new flood hazard maps along the Lane-Douglas shoreline.

**Figure 1-2. Three representative examples of the steps that may be taken to derive coastal flood hazard maps on the Pacific Northwest coast.**

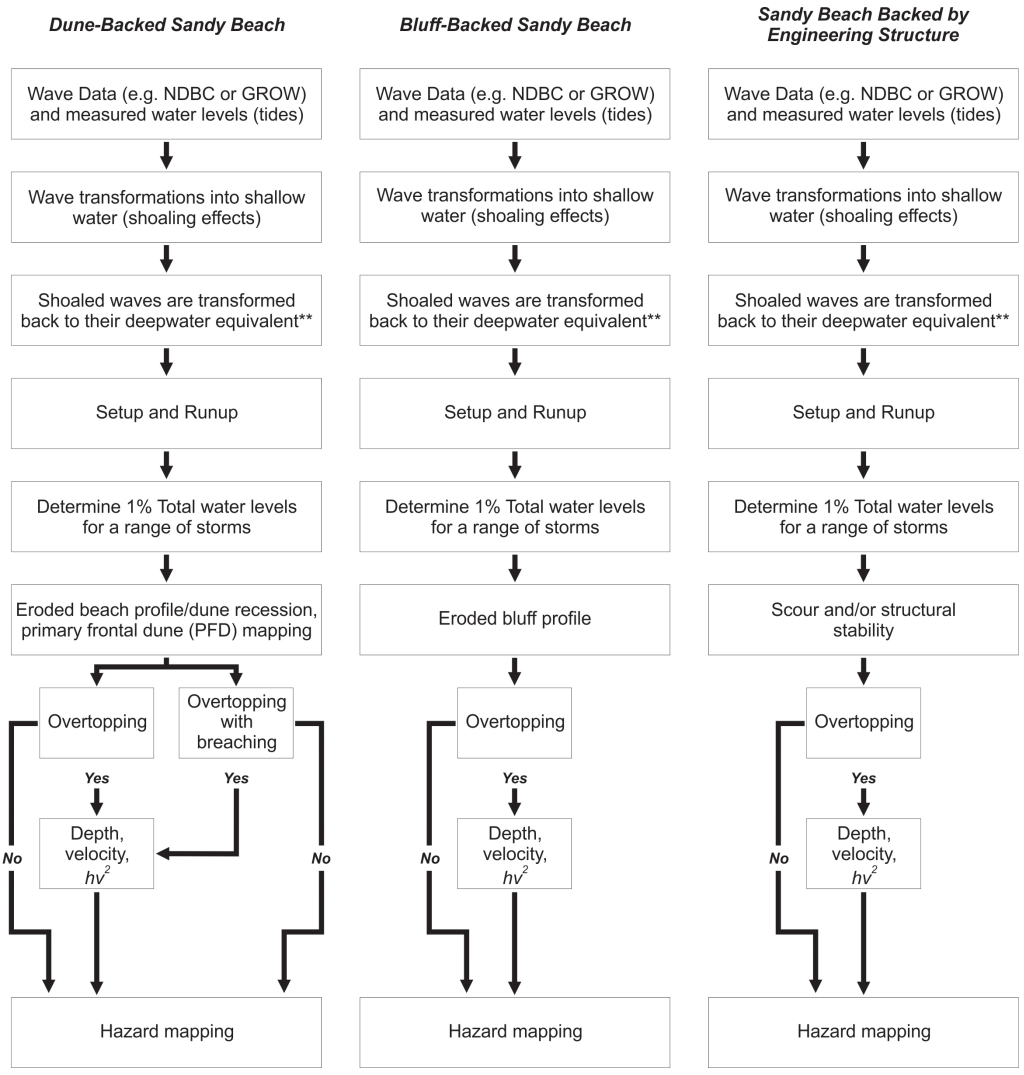


**Note: The waves are first shoaled using numerical models to account for the effect of wave changes (refraction/diffraction) that take place across the shelf and in the nearshore. Because many coastal engineering equations (e.g., wave runup) require deepwater inputs, the "shoaled" waves are then converted back to their deepwater equivalence.

# 2.0 COASTAL GEOLOGY AND GEOMORPHOLOGY OF LANE COUNTY AND DOUGLAS COUNTY

Lane County and Douglas County are located on the south central Oregon coast, between latitudes 44°16′34.19″N (Cape Perpetua) and 43°36′39.40″N (8 km north of Tenmile Creek, located in northern Coos County), and longitudes 124°13′7.52″W and 121°46′2.93″W. The terrain varies from low-elevation sandy beaches and dunes on the coast to elevations over 700 m (2,300 ft) (e.g., Buzzard Rock reaches 930 m [3,051 ft]) in Douglas County, while Cummins Peak in northern Lane County reaches 754 m [2,475 ft]). The Lane-Douglas coastal strip is ~85 km [53 mi] long and varies in its geomorphology from broad, low-sloping sandy beaches backed by dunes, to beaches backed by engineered structures, cobble and boulder beaches adjacent to the headlands, and cliff shorelines. Prominent headlands of resistant basalt (e.g., Heceta Head and Cape Perpetua) provide natural barriers to alongshore sediment transport (Komar, 1997), effectively dividing the county coastline into two main littoral cells. These are:

- Coos littoral cell (~90 km [56 mi]), the largest cell on the Oregon coast, extending from the north side of Cape Arago to Heceta Head; and
- Heceta cell (~45 km [28 mi]), extending from Heceta Head north to Cape Perpetua; the cell includes several smaller pocket beaches such as Stonefield Beach.

The Coos littoral cell is divided into subcells due to the presence of two estuaries (Umpqua and Siuslaw), both of which are bounded by prominent jetties (**Figure 1-1**). The counties are also characterized with two major rivers, including the Umpqua River in Douglas County and Siuslaw River in Lane County that terminate in the estuaries. The Siuslaw River is considered to carry little beach sediment out to the open coast today; instead it deposits much of its sediment in the estuary. In contrast, the Umpqua River has significantly higher river flows (fourth largest in the state); this likely contributes to greater bedload transport [Clemens and Komar, 1988]. However, due to the large tidal prism volume relative to river flow, Clemens and Komar suggest much of the sediment carried by the Umpqua probably remains in the lower estuary. As a result, the beaches of Lane and Douglas counties are thought to receive little sediment along the coast today other than from erosion of the backshore.

## 2.1 Local Geology

Along the Lane-Douglas coast the predominant geologic unit consists of latest Holocene beach sand present along the full length of the coastline (**Figure 2-1**) (Cooper, 1958). The dune sheet in this region ranges from 3 to 4.5 km [1.9–2.8 mi] in width and reflects the farthest inland penetration by dune masses on the Oregon coast. From Sea Lion Point north to the Lincoln County border near Yachats, the coastline is mostly rocky, characterized by intrusive rocks (Yachats basalt, of Tertiary age); the best examples of this include Sea Lion Point, Heceta Head, and Cape Perpetua at the northern end of the county coastline (**Figure 2-2**) (Schlicker and others, 1974). Along the coast, the rock is hard and dense and hence resistant to erosion. Nevertheless, rockfalls and landslides in these basalts do provide new material (e.g., gravel and boulders) to the beaches, albeit at relatively slow rates. Gravels also come from several small creeks (e.g., Tenmile Creek) that drain from the Coast Range. Erosion of bluffs containing colluvium is another mechanism supplying coarse sediment such as gravels to the coast. Combined, the various gravel sources produce gravel beaches (**Figure 2-3**), which accumulate at the back of the beach.

Near Stonefield Beach, approximately 12.8 km [8 mi] of the shore reflects bluffs that have eroded into marine terrace deposits. These bluffs contain small amounts of silty sand and gravel (**Figure 2-3** and **Figure 2-4**). The sediments are considered to be early Pleistocene in age (Schlicker and others, 1974).

**Figure 2-1. Looking north along Heceta Beach toward Heceta Head (first prominent headland) and Cape Perpetua in the far distance [photo: J. Allan, DOGAMI, 2011].**

**Figure 2-2. Looking east at Heceta Head, which is formed in Yachats basalt [photo: J. Allan, DOGAMI, 2011].**

**Figure 2-3. Looking east near Stonefield Beach. Early Pleistocene bluffs composed of silty sand and gravel characterize much of the shore. Note the extensive gravel beach seaward of the bluffs and perched on Yachats basalt. In this example, the bluffs are being undermined by wave processes along the bluff toe [photo: J. Allan, DOGAMI, 2011].**

**Figure 2-4. A perched gravel beach having formed north of Stonefield Beach near Bob Creek as result of erosion of colluvium contained in the bluffs, sediments from local creeks, and landsliding off the headlands. View is to the south [photo: J. Allan, DOGAMI, 2004].**

Much of the beach sand present on the Oregon coast consists of grains of quartz and feldspar. The beaches also contain small amounts of heavier minerals (e.g., garnet, hypersthene, augite, and hornblende [**Figure 2-5**]), which can be traced to various sediment sources along the Pacific Northwest (PNW) coast (Clemens and Komar, 1988). For example, garnet and hypersthene are derived from the Klamath Mountains located in southern Oregon and northern California. Because the headlands today extend well out in deep water, they effectively limit sand transport around their ends under the current process regime. This suggests that the heavier minerals were transported northward along the coast at a time when sea level was much lower, with few barriers to interrupt northward movement (Komar, 1997). With distance from their source, the sediments combined with other minerals derived locally from erosion processes in the Coast Range. As shown in **Figure 2-5**, concentrations of garnet and hypersthene decrease to the north, while concentrations of augite increase significantly; augite is a mineral prevalent in the volcanic rocks present throughout Tillamook County. At Tillamook Head, the concentration of garnet is very small. This suggests that Tillamook Head reflects the most northerly transport of garnet. North of Tillamook Head, it can be seen that concentrations of hypersthene and hornblende increase again in the sediments. These sediments are derived from the Columbia River, which contributed to the formation of the Clatsop Plains, Long Beach Peninsula, and Grayland Plains. Thus, sediments derived from the Columbia River were transported mainly to the north, supplying the Washington coast and shelf.

**Figure 2-5. Variations in the percent abundances of various heavy minerals observed on the central to northern Oregon coast (after Clemens and Komar, 1988).**

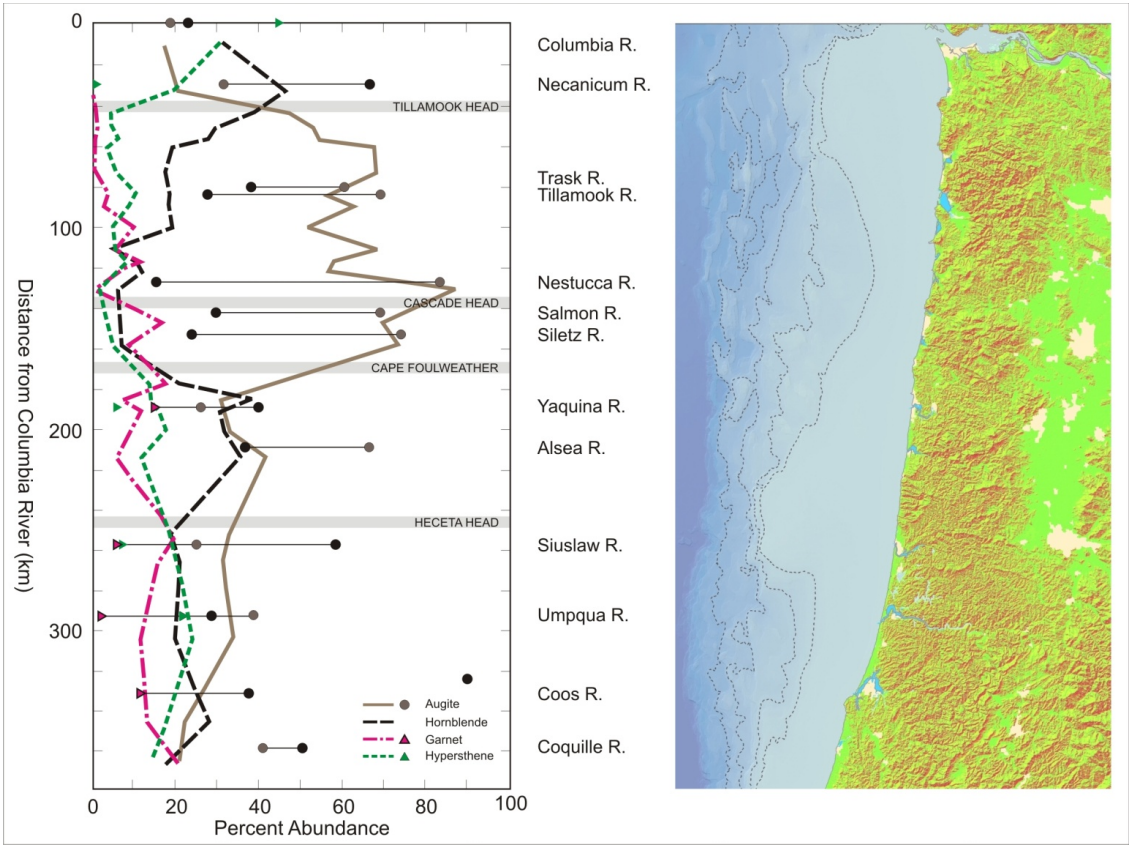

With the end of the last glaciations, sea level rose rapidly and the beaches began to migrate landward. New sediments were derived from erosion of the coastal plain that makes up the continental shelf today. At around 5,000 to 7,000 years ago, the rate of sea level rise slowed as it approached its current level (Komar, 1997). At this stage the prominent headlands would have begun to interrupt sediment transport. Modern barrier spits and beaches began to form within the headland-bounded littoral cells that make up the coast today.

Along the Tillamook County coast, the beaches contain abundant concentrations of augite, indicative of their having been derived locally (**Figure 2-5**). This implies that at the time, rivers and streams carried these sediments out to the coast, where they mixed with other sediments. These concentrations likely increased during the past 150 years as human settlement accelerated and led to increased deforestation (Peterson and others, 1984; Komar and others, 2004). This correspondingly contributed to increased sediment loads in the various rivers. However, analyses of the sediment characteristics in Tillamook Bay, the largest estuary in the county, indicated that while fine sediments pass through the estuary, the bulk of the coarser sediments remain behind where they accumulate as bars and shoals in Tillamook Bay (Komar and others, 2004). Furthermore, sediments within Tillamook Bay are predominantly of a marine origin (60%), while river sediments make up 40% of the sediment in the estuary. This finding is consistent with the work of Peterson and others (1984) and Clemens and Komar (1988), who observed that because of the combination of low river discharge and high tidal regime in Oregon estuaries, the majority of the estuaries are natural "sinks" for the sediment. Thus, the beaches of Oregon receive very little sediment input from rivers and streams today. Accordingly, sediment supply is essentially confined to those areas backed by coastal bluffs, particularly those areas overlain by more erosive Pleistocene marine terrace sandstones (raised ancient beach and dune sands) and more recent Holocene dune sands that drape the landscape.

Prior to the 1940s, many of the barrier spits were devoid of significant vegetation. Due to the introduction of European beach grass (*Ammophila arenaria*) in the early 1900s and its subsequent proliferation along the Oregon coast, dunes and barrier spits became more stable. The product today is an extensive foredune system, consisting of large "stable" dunes that contain significant volumes of sand. People have built structures on the stable-appearing dunes in the most desirable locations, typically on the most seaward foredune. As will be shown throughout this report, building homes and facilities in such areas poses a significant risk as, periodically, storms erode into the dunes. This has resulted in many cases where building foundations are undermined and eventually require riprap coastal engineering structures to mitigate the erosion problem.

## 2.2 Tsunami Hazards Associated with the Cascadia Subduction Zone and from Distant Earthquake Sources

A considerable geologic record from estuaries and coastal lakes along the Cascadia subduction zone provides evidence for episodic occurrences of abrupt coastal subsidence immediately followed by significant ocean flooding associated with major tsunamis that swept across the ocean beaches and also traveled well inland through the bays and estuaries. Coastal paleoseismic records document the impacts of as many as 13 major subduction zone earthquakes and associated tsunamis over the past ~7,000 years (Witter and others, 2003, 2010; Kelsey and others, 2005). Turbidite records within sediment cores collected in deep water at the heads of Cascadia submarine canyons provide evidence for at least 41 distinct tsunami events over the past ~10,000 years (Goldfinger and others, 2003; Goldfinger, 2009;

Goldfinger and others, 2009). The length of time between these events varies from as short as a century to as long as 1,200 years; the average recurrence interval for major Cascadia earthquakes (magnitude ($M_W$) > 9) is estimated to be ~530 years (Witter and others, 2010).

The most recent Cascadia subduction zone earthquake occurred on January 26, 1700 (Satake and others, 1996; Atwater and others, 2005) and is estimated to have been magnitude ($M_W$) 9 or greater based on the size of the tsunami documented along the coast of Japan. Correlations between tsunami deposits identified at multiple sites along the length of the PNW coast indicate this event probably ruptured the full length (~1,200 km, 750 miles) of the subduction zone (e.g., Darienzo and others, 1994; Nelson and others, 1995; Leonard and others, 2004; Atwater and others, 2005).

There is now increasing recognition in paleo-records that great earthquakes do not necessarily result in a complete rupture of the Cascadia subduction zone (i.e., rupture along the full 1,200-km fault zone), such that partial ruptures of the plate boundary have occurred due to smaller earthquakes with magnitudes ($M_W$) < 9 (Witter and others, 2003; Kelsey and others, 2005). These partial segment ruptures appear to occur more frequently on the southern Oregon coast, as determined from paleo-tsunami studies (stratigraphic coring, radiocarbon dating, and marine diatom analyses) undertaken at several locations, including Bradley Lake located just south of Bandon, the Sixes River, and the Coquille estuary. According to Kelsey and others (2005), initial estimates of the recurrence intervals of Bradley Lake tsunami incursion is typically shorter (~380–400 years) than the average recurrence intervals inferred for great earthquakes (~530 years). Furthermore, Kelsey and others have documented from those records that local tsunamis from Cascadia earthquakes recur in clusters (~250–400 years) followed by gaps of 700 of 1,300 years, with the highest tsunamis associated with earthquakes occurring at the beginning and end of a cluster.

Recent analyses of the turbidite records (Goldfinger, 2009; Goldfinger and others, 2009) suggest that of the 41 events in the geologic past:

- 20 events were probably associated with a rupture of the full Cascadia subduction zone, characterized by a magnitude ($M_W$) ~9 or greater earthquake;
- 2-3 events reflected a partial rupture (~75%) of the length of the subduction zone, characterized by an estimated earthquake magnitude ($M_W$) of ~8.5–8.8 earthquake;
- 10-11 events were associated with a partial rupture (~50%), characterized by an estimated earthquake magnitude ($M_W$) of ~8.3–8.5 earthquake; and,
- 8 events reflected a partial rupture (~25%), with an estimated earthquake magnitude ($M_W$) of ~7.6–8.4.

These last 19 shorter ruptures are concentrated in the southern part of the margin and have estimated recurrence intervals of about 240 to 320 years. Goldfinger (2009) estimated that time-independent probabilities for segmented ruptures range from 7–9% for full margin ruptures, to about 18% in 50 years for a southern segment rupture; time dependent rupture analyses indicate that the probability increases to about 25% in 50 years for the northern zone.

Aside from local tsunamis associated with the Cascadia subduction zone, the Oregon coast is also susceptible from tsunamis generated by distant events, particularly those along the coast of Japan, along the Aleutian Islands chain, and from the Gulf of Alaska. The most recent distant tsunami event, known as the Tōhoku tsunami, occurred on March 11, 2011, when a magnitude ($M_W$) 9.0 earthquake occurred 129 km (80 miles) offshore from the coast of Sendai, northeast Honshu, Japan (Allan and others, 2012a). This earthquake triggered a catastrophic tsunami that within minutes inundated the northeast coast of Japan and swept far inland; most recent reports indicate 18,000 dead (Suppasri and others, 2014). Measurements derived from a tide gauge on the affected shore (Ayukawa, Ishinomaki, Miyagi Prefecture)

recorded a tsunami amplitude of 7.6 m before the gauge was destroyed by the initial tsunami wave (Yamamoto, 2011), while post-tsunami surveys indicate that the tsunami water levels within the inundation zone reached as high as 19.5 m (Mori and others, 2011). The tsunami also propagated eastward across the Pacific Ocean, affecting coastal communities in Hawaii and along the west coast of the continental United States—Washington, Oregon, and California.

Damage in Oregon, Washington, and northern California from the tsunami was almost entirely confined to harbors, including Depoe Bay, Coos Bay, and Brookings in Oregon, and Crescent City, California. Damage was moderated by the arrival of the tsunami's highest waves during a relatively low tide (Allan and others, 2012a). At Crescent City, an open-coast breakwater, the to-and-fro surge of the water associated with the tsunami waves overturned and sank 15 vessels and damaged 47; several boats were swept offshore. Flood damage also occurred during the early hours of March 12. For example, an RV park near the mouth of Elk Creek was flooded when a 1.05-m (3.4 ft) tsunami wave arrived, coinciding with high tide. The total damage to the Crescent City harbor and from the effects of the flooding has been placed at $20 million (Wilson and others, 2013). At Brookings on the southern Oregon coast, 12 fishing vessels put to sea at about 6 am, prior to the arrival of the tsunami waves. However, the *Hilda*, a 220-ton fishing boat and the largest in the harbor, broke loose in the wave-induced currents; the vessel washed around the harbor, smashing into and sinking several other boats. Much of the commercial part of the harbor and about one third of the sports basin were destroyed; the total damage has been estimated at about $10 million (Allan and others, 2012a).

Prior to the Tōhoku tsunami, the most significant distant tsunami occurred on March 27, 1964, when a magnitude ($M_W$) 9.2 earthquake occurred near Prince William Sound in Alaska. The earthquake generated a catastrophic local tsunami, and effects of the tsunami were noted around the Pacific Basin. In Oregon the tsunami caused significant damage to infrastructure in the coastal communities of Seaside and Cannon Beach and killed four people camping along Beverly Beach in Lincoln County.

In 2009, DOGAMI initiated a multi-year study to accelerate remapping of the Oregon coast for tsunami inundation using state-of-the-art computer modeling and laser-based terrain mapping (lidar). The outcome of this effort was the creation of new and more accurate tsunami evacuation maps for the entire coast. DOGAMI, in collaboration with researchers at Oregon Health and Science University (OHSU) (Zhang and Baptista), Oregon State University (Goldfinger), and the Geological Survey of Canada (Wang), developed a new approach to produce a suite of next-generation tsunami hazard maps for Oregon (Priest and others, 2009; Witter and others, 2010). Modeling tsunami inundation on the southern Oregon coast began late in 2009 and consisted of a range of scenarios, including 15 Cascadia events and two distant earthquake source events (e.g., 1964 Prince William Sound earthquake magnitude [$M_W$] 9.2 earthquake; Witter, 2008). The last of the suite of new evacuation maps (TIM series) was released in 2013; the maps are also available in an online tsunami hazard portal (http://nvs.nanoos.org/TsunamiEvac).

Associated with great Cascadia earthquakes is a nearly instantaneous lowering (subsidence) of the coast by ~0.4 m (1.3 ft) to as much as 3 m (9.8 ft) (Witter and others, 2003). This process equates to raising sea level by the same amount along the entire Pacific Northwest coastline. Following the earthquake, coastal erosion is expected to accelerate everywhere as beaches and shorelines adjust to a new equilibrium condition that, over time, would likely decrease asymptotically (Komar and others, 1991). Komar and others have suggested that the extensive development of sea stacks offshore from Bandon on the southern Oregon coast may be evidence for that erosion response following the last major subduction zone earthquake in 1700. Over the past century, the erosion appears to have stabilized as there is little evidence for any progressive erosion trend. This suggests that uplift (estimated to be ~0.6 to 1.1 m) of the south coast has effectively ceased due to the Cascadia subduction zone becoming locked

again; strain is now building toward the next major earthquake. With release of that energy and the resulting land subsidence, cliff erosion along the Bandon shore (and elsewhere on the Oregon coast) would be expected to begin again.

## 2.3 Coastal Geomorphology

On the basis of geology and geomorphology, the Lane-Douglas shoreline can be broadly divided into three morphological beach types. These are depicted **Figure 2-6** to **Figure 2-8** and include:

1. ***Dune-backed beaches:*** Dune-backed beaches make up the entire length of the Douglas County shoreline and ~50% of the Lane County shoreline. The geomorphology of the beaches can be generalized as having wide, dissipative surf zones with low, sloping foreshores that are backed by high dunes containing significant sand volume (**Figure 2-1**). The highest dunes are concentrated in the region between the Siltcoos and Siuslaw Rivers (**Figure 1-1**), where the dunes reach heights of 17 to 20 m [56–66 ft], NAVD88 (**Figure 2-9**). Dunes along Heceta Beach and on the Umpqua Spit have generally lower dune crests and more consistent alongshore uniformity. These later dunes range in height from 9 to 11 m [30–36 ft] NAVD88 (**Figure 2-9**). Along the length of the coast, mean dune crest heights are ~11.7 m (38.4 ft), with most dunes being in the range of 8 to 16 m (26–52 ft). The average beach slope (tan $\beta$) for dune-backed beaches is summarized in **Figure 2-10**, where it is apparent that slopes vary significantly along the coast, with the lowest mean slopes occurring along Heceta Beach (mean = 0.025), and are generally steepest south of the Siuslaw River and north of the Siltcoos River (mean = 0.04). Overall, mean beach slopes average ~0.032.
2. ***Cliffed shore:*** Cliffed and rocky shorelines are the dominant geomorphic features at the northern end of the Lane County, accounting for ~26% of the geomorphic "type" in the county (**Figure 2-2**). Examples of this type of shore exist around Sea Lion Point and Heceta Head. This particular shore type invariably consists of near-vertical cliffs that plunge into the ocean. In some cases, the cliffs may be fronted by rock platforms and/or talus.
3. ***Bluff-backed beaches fronted by gravel and sand:*** Bluff-backed beaches fronted by a wide, dissipative sand beach and/or a gravel beach-face are the third most prominent geomorphic type in Lane and Douglas counties, comprising ~25% of the shore (**Figure 2-3**). This particular geomorphic type dominates the shoreline in the vicinity of Stonefield Beach and along Roosevelt Beach (**Figure 1-1**). The bluffs that back the beaches vary in height from ~5 m (16 ft) to greater than 70 m (230 ft). Beach slopes (tan $\beta$) seaward of the bluffs are similar to those observed throughout Lane and Douglas counties. Geomorphically, these beaches may be characterized as "composite" using the terminology of Beaulieu (1973) and Jennings and Shulmeister (2002), such that the beaches consist of a wide dissipative sandy beach, backed by a steeper upper foreshore composed of gravels.

**Figure 2-6. Geomorphic classification of coastal Douglas County.**

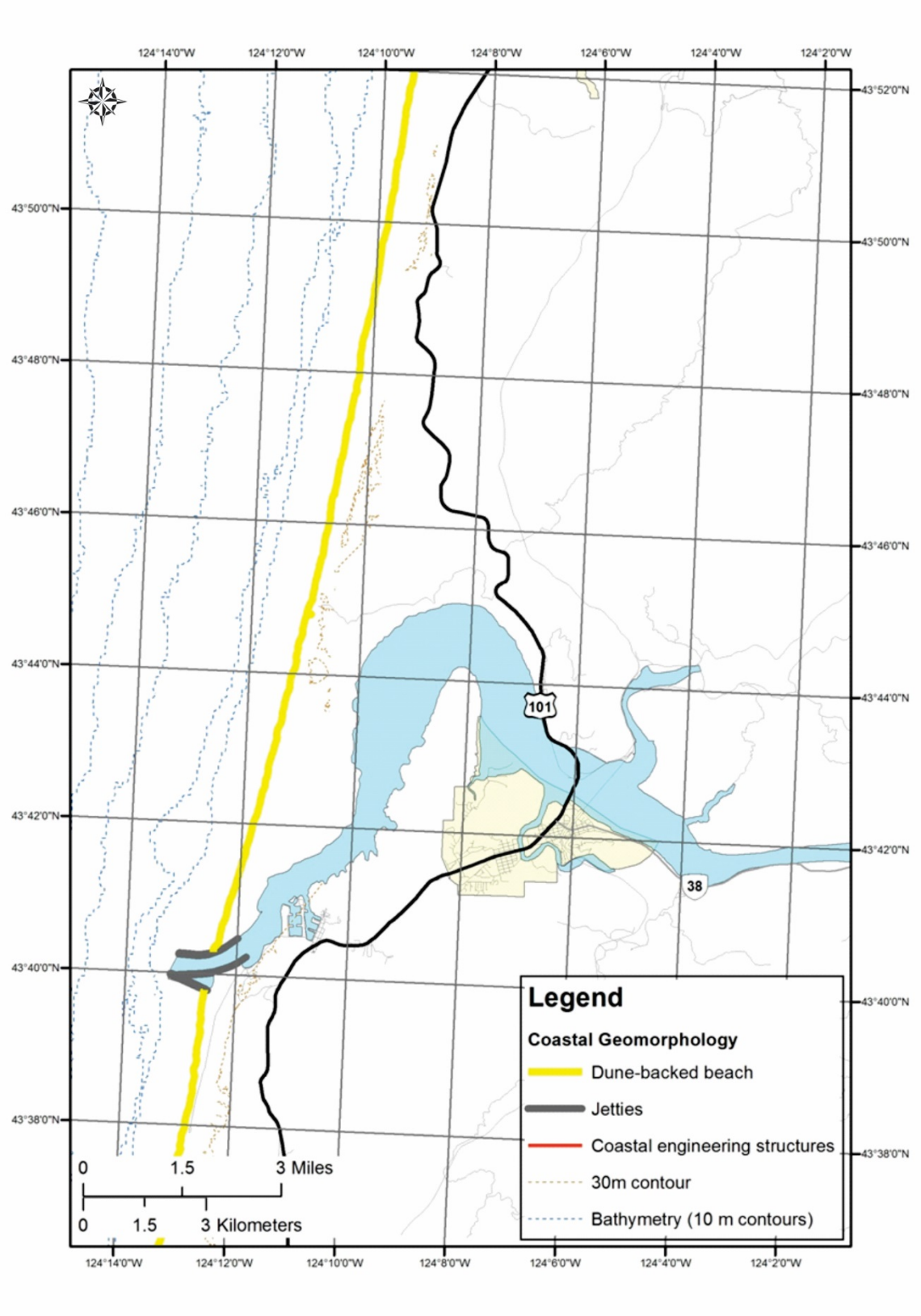

**Figure 2-7. Geomorphic classification of coastal southern Lane County.**

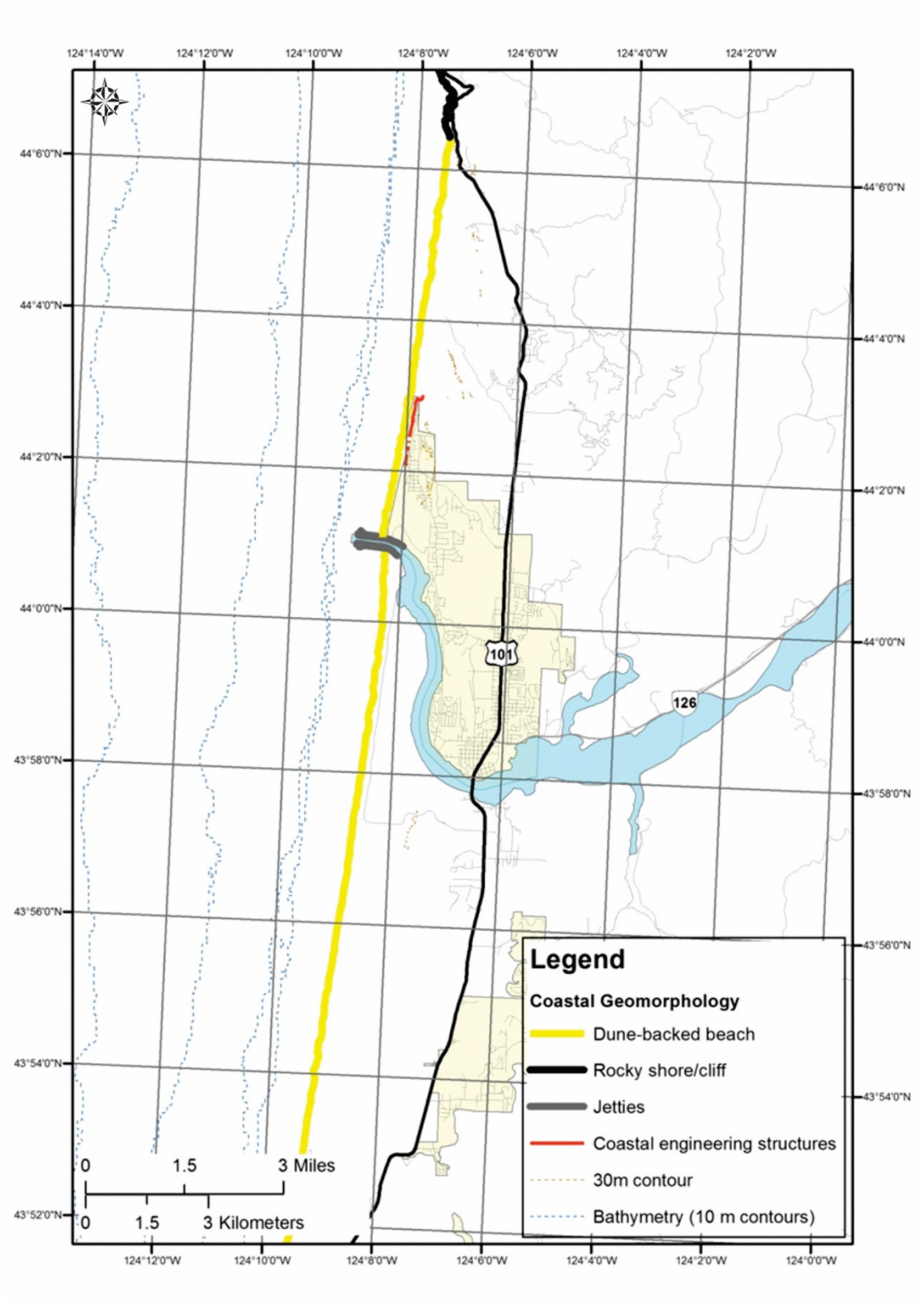

**Figure 2-8. Geomorphic classification of coastal northern Lane County.**

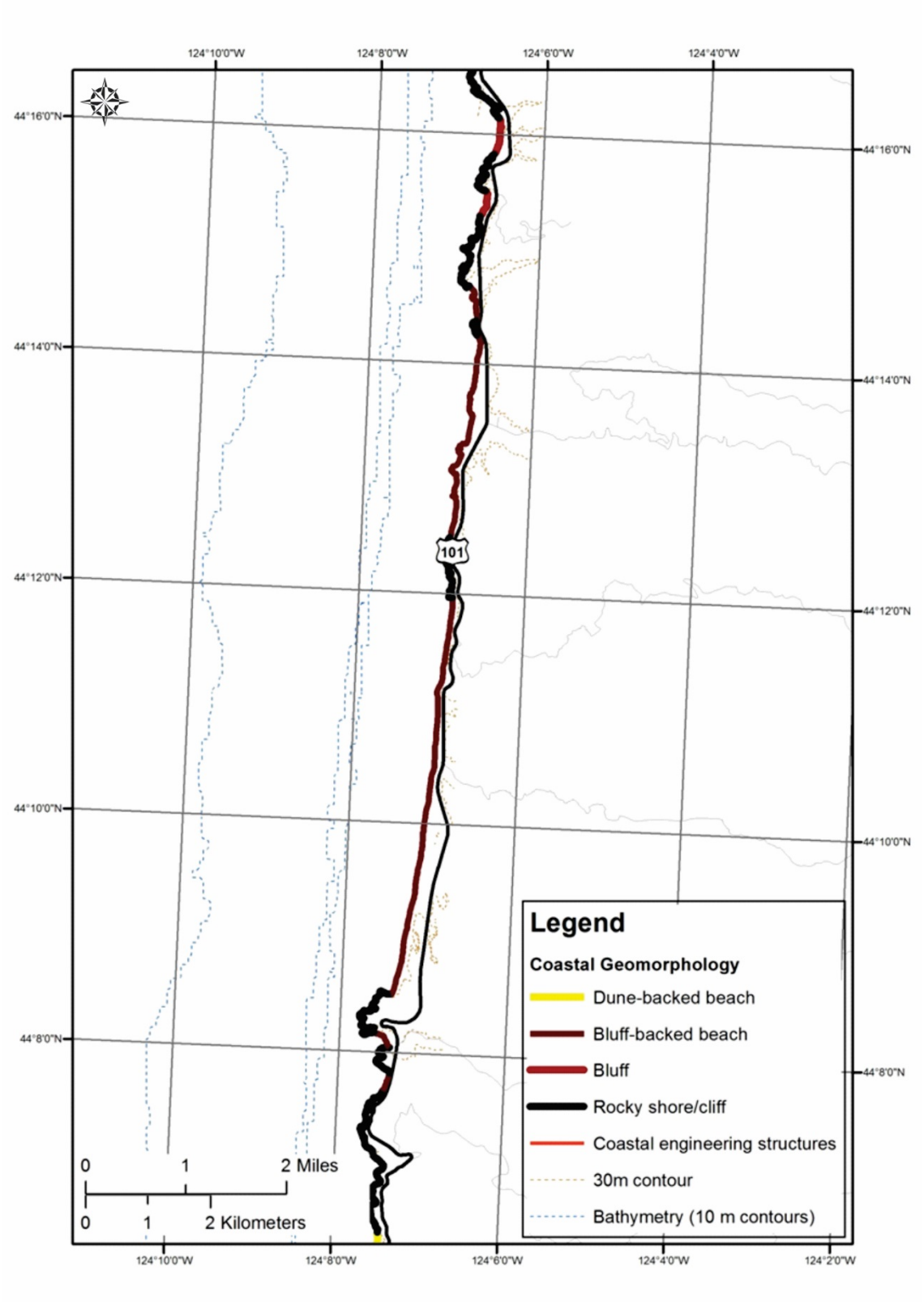

**Figure 2-9. Lane and Douglas County dune crest heights.**

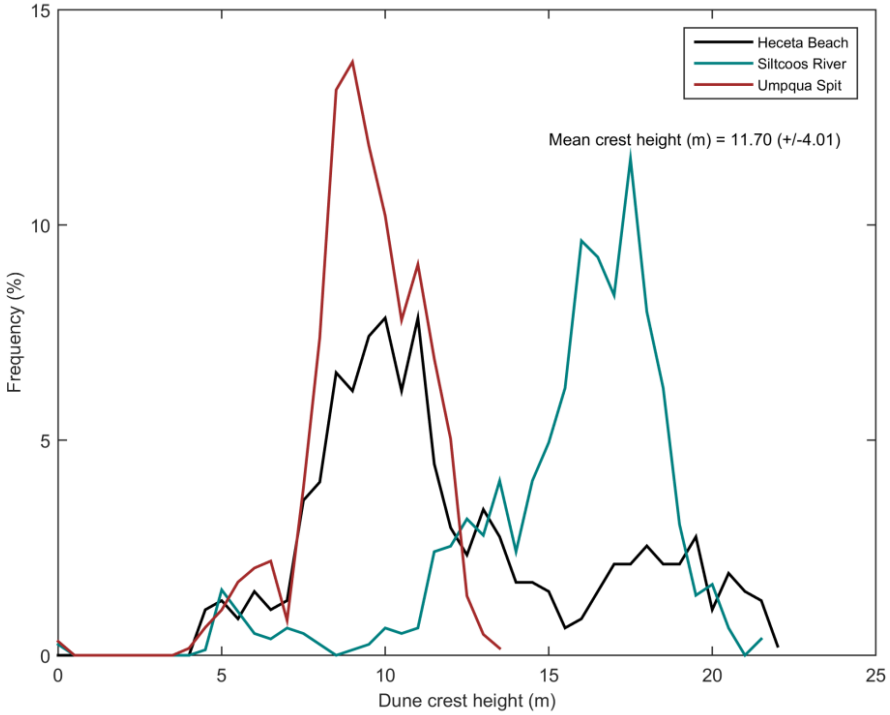


**Figure 2-10. Lane and Douglas County beach slopes.**

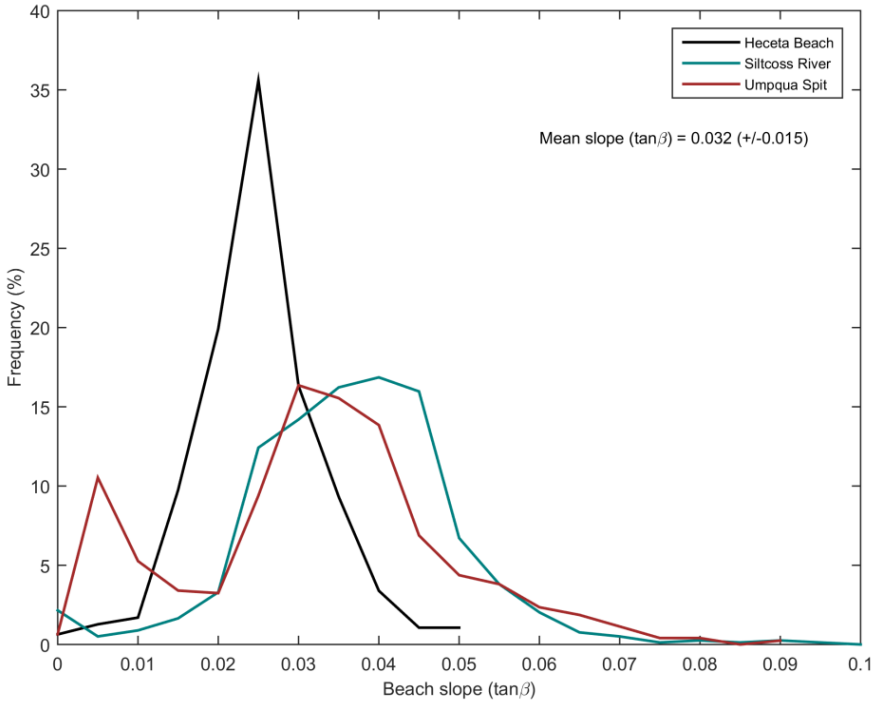

## 2.4 Coastal Erosion and Flood History

### 2.4.1 Lane-Douglas historical shoreline positions

This section presents a qualitative discussion of large-scale morphological changes derived from analyses of historical and contemporary shorelines derived for the Lane and Douglas County coastline. This summary stems from work undertaken by previous researchers (Ruggiero and others, 2013), as well as from updated analyses that incorporate recent lidar measurements of the coast.

National Ocean Service (NOS) Topographic (T)-sheet shoreline positions covering the 1920s were previously obtained from NOAA. These lines reflect the Mean High Water (MHW) line mapped by early NOS surveyors, on an average tide typically in mid- to late summer. Additional shorelines were derived from a variety of other sources including 1967 digital orthophotos (Ruggiero and others, 2013) and 1997, 1998, 2002, and 2010 lidar data. Pre-lidar historical shorelines use the High Water Line (HWL) as a shoreline proxy. The HWL has been used by researchers for more than 150 years because it could be visually identified in the field or from aerial photographs. In contrast, shorelines derived from lidar data are datum-based and can be extracted objectively using a tidal datum, such as Mean High Water (MHW) or Mean Higher High Water (MHHW). Studies by Moore (2000) and Ruggiero and others (2003) noted that HWL-type shoreline proxy is virtually never coincident with datum-based MHW-type shorelines. In fact, they are almost universally estimated to be higher (landward) on the beach profile when compared to MHW shorelines (Ruggiero and others, 2013). According to Ruggiero and others, the average absolute horizontal offset between the HWL and MHW ranges from ~6 m (~19 ft) to as much as 50 m (164 ft), while the average is typically less than 20 m (65 ft). Offsets are typically greatest on flat, dissipative beaches where the wave runup may be large and smallest where beaches are steep (e.g., gravel beaches).

Estimates of the uncertainty of HWL shoreline measurements have been assessed in a number of studies (e.g., Moore, 2000; Ruggiero and others, 2013). These uncertainties reflect the following errors: 1) mapping methods and materials for historical shorelines (including the offset between the HWL and MHW shoreline), 2) the registration of shoreline positions relative to Cartesian coordinates, and 3) shoreline digitizing. Average uncertainties are summarized in **Table 2-1**.

The approach adopted here is to describe the broad morphological changes identified along the coast, beginning in the north in the Heceta littoral cell, and progressing southward toward Cape Arago. **Figure 2-11** presents both long- (1920s to 2002 period) and short-term (1967 to 2002 period) estimates of erosion rates for the Coos and Heceta littoral cells, determined by Ruggiero and others (2013). Recall that the Coos cell extends from Cape Arago in the south to Heceta Head in the north, while the Heceta cell occurs north of Heceta Head and south of Cape Perpetua.

**Table 2-1. Average uncertainties for Pacific Northwest shorelines (Ruggiero and others, 2013).**

| | NOS T-sheets (1800s to 1950s) | DRGs (1940s to 1990s) | Aerial Photography (1960s to 1990s) | Lidar |
|---|---|---|---|---|
| Total shoreline position uncertainty | 18.3 m (60 ft) | 21.4 m (70 ft) | 15.1 m (50 ft) | 4.1 m (14 ft) |

#### 2.4.1.1 Heceta Beach

Over the long term, the analyses of Ruggiero and others (2013) indicate that the Heceta cell has been gradually eroding at a rate of ~–0.4 m/yr (–1.3 ft/yr). However, since the late 1960s the short-term rate has decreased such that this section of shore shows no significant trend, with the measured rates fluctuating between minor erosion and accretion.

#### 2.4.1.2 Coos Cell

South of Heceta Head in the Coos littoral cell, the shoreline variability indicates a variety of responses over the long term (1920s to 2002 period). Adjacent to each of the estuaries (**Figure 2-11**), the beaches accreted significantly, reaching mean rates of ~6.5 m/yr (21 ft/yr) at the Siuslaw River, and as much as 8 m/yr (26 ft/yr). These changes are entirely due to construction of jetties at the mouths of the Siuslaw, Umpqua, and Coos estuaries. For example, 69 acres of new land were created south of the Siuslaw jetty and 156 acres to the north (Lizarraga-Arciniega and Komar, 1975). The larger accumulation in the north resulted from the jetty construction, thus leaving a larger area to be filled. Furthermore, most of these changes took place within a few decades following jetty construction, after which the accretion rates slowed.

North of the Umpqua River and south of the Siuslaw River, the beaches accreted at an average rate of ~0.5 m to 1 m/yr (1.6–3.3 ft/yr) over the long term (1920s to 2002). In contrast, south of the Umpqua and north of the Coos (**Figure 2-11**), the beaches and dunes eroded slowly at rates of ~–0.1 m/yr (0.3 ft/yr).

Since the 1960s, the patterns of shoreline response in the Coos cell show significantly greater variability (**Figure 2-11**). Aside from the Siuslaw River jetty, which continued to experience considerable accretion (~4–6 m/yr [13–20 ft/yr]) up to the present, the Umpqua jetties indicate generally negligible change over the past four decades (i.e., minor erosion and accretion), while erosion has characterized the response of the beach next to the north jetty at Coos Bay. This latter response was largely due to the occurrence of several major storms that occurred in the late 1990s.

The overall pattern continued to reflect one of erosion south of the Umpqua River, while accretion remains generally prevalent north of the river. In general, the erosion rates increased to ~–0.5 m/yr (–1.6 ft/yr) to as much as –2 m/yr (–6.6 ft/yr) south of the Umpqua. North of the Umpqua, the beach and shoreline variability ranged by as much as ± 2 m/yr (–6.6 ft/yr), with some of the greatest change taking place adjacent to the mouths of smaller creeks (e.g., Siltcoos and Tahkenitch Creek). Furthermore, the analyses suggest localized re-orientation of the shorelines, with generally higher erosion on the north side of Tenmile, Tahkenitch, and Siltcoos creeks and the Umpqua River (**Figure 2-11**, dashed red lines, middle panel), which progressively changes to one of accretion approximately 10 km north of the creeks and river.

**Figure 2-11. Long- (1920s through 2002) and short-term (1960 through 2002) shoreline change rates for the Coos and Heceta littoral cells. Shaded areas depict uncertainty in the shoreline change calculations. Dashed red lines depict shoreline segments where erosion has occurred adjacent to creeks and rivers, with subsequent alongshore displacement of sand to the north (Ruggiero and others, 2013).**

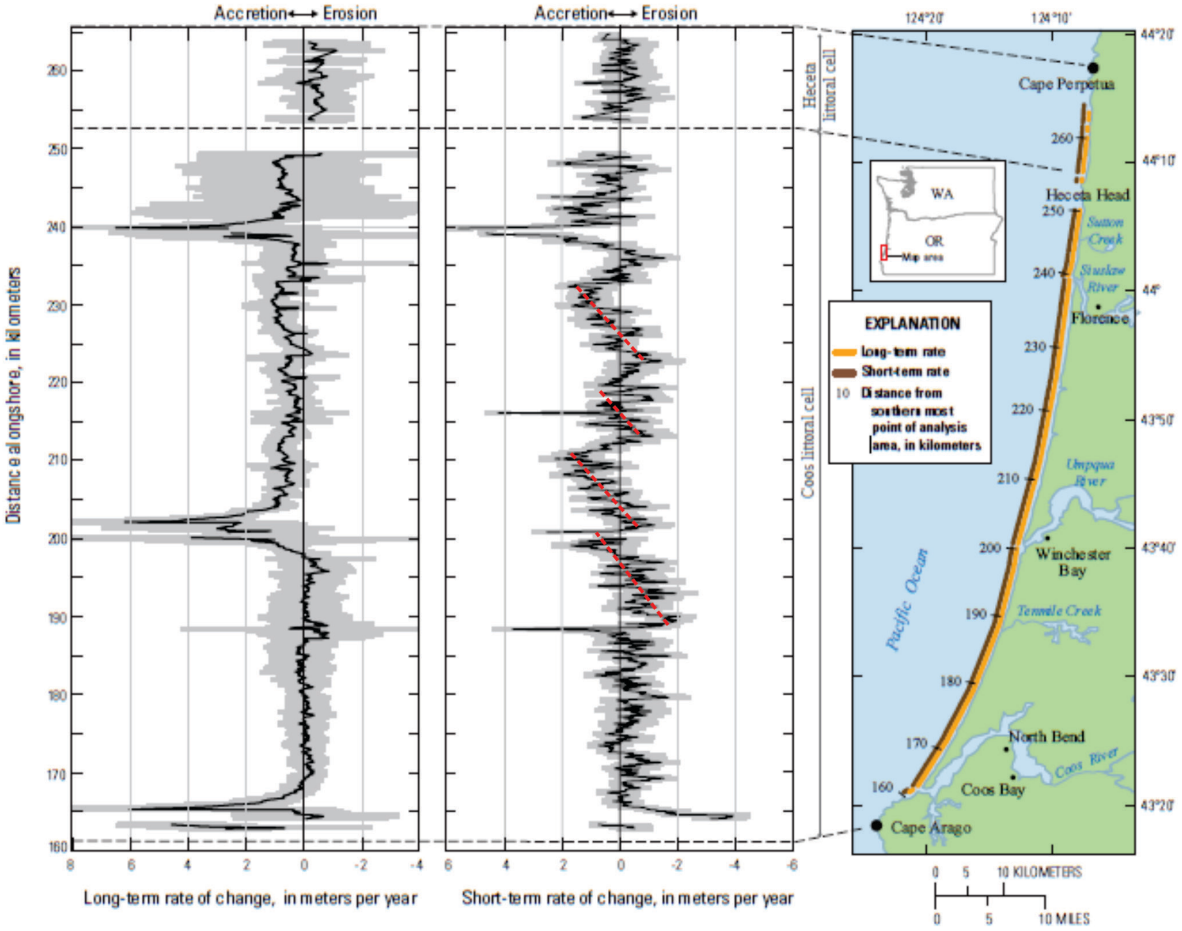

# 3.0 BEACH AND BLUFF MORPHOLOGY ASSESSMENTS

Field surveys were undertaken throughout Lane and Douglas counties in the winter and summer of 2014; the former was used to better define the winter variability. These surveys serve two important objectives:

1) To establish beach profile transects along discrete but representative sections of shoreline geomorphology/geology, including sections of coast where coastal engineering structures have been constructed, for the purposes of coastal hydraulic analyses.
2) To provide representative measurements of the beach in its winter state whether it be derived from lidar or GPS data, in order to define the morphology, elevation, and slope of the beach face for use in subsequent wave runup and overtopping computations.

Surveying along the Lane and Douglas County coast was carried out in March 2014 and again in July. The surveys were completed late in the winter season when Oregon beaches are typically in their most eroded state (Aguilar-Tunon and Komar, 1978; Komar, 1997; Allan and Komar, 2002a; Allan and Hart, 2008). In total, 57 beach profile transects were established along the length of Lane County[1] (**Figure 3-1** and **Figure 3-2**) and can be subdivided according to the following littoral cells:

- Heceta Beach: 24 sites;
- Heceta Head: 6 sites;
- Muriel Ponsler: 7 sites; and
- Stonefield Beach 20 sites.

## 3.1 Survey Methodology

Beach profiles that are oriented perpendicular to the shoreline can be surveyed using a variety of technologies, including a simple graduated rod and chain, surveying level and staff, total station theodolite and reflective prism, lidar airborne altimetry, and Real-Time Kinematic Differential Global Positioning System (RTK-DGPS) technology. Traditional techniques such as leveling instruments and total stations are capable of providing accurate representations of the morphology of a beach but are demanding in terms of time and effort. At the other end of the spectrum, high-resolution topographic surveys of the beach derived from lidar data are ideal for capturing the three-dimensional state of the beach over an extended length of coast within a matter of hours. Other forms of lidar technology are now being used to measure nearshore bathymetry out to moderate depths but are dependent on water clarity. However, lidar technology remains expensive and is impractical along small segments of shore and, more importantly, the high cost effectively limits the temporal resolution of the surveys and hence the ability of the end-user to understand short-term changes in the beach morphology (Bernstein and others, 2003).

Within this range of technologies, the application of RTK-DGPS for surveying the morphology of both the subaerial and subaqueous portions of the beach has effectively become the accepted standard (Morton and others, 1993; Ruggiero and Voigt, 2000; Bernstein and others, 2003; Ruggiero and others, 2005) and is the surveying technique used in this study. The Global Positioning System (GPS) is a worldwide radio-navigation system formed from a constellation of 24 satellites and their ground stations, originally developed by the U.S. Department of Defense; in 2007 the Russian government made their GLONASS satellite network available increasing the number of satellites to ~46 (as of February 2011). In its simplest form, GPS can be thought of as triangulation with the GPS satellites acting as reference points, enabling users to calculate their positions to within several meters (e.g., using inexpensive off-the-shelf handheld

[1] No transects were established along the Douglas County shoreline as the entire shore length is unpopulated.

units), while survey-grade GPS units are capable of providing positional and elevation measurements that are accurate to a centimeter. At least four satellites are needed mathematically to determine an exact position, although more satellites are generally available. The process is complicated because all GPS receivers are subject to error, which can significantly degrade the accuracy of the derived position. These errors include the GPS satellite orbit and clock drift plus signal delays caused by the atmosphere and ionosphere and multipath effects (where the signals bounce off features and create a poor signal).

For example, hand-held autonomous receivers have positional accuracies that are typically less than about 10 m (<~30 ft), but can be improved to less than 5 m (<~15 ft) using the Wide Area Augmentation System (WAAS). This system is essentially a form of differential correction that accounts for the above errors, which is then broadcast through one of two geostationary satellites to WAAS-enabled GPS receivers.

Greater survey accuracies are achieved with differential GPS (DGPS) using two or more GPS receivers to simultaneously track the same satellites, thereby enabling comparisons to be made between two sets of observations. One receiver is typically located over a known reference point and the position of an unknown point is determined relative to that reference point. With the more sophisticated 24-channel dual-frequency RTK-DGPS receivers, positional accuracies can be improved to the subcentimeter level when operating in static mode and to within a few centimeters when in RTK mode (i.e., as the rover GPS is moved about). In this study we used Trimble® 24-channel dual-frequency R7/R8 GPS receivers. This system consists of a GPS base station (R7), Zephyr Geodetic™ antenna (model 2), HPB450 radio modem, and R8 "rover" GPS (**Figure 3-3**). Trimble reported that the R7/R8 GPS systems have horizontal errors of approximately ±1 cm + 1 ppm (parts per million × the baseline length) and ±2 cm in the vertical (Trimble, 2005).

To convert a space-based positioning system to a ground-based local grid coordinate system, a precise mathematical transformation is necessary. Although some of these adjustments are accomplished by specifying the map projection, datum, and geoid model prior to commencing a field survey, an additional transformation is necessary whereby the GPS measurements are tied to known ground control points (**Figure 3-4**). This latter step is called a GPS site calibration, such that the GPS measurements are calibrated to ground control points with known vertical and horizontal coordinates using a rigorous least-squares adjustment procedure. The calibration is initially undertaken in the field by using the Trimble TSC2 GPS controller and then is re-evaluated in the office by using Trimble Business Office software (v2.5).

**Figure 3-1. Location map of beach profiles measured along the Heceta Beach shoreline (transects 1 to 25). Yellow circles denote the locations of benchmarks used in local site calibrations.**

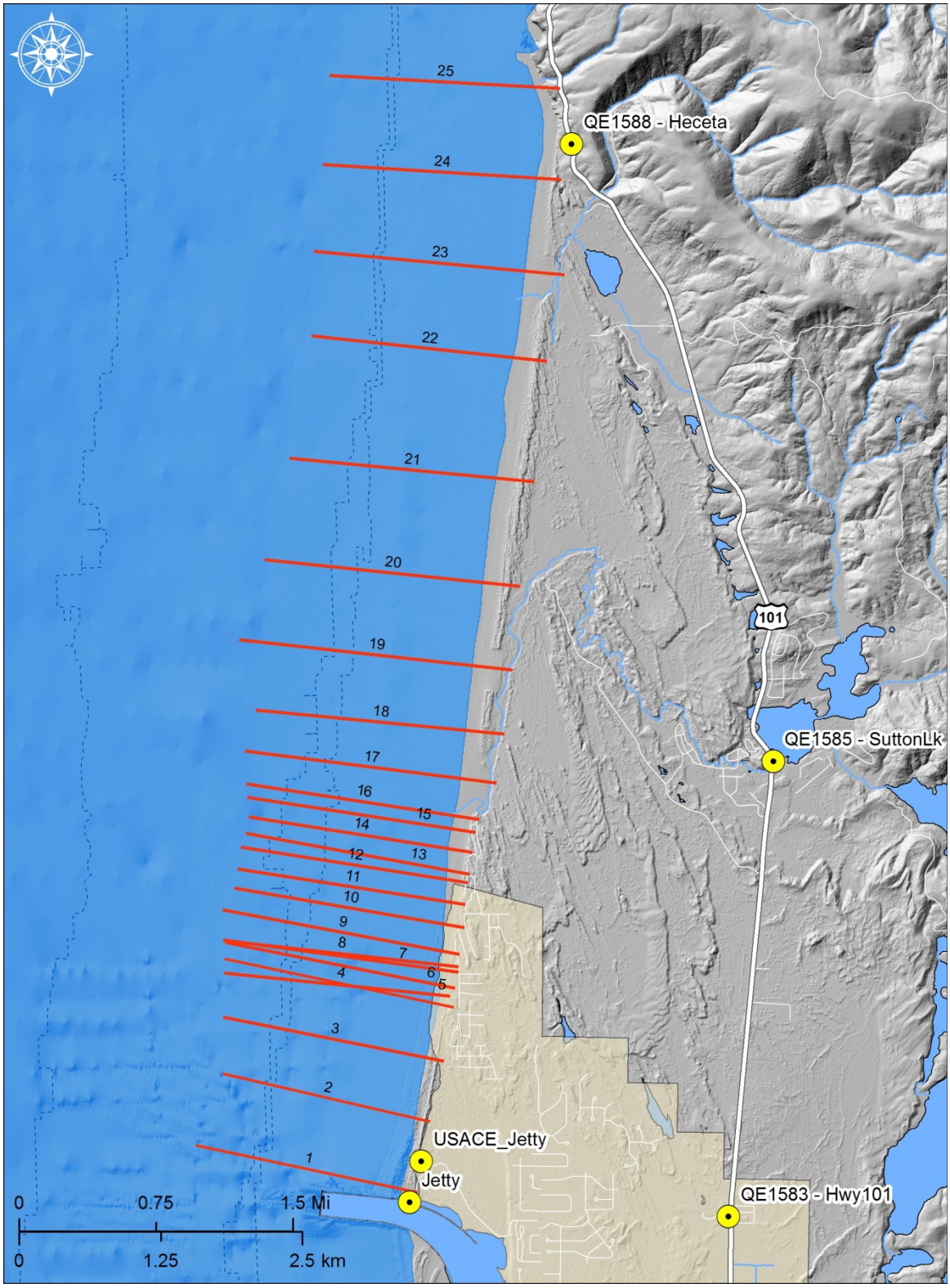

**Figure 3-2. Left) Location map of beach profiles measured adjacent to Heceta Head and along Roosevelt Beach (transects 26–36); Right) and along Stonefield Beach (transects 36–57). Yellow circles denote the locations of benchmarks used in local site calibrations.**

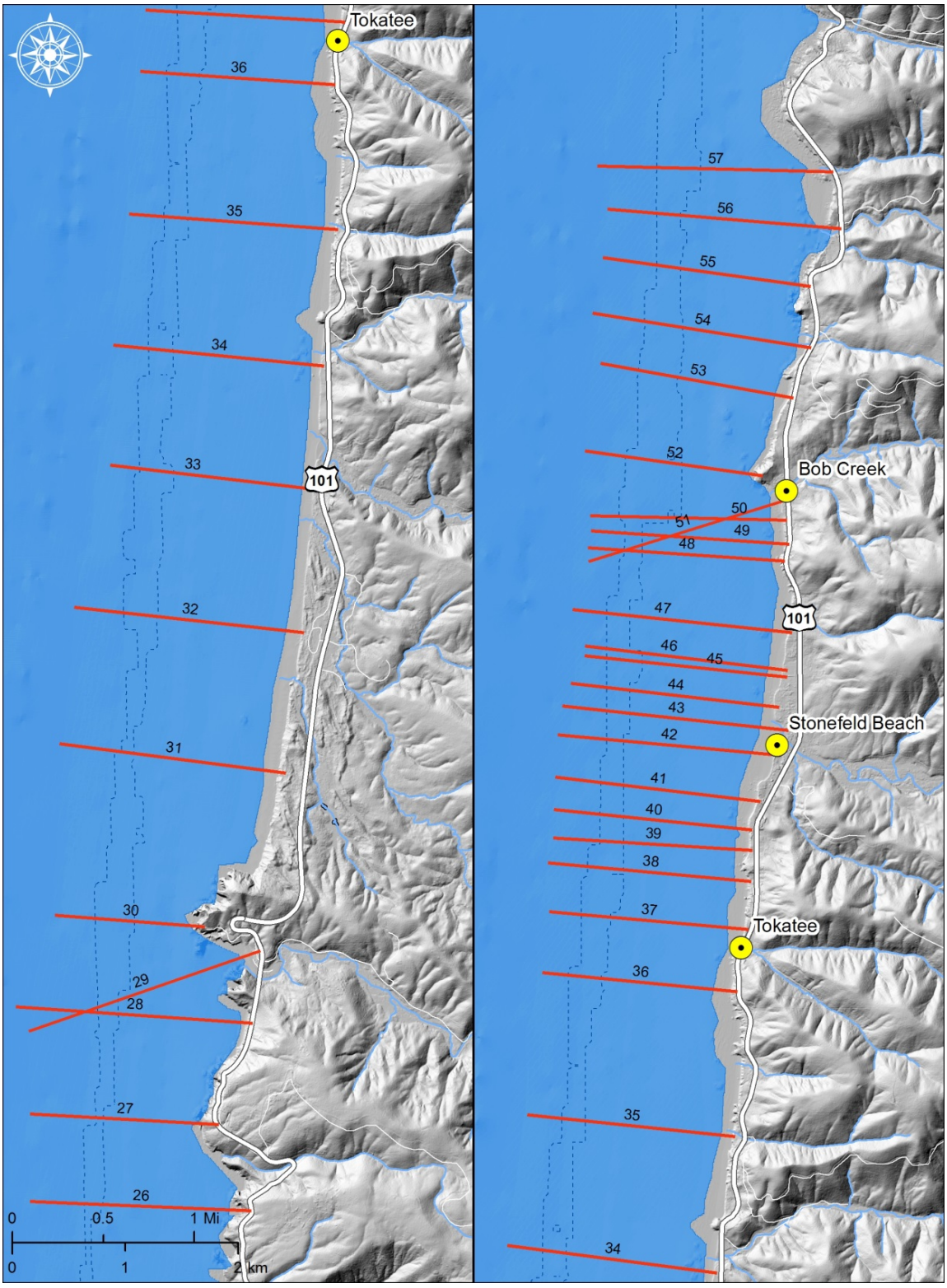

**Figure 3-3. The Trimble R7 base station antenna in operation on the Tillamook Plains. Corrected GPS position and elevation information is then transmitted by an HPB450 Pacific Crest radio to the R8 GPS rover unit.**

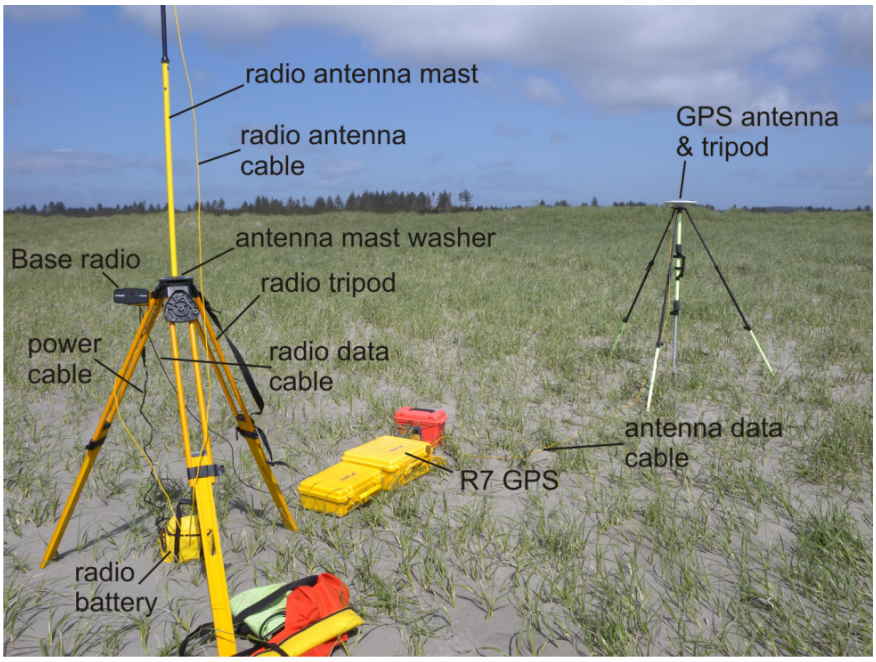


**Figure 3-4. A 180-epoch calibration check is performed on a survey monument (near QE1588) established at the north end of the Coos littoral cell in northern Lane County. This procedure is important for bringing the survey into a local coordinate system and for reducing errors associated with the GPS survey (Photo: J.C. Allan, DOGAMI).**

### 3.1.1 Lane and Douglas County survey control procedures

Survey control (**Table 3-1**) along the Lane and Douglas County shore was provided by occupying multiple benchmarks established by the DOGAMI Coastal Field Office. The approaches used to establish the benchmarks are fully described by Allan and Hart (2007, 2008).

Coordinates assigned to the benchmarks (**Table 3-1**), were derived by occupying a Trimble R8 GPS receiver over the established benchmark, which then receives real-time kinematic corrections via the Oregon Real Time GPS Network (ORGN, http://www.theorgn.net/). The ORGN is a network of permanently installed, continuously operating GPS reference stations established and maintained by ODOT and partners (essentially a CORS network similar to those operated and maintained by the National Geodetic Survey [NGS]) that provide real-time kinematic (RTK) correctors to field GPS users over the internet via cellular phone networks. As a result, GPS users that are properly equipped to take advantage of these correctors, such as the Trimble system used in this study, can survey in the field to the 1-cm horizontal accuracy level in real time. Each benchmark was observed on at least two occasions, at different times of the day or on alternate days; the derived values were then quality controlled, and, if reasonable, were averaged. Furthermore, additional checking was undertaken for each of the GPS base station sites (**Table 3-1**), by comparing the multi-hour GPS measurements to coordinates and elevations derived using the Online Positioning User Service (OPUS) maintained by the NGS (http://www.ngs.noaa.gov/OPUS/ [Soler and others, 2011]). OPUS provides a simplified way to access high-accuracy National Spatial Reference System (NSRS) coordinates using a network of continuously operating GPS reference stations (CORS, http://www.ngs.noaa.gov/CORS/). In order to use OPUS, static GPS measurements are typically made using a fixed-height tripod for periods of 2 hours or greater. OPUS returns a solution report with positional accuracy confidence intervals for adjusted coordinates and elevations for the observed point. In all cases we used the Oregon State Plane coordinate system, southern zone (meters), while the vertical datum is relative to the North American Vertical Datum of 1988 (NAVD88).

**Table 3-1. Survey benchmarks used to calibrate GPS surveys of the beach along the Lane County coastline. Asterisk signifies the location of the GPS base station during each respective survey. NGS denotes National Geodetic survey monument, ORGN signifies Oregon Real Time GPS Network. See Figure 3-1 and 3-2 for benchmark locations.**

| Study Area | Benchmark Primary Identification (PID) Name[1] | Northing (m) | Easting (m) | Elevation (m) |
|---|---|---|---|---|
| Heceta Beach | Siuslaw jetty - DOGAMI/ORGN* | 1208582.256 | 267927.351 | 4.361 |
| | Jetty - DOGAMI/ORGN | 1208465.962 | 267571.981 | 5.913 |
| | QE1585 - NGS/ORGN | 1211795.911 | 271378.059 | 15.374 |
| | QE1583 - NGS/ORGN | 1211277.865 | 267359.026 | 32.218 |
| | QE1588 - NGS/ORGN | 1210173.559 | 276889.273 | 52.453 |
| Stonefield Beach | Stonefield - DOGAMI/ORGN* | 1211496.217 | 290356.734 | 6.699 |
| | Tokatee - DOGAMI/ORGN | 1211176.595 | 288560.847 | 17.424 |
| | Bob Creek - DOGAMI/ORGN | 1211580.022 | 292605.750 | 10.216 |

Notes: Coordinates are expressed in the Oregon State Plane Coordinate System, southern zone (meters) and the vertical datum is NAVD88.

[1] Control provided using both horizontal and vertical values derived by averaging multiple separate GPS occupations with survey control provide by the Oregon Reference Geodetic Network (ORGN).

For each of the discrete shore reaches, the R7 GPS base station was located on the prescribed base station monument (e.g., Siuslaw Jetty, Stonefield, **Table 3-1**), using a 2.0-m fixed-height tripod. Survey control was provided by undertaking 180 GPS epoch measurements (~3 minutes of measurement per calibration site) using the calibration sites indicated in **Table 3-1**, enabling us to perform a GPS site calibration that brought the survey into a local coordinate system. This step is critical in order to eliminate various survey errors that may be compounded by factors such as poor satellite geometry, multipath, and poor atmospheric conditions, which can combine to increase the total error to several centimeters. **Table 3-2** shows the relative variability identified when comparing the standard deviation of all derived benchmark coordinate and elevations values, relative to each successive ORGN/OPUS derivation. As can be seen from **Table 3-2**, differences in the horizontal and vertical values at the various benchmarks were typically less than 2 cm (i.e., within one standard deviation [σ]).

**Table 3-2. Comparison of horizontal and vertical coordinates (expressed as a standard deviation) at each of the benchmark locations, compared to the final coordinates referenced in Table 3-1.**

| Study Area | Benchmark Primary Identification (PID) Name[1] | Northing (m) σ | Easting (m) σ | Elevation (m) σ |
|---|---|---|---|---|
| Heceta Beach | Siuslaw jetty | 0.018 | 0.008 | 0.015 |
| | Jetty | 0.004 | 0.009 | 0.002 |
| | QE1585 | 0.006 | 0.003 | 0.006 |
| | QE1583 | 0.008 | 0.003 | 0.004 |
| | QE1588 | 0.007 | 0.023 | 0.032 |
| Stonefield Beach | Stonefield | 0.008 | 0.004 | 0.009 |
| | Tokatee | 0.002 | −0.007 | −0.047 |
| | Bob Creek | −0.005 | −0.010 | −0.020 |

[1] Control provided using both horizontal and vertical values derived by averaging multiple separate GPS occupations with survey control provide by the Oregon Reference Geodetic Network (ORGN).

A local site calibration having been completed (**Figure 3-4**), cross-shore beach profiles were surveyed with the R8 GPS rover unit mounted on a backpack, worn by a surveyor (**Figure 3-5**). This was undertaken during periods of low tide, enabling more of the beach to be surveyed. The approach was to generally walk from the landward edge of the primary dune or bluff edge, down the beach face, and out into the ocean to approximately wading depth. A straight line, perpendicular to the shore was achieved by navigating along a pre-determined line displayed on a hand-held Trimble TSC2 computer controller, connected to the R8 receiver. The computer shows the position of the operator relative to the survey line and indicates the deviation of the GPS operator from the line. The horizontal variability during the survey is generally minor, being typically less than about ±0.25 m either side of the line (**Figure 3-6**), which results in negligible vertical uncertainties due to the relatively uniform nature of beaches characteristic of much of the Oregon coast (Ruggiero and others, 2005). From our previous research at numerous sites along the Oregon coast , this method of surveying can reliably detect elevation changes on the order of 4-5 cm, that is, well below normal seasonal changes in beach elevation, which typically varies by 1–2 m (3–6 ft) (Ruggiero and others, 2005; Allan and Hart, 2007, 2008).

Analysis of beach survey data involved several stages. The data were first imported into Mathworks® MATLAB®[2] using a customized script. A least squares linear regression was then fit to the profile data. The purpose of this script is to examine the reduced data and eliminate data point residuals (e.g., **Figure 3-6**) that exceed a ±0.75-m threshold (i.e., the outliers) either side of the predetermined profile line. The data are then exported into a Microsoft® Excel® spreadsheet for archiving purposes. A second MATLAB script uses the Excel profile spreadsheet to plot the survey data (relative to the earlier surveys) and outputs the generated image as a Portable Network Graphics (png) file. Appendix C shows the reduced beach profile plots for the Lane and Douglas County transects.

To supplement the GPS beach and bluff data, high-resolution lidar data measured by Watershed Sciences, Inc. (WSI) in 2009 for DOGAMI were also analyzed and integrated into the beach profile dataset. This was especially important for backshore areas where it was not possible to survey easily with the GPS gear. In addition, lidar data acquired by the USGS/NASA/NOAA in 1997, 1998, and 2002 were used to extend the time series of the beach and bluff profile data. In particular, the 1998 lidar data measured at the end of the major 1997-1998 El Niño was analyzed, providing additional measurements of the beach in an eroded state that can be compared with more recent winter surveys of the beach. The 1997, 1998, and 2002 lidar data were downloaded from NOAA's Coastal Service Center[3], gridded in Esri® ArcGIS® using a triangulated irregular network (TIN) algorithm, and distance and elevation data were extracted from the grid lidar digital elevation models (DEMs).

**Figure 3-5. Surveying the morphology of the beach at Bandon using a Trimble 5800 "rover" GPS.**

[2] Computer programming languages.

[3] http://www.csc.noaa.gov/digitalcoast/data/coastallidar/index.html

**Figure 3-6. Residuals of GPS survey points relative to zero (transect) line. Example reflects the Cannon Beach 10 profile line. Dark grey shading indicates 68.3% of measurements located ±0.15 m (1σ) from the transect line, while 95.5% (2σ) of the measurements are located within ±0.30 m of the profile line (grey shading).**

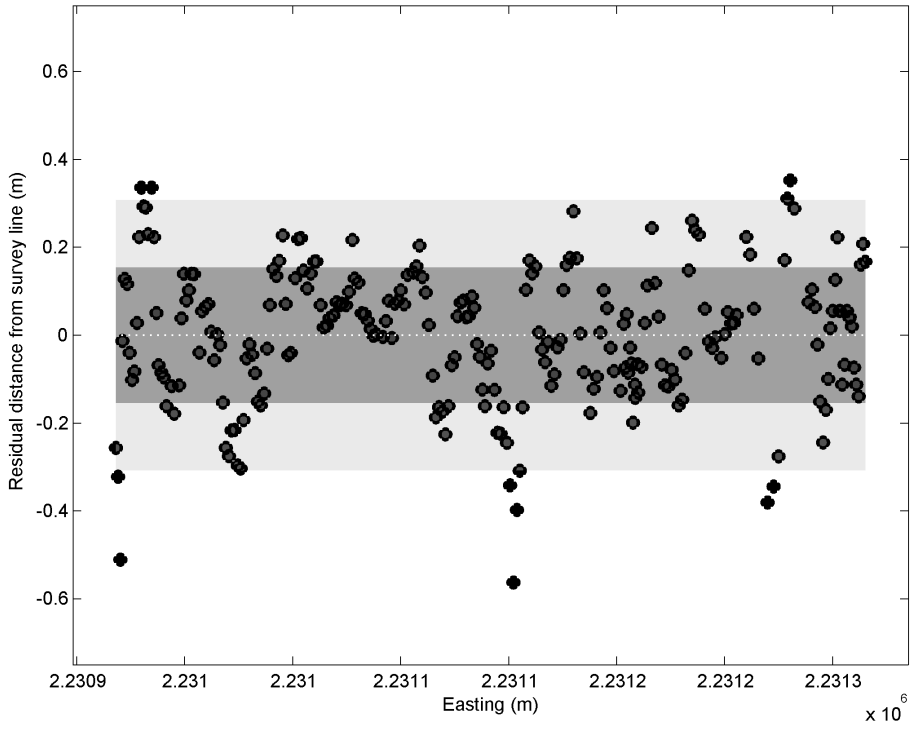


## 3.2 Beach Characterization

Analyses of the beach profile data were undertaken using additional scripts developed in MATLAB. These scripts require the user to interactively locate the positions of the seaward edge and crest of the primary frontal dune (PFD) backing the beach, and then evaluate the beach-dune junction ($E_j$) elevations and beach slopes (tan $\beta$) for the 1997, 1998, 2002, 2008-2009, and 2014 surveys along each of the profile sites. Beach slope was determined by fitting a linear regression through the measured profile data. In all cases, the slope of the beach face was determined to be the region of the beach located between Mean Sea Level (~1.4 m, MLLW) and the highest observed tide (~3.8 m, MLLW), an approach that is consistent with methodologies adopted by (Ruggiero and others, 2005; Stockdon and others, 2006). Determination of the location of the beach-dune junctions ($E_j$) was accomplished interactively using the MATLAB scripts and from local knowledge of the area. In general, the beach-dune junction ($E_j$) reflects a major break in slope between the active part of the beach face and the toe location of the primary dune or bluff. For most sites along the Oregon coast, beach-dune junctions ($E_j$) typically occur at elevations between about 4 and 6 m (NAVD88). **Figure 3-7** provides an example of the identified beach-dune junction ($E_j$) for one site, LD 22, after it has been eroded (described in **SECTION 7**), and is located at the north end of Heceta Beach (**Figure 3-1**). In this example, it is apparent that the dune has experienced significant accretion during the past two decades: the dune has aggraded vertically by ~2–4 m (~6–13 ft) since 1997. Nevertheless, it is apparent that despite the addition of significant new sand to the dune, the mean position of the beach face has not changed (i.e., neither accreted seaward nor eroded landward). Examination of the profile data

indicates that the beach-dune junction ($E_j$) has varied in elevation, a function of repeated phases of both erosion and accretion events. As of winter 2014, an erosion scarp had formed and the beach-dune junction reflected the toe of the scarp, located at an elevation of ~5 m (16.4 ft). **Figure 3-7** also includes the derived beach slope (tan $\beta$ = 0.057), the crest of the primary dune, and the landward boundary of the primary frontal dune. These data are used later to develop new VE flood zones along the Lane and Douglas County coast.

To estimate beach erosion and profile changes for a specific coastal setting that occurs during a particular storm, it is essential to first define the initial conditions of the morphology of the beach prior to the actual event of interest (NHC, 2005). This initial beach profile is referred to as the most likely winter profile (MLWP) condition for that particular coastal setting and is depicted in **Figure 3-7** as the heavy black line. The MLWP was assessed based on an examination of the combined profile and lidar data. In the **Figure 3-7** example, the 2009 lidar survey of the primary dune and backshore was found to best characterize the landward component of the MLWP, while the April 1998 lidar survey best captured the state of the active beach and seaward edge of the foredune. Landward of the dune crest, information on the backshore topography was derived by incorporating the measured GPS data because those data provided the best representation of the actual ground surface. Where GPS survey data were not available, we used topographic data derived from the 2009 lidar flown for DOGAMI.

**Figure 3-7. Plot showing various beach cross-sections at the LD 22 profile site. In this example, the Most Likely Water Profile (MLWP) is depicted as the heavy black line, the *eroded* beach-dune junction location, dune crest, and primary frontal dune location (PFD) are characterized respectively by the magenta, red, and blue circles. The plot also provides an excellent example of the extent of accretion that has taken place on the primary dune, which has aggraded vertically by ~2–4 m (~6–13 ft) along this section of Heceta Beach.**

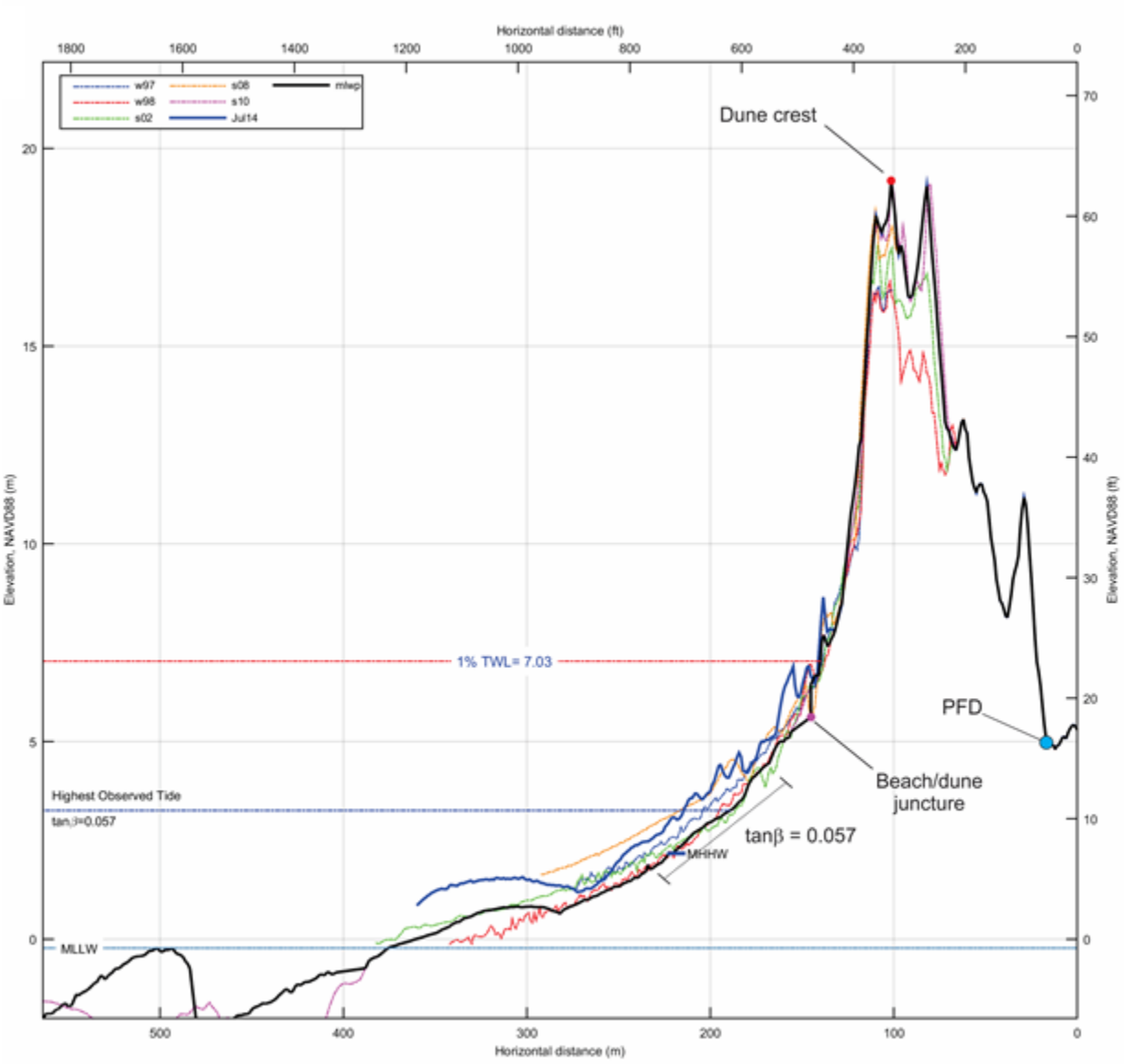

**Table 3-3** summarizes the various morphological parameters identified for each transect site along the Lane and Douglas County coastline, including their geomorphic classification. **Figure 3-8** provides a plot of the alongshore changes in beach slopes (tan $\beta$), mean sediment grain sizes ($M_z$), beach-dune junction ($E_j$) elevations, and the dune/bluff/structure crest heights. In general, the steepest slopes are confined to those beaches with coarse sediments on the foreshore (e.g., near Stonefield Beach, **Figure 2-4**), while sites containing finer sediments are characterized by generally lower beach slopes (e.g., Heceta Beach, **Figure 2-1**). Mean grain-sizes in the Neskowin littoral cell are characterized as medium sand ($M_z$ = 1.9Ø (0.278 mm [Peterson and others, 1994]). The steepest beach slopes are typically identified adjacent to the headlands, where the beach is composed predominantly of gravels and boulders and the sediment is locally sourced from the headlands as a result of landslides. At several of the beach study sites, sediment grain-sizes vary in both the alongshore and the cross-shore directions. For example, beaches at Stonefield and to the north may be characterized as "composite" using the nomenclature of Jennings and Shulmeister (2002), that is, consisting of a wide dissipative sandy beach composed of fine sand (**Figure 2-4**), backed by an extensive gravel beach on the upper foreshore.

**Figure 3-8** also plots the beach-dune and bluff-beach junction elevations ($E_j$) for the various study sites. Values for $E_j$ vary significantly along the length of the Lane and Douglas County coast. The lowest $E_j$ values tend to occur along the toe of the cliffs, and beaches backed by gravel and boulders. In general, the highest beach-dune junction elevations are found along Roosevelt and Stonefield Beaches. Finally here, **Figure 3-8** (bottom) indicates dune/bluff/structure crest elevations. Because these heights are indicative of the potential for flooding, with higher crests generally limiting flood overtopping, it can be seen that the risk from coastal flooding and inundation is likely to be highest along the southern half of Heceta Beach. Along the remainder of the shore, the beaches are protected by prominent bluffs (e.g., Stonefield Beach) and/or dunes (e.g., northern Heceta Beach) with crest elevations that range from 10 to 30 m (33–98 ft) that effectively preclude wave overtopping and hence inundation in those areas. Nevertheless, some of these sites are subject to erosion hazards that likely will influence the extent of the flood zones in those areas, after factoring the potential for erosion from storms.

**Figure 3-8. Alongshore changes in beach slopes (tan $\beta$), beach-dune junction ($E_J$) elevations, and dune/bluff crest/tops along Lane County. Red squares indicate mean sediment grain-sizes measured by Peterson and others (1994). Vertical blue shading denotes the location of the Siuslaw River mouth, while the red shading denotes the locations of headlands.**

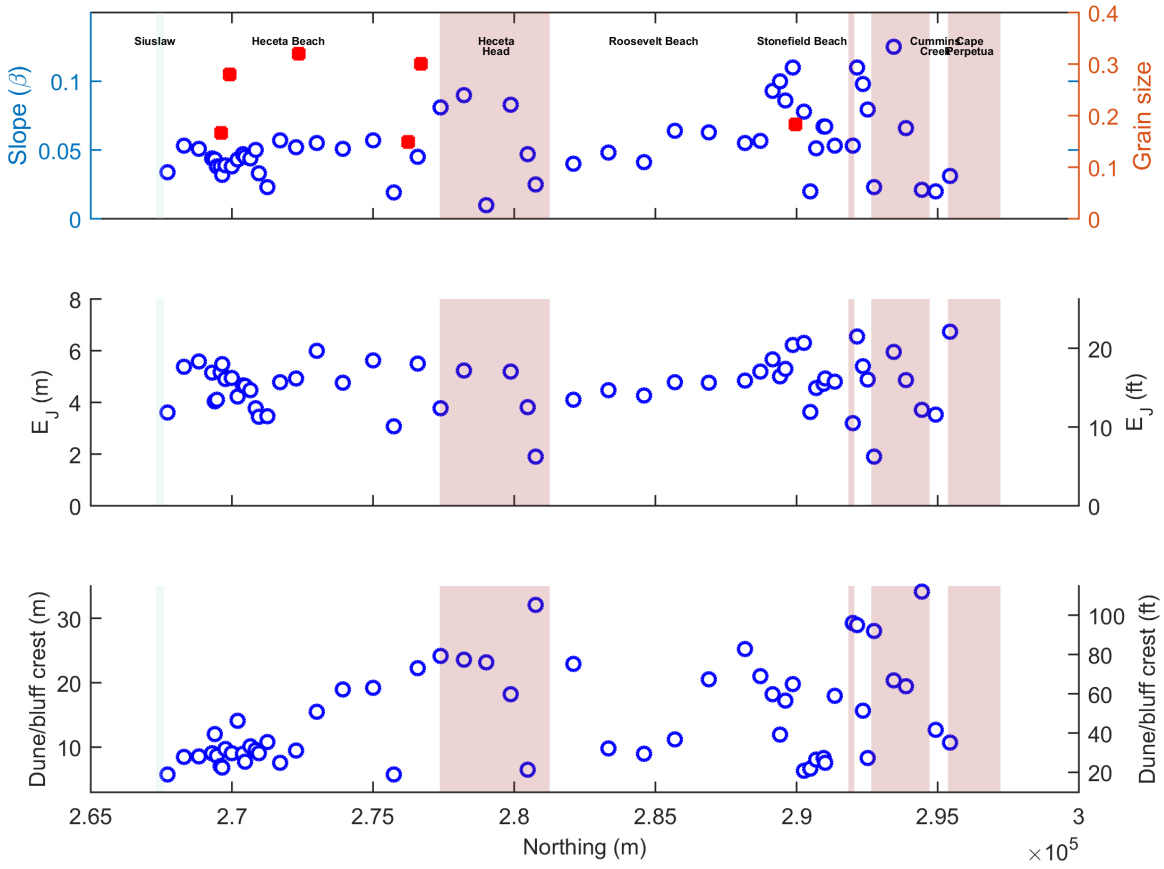

**Table 3-3. Identified beach morphological parameters from the most likely winter profile (MLWP) along the Lane County shoreline. Parameters include the beach-dune junction elevation ($E_j$_MLWP), beach slope (tan $\beta$) and a site description.** ***(Table continued on next page.)***

| Reach | Transect | Dune Crest/Bluff Top (m) | $E_j$_MLWP (m) | Beach Slope (tan $\beta$) | Description |
|---|---|---|---|---|---|
| Heceta | LD 1 | 5.726 | 3.618 | 0.034 | sand beach backed by dunes |
| Beach | LD 2 | 8.491 | 5.387 | 0.053 | sand beach backed by dunes |
| | LD 3 | 8.549 | 5.578 | 0.051 | sand beach backed by dunes |
| | LD 4 | 9.081 | 5.154 | 0.044 | sand beach backed by dunes & bluff |
| | LD 5 | 12.038 | 4.041 | 0.043 | sand beach backed by riprap & bluff |
| | LD 6 | 8.643 | 4.100 | 0.038 | sand beach backed by riprap |
| | LD 7 | 7.106 | 5.181 | 0.038 | sand beach backed by riprap |
| | LD 8 | 6.852 | 5.471 | 0.032 | sand beach backed by dune ramp |
| | LD 9 | 9.730 | 4.908 | 0.039 | sand beach backed by riprap |
| | LD 10 | 9.034 | 4.953 | 0.038 | sand beach backed by dunes |
| | LD 11 | 14.080 | 4.229 | 0.043 | sand beach backed by riprap |
| | LD 12 | 8.948 | 4.666 | 0.047 | sand beach backed by riprap |
| | LD 13 | 7.768 | 4.634 | 0.045 | sand beach backed by riprap |
| | LD 14 | 10.151 | 4.476 | 0.044 | sand beach backed by riprap |
| | LD 15 | 9.572 | 3.771 | 0.050 | sand beach backed by riprap |
| | LD 16 | 9.097 | 3.439 | 0.033 | sand beach backed by riprap |
| | LD 17 | 10.822 | 3.474 | 0.023 | sand beach backed by dunes |
| | LD 18 | 7.585 | 4.778 | 0.057 | sand beach backed by dunes |
| | LD 19 | 9.449 | 4.924 | 0.052 | sand beach backed by dunes |
| | LD 20 | 15.475 | 6.005 | 0.055 | sand beach backed by dunes |
| | LD 21 | 18.978 | 4.759 | 0.051 | sand beach backed by dunes |
| | LD 22 | 19.185 | 5.617 | 0.057 | sand beach backed by dunes |
| | LD 23 | 5.730 | 3.065 | 0.019 | sand beach backed by dunes |
| | LD 24 | 22.259 | 5.495 | 0.045 | sand beach backed by dunes |
| Heceta Head | LD 25 | 24.190 | 3.765 | 0.081 | basalt cliff |
| | LD 26 | 23.581 | 5.238 | 0.090 | sand beach backed by high bluff |
| | LD 27 | 23.154 | −0.506 | 0.010 | basalt cliff |
| | LD 28 | 18.233 | 5.192 | 0.083 | sand beach backed by high bluff |
| | LD 29 | 6.490 | 3.820 | 0.047 | sand beach backed by high bluff |
| | LD 30 | 32.039 | 1.904 | 0.025 | basalt cliff |
| Muriel | LD 31 | 22.957 | 4.097 | 0.040 | sand beach backed by high bluff |
| O'Ponsler | LD 32 | 9.775 | 4.467 | 0.048 | sand beach backed by low bluff |
| | LD 33 | 8.982 | 4.273 | 0.041 | sand beach backed by low bluff |
| | LD 34 | 11.208 | 4.774 | 0.064 | sand beach backed by low bluff |
| | LD 35 | 20.565 | 4.759 | 0.063 | sand beach backed by high bluff |
| | LD 36 | 25.230 | 4.850 | 0.055 | moderately wide rock platform backed by high bluff |
| Stonefield | LD 37 | 21.045 | 5.183 | 0.057 | sand beach backed by high bluff |
| Beach | LD 38 | 18.245 | 5.670 | 0.093 | moderately wide rock platform backed by high bluff |
| | LD 39 | 11.970 | 5.003 | 0.100 | sand beach backed by high bluff |
| | LD 40 | 17.186 | 5.301 | 0.086 | moderately wide rock platform backed by high bluff |
| | LD 41 | 19.745 | 6.222 | 0.110 | sand beach backed by high bluff |

| Reach | Transect | Dune Crest/Bluff Top (m) | $E_i$_MLWP (m) | Beach Slope (tan $\beta$) | Description |
|---|---|---|---|---|---|
| | LD 42 | 6.331 | 6.301 | 0.078 | sand beach backed by dunes |
| Stonefield | LD 43 | 6.693 | 3.624 | 0.020 | sand beach backed by low bluff |
| Beach | LD 44 | 8.058 | 4.562 | 0.051 | moderately wide rock platform backed by high bluff |
| | LD 45 | 8.314 | 4.726 | 0.067 | sand beach backed by low bluff |
| | LD 46 | 7.542 | 4.919 | 0.067 | sand beach backed by low bluff |
| | LD 47 | 17.942 | 4.797 | 0.053 | sand beach backed by high bluff |
| | LD 48 | 29.229 | 3.201 | 0.053 | moderately wide rock platform backed by high bluff |
| | LD 49 | 28.958 | 6.552 | 0.110 | moderately wide rock platform backed by high bluff |
| | LD 50 | 15.647 | 5.408 | 0.098 | moderately wide rock platform backed by high bluff |
| | LD 51 | 8.330 | 4.894 | 0.080 | mixed sand and gravel beach backed by low bluff |
| Cummins Creek / Cape Perpetua | LD 52 | 28.047 | 1.906 | 0.023 | narrow rock platform backed by high bluff |
| | LD 53 | 20.355 | 5.944 | 0.125 | narrow rock platform backed by high bluff |
| | LD 54 | 19.471 | 4.871 | 0.066 | sand beach backed by high bluff |
| | LD 55 | 34.099 | 3.709 | 0.021 | moderately wide rock platform backed by high bluff |
| | LD 56 | 12.687 | 3.535 | 0.020 | sand beach backed by low bluff |
| | LD 57 | 10.730 | 6.739 | 0.031 | narrow rock platform backed by low bluff |

## 3.3 Recent Coastal Changes in Lane and Douglas County

This section briefly reviews beach profile changes that have occurred during the past 15 years, as documented by lidar and GPS surveys of the shore.

The overall approach used to define the morphology of the beach and dune system, including the location of the PFD along the length of county shoreline, and shoreline changes over the past decade, was based on detailed analyses of lidar data measured by the USGS/NASA/NOAA in 1997, 1998, and 2002, by DOGAMI in 2009, and by the USACE in 2010. Lidar data acquired by the USGS/NASA/NOAA/USACE are of relatively poor resolution (~1 point/m$^2$) and reflect a single return (i.e., the data include vegetation where present), whereas lidar data acquired by DOGAMI have a higher resolution (8 points/m$^2$) and are characterized by multiple returns, enabling the development of a bare-earth digital elevation model (DEM). Therefore, determination of the most critical beach-dune morphological features was based entirely on analysis of the 2009 DOGAMI lidar data.

Lidar data flown in 1997, 1998, 2002, and 2010 were downloaded from NOAA's Coastal Service Center and gridded in ArcGIS using a TIN algorithm (Allan and Harris, 2012); a similar approach was undertaken with the 2009 lidar data. Transects spaced 20 m apart were cast for the full length of the county coastline using the Digital Shoreline Analysis System (DSAS) developed by the USGS (Thieler and others, 2009). For each transect, *xyz* values for the 1997, 1998, 2002, and 2009 lidar data were extracted at 1-m intervals along each transect line and were saved as a text file using a customized ArcGIS script.

Processing of the lidar data was undertaken in MATLAB using a custom beach profile analysis script developed by DOGAMI. This script requires the user to interactively define various morphological features including the dune/bluff crest/top, bluff slope (where applicable), landward edge of the PFD, beach-dune junction elevations for each year, and the slope of the beach foreshore.

Shoreline positions defined at the 6-m (19.7 ft) elevation contour in 2002, 2009, and 2010, relative to original position in 1998 are shown in **Figure 3-9**, **Figure 3-10**, and **Figure 3-11**. In each example, red (blue) dots denote erosion (accretion), while the green dashed line reflects the mean shoreline response ±1σ. A moving average filter with zero phase shift has also been fit to the data to better document the alongshore spatial patterns of variability.

**Figure 3-9** indicates that on average the Lane and Douglas County shoreline was tending toward being slightly erosional during this initial period. This is probably not surprising as these data reflect the effects of the major 1997-98 El Niño and 1998-99 La Niña winter storms, which resulted in extensive erosion along the entire Oregon coast (Allan and others, 2009). By far the largest observed changes can be seen adjacent to the mouths of creeks and rivers (**Figure 3-9**), where the shoreline excursions range from −40 to +60 m (131 to 197 ft, e.g., adjacent to the Siuslaw River). North of Heceta Head, the shoreline responses are relatively minor, fluctuating between minor erosion and accretion. South of the Siuslaw and north of the Siltcoos Rivers, it can be seen that the shoreline is characterized by mostly accretion (~+4.3 m (14.1 ft) since 1998). With progress south of the Siltcoos River, the measured shoreline changes shift progressively to erosion. On average, this shore section eroded by ~5.5 m (~18 ft) between 1998 and 2002.

**Figure 3-10** describes the net change between 1998 and 2009. For the most part the broad patterns described previously are reflected in this latter period. Given the local geology of the coastline north of Heceta Head, it is once again not surprising to see the generally minor shoreline responses observed on this coast. Adjacent to the creeks and river mouths, the changes are clearly much more dramatic, with the beach on both sides of the Siuslaw having prograded seaward by tens of meters. Accretion continues to dominate the region of shore north of the Siuslaw River, having increased from a mean of −0.8 m (−2.6 ft) to +14.1 m (46.3 ft) by 2009. Net accretion also changes substantially north of the Siltcoos to Siuslaw Rivers, which increases from a mean accretion of +4.3 m (14.1 ft) during the 1998–2002 period to +9.9 m (ft) in the current period. South of the Siltcoos River, the shoreline remains largely erosional, with the mean shoreline change averaging ~−8 m (−26 ft). Nevertheless, it is not uncommon to see large shoreline excursions (reaching ~−80 m [262 ft]) near the mouths of the creeks and rivers, due to the interplay between coastal processes and river/creek flows. In general the former tends to block up the mouths, forcing the river/creek mouths to shift laterally along the shore toward the south, effectively eroding into the banks of the channels.

**Figure 3-11** presents the most current shoreline change information for Lane and Douglas County. However, these data have more gaps and hence large sections of the shore have little to no information. Once again, it can be seen that the overall patterns described for the 1998–2009 period are reflected in the 1998–2010 data.

**Figure 3-9. Net shoreline excursions along Lane and Douglas County as measured at the 6-m (19.6 ft) contour for the period 1998–2002. Blue bands denote the locations of various estuaries, rivers, and creeks, while the orange band defines the location of a headland. Red (blue) dots indicate erosion (accretion), while the green dashed line indicates the mean shoreline change ±1σ calculated for the entire shoreline length. Solid black line reflects a moving average filter with zero phase shift.**

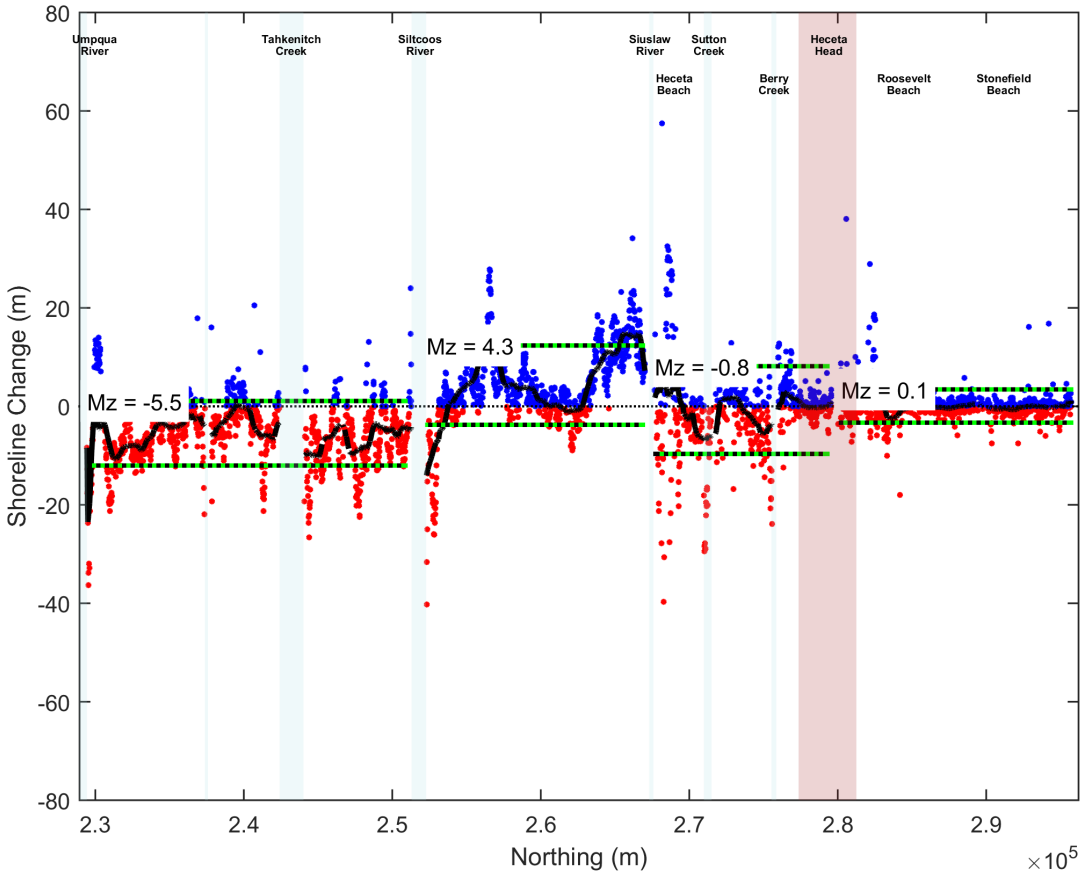

**Figure 3-10. Net shoreline excursions along Lane and Douglas County as measured at the 6-m (19.6 ft) contour for the period 1998–2009. Blue bands denote the locations of various estuaries, rivers, and creeks, while the orange band defines the location of a headland. Red (blue) dots indicate erosion (accretion), while the green dashed line indicates the mean shoreline change ±1σ calculated for the entire shoreline length. Solid black line reflects a moving average filter with zero phase shift.**

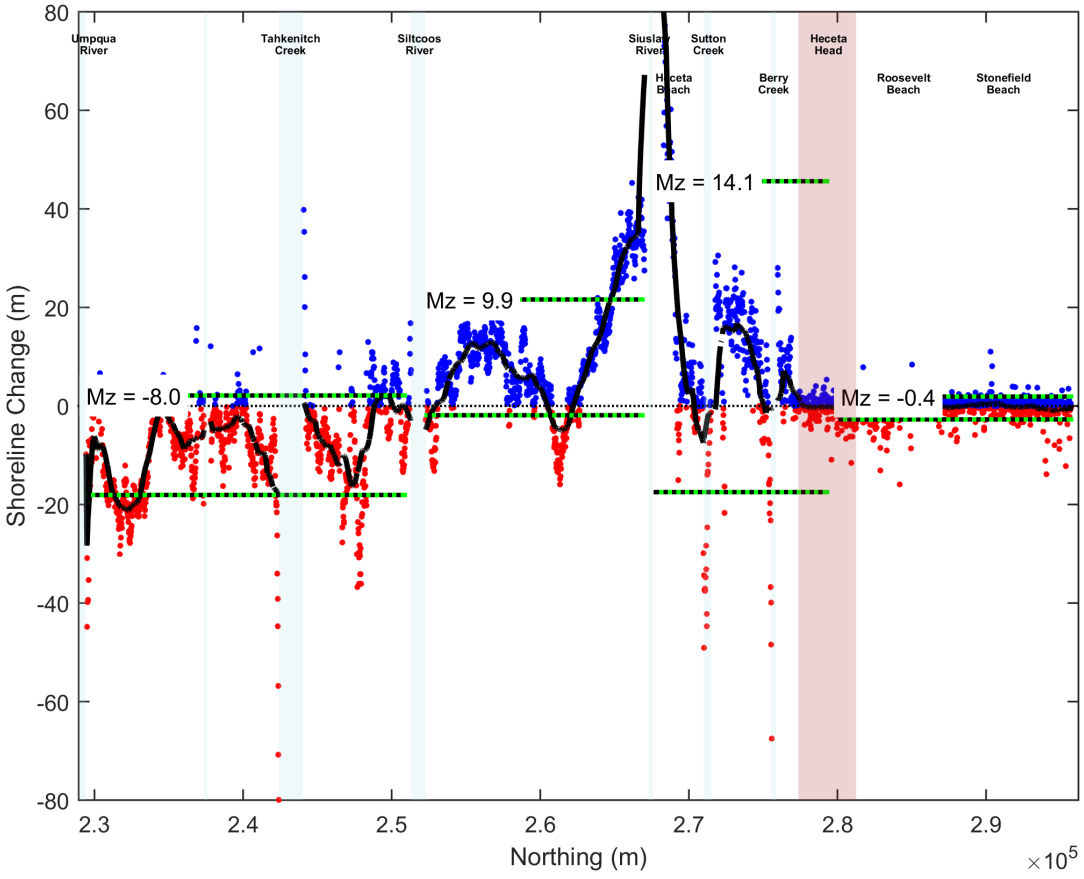

**Figure 3-11. Net shoreline excursions along Lane and Douglas County as measured at the 6-m (19.6 ft) contour for the period 1998–2010. Blue bands denote the locations of various estuaries, rivers, and creeks, while the orange band defines the location of a headland. Red (blue) dots indicate erosion (accretion), while the green dashed line indicates the mean shoreline change ±1σ calculated for the entire shoreline length. Solid black line reflects a moving average filter with zero phase shift.**

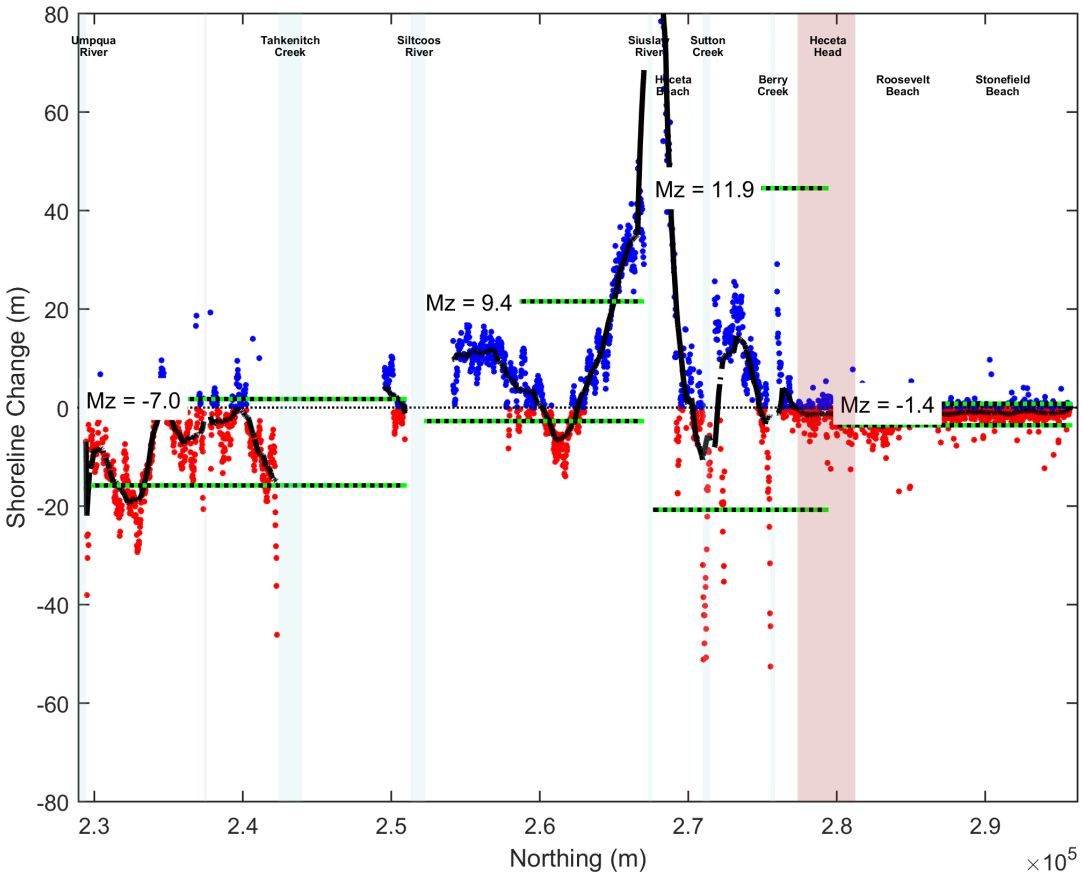


## 3.4 Bathymetry

Important for calculating wave transformations and determining nearshore beach slopes is information on the local bathymetry offshore from the Lane and Douglas County coast. For the purposes of this study we have adopted two approaches:

1) For SWAN numerical wave modeling, we used bathymetric data compiled by the National Geophysical Data Center (NGDC), an office of the National Oceanic and Atmospheric Administration (NOAA). These integrated bathymetric-topographic digital elevation models (DEMs) were originally developed for tsunami inundation modeling.
2) For erosion assessments and wave runup calculations, we used bathymetric data collected in mid summer 2014 with the aid of personal watercrafts (Tuba Özkan-Haller and others, 2009).

For the purposes of developing an integrated bathymetric-topographic digital elevation model (DEM) that can be used for tsunami inundation modeling, the National Geophysical Data Center (NGDC), an office of the National Oceanic and Atmospheric Administration (NOAA) has compiled detailed bathymetric data across the continental shelf from multiple agencies. The synthesized bathymetric-topographic DEM (Central Oregon Coast[4], Port Orford[5]) is a 1/3 arc-second (approximately 10 m [~33 ft]) DEM of the north central Oregon coast that spans all of Lane and Douglas County and includes the offshore rocks, small islands, and reefs that would affect wave shoaling. The DEM was generated from a diverse suite of digital datasets that span the region (Carignan and others, 2009a; Carignan and others, 2009b). A summary of the data sources and methods used to synthesize the data to develop the Central Oregon coast and Port Orford DEMs is described in the reports by Carignan and others (2009a,b). In general, the best available data were obtained by the NGDC and shifted to common horizontal and vertical datums: North America Datum 1983 (NAD 83) and mean high water (MHW).

NGDC used shoreline, bathymetric, and topographic digital datasets (**Figure 3-12**) from several U.S. federal, state, and local agencies (e.g., NOAA's National Ocean Service [NOS], Office of Coast Survey [OCS] and Coastal Services Center [CSC]; the U.S. Geological Survey [USGS]; the U.S. Army Corps of Engineers [USACE]; and the Marine Resource Program of the Oregon Department of Fish and Wildlife [ODFW]). After all the data had been converted to a common coordinate system and vertical datum, the grid data were checked for anomalous data and corrected accordingly. Because the datasets, particularly in deep water and near to the coast, were relatively sparse, further manipulation and smoothing was required to create a uniform grid. These products were then compared with the original surveys to ensure grid accuracy. According to Carignan and others (2009a) the final DEM is estimated to have an accuracy of up to 10 m (~33 ft), while some portions of the grid are more accurate (e.g., the coastal strip where high-resolution lidar data were available). The bathymetric portion of the dataset is estimated to have an accuracy of between 0.1 m (0.33 ft) and 5% of the water depth, again depending on the type of survey data that was used to calibrate the final grid development.

Despite all these efforts, it is important to note that a limitation of the DEMs being developed by NGDC is the virtual absence of suitable bathymetric data in the nearshore (effectively landward of the 10-m [33 ft] bathymetric contour), because few boats are able to venture into this highly turbulent portion of the surf zone. The exception to this is where surveys have been undertaken by the USACE in the entrance channels to those estuaries where navigable water depths need to be maintained. Thus, there is some uncertainty about estimating nearshore slopes for the surf zone due to the absence of sufficient data for this region, with the user having to make some assumptions based on the best available data present outside the surf zone and information at the shoreface. This is a recognized problem with all coastal flood analyses. To resolve this problem, we used a Coastal Profiling System (CPS) that has been developed for nearshore bathymetric surveys by Dr. Peter Ruggiero (Department of Geosciences, Oregon State University [Ruggiero and others, 2005]). The CPS consists of a highly maneuverable personal watercraft that is equipped with a survey grade GPS receiver and antenna, an echo sounder and an onboard computer. Repeatability tests undertaken by Ruggiero and colleagues indicate subdecimeter accuracy on the order of 0.15 m (0.5 ft) (Tuba Özkan-Haller and others, 2009). **Figure 3-13** provides an example of the CPS system, while **Figure 3-14** presents the mapped coverage of our bathymetric surveys undertaken in summer 2014. An example of two of the bathymetric transects undertaken in Lane County is presented in **Figure 3-15**.

[4] http://www.ngdc.noaa.gov/dem/squareCellGrid/download/320

[5] http://www.ngdc.noaa.gov/dem/squareCellGrid/download/410

**Figure 3-12. U.S. federal, state, and local agency bathymetric datasets used to compile the Astoria DEM [Carignan and others, 2009a].**

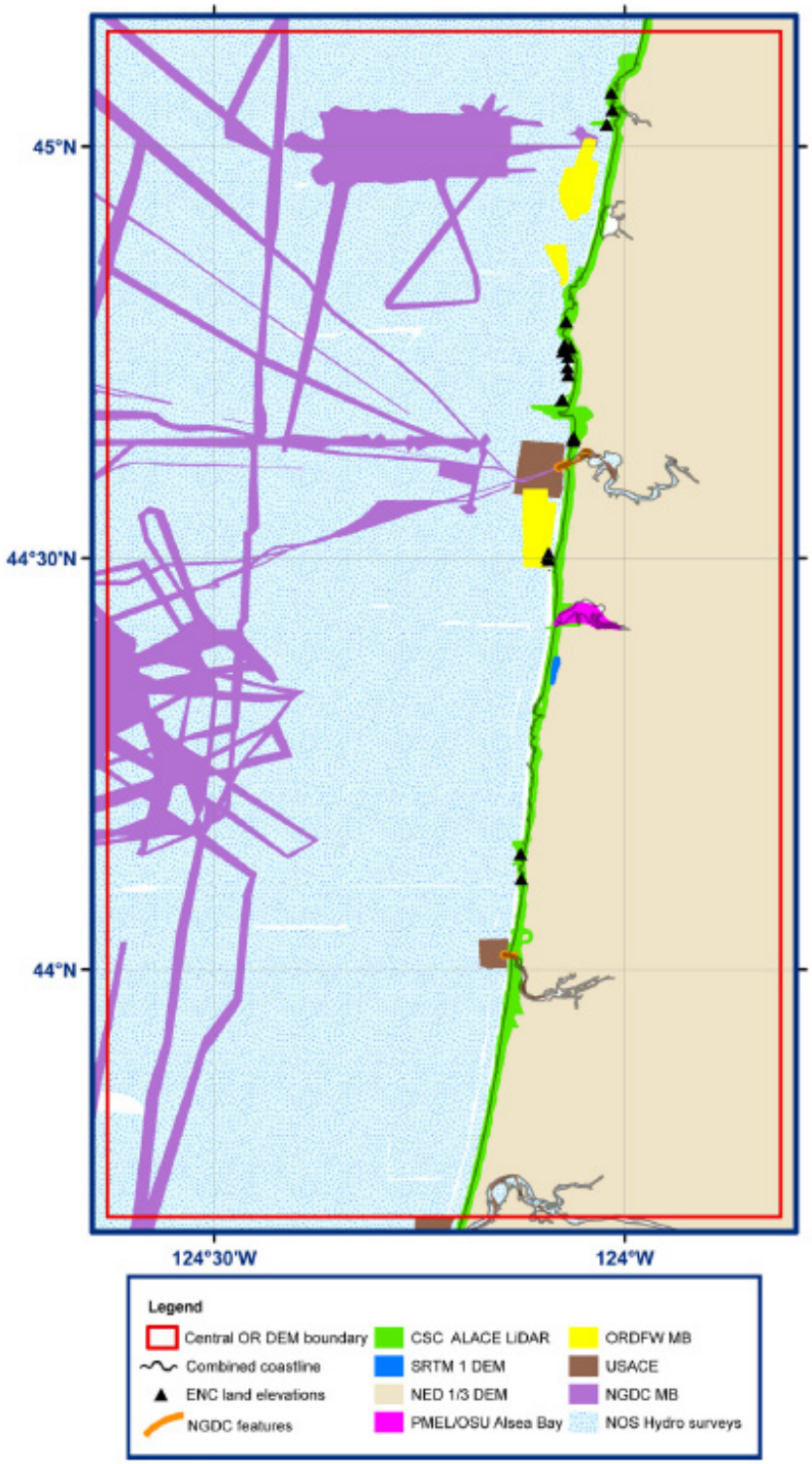

**Figure 3-13. Data acquisition boat and onboard equipment (photo: courtesy of P. Ruggiero, OSU).**

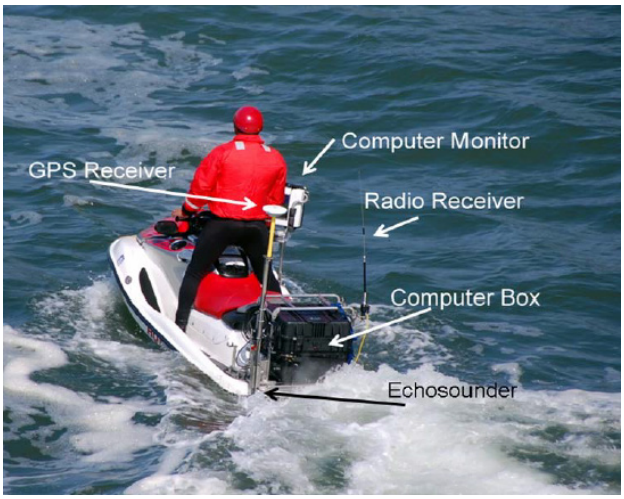


**Figure 3-14. Collected bathymetry transects measured offshore the coast of the Coos and Heceta littoral cells, Lane County, Oregon.**

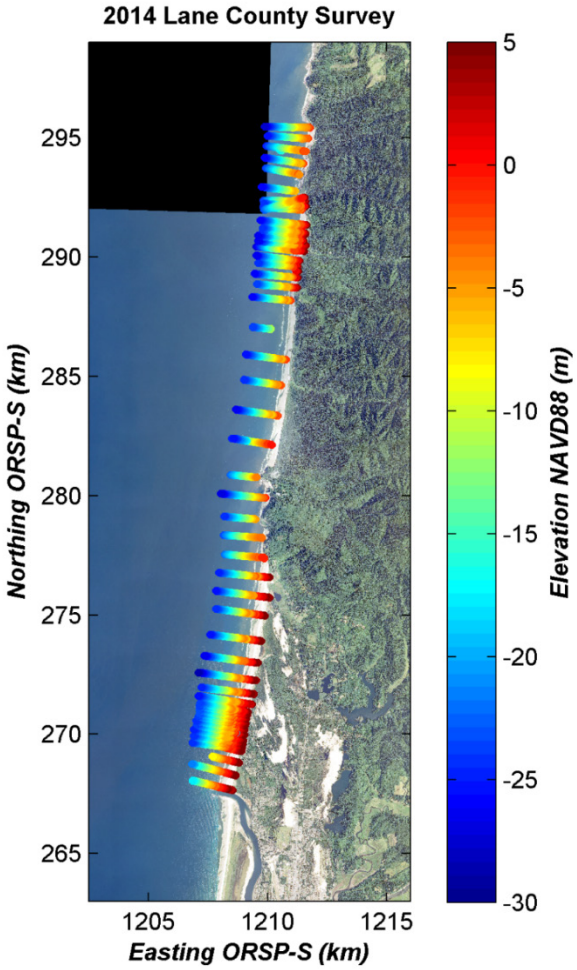

**Figure 3-15. Combined topographic and bathymetric cross-shore transects measured offshore from Heceta Beach and Roosevelt Beach (respectively, southern and northern Lane County) showing the presence of sand bars. Profile locations are shown in Figures 3-1 and 3-2.**

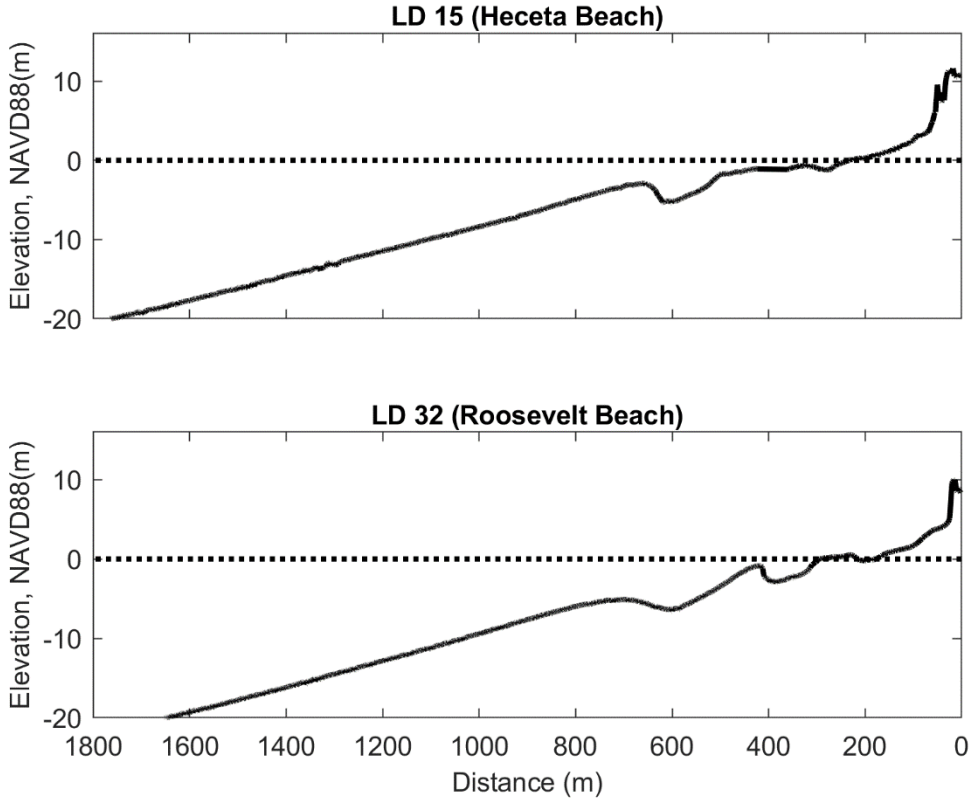

# 4.0 TIDES

Measurements of tides on the Oregon coast are available from various tide gauges[6] operated by NOS. Hourly tidal records are available from the following coastal sites (**Table 4-1**): the Columbia River (Astoria, #9439040), Tillamook Bay (Garibaldi, #9437540), Newport (South Beach, #9435380), Coos Bay (Charleston, #9432780) and at Port Orford (#9431647) on the southern Oregon coast. Long-term tidal records are also available from the Crescent City tide gauge (#9419750), located in northern California. The objective of this section is to establish which tide gauge is most appropriate in applications directed toward FEMA wave and total water level analyses for the Tillamook coastline. Results presented here will also help guide future total water level (TWL) analyses scheduled for Lincoln County.

The six tide gauges in this region and their record intervals are listed in **Table 4-1**. **Figure 4-1** maps the locations of the most pertinent tide gauges present on the central to northern Oregon coast, along with the locations of various wave buoys operated by the National Data Buoy Center (NDBC) and the Coastal Data Information Program (CDIP), and Global Reanalysis of Ocean Waves (GROW) Fine Northeast Pacific wave hindcast data. These latter stations are pertinent to discussions of the wave climate and modeling described in **SECTION 5** and, ultimately, in calculations of wave runup and overtopping.

**Table 4-1. Pacific Northwest NOAA tide gauges.**

| Gauge Site | Gauge Location | Record Interval | Years |
|---|---|---|---|
| Oregon | | | |
| Astoria (AST) | Astoria | Feb. 1925–present | 87.6 |
| Garibaldi (GB) | Tillamook Bay, near the inlet mouth | Jul. 2005–present | 7.2 |
| South Beach (SB) | Yaquina Bay, near the inlet mouth | Feb.1967–present | 45.6 |
| Charleston (CH) | Coos Bay, near the inlet mouth | Apr. 1970–present | 42.4 |
| Port Orford (PO) | Port Orford, open coast harbor | Oct. 1977–present | 35.0 |
| California | | | |
| Crescent City (CC) | Crescent City, open coast harbor | Sep. 1933–present | 79.8 |

As can be seen in **Table 4-1**, a number of the gauges have long records (30+ years) suitable for coastal flood analyses. The longest tide-gauge records (87 and 80 years, respectively) are from Astoria (AST), located 23.5 km up-channel from the mouth of the Columbia River, and at Crescent City (CC) in northern California. The South Beach (SB), Charleston (CH), and Port Orford gauges have moderately long records of about 45, 42, and 35 years, respectively (**Table 4-1**). The SB gauge is located within Yaquina Bay, ~2 km from the open coast, and the CH gauge is close to the mouth of Coos Bay, while the Port Orford (PO) gauge is the only true open coast site. The shortest record (about 7 years), is for the Garibaldi (GB) gauge, located near the mouth of Tillamook Bay. All hourly tide data were purchased from NOS and were processed using scripts developed in MATLAB. In addition to the measured tides, hourly tide predictions were calculated for all years using the NOS tide prediction program NTP4.

[6] http://www.co-ops.nos.noaa.gov/station_retrieve.shtml?type=Tide%20Data&state=Oregon&id1=943

**Figure 4-1. Location map of NDBC (black) and CDIP (yellow) wave buoys, tide gauges (red), and GROW wave hindcast stations (green).**

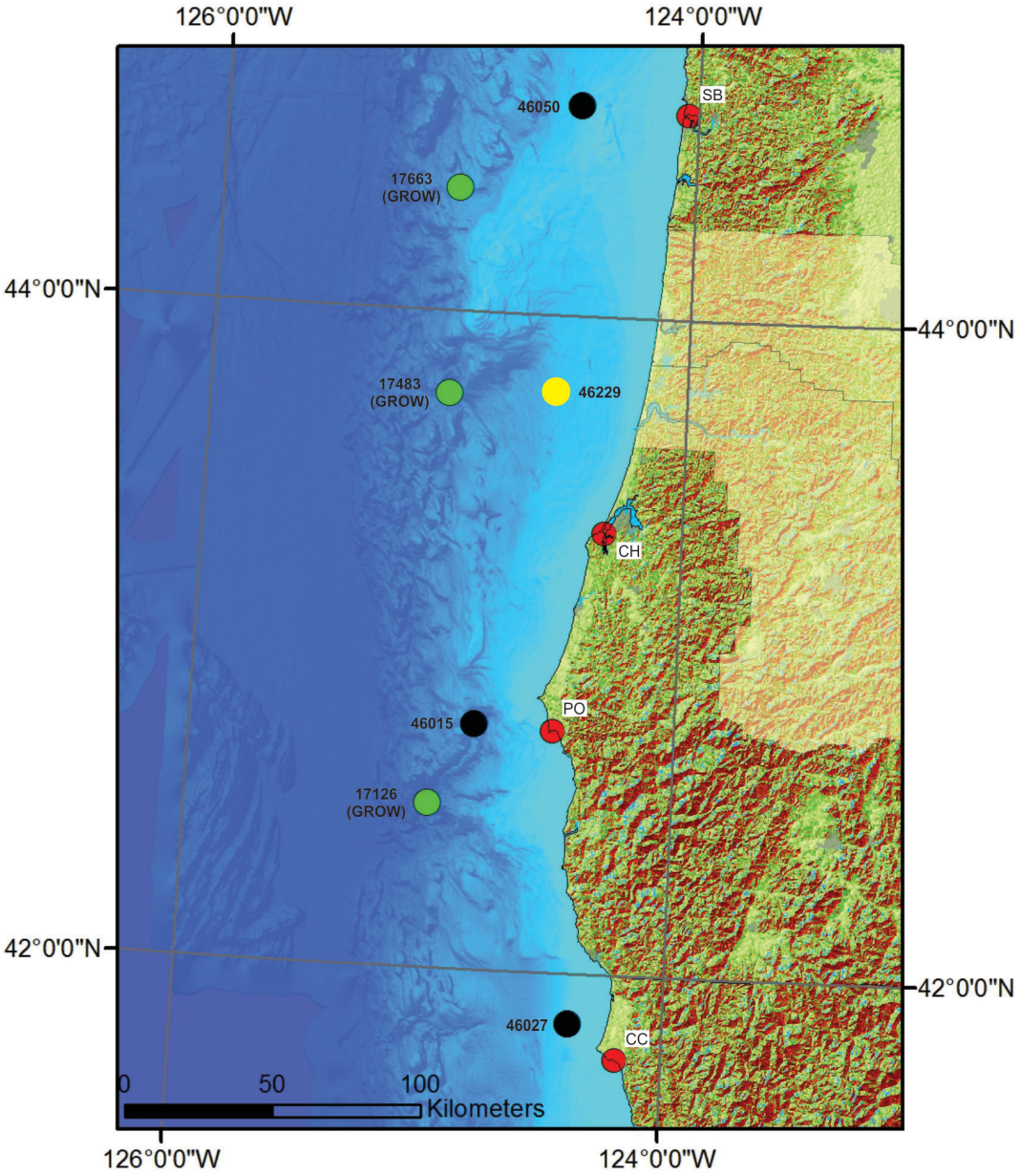

## 4.1 Tide Characteristics on the Central to Southern Oregon Coast

Tides along the Oregon coast are classified as moderate, with a maximum range of 4.3 m (14 ft) and an average range of about 1.8 m (6 ft) (Komar, 1997). There are two highs and two lows each day, with successive highs (or lows) generally having markedly different levels. Tidal elevations are given in reference to the mean of the lower low water levels (MLLW) and can be easily adjusted to the NAVD88 vertical datum[7]. As a result, most tidal elevations are positive numbers with only the most extreme lower lows having negative values.

Initial analyses of the measured tides focused on developing empirical probability density function (PDF) plots of the measured tidal elevations for the four tide gauges located between Newport, Oregon, and Crescent City, California. The objective here is to assess the measured tides along the south and central Oregon coast in order to identify any significant characteristics (including differences) between the gauges. **Figure 4-2** presents a series of PDF plots from each of the gauges. Because the gauges are characterized by varying record lengths, we have initially truncated the analyzed data to the period 2006–2014, when measurements were available from all four gauges.

As seen in the top plot of **Figure 4-2,** the gauges can be broadly characterized into three distinct regions. The SB gauge, on the central Oregon coast, indicates a slightly higher incidence of water levels between ~2 m and 3 m (6.6–9.8 ft, i.e., MSL to MHW). This contrasts with the measured water levels down at Crescent City (CC), which indicate generally lower water levels and in particular a lower incidence of water levels in the same range as at SB and on the south central Oregon coast (CH and PO). Water levels at CH and PO exhibit essentially the same distribution and range, suggesting these two sites are most compatible. The differences are probably related to a combination of effects associated with the regional oceanography (upwelling, shelf currents, and Coriolis effects that deflect the currents toward the coast). The lower plot in **Figure 4-2** shows the same PDF, but clipped to span tidal elevations between 2 and 4 m (6.5–13 ft). On this lower plot, the higher water levels characteristic of SB stand out, being about 0.3 m (1 ft) higher than at PO and CH, and significantly higher (~0.5 m [1.6 ft]) than at CC.

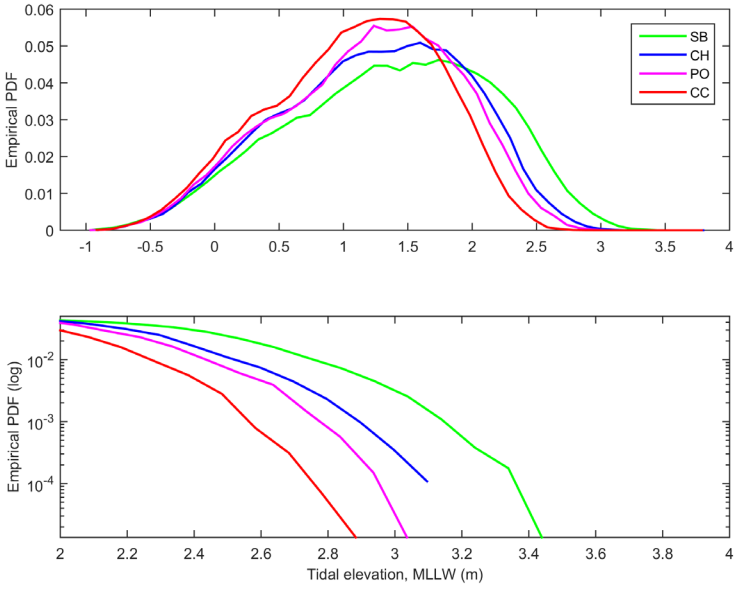


**Figure 4-2. Empirical probability density function (PDF) plots for tide gauges for the period 2006–2014. SB is South Beach; CH is Charleston; PO is Port Orford; CC is Crescent City. Top) PDF plots showing complete range of tidal elevations. Bottom) PDF plots clipped to higher water levels.**

[7] MLLW to NAVD88 conversions may be performed by using values provided for a specific tide gauge by the NOS, or by using the VDATUM (http://vdatum.noaa.gov/) tool developed by NOAA.

**Figure 4-3** is broadly similar to **Figure 4-2**, with the exception that the PDFs now include the complete time series of data measured by the tide gauges. As previously noted, the SB gauge is characterized by a higher incidence of water levels above 2.0 m (>6.9 ft), and a lower incidence of water levels between about 0 and 1.0 m (−0.6–3.3 ft). This clearly contrasts with the CH and PO gauges, which show a higher incidence of water levels between ~1.0 and 1.8 m (3.3–5.9 ft). Detailed examination of the hourly tides indicates that the higher incidence of SB water levels in the wings of the PDF reflect that the Higher Highs are generally larger at SB when compared with CH and PO, while the Higher Lows are generally more frequent at CH and PO compared with the SB gauge.

At the extreme high end of the PDF plots (**Figure 4-3**), the highest water levels measured at SB, CH, PO, and CC (when not constrained to the same time period) are, respectively, 3.71, 3.39, 3.34, and 3.28 m (12.2, 11.1, 11.0, and 10.8 ft). These results equate to a difference of ~0.3 m (~1 ft) between SB and CH and PO and 0.4 m (1.4 ft) between SB and CC. The highest water level measured at SB occurred in December 1969. Thus, it is possible that much higher water levels could have occurred at the CH and PO gauges, had they been operating over the same temporal period as SB. Overall, the relative consistency in PDF plots generated for each gauge is indicative of the areal impact of major North Pacific extratropical storms, which can affect stretches of coast up to 1,500 km long (932 miles; i.e., 3 times the length of the Oregon coast) (Davis and Dolan, 1993; Allan and Komar, 2002a).

**Figure 4-3. Empirical probability density functions (PDFs) for tide gauges SB (South Beach), CH (Charleston), PO (Port Orford), and CC (Crescent City) based on all available data. Top) PDF plot showing the complete range of tidal elevations. LL, LH, HL, and HH denote the Lower Lows, Lower Highs, Higher Lows, and Higher Highs in the tide data. Bottom) PDF truncated to higher water levels.**

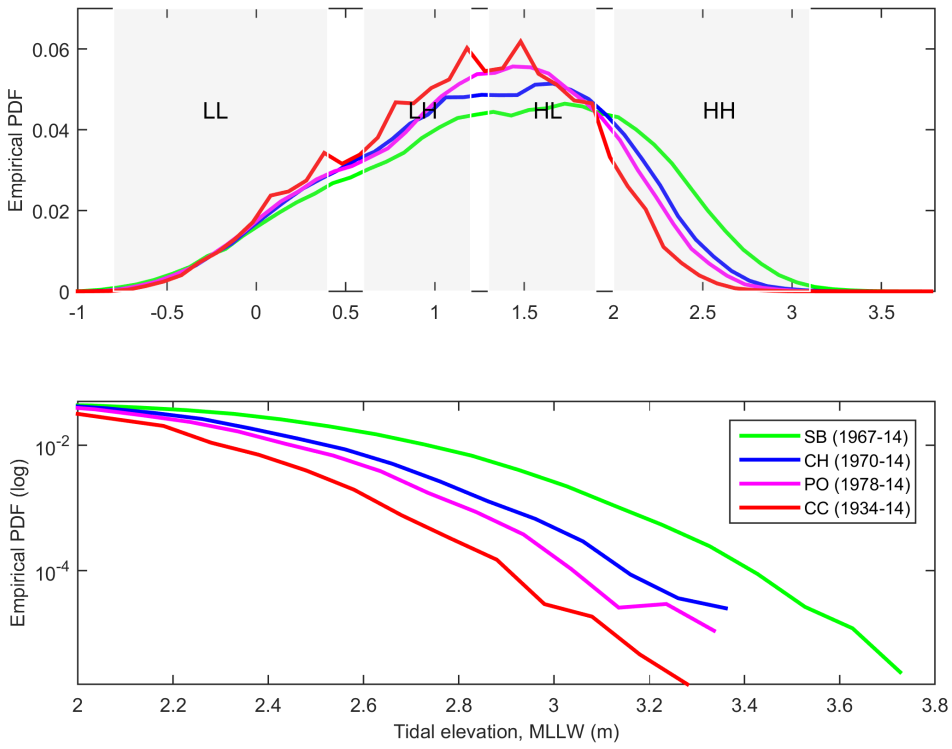

## 4.2 Seasonal Changes

**Figure 4-4** presents a plot of the characteristic seasonal cycle determined for the four gauges, enabling further examination of their characteristics. All four gauges depict the typical seasonal cycle that reflects the combination of ocean upwelling effects along the coast and seasonal reversals in the California current system. In general, water levels tend to be highest during the months of December through March and decrease to minimum levels between May and July. **Figure 4-4** also depicts a pattern whereby the winter peaks progressively increase toward the north, from CC to SB. In contrast to this, **Figure 4-4** indicates a southward increase in the water levels during late summer to early fall, reaching a peak at CC in September; in fact the latter pattern continues south along the U.S. West Coast such that as far south as Los Angeles the peak in the seasonal cycle has been shifted from its winter peak on the PNW coast to a late summer (September) peak on the southern California coast.

Finally, although not shown in **Figure 4-4**, all the tide gauges are strongly influenced by the El Niño Southern Oscillation phenomenon, which periodically causes mean sea levels along the U.S. West Coast to increase (Komar and others, 2011). This response is due to an intensification of the processes, especially enhanced ocean sea surface temperatures offshore from the Oregon coast. This occurred particularly during the unusually strong 1982-83 and 1997-98 El Niños, whereby mean sea levels increased by approximately 20–25 cm (~0.8 ft) above the normal seasonal cycle in mean sea level depicted in **Figure 4-4** (i.e., for a total mean sea level rise of up to 50 cm (1.6 ft) relative to the preceding summer). As a result, under these latter conditions wave swash processes are able to reach to much higher elevations on the beach, potentially eroding dunes and bluffs.

**Figure 4-4. Seasonal plot of tides along the central to southern Oregon coast. SB is South Beach, CH is Charleston, PO is Port Orford, and CC is Crescent City tide gauge.**

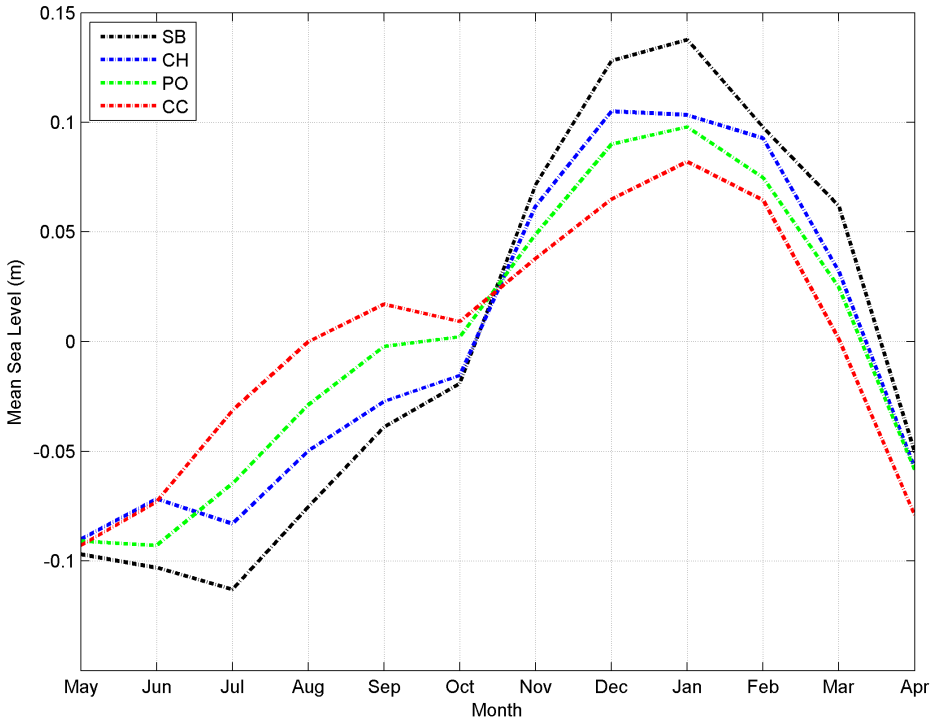

## 4.3 Oregon Storm Surges

The actual level of the measured tide can be considerably higher than the predicted tides provided in standard Tide Tables, and is a function of a variety of atmospheric and oceanographic forces, which ultimately combine to raise the mean elevation of the sea. These processes also vary over a wide range of timescales and may have quite different effects on the coastal environment. For example, strong onshore winds coupled with the extreme low atmospheric pressures associated with a major storm can cause the water surface to be locally raised along the shore as a storm surge; such surges have been found in tide-gauge measurements to be as much as 1.5 m (4.9 ft) along the Pacific Northwest coast (Allan and Komar, 2002a). However, during the summer months these processes can be essentially ignored due to the absence of major storm systems.

Analyses have been undertaken to examine the non-tidal residuals and ultimately the storm surges identified at the various tide gauges on the south central Oregon coast and in northern California. The objective of this analysis is to provide a better understanding of the spatial and temporal variability of storms as they track across the North Pacific, the magnitudes (and frequency) of the surges, and the potential differences in the non-tidal residuals between the gauges due to variations in the storm tracks, barometric pressures, and winds. This last point is particularly important in terms of finalizing the tide gauge time series to be used in the Lane County total water level analyses.

For the PNW, the measured water level ($h_t$) at a particular tide gauge is given by the following relationship:

$$h_t(t) = z_o + X_{at}(t) + X_{oc}(t) + S(t) \tag{4-1}$$

where $z_o$ is the mean water level, $X_{at}$ is the predicted astronomical tide, $X_{oc}$ is the altered mean water level due to ocean processes (water temperatures, currents, and El Niño "sea-level" waves), and $S$ is the contribution by the storm surge at time $t$. The predicted astronomical tide for the specific tide gauge is calculated using its harmonic constituents:

$$x_t = \sum_{i=1}^{M} H_i \cos(\sigma_i t + \varphi_i) \tag{4-2}$$

where $M$ is the number of tidal constituents included in the analysis, $H_i$ is the amplitude of the constituent $i$, $\sigma_i$ is its frequency, and $\varphi_i$ the phase of the constituent.

## 4.4 Non-Tidal Residual Analyses

The procedures used to analyze the non-tidal residuals and storm surge incidence follow those developed by Allan and others (2011), which used a harmonic analysis method of least squares (HAMELS) approach developed in MATLAB to estimate the amplitude and phase for any set of tidal constituents at each of the tide gauge sites (Boon, 2004). The purpose here is to develop a predicted time series of the water levels produced entirely by astronomic forces that excludes the seasonal component produced by ocean-ographic processes on the West Coast; the seasonal component can be integrated into tide predictions through the solar annual (Sa) and solar semiannual (Ssa) tide and is integrated as an *average term* in the predicted tides provide by NOS.

HAMELS analyses of tide gauge data have previously been completed for the SB and TP tide gauges (Allan and others, 2011). Thus, similar analyses were undertaken using the CH, PO, and CC tide gauges. The specific steps included the following:

- HAMELS was used to derive an estimate of the amplitude and phase for the tidal constituents. This was initially done using just a spring-summer dataset for testing purposes and then expanded to the full year of data;
- Having determined the tidal constituents, HAMELS was used to derive the astronomic tide predictions for the entire record on a year-by-year basis (which eliminates any long-term trend). The non-tidal residuals (NTRs) were calculated by subtracting the astronomic tide from the measured tides;
- The NTR time series were then filtered using a moving average filter (averaged over ±30 days) with zero phase shift, and the seasonal cycle was removed from the NTRs;
- The winter standard deviation was calculated, and those events exceeding 2*$\sigma$ were used to define individual surge events (Zhang and others, 2001).

**Figure 4-5** presents a series of regression plots of the derived NTRs for the various tide gauges. These data reflect the corresponding NTRs associated with the higher highs and higher lows of the diurnal tidal cycle, which were determined using a peak detection algorithm in MATLAB. Analyses here span the period of record for the respective tide gauges. Correlation ($R^2$) values calculated for the three plots are 0.89, 0.77, and 0.76. Due to their close proximity to one another, the strongest correlations are found between the SB and CH gauges ($R^2$ = 0.89, **Figure 4-5**). Although not included in the figure, a similar comparison was performed between the SB and CC gauges, which resulted in the weakest correlation ($R^2$ = 0.56).

**Figure 4-5. Comparison of non-tidal residuals determined for CH versus SB, PO versus SB, and PO versus CH tide gauges. Values plotted here reflect the daily peak values.**

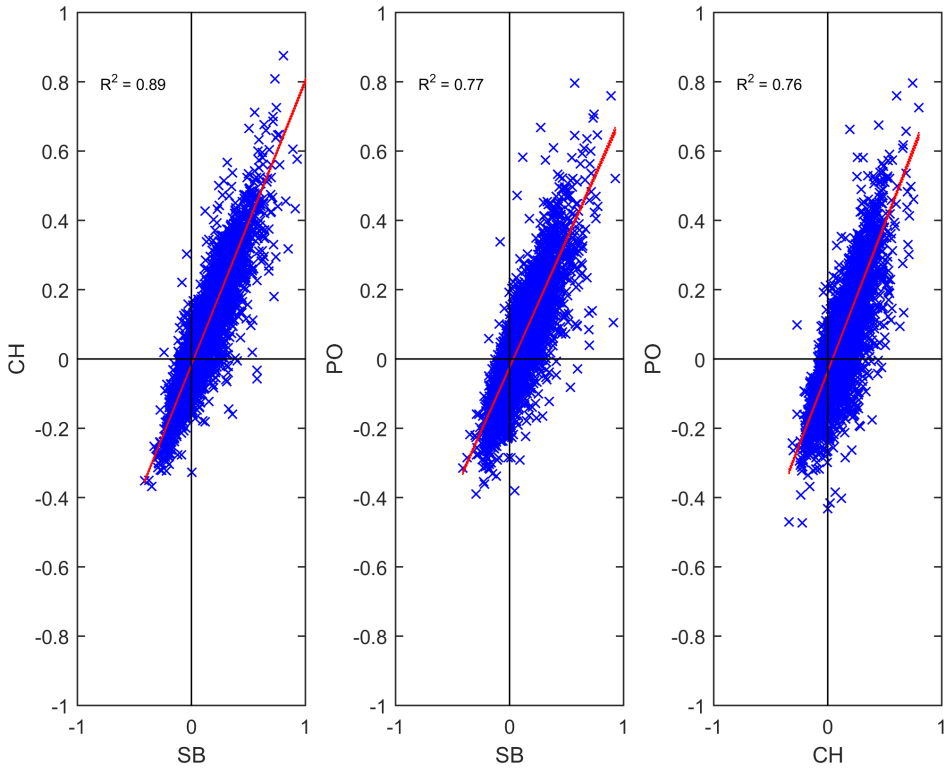

**Figure 4-6** presents the actual time series of de-seasoned NTRs derived for the SB, CH, PO, and CC tide gauges for the 2007-2008 winter. In this example, the NTRs have been time adjusted to a single station. As can be seen in this example, the three Oregon tide gauges tend to track very closely to each other, consistently capturing the same peaks and troughs. In contrast, the CC gauge shows both greater variability as well as phase differences, when compared to the Oregon tide gauges. These differences are further highlighted in the anomaly plot (**Figure 4-6**, bottom), which indicates more subtle differences between the three Oregon tide gauges; this latter plot has been smoothed using a locally weighted robust regression (LOESS) filter. As can be seen from **Figure 4-6** (bottom), the difference between the CH and PO gauges is characterized by generally lower anomalies (±0.1 m [0.33 ft]). In contrast, anomalies between the PO and CC tide gauges reveal much larger differences. Such variability is largely a function of differences in the position of the storms relative to the tide gauges, the storms' barometric pressures, winds, and the associated wave forcing along the coast. Overall, differences between the Oregon tide gauges probably reflect mostly subtle shifts in the timing of the events as they impact the coast, reinforcing our confidence that the effects of North Pacific extratropical storms are indeed widespread, affecting large tracts of the coast at similar times.

**Figure 4-6. Comparison of Top) non-tidal residuals (NTRs), and Bottom) their differences between the SB, CH, PO, and CC tide gauges for the 2007-2008 winter.**

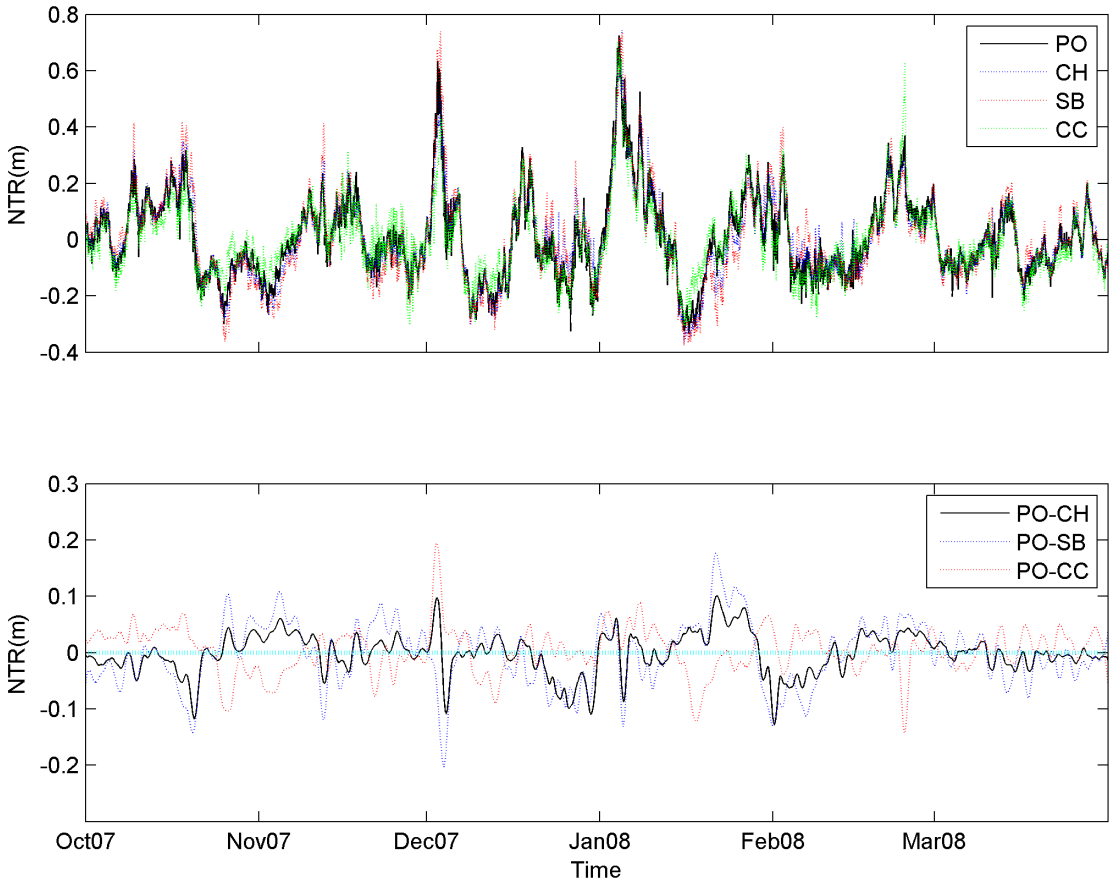

After NTRs for each of the tide gauges were identified, individual storm surge events were identified by following the procedures of Zhang and others (2001) and Allan and others (2011). **Figure 4-7** (left) presents a log number plot of all surge events for SB, CH, PO, and CC gauges. The plot indicates that for the most part the four gauges show relatively similar patterns in terms of storm surge magnitudes. In general, mean storm surges increase northward (0.42 m (1.4 ft) at CC to 0.5 m (1.6 ft) at SB), while the highest surges have occurred at SB (1.42 m [4.7 ft]); the highest surge observed at CC reached 0.91 m (3.0 ft). **Figure 4-7** (right) presents the empirical cumulative distribution function (CDF) plot calculated for the four gauges, further highlighting the progressive shift in the surge magnitudes to the north. Again, the SB gauge stands out, characterized by higher surges. Of interest, the CDF plot for PO (**Figure 4-7**, right) is generally higher when compared to the CH gauge. This difference probably reflects the fact that the PO gauge is truly an open coast site, whereas the CH (and the other gauges) are located within the estuaries such that their measurements may be somewhat muted when compared to the open coast.

**Figure 4-7. Plots of storm surge events on the Oregon and northern California coast. Left) Frequency distribution plot showing the incidence and magnitude of storm surges, and Right) cumulative distribution function (CDF) plot.**

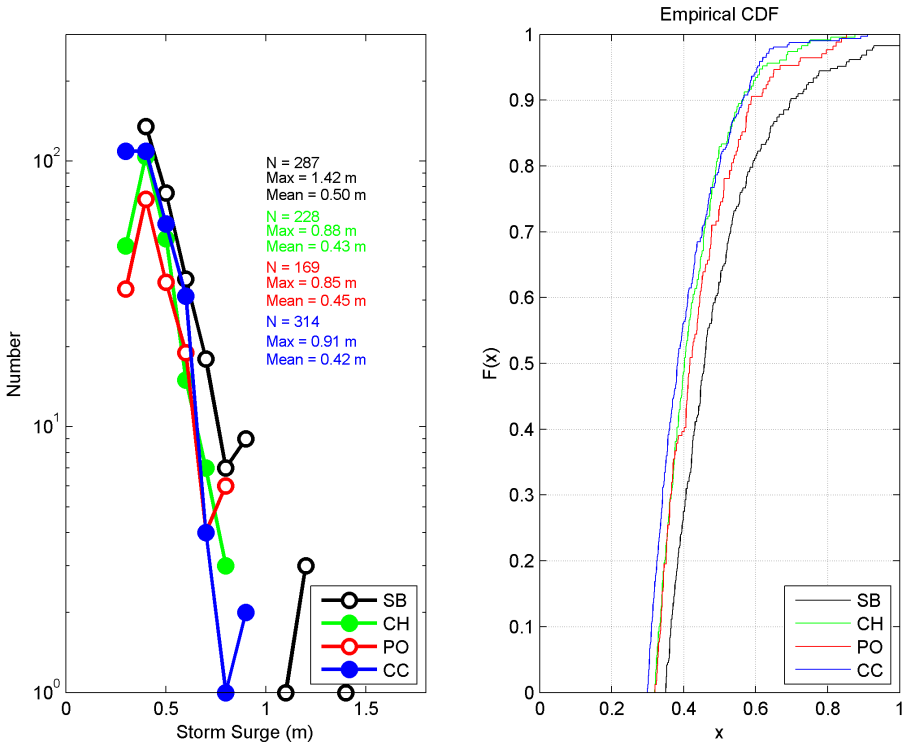


Taken together, these analyses confirm that the tide gauges located in South Beach in Yaquina Bay and at Charleston in Coos Bay overall provide the best measure of the open-coast still water levels, important in FEMA total water level and overtopping analyses. The main distinction between these two stations is the length of available measurements, with the CH site having a slightly shorter record (~42 years), while the PO gauge has the shortest temporal record. Furthermore, from our analyses we believe that the measured tides at Crescent City are significantly different from the South Beach gauge such that the CC gauge should not be used in FEMA flood analyses for the Lane and Douglas County open coast.

## 4.5 Lane and Douglas County Tides

For the purposes of this study we have based our still water level (SWL) and wave runup calculations on a combined time series that encompasses tides measured primarily at the South Beach gauge (#9435380, 1967–2014) and at the Charleston tide gauge (#9432780) in Coos Bay (1970–2014). Gaps have been filled using data from the Port Orford (#9431647) tide gauge, for a combined time series of 1967–2014. **Figure 4-8** shows the tidal elevation statistics derived from the South Beach tide gauge (the longest temporal record), with a mean range of 1.91 m (6.3 ft) and a diurnal range of 2.54 m (8.3 ft). The highest tide measured from this record reached 3.73 m (12.2 ft), recorded in December 1969 during a major storm. These values are comparable to those measured at the Charleston site (mean = 1.73 m (5.69 ft), diurnal = 2.32 m [7.62 ft]), with the only real difference being the fact that this latter gauge recorded a peak water level of 3.41 m (11.2 ft) in January 1983. **Figure 4-9** presents a summary empirical probability density function (PDF) plot of the measured tidal elevations from the four tide gauges and the synthesized tide data (solid black line) centered on the South Beach gauge. As can be seen in the figure, the synthesized PDF is essentially emulating the South Beach PDF at all tide stages.

**Figure 4-8. Daily tidal elevations measured at South Beach, on the central Oregon coast. Data from the National Ocean Service (https://tidesandcurrents.noaa.gov/benchmarks.html?id=9435380).**

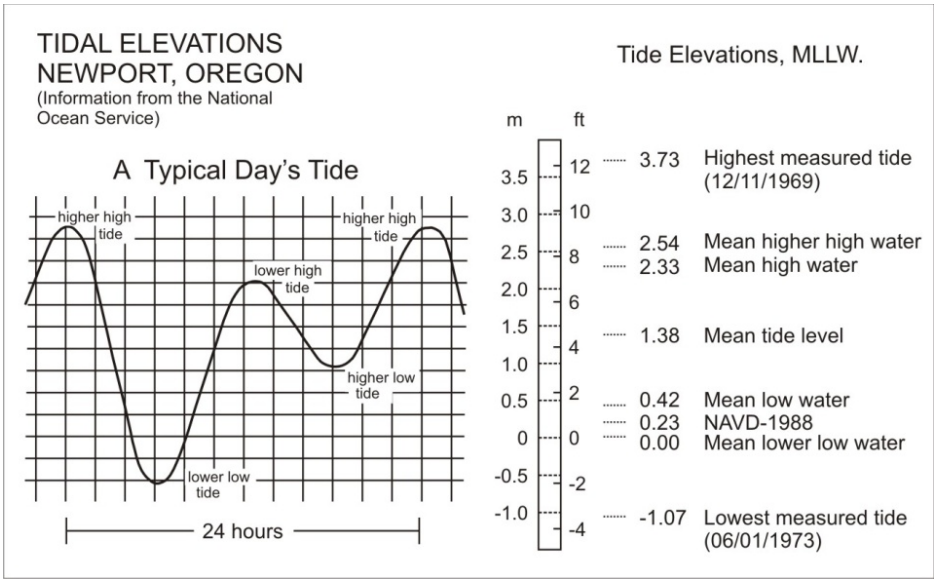


As noted previously, tides on the Oregon coast tend to be enhanced during the winter months due to warmer water temperatures and the presence of northward flowing ocean currents that raise water levels along the shore, persisting throughout the winter rather than lasting for only a couple of days as is the case for a storm surge. This effect can be seen in the monthly averaged water levels derived from the combined time series (**Figure 4-10**), but where the averaging process has removed the water-level variations of the tides, yielding a mean water level for the entire month. Based on 45 years of data, the results in **Figure 4-10** show that, on average, monthly-mean water levels during the winter are 25 cm (0.8 ft) higher than in the summer. Water levels are most extreme during El Niño events, due to an intensification of the processes, largely enhanced ocean sea surface temperatures offshore from the Oregon coast. This occurred particularly during the unusually strong 1982-83 and 1997-98 El Niños. As seen in **Figure 4-10**, water levels during those climate events were approximately 25–30 cm (0.8–1 ft)

higher than the seasonal peak, and as much as 52 cm (1.7 ft) higher than during the preceding summer. These levels enabled wave swash processes to reach much higher elevations on the beach during the winter months, with storm surges potentially raising water levels still further.

**Figure 4-9. Empirical probability density function (PDF) plots for various tide gauges for overlapping years of data (1978–2014), and the synthesized time series centered on the South Beach tide gauge. Top) PDF plots showing the full range of tidal elevations; Bottom) truncated to higher water levels.**

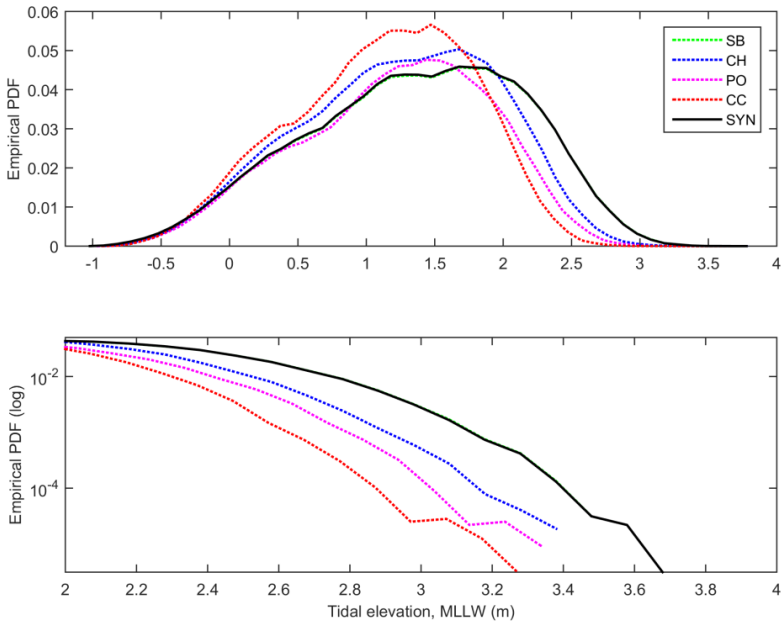


**Figure 4-10. Seasonal cycles in monthly-mean water levels based on data from the combined South Beach and Charleston measured tides.**

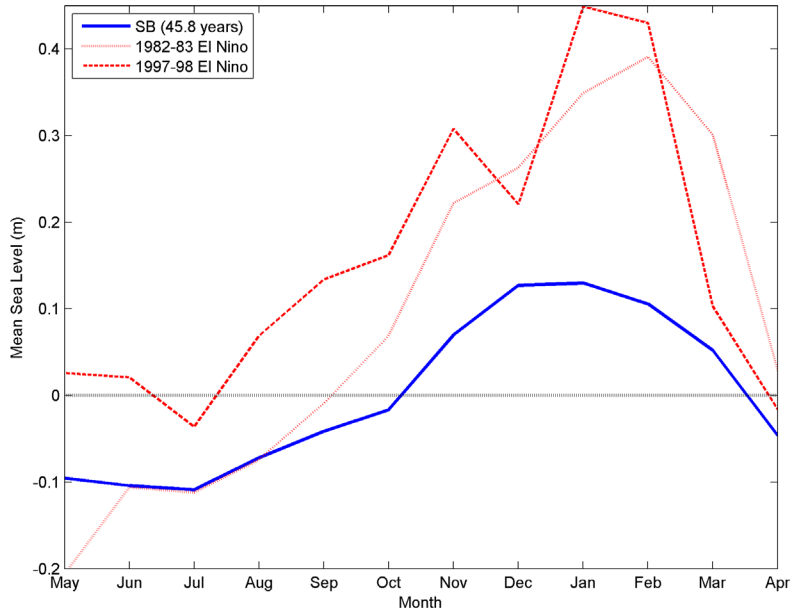

Aside from seasonal to interannual effects of climate events on ocean water levels, also of interest are the long-term trends associated with relative sea level changes due to climate change along the Lane/Douglas County coastline. **Figure 4-11** presents results from an analysis of the South Beach time series based on a separate analysis of the summer and winter tide levels. For our purposes, "winter" is defined as the combined average tide level measured over a 3-month period around the peak of the seasonal maximum in winter water levels, typically the months of December through February. Similarly, "summer" water levels reflect the combined average tide level measured over a 3-month period around the seasonal minimum, typically the months between May through July when water levels also tend to be less variable (Komar and others, 2011). As noted previously in **Figure 4-10**, the winter tidal elevations are systematically displaced upward by about 25 cm (0.8 ft) above the summer water levels. **Figure 4-11** also emphasizes the extremes associated with major El Niños, with the peaks between the 1983 and 1997 major events having been systematically shifted upward over the years due to relative sea level changes along this particular section of the coast. In contrast, the summer regression line is characterized by significantly less scatter in the residuals because it effectively excludes the influence of storms and El Niños that are dominant during the winter. By using this approach, it can be seen that the central Oregon coast is slowly being transgressed at a rate of ~1.6 ±0.80 mm/yr, and is lower than that reported by NOS (~2.04 ±0.8 mm/yr). However, work by Burgette and others (2009) revealed that the SB tide gauge was been affected by localized subsidence, particularly in the late 1960s and early 1970s, that continued to decrease over time up until the mid 1990s. Since then, repeat surveys of NGS benchmark indicate that the land appears now to be stable. Accounting for these effects reduces the rate of sea level rise at the SB gauge to ~1.6 ±0.80 mm/yr.

**Figure 4-11. The trends of "winter (red)" and "summer (blue)" mean-sea levels measured by the South Beach tide gauge. Results for the summer regression are statistically significant, while the estimated winter rate is not significant at the 95% confidence level.**

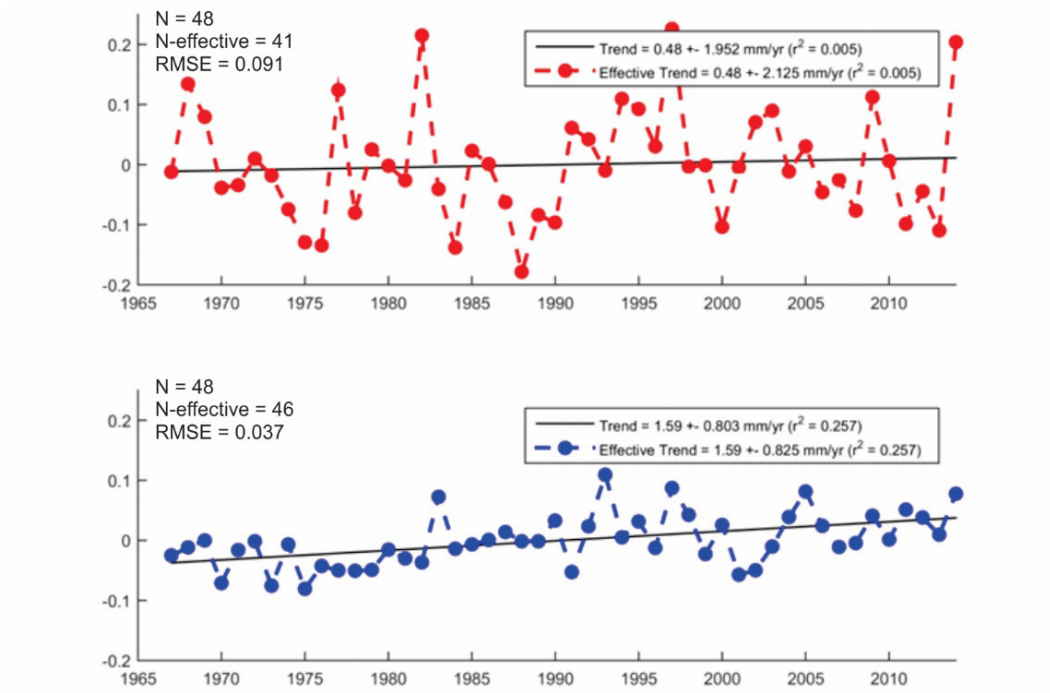

Finally, it is important to appreciate that the trends shown in **Figure 4-11** reflect relative sea level changes due not only to the influence of regional tectonics on land elevation in the Pacific Northwest but also to the global rise in sea level; the net change is significant for both coastal erosion and flood hazards. **Figure 4-12** presents a synthesis of both tectonic land elevation changes and sea level trends derived for multiple stations along the PNW coast (Komar and others, 2011), correlated against differential surveys of first-order NGS benchmarks [e.g., Burgette and others, 2009], and GPS CORS stations. Results here indicate that in general the southern Oregon coast is an emergent coast with tectonic uplift of the land outpacing sea level rise, consistent with the results depicted in **Figure 4-11**. In contrast, the central to northern Oregon coast is slowly being transgressed by sea level. In the far north in Clatsop County, the overall pattern suggests that this portion of the coast varies from slight submergence in the southern county to emergent in the north along the Clatsop Plains.

**Figure 4-12. Assessments of changes in relative sea level (RSL) based on tide-gauge records compared with benchmark and GPS measurements of land-elevation changes, with their corresponding RSL rates obtained by adding the 2.28 mm/yr Pacific Northwest eustatic rise in sea level.**

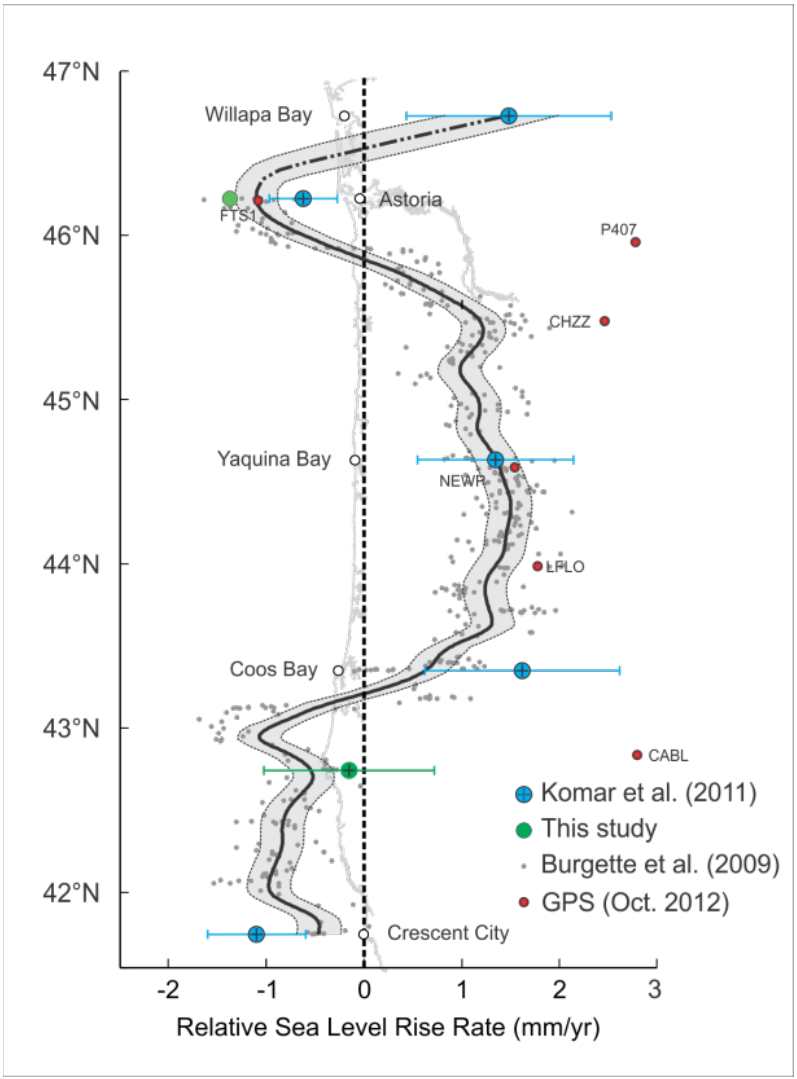

## 4.6 Still Water Level (SWL)

The still water level (SWL) is the sum of the predicted astronomical tide listed in Tide Tables, plus the effects of processes such as an El Niño or storm surge that can elevate the measured tide above the predicted tide (NHC, 2005). Of importance to erosion and flooding hazards are the extremes of the measured tides. In conventional analyses of extreme values, the general assumption is that the data being analyzed (e.g., the annual maxima) represent independent and identically distributed (stationary) sequences of random variables. The generalized extreme value (GEV) family of distributions is the cornerstone of extreme value theory, in which the cumulative distribution function is given as:

$$G(z, \mu, \sigma, \xi) = \exp\left\{-\left[1 + \xi\left(\frac{z-\mu}{\sigma}\right)\right]^{-1/\xi}\right\} \quad (4.3)$$

defined on

$$\left\{z: 1 + \frac{\xi(z-\mu)}{\sigma} > 0\right\},$$

where the parameters satisfy $-\infty < \mu < \infty$, $\sigma > 0$, $-\infty < \xi < \infty$ (Coles, 2001). The model has three parameters; $\mu$ is a location parameter, $\sigma$ is a scale parameter, and $\xi$ is a shape parameter. The EV-II (Frechet) and EV-III (Weibull) classes of extreme value distributions correspond respectively to the cases of $\xi > 0$ and $\xi < 0$. When $\xi = 0$, equation 4.3 collapses to the Gumbel or EV-I type extreme value distribution. By inferring the shape parameter $\xi$ (estimated here, along with the other parameters, by maximizing the log-likelihood function), the data themselves determine the most appropriate type of tail behavior and it is not necessary to make an a priori assumption about which individual extreme family to adopt as in a classical Weibull-type extreme wave height analysis (Coles, 2001).

The GEV is often applied to annual maxima data in an approach referred to as the annual maximum method (AMM). However, one of the primary shortcomings of fitting an extreme-value distribution with annual maximum data is that useful information about the extremes is inherently discarded, particularly when data are sampled on either a daily or an hourly basis (as in the case of the measured tides and deepwater significant wave heights measured by the Charleston tide gauge and NDBC wave buoys). Two well-known approaches exist for characterizing extremes by utilizing data other than simply annual (block) maxima. The first is based on the behavior of the r-largest-order statistics within a block, for low r, and the second is based on exceedances above a high threshold value. For the purposes of this study, we use the peak-over-threshold (POT) approach for determining the extreme SWL and wave heights.

In the peak-over-threshold (POT) method, a high threshold, $u$, is chosen in which the statistical properties of all exceedances over $u$ and the amounts by which the threshold is exceeded are analyzed. It is assumed that the number of exceedances in a given year follows a Poisson distribution with annual mean $\nu T$, where $\nu$ is the event rate and $T = 1$ year, and that the threshold excesses $y > 0$ are modeled using the generalized Pareto distribution (GPD) given by:

$$H(y, \sigma, \xi) = 1\text{-}\left(1 + \frac{\xi y}{\sigma}\right)^{-1/\xi} \quad (4\text{-}4)$$

where $\xi$ is the shape parameter of the GEV distribution and $\sigma$ is a scale parameter related to GEV parameters by $\sigma = \sigma + \xi(u - \mu)$. The event rate can also be expressed in a form compatible with the GEV distribution provided that $v = [1 + \xi(u - \mu)/\sigma]\text{^}(-1/\xi)$. Estimates of extreme quantiles of the distributions are obtained by inverting the distributions in equation 4.4. For GPD-Poisson analyses the *N*-year return level, $y_N$, is given as:

$$y_N = \mu + \frac{\sigma}{\xi}\left[(Nn_y\zeta_u)^{\xi} - 1\right] \tag{4-5}$$

where $n_y$ is the number of observations per year and $\zeta_u$ is the probability of an individual observation exceeding the threshold $u$.

**Figure 4-13** presents results of the GEV analyses for the combined SB and CH measured tides; the top plot depicts the annual maxima, while the bottom plot presents the peak-over-threshold results. In constructing the bottom plot, we used a threshold of 2.85 m (9.4 ft). Included in the figure are the calculated 1- through 500-year SWLs. As can be seen in Figure 4-13 (bottom), the 1% SWL calculated for the combined time series is 3.48 m (11.42 ft, relative to NAVD88). The 500-year SWL is estimated to be 3.55 m (11.7 ft) relative to the NAVD88 vertical datum. The highest tide measured in the combined time series reached 3.5 m (11.48 ft, relative to NAVD88).

**Figure 4-13. Extreme-value analyses of the still water level (SWL) determined for the combined South Beach and Charleston tide gauge time series. These data are relative to the NAVD88 vertical datum. Black dots reflect the discrete peak tidal events and the red line is the extreme value distribution fit to those data. Green dashed line reflects the 95% confidence boundary.**

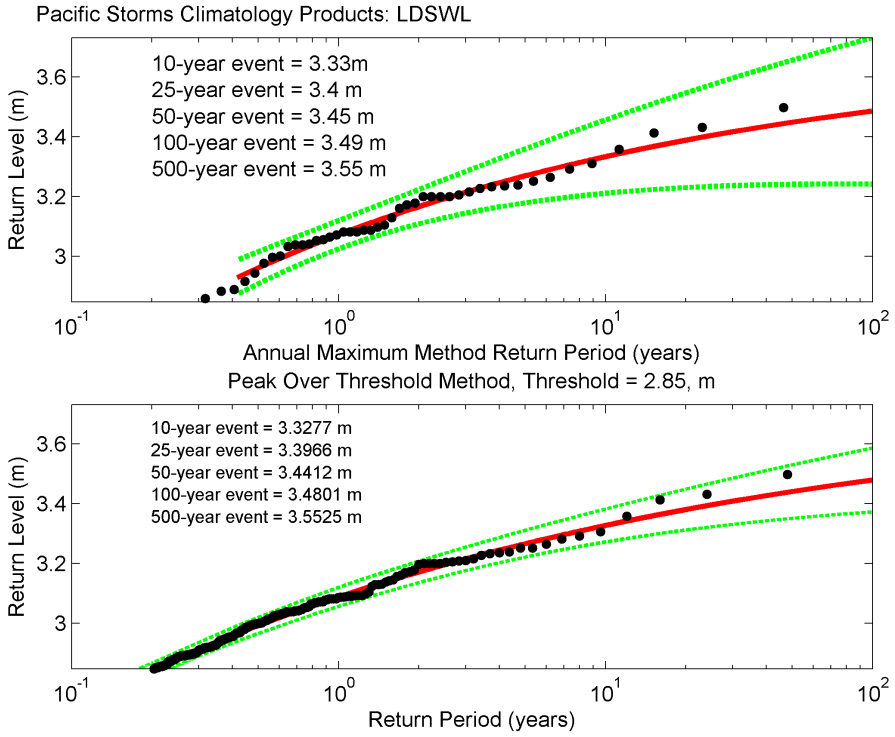

# 5.0 PACIFIC NORTHWEST WAVE CLIMATE

The wave climate offshore of the Oregon coast is among the most extreme in the world, with winter storm waves regularly reaching heights in excess of several meters. This is because the storm systems emanating from the North Pacific travel over fetches that are typically a few thousand kilometers in length and are characterized by strong winds: the two main factors that account for the development of large wave heights and long wave periods (Tillotson and Komar, 1997). These storm systems originate near Japan or off the Kamchatka Peninsula in Russia and typically travel in a southeasterly direction across the North Pacific toward the Gulf of Alaska, eventually crossing the coasts of Oregon and Washington or along the shores of British Columbia in Canada (Allan and Komar, 2002a).

Wave statistics (heights, periods and, more recently, wave direction) have been measured in the Eastern North Pacific using wave buoys and sensor arrays since the mid 1970s. These data have been collected by the NDBC and by the Coastal Data Information Program (CDIP) of Scripps Institution of Oceanography. The buoys cover the region between the Gulf of Alaska and Southern California and are located in both deep and intermediate to shallow water over the continental shelf. The NDBC operates some 30 stations along the West Coast of North America, while CDIP has at various times carried out wave measurements at 80 stations. Presently there is one CDIP buoy, operating offshore from the mouth of the Umpqua River (#46229), and three NDBC buoys (Port Orford [#46015], Oregon [#46002], and Stonewall Bank [#46050]) off south central Oregon (**Figure 5-1**). Wave measurements by NDBC are obtained hourly and are transmitted via satellite to the laboratory for analysis of the wave energy spectra, significant wave heights, and peak spectral wave periods. CDIP provides measurements every 30 minutes. Observational data from both the NDBC and CDIP buoys can be obtained directly from the NDBC website[8].

An alternate source of wave data appropriate for FEMA flood modeling is hindcast wave data such as the Global Reanalysis of Ocean Waves Fine Northeast Pacific Hindcast (GROW-FINE NEPAC) available through Oceanweather Inc., and Wave Information Studies (WIS)[9] hindcasts developed by the USACE (W.F. Baird and Associates, 2005). GROW is a global wave model, while GROW–FINE NEPAC extends the global model by incorporating a higher-resolution model grid (4 times as many data nodes), basin-specific wind adjustments based on QUIKSCAT scatterometry, enhancements in incorporating Southern Ocean swells, and the inclusion of shallow water physics (Oceanweather, 2010). GROW-FINE NEPAC data were purchased for three nodes offshore the Oregon coast, although the data were found to agree poorly with observational data, as outlined in the Tillamook and Lincoln County costal flood hazard studies (Allan and others, 2015a,b). Therefore the GROW data were not used in the wave analysis for Lane and Douglas counties. However, consistent with these previous studies, hourly deepwater wave hindcast information was obtained from the USACE Wave Information Studies (WIS) station #81055 located adjacent to NDBC buoy 46002.

Analyses of the wave climate offshore from Lane and Douglas counties was undertaken by DOGAMI staff and, as a subcontract, by Dr. Peter Ruggiero's team at the College of Earth, Ocean, and Atmospheric Sciences (CEOAS) at Oregon State University (OSU). This work included numerical analyses of the 1%, or 100-year, extreme total water levels (TWLs), which reflect the calculated wave runup superimposed on the tidal level (i.e., the still water level [SWL]) to help determine the degree of coastal flood risk along the coast of Lane and Douglas counties.

As part of this study, OSU performed a series of tests and analyses including wave transformations, empirical wave runup modeling, and TWL modeling. For the purposes of this study, OSU used the SWAN

[8] http://www.ndbc.noaa.gov/maps/Northwest.shtml

[9] http://wis.usace.army.mil/wis.shtml

(Simulating WAves Nearshore [Booij and others, 1999; Ris and others, 1999]) wave model to transform deepwater waves to the nearshore (typically the 20-m [65.6 ft] contour). The transformed waves were then linearly shoaled back into deep water to derive a refracted deepwater equivalent wave parameterization (wave height, peak period, and dominant direction) that can be used to calculate runup levels that, combined with tides, are used to estimate the flood risk along the shoreline.

In our Coos County FEMA study (Allan and others, 2012b), we developed an approach that involved several stages:

1. A time series of deepwater wave heights, periods, and directions was first defined for a particular location offshore of the shelf break, which we used to calculate an initial wave runup and TWL time series based on two representative beach slopes characteristic of beaches in the Coos County detailed study areas.
2. Using the above approach we defined ~135 discrete storm events for the two different slope types. We transformed the deepwater wave statistics associated with these events into the nearshore (20-m water depth) to account for wave refraction and shoaling effects. Depth limited breaking, wind growth, quadruplets, and triad interactions were all deactivated in the SWAN runs. The derived nearshore wave statistics were then converted back to their adjusted deepwater equivalent wave height in order to perform the wave runup analyses and ultimately compute the 1% TWLs.

**Figure 5-1. Locations of wave and tidal (SB = South Beach, OR; CH = Charleston, OR) data sources used for this study.**

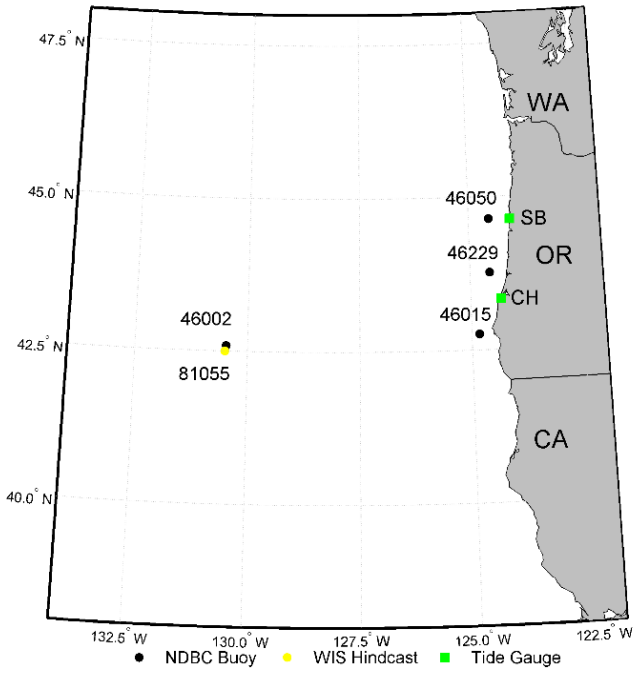

The main limitations associated with this approach were:

1. Only a limited number of model runs were performed, ~135 per representative beach slope.
2. Because we used only two representative beach slopes, we may have missed a particular wave condition (wave height [$H_s$], period [$T_P$], direction [$D_d$]) and beach slope (tan $\beta$) combination that resulted in a higher TWLs at the shoreline.
3. The structural function approach used to generate the initial extreme TWLs and therefore to pick the offshore wave conditions input in SWAN is fundamentally limited. Nature gave us only one combination of waves and water levels during the 30 years we used to generate input conditions, which is not necessarily a statistically robust sample.

For the purposes of the Lane and Douglas County study, including other detailed FEMA coastal studies recently completed or underway for Oregon, we developed a more refined approach that reflects the following enhancements.

1. Rather than steps 1 and 2 as described for our Coos County study, modeling was carried out based on analyses of the full range of wave and tide combinations observed over the historical period. This approach ultimately provides a more robust measure of the 1% (and other desired return periods) TWLs.
2. We have developed a lookup table approach for analyzing thousands of possible storm combinations rather than only a few hundred as performed in Coos County. The general idea is that a "lookup table" can be developed by transforming all combinations of wave quadruplets ($H_S$, $T_P$, $D_d$, and water levels). We used SWAN to compute the transformed wave characteristics of these waves up to approximately the 20-m contour.
3. Our approach still suffers from the third limitation listed above for the Coos County study.

The area over which the SWAN grid was set up is shown in **Figure 5-2**. In general, our analyses proceeded in the following order:

1. Develop a long time series of both measured (NDBC) and modeled (WIS) wave conditions (~30 years long) at approximately the shelf edge offshore of the study area.
2. Run the SWAN model with a full range of input conditions, using constant offshore boundary conditions, to compute bathymetric induced wave transformations up to wave breaking.
3. Develop 'lookup tables" from the suite of SWAN simulations.
4. Transform the long time series through the "lookup tables" such that we generate alongshore varying time series at approximately the 20-m depth contour throughout the study area.
5. Using the deepwater equivalent alongshore varying wave conditions and the appropriate measured tides from the combined Port Orford/Charleston/Yaquina Bay time series compute time series of TWLs for 57 primary beach profile sites along the Lane County coast from the Siuslaw River inlet to Cape Perpetua. While the SWAN model was run for both Lane and Douglas counties, no beach profile sites were specifically analyzed within Douglas County.
6. Using a Poisson-Generalized Pareto Distribution, compute the 1-, 10-, 25-, 50-, 100-, and 500-year TWL elevations using a peak-over-threshold (POT) approach.
7. Compare extreme TWLs with topographic elevations of various beach backing features to determine the potential extent of coastal flooding during extreme events.

The following sections describe in more detail the procedures used in each of the aforementioned steps in this analysis.

**Figure 5-2. The SWAN model domain developed for Lane and Douglas County. The model bathymetry was developed using 1/3 arc-second (~10 m) NOAA NGDC DEMs for shallow water (< 150 m) and ETOPO1 (1 arc minute) data for bathymetry on the shelf.**

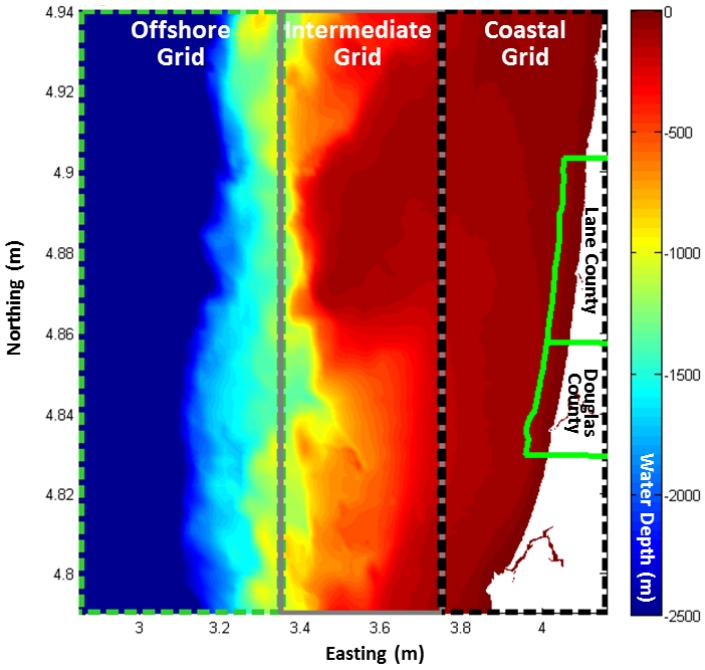


## 5.1 Development of a Synthesized Wave Climate for Input into SWAN

Our primary goal was to use existing measured and hindcast wave time series to generate as long a time series of the deepwater wave climate as possible at the offshore boundary of the SWAN model, approximately the edge of the continental shelf break. To this end, we downloaded all available National Data Buoy Center (NDBC, http://www.ndbc.noaa.gov/) and Coastal Data Information Program (CDIP, http://cdip.ucsd.edu/) hourly wave buoy data in the region for several wave buoys. **Figure 5-1** shows the buoys used to derived a synthesized southern Oregon coast wave dataset (data availability shown in **Figure 5-3**). Besides the hourly measured wave buoy data, we also obtained wave hindcast information on the deepwater wave climate determined through the Wave Information Studies (WIS, http://wis.usace.army.mil/hindcasts.html?dmn=pacific) (W.F. Baird and Associates, 2005). For the purposes of this study, we used wave hindcast data determined for WIS station 81055 (**Figure 5-1**), which is located adjacent to NDBC buoy #46002. While NDBC #46002 has a high-quality, long record of data (~1975–2013), it is located in 3,444 m (11,300 ft) of water and is located 400–500 km (250–310 miles) from the shelf edge. Therefore, NDBC #46229, an intermediate water depth buoy, was selected as the priority buoy for this analysis, and the data from NDBC #46299 were linearly reverse shoaled to deep water to account for wave height changes in intermediate depths. The on-shelf buoys (Port Orford, #46015, Stonewall Bank #46050) were also included in this analysis and the data were also reverse shoaled to deep water. Because of the variation in location and water depth of the buoys, we needed to develop a methodology to transform these "off-shelf" and "on-shelf" waves to the "shelf-edge" offshore boundary condition of the SWAN model. This was necessary as the wave climates observed at #46002 are different than the climate observed at the shallow water CDIP Umpqua buoy (#46229, 183 m) buoy (**Figure 5-4***).*

**Figure 5-3. Available wave data sets timeline (after Harris, 2011).**

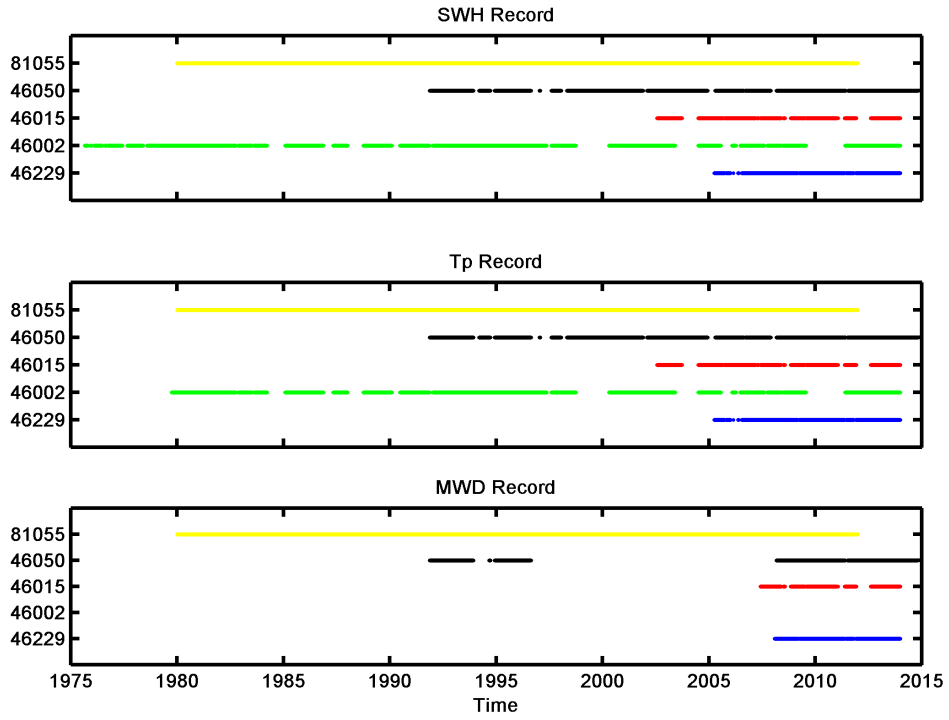


**Figure 5-4. Differences in the empirical probability density functions of the onshore and offshore buoys. Onshore buoys here have been reverse-shoaled to deep water.**

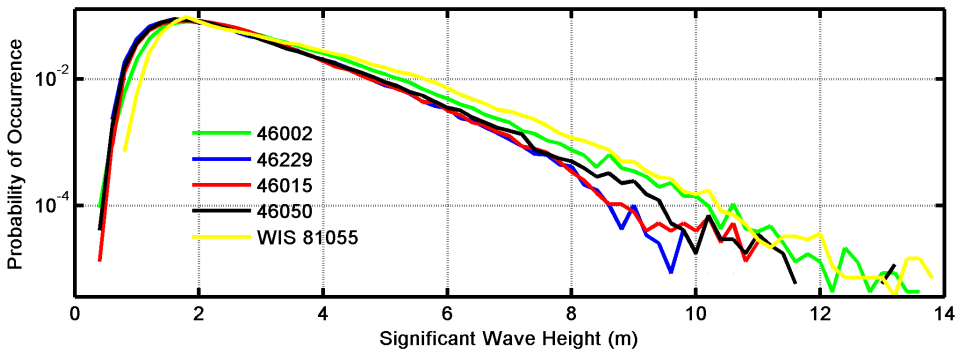

To transform the observed wave data to the shelf edge, we created wave period bins (0–6, 6–8, 8–10, 10–12, 12–14, 14–16, 16–21, 21–30 s[10]) to evaluate if wave period dependent difference in wave heights is observed at Coos Bay 46002, Port Orford 46015, and Stonewall Bank 46050 compared with the Umpqua 46229 buoy. For our comparisons, the time stamps associated with waves measured at offshore and onshore buoys were adjusted based upon the group celerity (for the appropriate wave period bin) and travel time it takes the wave energy to propagate to the wave gauge locations. For example, for waves in the period range 10–12 s, the group celerity is about 8.3 m/s and therefore it takes 17 hours for the energy to propagate from Coos Bay 46002 to the Umpqua 46229 buoy (**Figure 5-5**).

After correcting for the time of wave energy propagation, the differences in wave heights between the two buoys, for each wave period bin, were examined in two ways as illustrated in **Figure 5-5**:

1. A best fit linear regression through the wave height differences was computed for each wave period bin; and,
2. A constant offset was computed for the wave height differences for each period bin.

After applying wave height offsets to the necessary buoys, gaps in the Umpqua Offshore 46229 time series were filled in with data from the Stonewall Bank, Port Orford, and Coos Bay buoys. Where there were still gaps following this procedure we filled in the time series with corrected WIS data. Because wave transformations (particularly refraction) computed by SWAN are significantly dependent on wave direction, when this information was missing in the buoy records it was replaced with WIS data for the same date in the time series (but the wave height and period remained buoy observations where applicable).

[10] The NDBC wave buoys only relatively coarsely resolve long-period waves. Between 21 and 30 s, only a wave period of 25 s is populated in the data set. There are no 30-s waves in the time series. Of the waves with periods between 16 s and 20 s over 80 percent are at approximately 16 s. Only a few waves in the record have recorded periods of 17, 18, and 19 s, respectively. This coarse resolution in the raw data determined our choice of period bin widths.

**Figure 5-5. Example development of transformation parameters between the Coos Bay buoy (46002) and the Umpqua (46229) buoy for period range 10–12 s. In the top panel the dashed black line is the linear regression and the dashed red line is the constant offset. Blue error bars represent the standard deviation of the wave height differences in each period bin (Harris, 2011).**

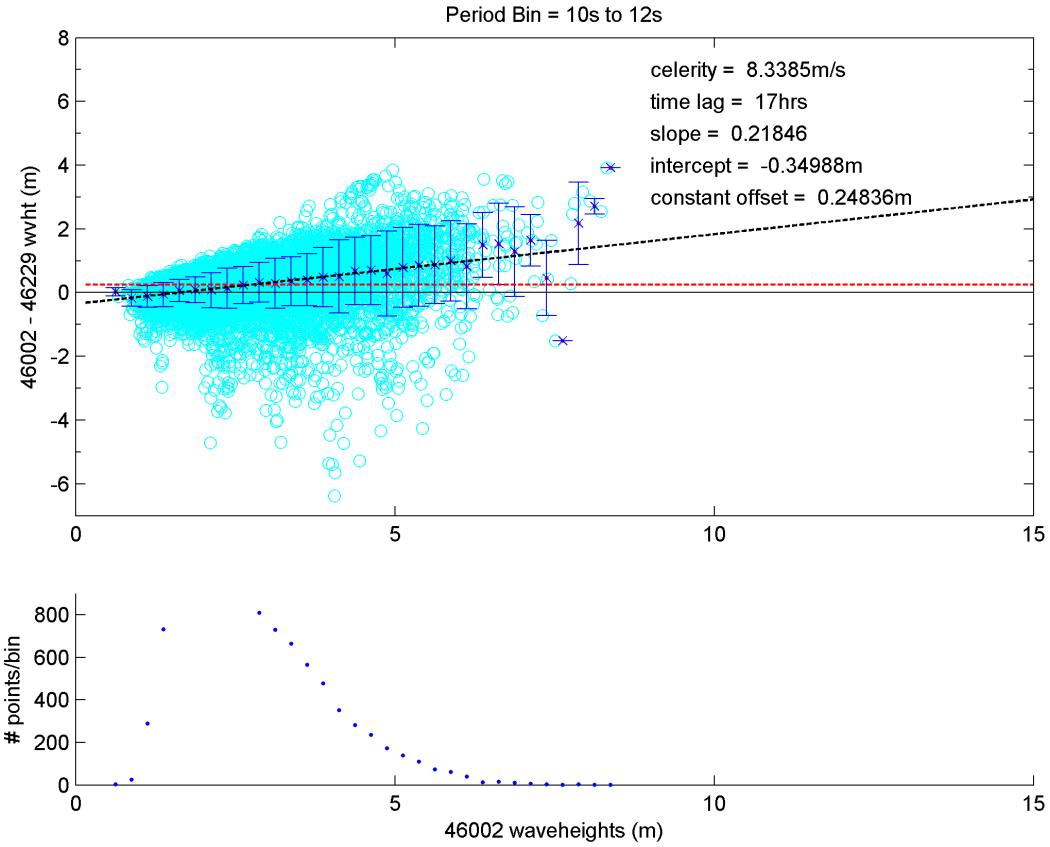

Upon examination of the empirical probability density functions (PDFs) of the buoys' raw time series (using only the years where overlap between the buoys being compared occurred) and after applying both transformation methods (**Figure 5-6**), it was determined that the constant offset method did a superior job of matching the PDFs, particularly at high wave heights. Therefore, a constant offset adjustment dependent on the wave period was applied to the wave heights of buoys offshore and onshore of the Umpqua Offshore buoy. Because the WIS hindcast data used in this study were also located well beyond the boundary of the SWAN model (basically at the location of 46002), the same series of steps comparing WIS wave heights to the Umpqua Offshore buoy was carried out, with a new set of constant offsets having been calculated and applied.

**Figure 5-6. Adjusted probability density functions (corrected using the constant offset approach) for buoys 46002 (green line), 46015 (red line), 46050 (black line), and WIS station 81055 (yellow line) as compared to the raw probability density function for buoy 46229 (blue line).**

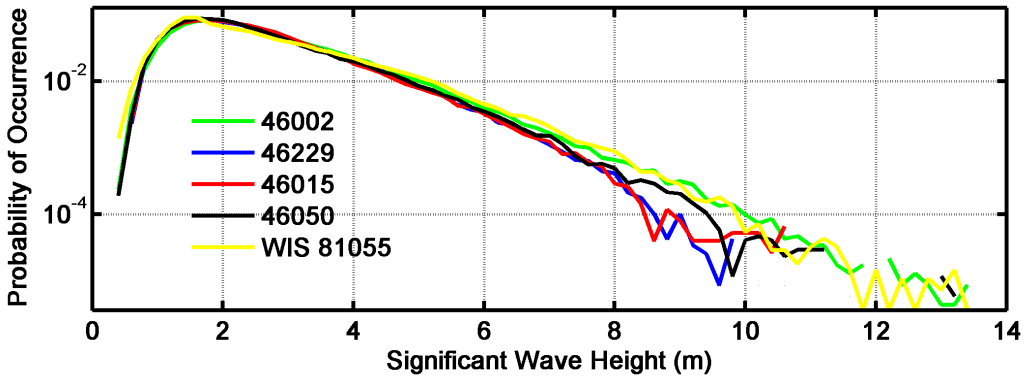

The final synthesized wave time series developed for Lane and Douglas County extends from October 1979 through to November 3, 2014, and consists of approximately 35 years of data (measurements including at least wave height and periods) (**Figure 5-7**). Thirty-five percent of the synthesized wave climate is from NDBC 46050, 32% from NDBC 46002, 23% from NDBC 46229, 9% from WIS station 81055, and ~1% from 46015. As can be seen from **Figure 5-7A**, the wave climate offshore from the south central Oregon coast is characterized by episodic, large wave events (> 8 m [26 ft]), with some storms having generated deepwater extreme waves on the order of 13.3 m (43 ft). The average wave height offshore from Lane and Douglas County is 2.4 m (7.9 ft), while the average peak spectral wave period is 11.0 s, although periods of 20–25 s are not uncommon (**Figure 5-7B**).

**Figure 5-7. Synthesized wave climate developed for Lane and Douglas County. A) Significant wave height with mean wave height denoted (dashed line), B) Peak spectral wave period with mean period denoted (dashed line), C) Probability distribution of wave heights plotted on a semi-log scale, and D) Significant wave height cumulative frequency curve plotted on a semi-log scale.**

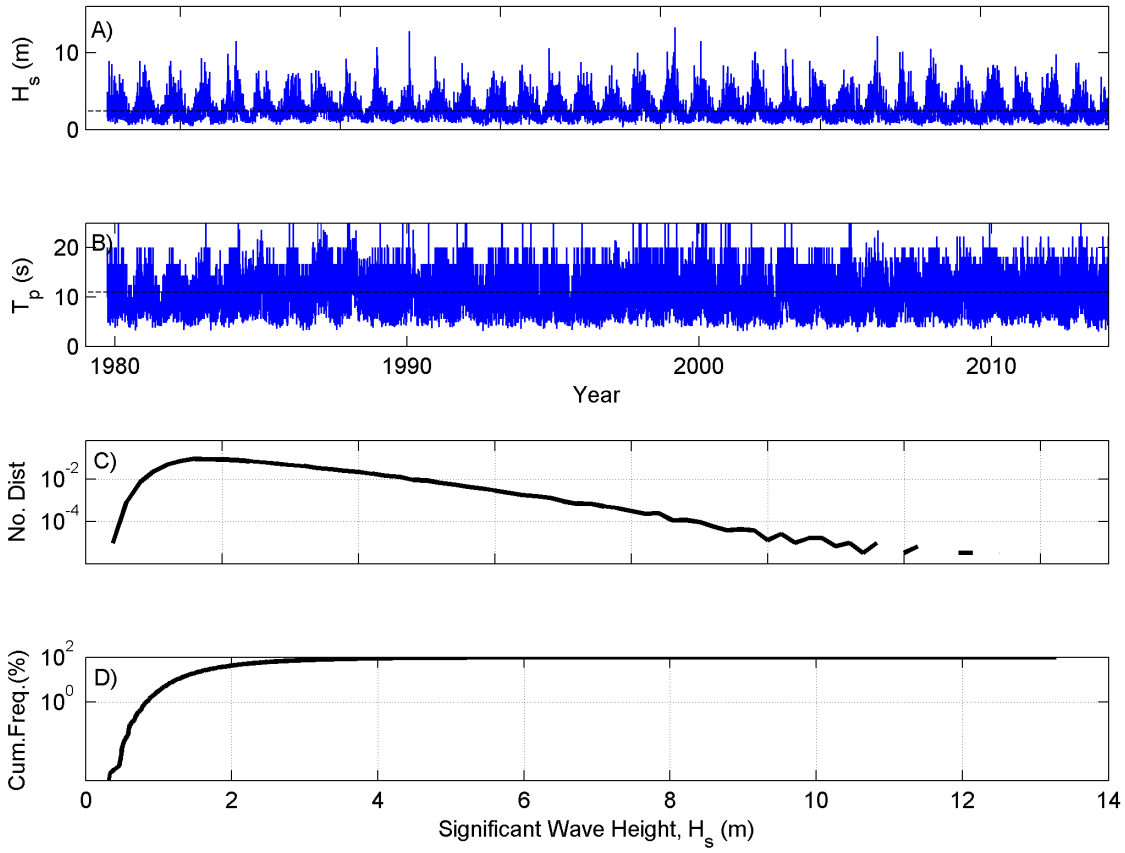

The PNW wave climate is characterized by a distinct seasonal cycle that can be seen in **Figure 5-8** by the variability in the wave heights and peak periods between summer and winter. Monthly mean significant wave heights are typically highest in December and January (**Figure 5-8**), although large wave events (>10 m [32.8 ft]) have occurred in all of the winter months except October. The highest significant wave height observed in the wave climate record is 13.3 m (43.6 ft). In general, the smallest waves occur during late spring and in the summer, with wave heights typically averaging ~1.6 m during the peak of the summer (July-August). These findings are consistent with other studies that have examined the PNW wave climate (Tillotson and Komar, 1997; Allan and Komar, 2006; Ruggiero and others, 2010b). **Figure 5-7C** shows a probability density function determined for the complete time series, while **Figure 5-7D** is a cumulative frequency curve. The latter indicates that for 50% of the time waves are typically less than 2.2 m (7.2 ft), and less than 4.0 m (13.1 ft) for 90% of the time. Wave heights exceed 6.1 m (20.0 ft) for 1% of the time. However, it is these large events that typically produce the most significant erosion and flooding events along the Oregon coast.

**Figure 5-8. Seasonal variability in the deepwater wave climate offshore from the northern Oregon coast. Top) Monthly average wave height (blue line) and standard deviation (dashed line); Bottom) Maximum monthly significant wave height.**

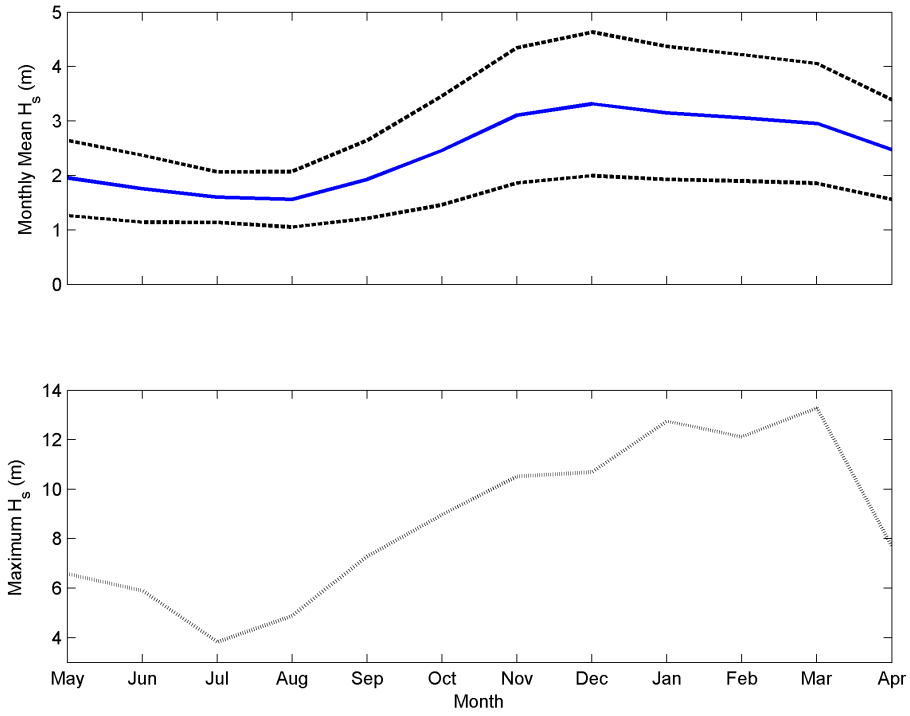

Finally, **Figure 5-9** provides a wave rose of the significant wave height versus direction developed for the south central Oregon coast. In general, the summer is characterized by waves arriving from the northwest, while winter waves typically arrive from the west or southwest (Komar, 1997). As can be seen in **Figure 5-9**, summer months are characterized by waves arriving from mainly the west-northwest (~21%) to northwesterly quadrant (~30%), with few waves from the north (< 10%) and out of the southwest. The bulk of these reflect waves with amplitudes that are predominantly less than 3 m (9.8 ft). In contrast, the winter months are dominated by much larger wave heights out of the west (~23%), and the northwest (~38%), while waves from the southwest account for ~20% of the waves.

**Figure 5-9. Left) Predominant wave directions for the summer months (June-August), and Right) winter (December-February). Colored scale indicates the significant wave height in meters.**

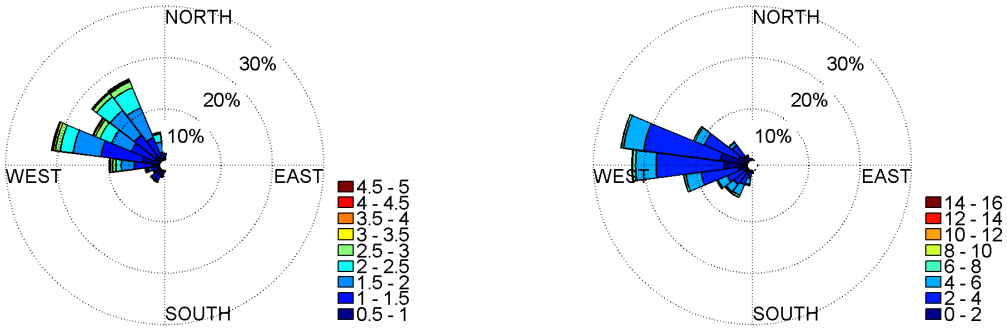


## 5.2 SWAN Model Development and Parameter Settings

We used the historical bathymetry assembled by the National Geological Data Center (NGDC) (described in **SECTION 3.4**) and created a model grid that covers a large portion of the southern Oregon coast (**Figure 5-2**).

SWAN (Simulating WAves Nearshore) version number 41.01, a third-generation wave model developed at the Technical University of Delft in the Netherlands (Booij and others, 1999; Ris and others, 1999), was used in this study. The model solves the spectral action balance equation using finite differences for a spectral or parametric input (as in our case) specified along the boundaries. For computational reasons, we performed five different model runs for this Lane and Douglas County study. A shelf scale model was developed with a horizontal resolution of 2,000 m, extending south of Charleston, Oregon, north to Newport, Oregon, and west to 125.65° W. This model was used to propagate waves over the shelf edge to about 1,000 m water depth. At 125°W, spectral output from the shelf grid was used to force an intermediate grid with horizontal resolution of 500 m and that had the same northern and southern extents as the shelf grid. At 124.54°W (approximately 150-m water depth), the intermediate grid was used to force an adjacent coastal grid with dimension of 100 × 100 m. This coastal grid covers 40 km by 150 km in length, which yields 410 × 1,501 computational nodes.

All three of the SWAN model grids were additionally forced at the northern and southern boundaries by one-dimensional SWAN grids with 100-m resolution that were initialized at the offshore boundary by the same wave spectrum as provided to the shelf grid. Bathymetry used for the SWAN model implementation (Booij and others, 1999) was put together by combining ETOPO1 (Amante and Eakins, 2009) and NOAA Tsunami Bathymetry (Carignan and others, 2009a,b) datasets. The SWAN runs were

executed in stationary mode and included physics that accounted for shoaling, refraction, and breaking; model settings that varied from the default values are discussed in more detail below.

The north, south, and west boundaries of the model were forced using a parameterized JONSWAP spectrum. The functions for spectral peakedness parameters $\gamma$ and $nn$ in the JONSWAP directional spectra are given as:

$$\gamma = \begin{cases} 3.3 & \text{if } Tp < 11s \\ 0.5Tp - 1.5 & \text{if } Tp \geq 11s \end{cases}$$
$$nn = \begin{cases} 4 & \text{if } Tp < 11s \\ 2.5Tp - 20 & \text{if } Tp \geq 11s \end{cases} \quad (5.1)$$

Thus, the directional distribution is generated by multiplying the standard JONSWAP frequency spectrum by $\cos^{nn}(\theta - \theta_{peak})$ (Smith and others, 2001). Wind wave spectra are broad (low $\gamma$ and $nn$ values), while swell typically have narrow distributions (high $\gamma$ and $nn$ values). The values used in the SWAN wave modeling were based on the input peak periods that ranged from $4.055 \leq \gamma \leq 11.03$ and $7.775 \leq nn \leq 42.65$. To ensure that the wave directional spread is sufficiently resolved by the model, we specified directional bins giving a 6-degree directional resolution. The spectrum was discretized in frequency space with 36 bins from 0.025 to 1 Hz. Wind was not included in the SWAN simulations and therefore no energy growth due to wind, or quadruplet wave-wave interactions occurs in the simulations. Triad interactions, diffraction, and wave setup also were not activated in the model. We used the Janssen frictional dissipation option, which has a default friction coefficient of $0.067 m^2/s^3$. No model calibration was performed in this study, although several numerical experiments were implemented to test various assumptions in the wave modeling (e.g., not to use winds).

### 5.2.1 Wind effects

The decision not to model the effect of winds on wave growth over the continental shelf in our Coos County study was based on two observations:

1. To develop our combined wave time series described previously, we performed a "statistical" wave transformation between NDBC buoy 46002 and the buoys at the edge of the continental shelf and found that in general the wave heights during storm events decreased even with hundreds of kilometers of additional fetch. Without understanding the details of this phenomenon (e.g., white capping versus wind wave growth) and with no data for calibration we felt that attempting to model wind growth would add to the uncertainty of our input wave conditions.
2. We have previous experience with SWAN wave modeling in the region (U.S. Pacific Northwest) in which sensitivity runs including wind were performed with only minor impact on results (Ruggiero and others, 2010a).

To test the validity of the assumptions made in our Coos County study, several wave modeling experiments were performed in order to specifically examine the role of additional wind wave development over the shelf. The basic question that was addressed is: How much do wind fields result in wave growth between locations seaward of the shelf break, roughly equivalent to the offshore extent of the Tillamook (46089) buoy shown in **Figure 5-1** and the inner shelf? The latter was defined as the 100-m (300 ft) isobath. To address this question, hindcast waves were modeled for the months of January and

February (i.e., peak of the winter season) and for two representative years (2006 and 2010). The wave modeling was accomplished by running a regional Eastern North Pacific (ENP) model and a 3 arc-min grid for the Oregon coast, with the outer boundary coinciding with the Tillamook buoy station (**Figure 5-10**). The model runs were forced by analyzed Global Forecast System winds with a temporal resolution of 6 hours and a spatial resolution of 1 arc-degree. A similar run was undertaken without winds over the same 3 arc-min grid, just propagating the boundary conditions. Hindcast wave data were obtained from selected points across the shelf at contour depths of 500, 400, 300, 200, and 100 m along a cross-shore transect (A and B in **Figure 5-10**).

**Figure 5-10. Left) Map showing the locations of the northern Oregon coast buoys, and transect lines (labeled A and B), and Right) model domain (green box; see text).**

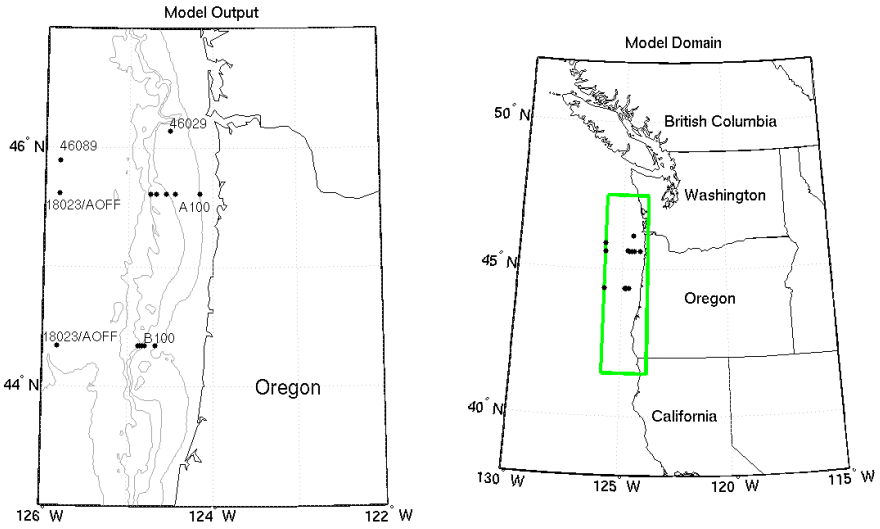


Results from the model runs (with and without winds) are presented in **Figure 5-11** and **Figure 5-12**. Modeled and measured waves for two NDBC buoys (46029 and 46089) are included for comparative purposes (**Figure 5-13** and **Figure 5-14**). In general, our experiments indicated that although the addition of wind sometimes changed the timing of the large wave events, producing at times a relatively large percentage error for part of the "wave hydrograph," the peaks of the wave events showed very little difference between cases where wind was included or excluded (**Figure 5-11** and **Figure 5-12**). Furthermore, in the majority of cases, the differences in the derived wave heights between model runs including (excluding) wind (no wind) were on the whole minor. This finding was also observed in the derived peak wave periods, which appear to be virtually identical in all the plots. Of greater concern in these model tests are the occasional large differences between the modeled runs (irrespective of whether wind/no wind is applied) and the actual measurements derived from NDBC wave buoys (**Figure 5-13** and **Figure 5-14**), as well as the GROW data derived for station 18023. These findings will be explored in more detail later in this section.

These experiments support our decision to not include wind growth in our model runs and therefore quadruplet wave-wave interactions were also not incorporated in the simulations. Further, wave setup is not included in the simulations because we extract the transformed wave parameters at the 20-m depth contour and use the Stockdon and others (2006) empirical model to compute wave runup (which incorporates setup) along the coast.

**Figure 5-11. Model-model comparison at 500-m depth on transect A for the 2006 simulation.**

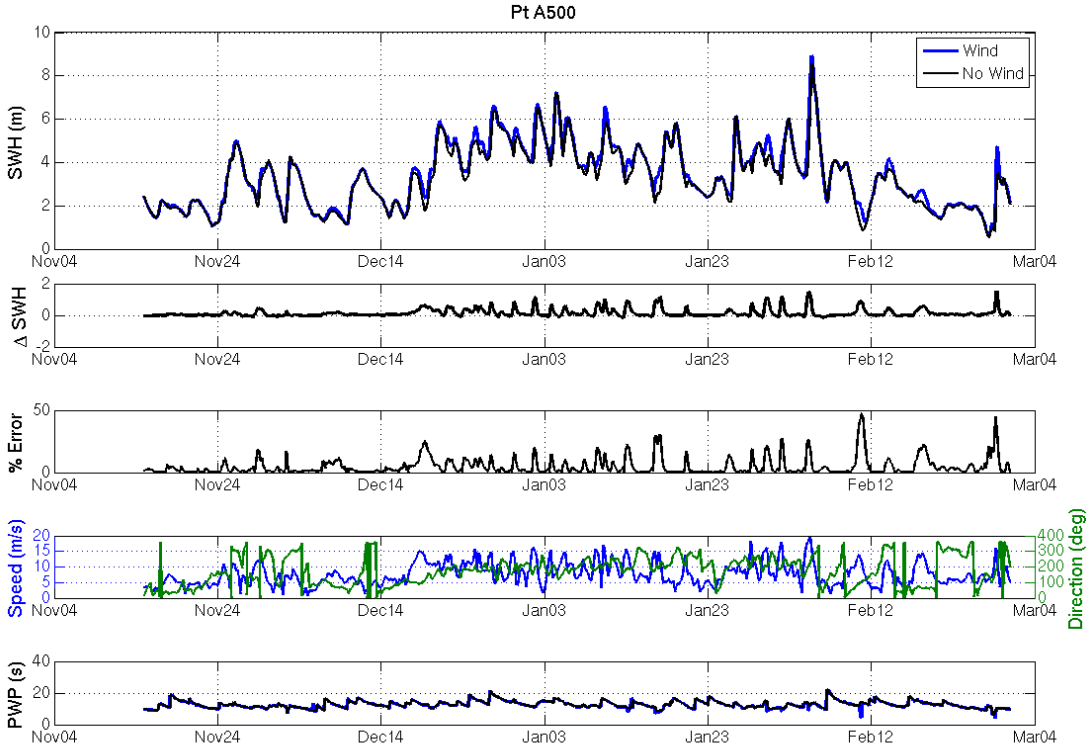


**Figure 5-12. Model-model comparison at 100-m depth on transect A for the 2006 simulation.**

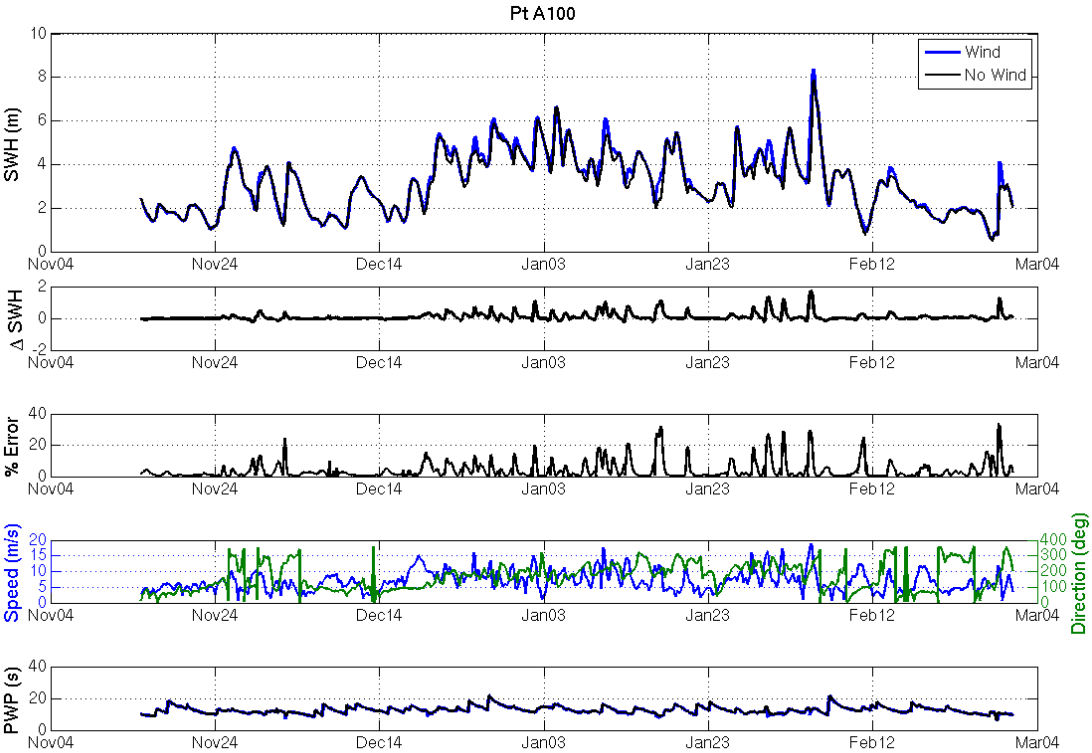

**Figure 5-13. Model data comparison at NDBC buoy #46029 for the 2006 simulations.**

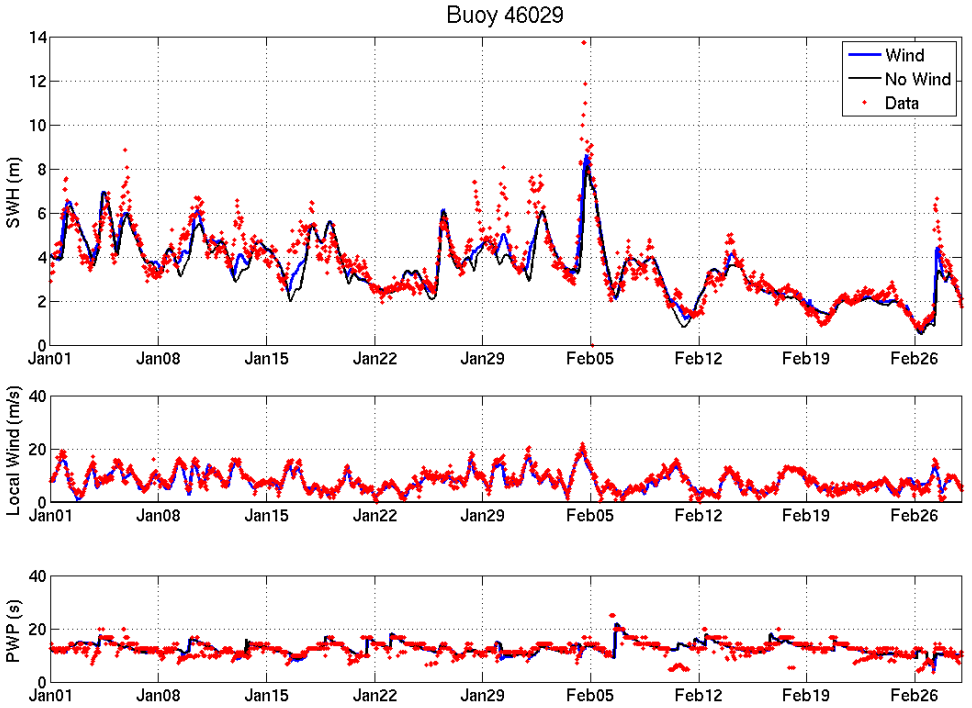


**Figure 5-14. Model data comparison at Station Aoff (GROW station location) versus buoy #46089 for the 2010 simulations.**

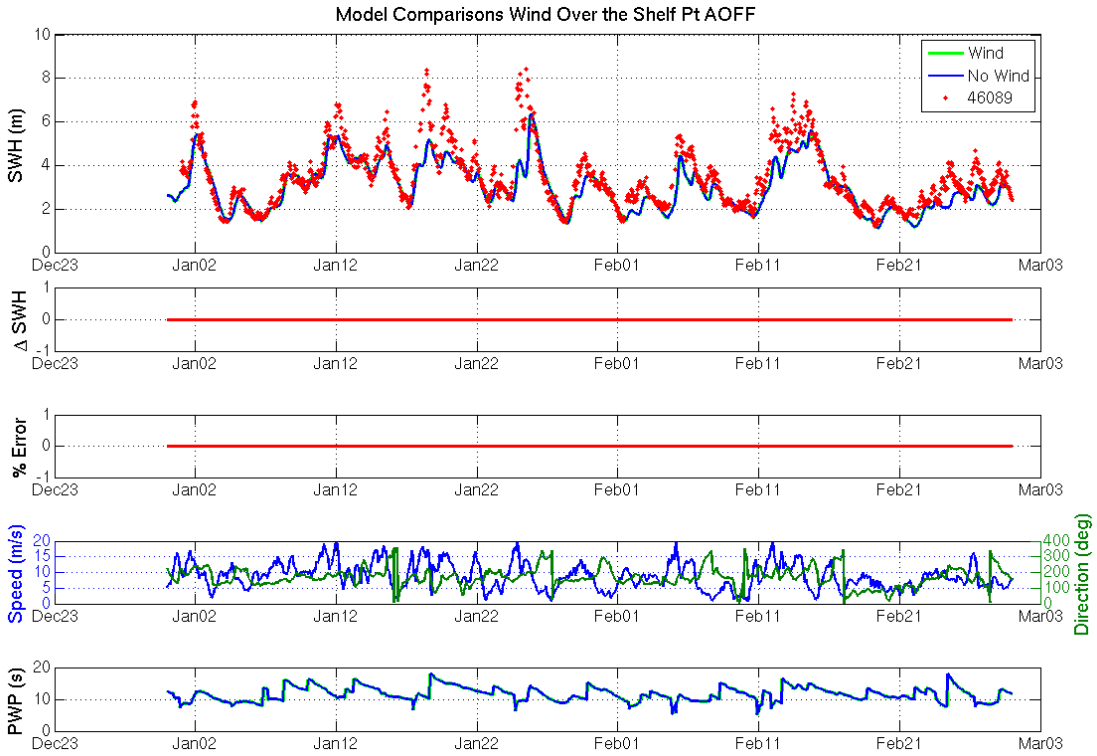

### 5.2.2 Frictional dissipation and dissipation due to whitecapping

Additional testing was undertaken to explore the effect of not including friction and whitecapping. **Figure 5-15** and **Figure 5-16** provide two test-case conditions: for a significant wave height of 10 m and peak period of 20 s, with the wave approaching from a direction of 285 degrees (NW), and for a significant wave height of 14 m, peak period of 14 s, with the wave approaching from a direction of 270 degrees (W). **Figure 5-15** indicates that for this particular condition, the modeled results are relatively similar until immediately prior to wave breaking, where significant differences arise. However, as the significant wave height increases (**Figure 5-16**), the effect of excluding bottom friction and whitecapping becomes considerably larger. The exclusion of these processes results in an overestimation of wave heights prior to breaking. Therefore, we have chosen to include frictional dissipation and dissipation due to whitecapping in our modeling.

### 5.2.3 Lookup table development

Having demonstrated that winds have little impact in terms of additional wave development across the continental shelf of Oregon, our next goal was to develop an efficient methodology that could be used to minimize the total number of SWAN runs needed to perform the actual wave modeling and transformations, while ensuring that we resolved the influence of varying parameters on the wave transformations. To do this we discretized the significant wave height ($H_s$), peak period ($T_p$), wave direction ($D_p$), and water level ($WL$) time series.

**Figure 5-15. The impact of ignoring bottom frictional dissipation and dissipation due to whitecapping for a 10-m significant wave height with a peak period of 20 s approaching from a direction of 285 degrees.**

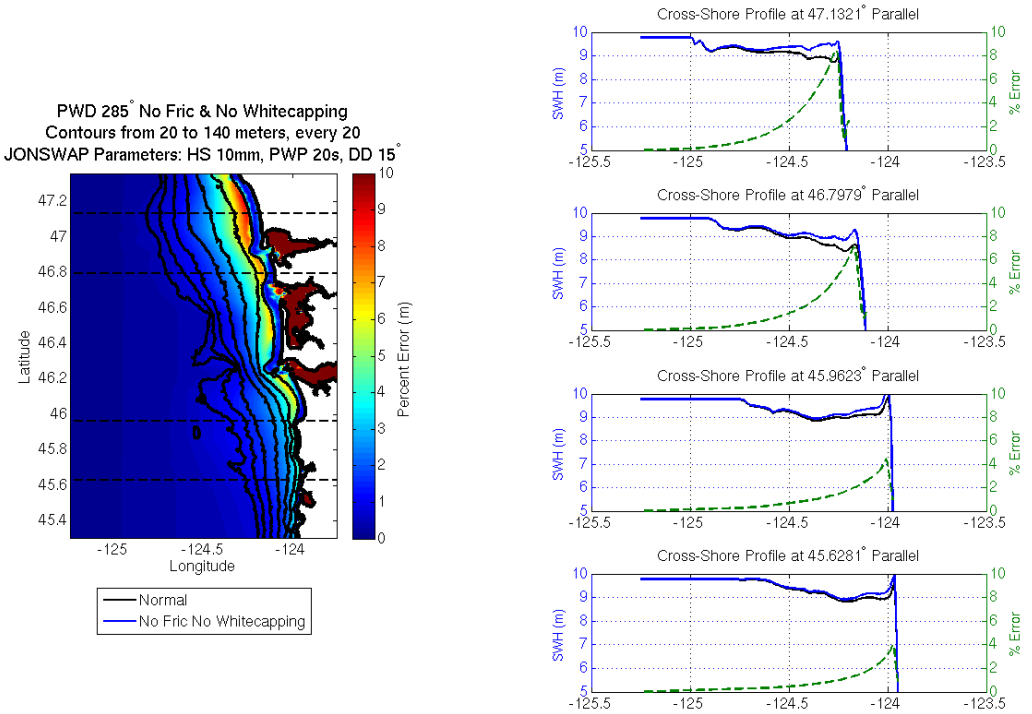


**Figure 5-16. The impact of ignoring bottom frictional dissipation and dissipation due to whitecapping for a 14-m significant wave height with a peak period of 14 s approaching from a direction of 270 degrees.**

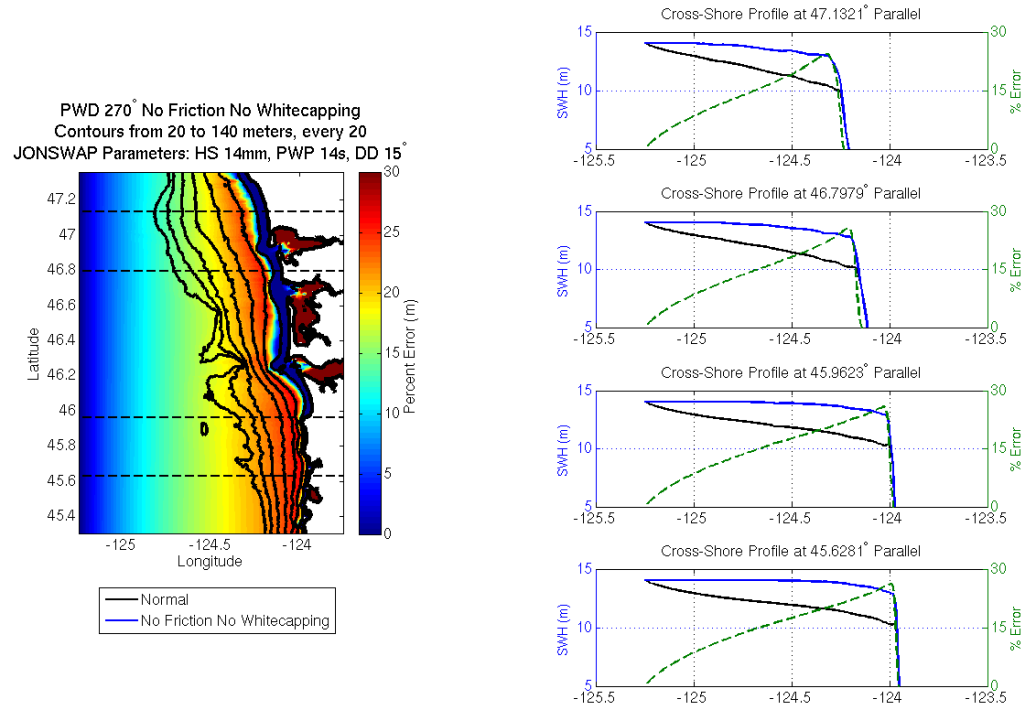

For the direction bins ($D_p$), the bin widths were made approximately proportional to the probability distribution function of the synthesized wave climate time series. In application of this approach in our Clatsop County study, 11 directional bins were created that have approximately an equal probability of occurrence (**Figure 5-17**). As originally defined, the bin edges were: $D_p$ = [170, 225, 240, 251, 260, 268, 277, 288, 304, 331, 370] and were subsequently refined in SWAN to $D_p$ = [170, 225, 240, 250, 260, 270, 280, 290, 305, 330, 370], resulting in 11 direction cases for our Clatsop County SWAN runs. At the bin edges, linear interpolation is used to derive the wave parameters. From initial sensitivity runs undertaken as part of our Clatsop County study (Allan and others 2015c), we have determined that these bin widths are more than adequate. **Figure 5-18** shows the result of interpolating over a 20-degree bin spacing.

For the purposes of the Lane and Douglas County work, we further refined our original approach to include an additional two directional bins. This was accomplished by refining the spread of the bins to better reflect the observed conditions offshore Tillamook and Lincoln counties. The final bin edges are defined as $D_p$ = [175, 205, 225, 240, 250, 260, 270, 280, 290, 300, 315, 335, 365].

**Figure 5-17. Joint probability of wave height and dominant wave direction from the combined time series. The white dots represent bin centers, from a much smaller mesh, in which this combination of $H_s$ and $D_p$ does not exist in the combined time series.**

**Figure 5-18. SWAN wave modeling and calculated alongshore wave variability using the lookup table approach. The left red line represents the alongshore variable wave height at the 20-m depth contour for an incident angle of 240 degrees ($H_s$ = 10, $T_p$ = 15 s) and the right red line is for an angle of 260 degrees. The blue line is the wave height for an angle of 250 degrees as modeled in SWAN, while the green line is the linearly interpolated wave heights using the lookup table. Note that this is a preliminary SWAN model run, meant for testing the interpolation scheme, and the lateral boundary conditions are not dealt with in the same manner as in our production SWAN runs.**

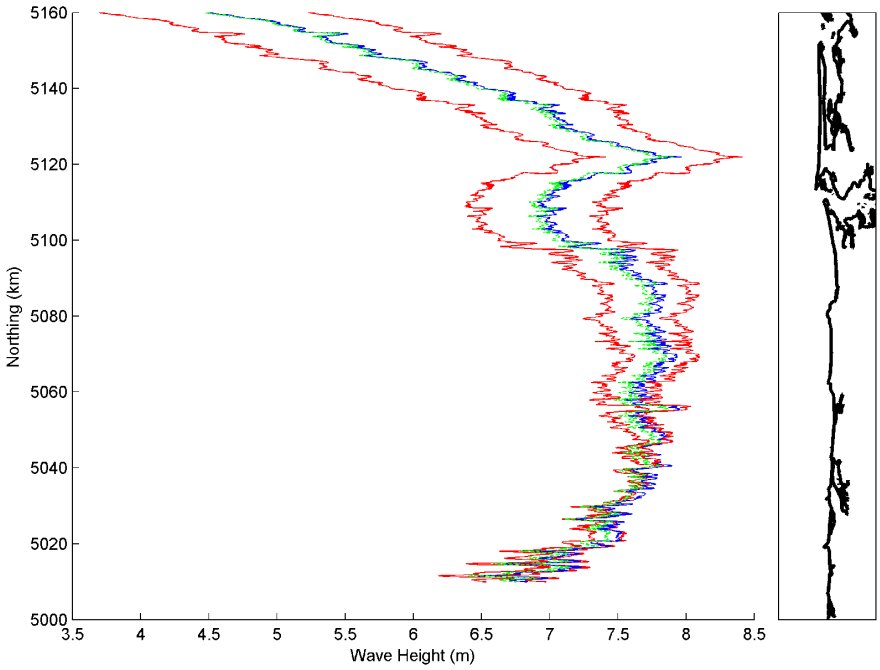


For the significant wave heights bins, we identified the following deepwater significant wave heights for inclusion in SWAN: $H_s$ (m) = [0.25, 1.5, 2.5, 3.5, 5, 7, 10, 13, 16.5], which gives us nine cases. From on our sensitivity tests we found that a bin width of 3 m for large waves is sufficient for resolving the linearly interpolated wave conditions (**Figure 5-19**). In the case of the deepwater peak periods, our analyses identified the following period bins for inclusion in SWAN: $T_p$ (s) = [2, 4, 6, 9, 11, 13, 15, 17, 20, 23, 26], which provides a total of 11 additional cases. From on our sensitivity tests, we found that the linear interpolation approach for wave period is not quite as good as for direction and wave height. Because wave period affects breaking, shoaling, and whitecapping, there is significant variability in the wave transformations as a function of wave period. For our sensitivity run of $H_s$ = 10 m, and $D_p$ = 260 degrees, **Figure 5-20** illustrates the impact of linear interpolation. However, for the most part in our parameter space we will have interpolation errors only around 10%. In this particular example the maximum error is only approximately 4%.

**Figure 5-21** presents the joint probability of wave height and peak period from the combined time series. The white dots represent bin centers, from a much smaller mesh, in which this combination of $H_s$ and $T_p$ does not exist in the time series. The red line represents the theoretical wave steepness limit below which waves are non-physical. We can use this information to reduce the overall matrix of model runs.

**Figure 5-19. SWAN wave modeling and calculated alongshore wave variability using the lookup table approach for an 11-m and 15-m incident wave. In this example the red lines are the alongshore varying wave height in 20 m. The blue line is the modeled transformed 13-m wave height while the green represents a linear interpolation between the 11- and 15-m results.**

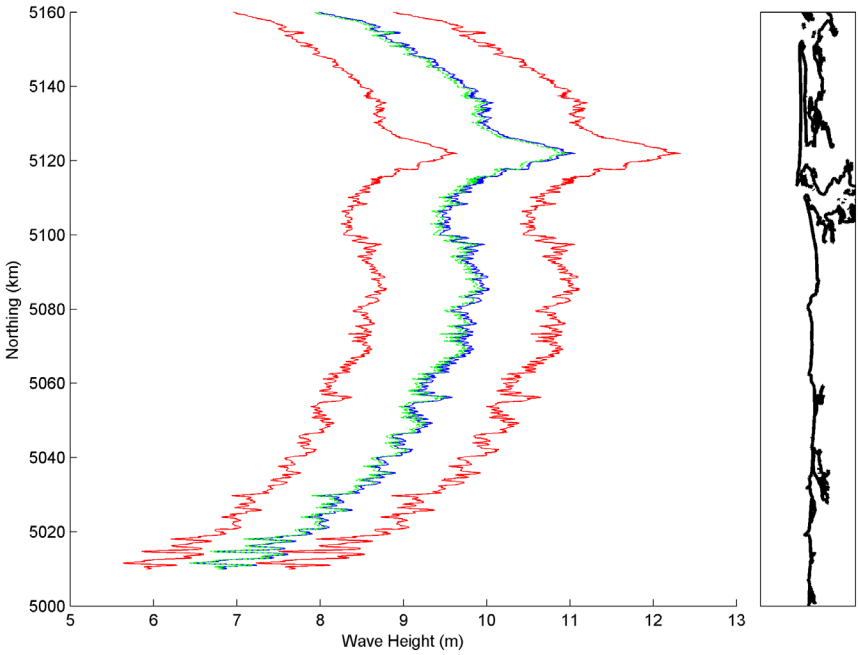


**Figure 5-20. SWAN wave modeling and calculated alongshore wave variability using the lookup table approach for a 10-m wave. In this example the red lines are the alongshore varying wave height for a wave arriving from 260 degrees for 20 s and 24 s. The blue line is the modeled wave height for 22 s and the green line represents a linear interpolation.**

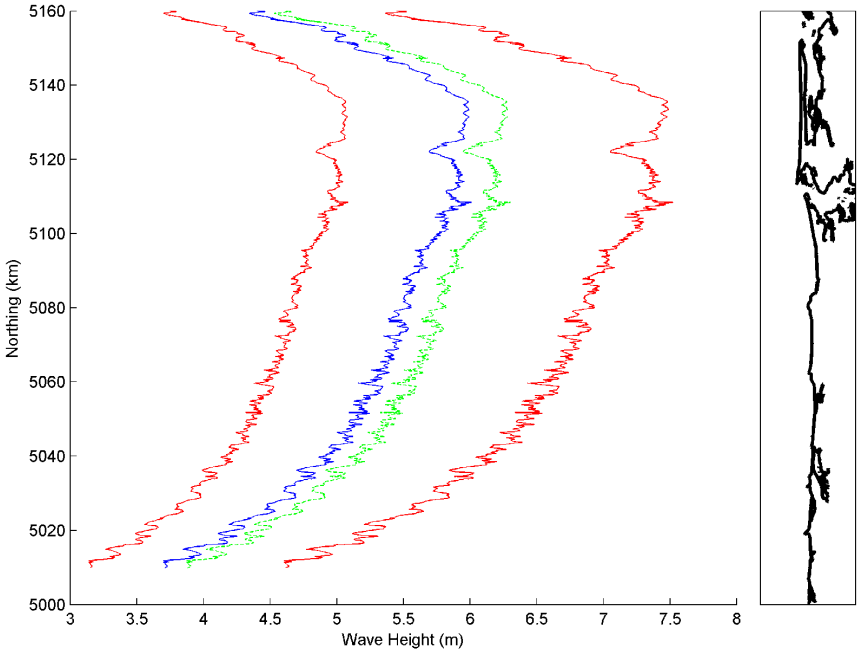

**Figure 5-21. Joint probability of wave height and peak period from the combined time series. The white dots represent bin centers, from a much smaller mesh, in which this combination of $H_s$ and $T_p$ does not exist in the combined time series. The red line represents the theoretical wave steepness limit below which waves are non-physical.**

**Figure 5-22** is the joint probability of peak period and dominant wave height shown here for completeness. Finally, we illustrate our bin choice on the individual parameter PDFs in **Figure 5-23** (buoy data).

In summary, the lookup tables were generated using all wave parameter cases and two contrasting water levels. Our sensitivity tests indicated that varying water levels have a negligible impact on the model and linearly transformed waves. The following matrix of SWAN runs is considered for lookup table development for transforming waves offshore from Lane and Douglas County:

$D_p$ = [175, 205, 225, 240, 250, 260, 270, 280, 290, 300, 315, 335, 365] (degrees) — 13 cases
$H_s$ = [0.25, 1.5, 2.5, 3.5, 5, 7, 10, 13, 16.5] (m) — 9 cases
$T_p$ = [2, 4, 6, 9, 11, 13, 15, 17, 20, 23, 26] (s) — 11 cases
$WL$ = [−1.5, 4.5] — 2 cases

In total, this equates to 2,574 model cases that can be used for linearly interpolating the waves from a time series of data. However, **Figure 5-21** indicates that several $H_s$-$T_p$ combinations are physically not realistic. Multiplying these bins by the $D_p$ and $WL$ bins means that we can eliminate 390 bins for a new total of only 2,184 model runs.

**Figure 5-22. Joint probability of dominant direction and peak period from the combined time series. The white dots represent bin centers, from a much smaller mesh, in which this combination of $D_p$ and $T_p$ does not exist in the combined time series.**

**Figure 5-23. Individual parameter probability density functions (PDFs) and bin edges using the combined buoy wave time series.**

## 5.3 Summary of SWAN Results

Significant alongshore variability is apparent in many of the conditions examined with SWAN (**Figure 5-24**). Differences in significant wave height of over a meter along the 20-m isobaths are not uncommon in Lane and Douglas counties. To calculate the wave runup along the Lane County shoreline we subsequently extracted the wave characteristics along the 20-m contour, or the seaward most location where the wave breaking parameter equaled 0.4, throughout the model domain (**Figure 5-24**). Because all of the parametric runup models used in this study rely on information on the deepwater equivalent wave height and peak periods as inputs, we then computed the linear wave theory shoaling coefficient and back shoaled our transformed waves to deep water. These transformed deepwater equivalent waves were then used to calculate the wave runup and generate the TWL conditions used in the subsequent extreme value analysis.

**Figure 5-24. Example SWAN simulation offshore from Lane and Douglas counties (offshore significant wave height of 5 m, peak wave period of 10 s, and peak wave direction of 225 degrees). Significant wave height in the modeling domain is shown in colors. Dissipation processes generate differences in the inner shelf wave height. Obscured text at top of figure is "× $10^6$".**

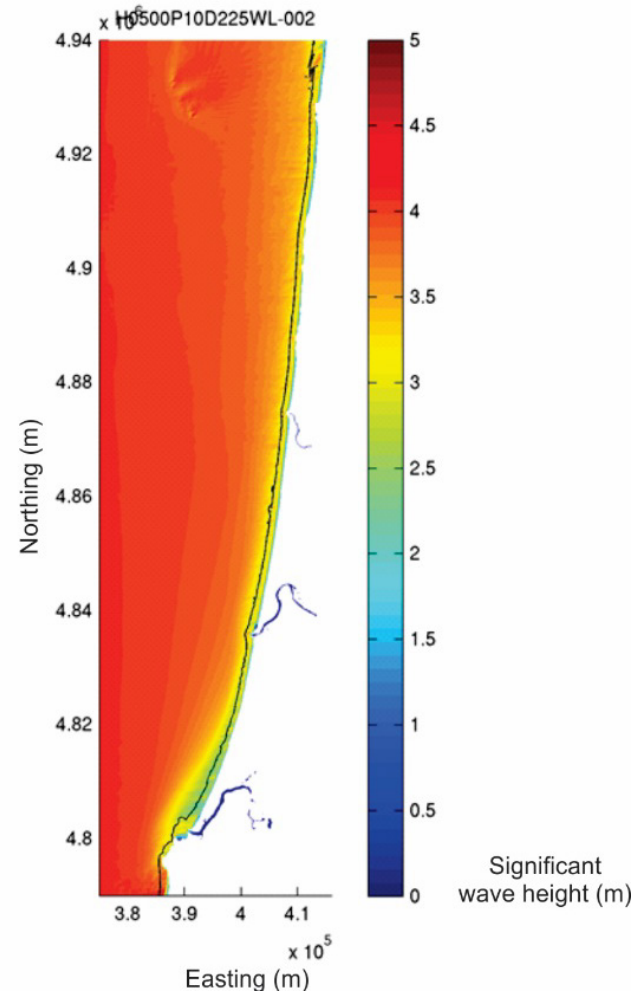

To confirm that our approach of interpolating wave transformations using lookup tables is appropriate, we ran several additional SWAN runs that were not part of our original matrix. These additional runs extended across a range of conditions, including extreme events capable of forcing high water levels at the coast. We then compare the results from using the lookup tables to these additional direct SWAN computations at the 20-m contour location. **Figure 5-25** to **Figure 5-27** show a sample of these results for wave height, peak period, and direction, respectively, for a SWAN run driven with an offshore boundary condition of $H_s$ = 5 m, $T_p$ = 10 s, $D_p$ = 225, and a water level of −1.5 m NAVD88. In all cases, the percentage error between lookup table and direct computation is low, typically averaging less than 5%.

**Figure 5-25. Comparison of alongshore varying wave height at the 20-m contour extracted from the lookup tables (blue line) and from a direct SWAN computation (black line) with an offshore boundary condition characterized as $H_s$ = 5 m, $T_p$ = 10, $D_p$ = 225, and a water level of −1.5 m NAVD88. Solid red line denotes Lane and Douglas County boundaries.**

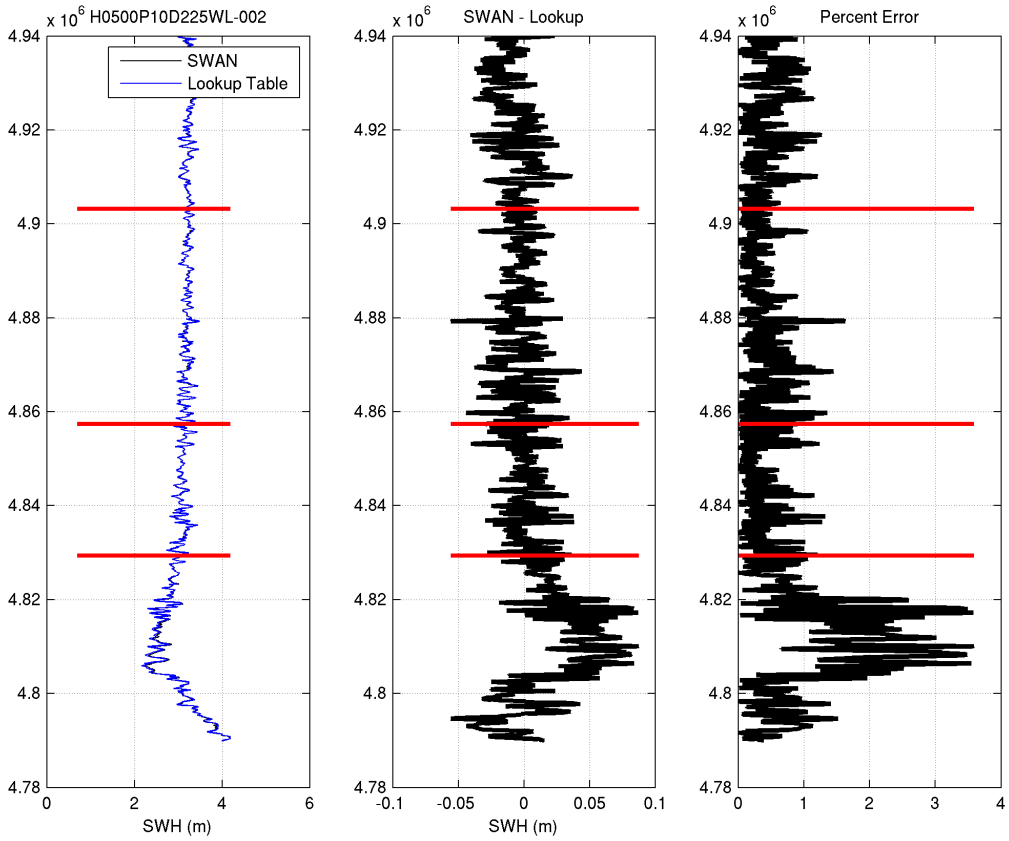

**Figure 5-26. Comparison of alongshore varying wave period at the 20-m contour extracted from the lookup tables (blue line) and from a direct SWAN computation (black line) with an offshore boundary condition characterized as $H_s$ = 5 m, $T_p$ = 10, $D_p$ = 225, and a water level of −1.5 m NAVD88. Solid red line denotes Lane and Douglas County boundaries.**

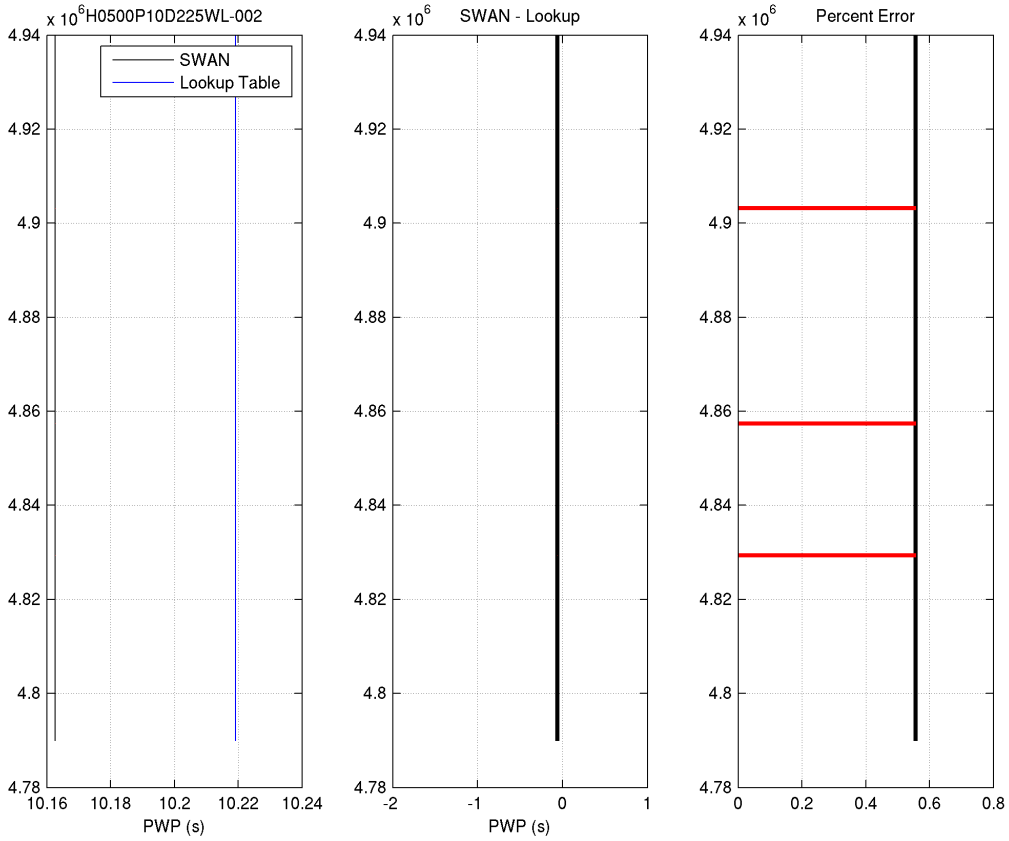

**Figure 5-27. Comparison of alongshore varying wave direction at the 20-m contour extracted from the lookup tables (blue line) and from a direct SWAN computation (black line) with an offshore boundary condition characterized as $H_s$ = 5 m, $T_p$ = 10, $D_p$ = 225, and a water level of −1.5 m NAVD88. Solid red line denotes Lane and Douglas County boundaries.**

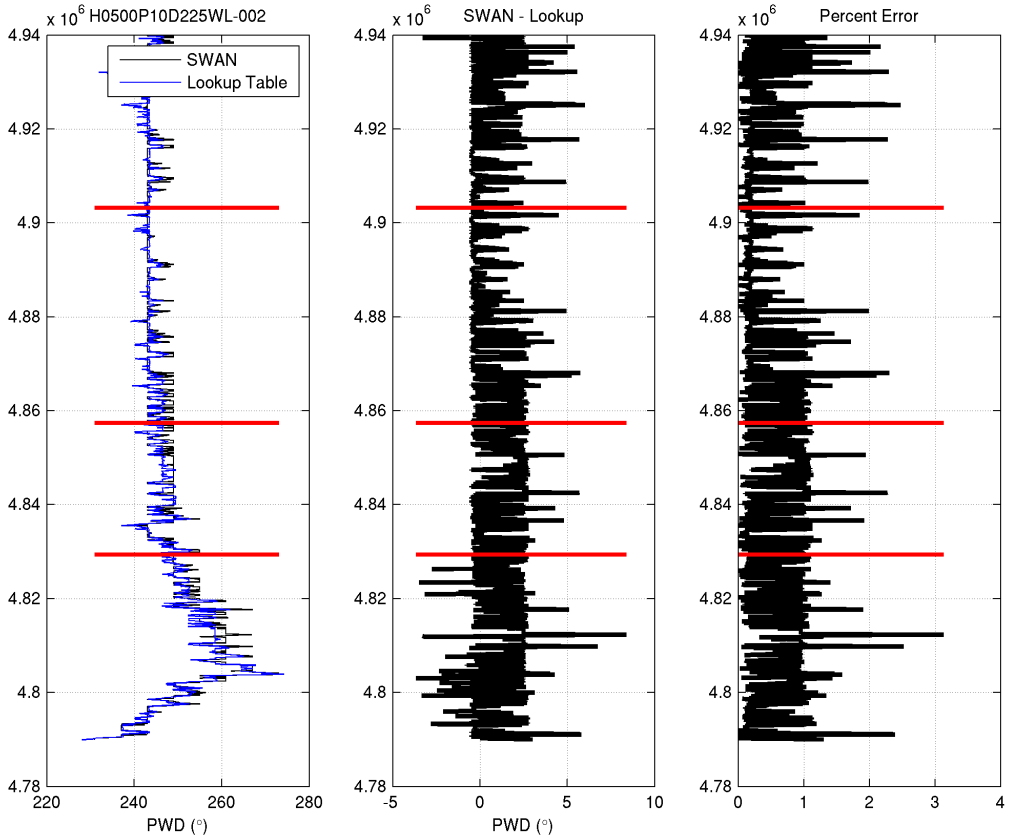

# 6.0 WAVE RUNUP AND OVERTOPPING

Wave runup is the culmination of the wave breaking process whereby the swash of the wave above the still water level is able to run up the beach face, where it may encounter a dune, structure, or bluff, potentially resulting in erosion or overtopping and flooding of adjacent land (**Figure 6-1**). Runup, *R*, or wave setup plus swash, is generally defined as the time-varying location of the intersection between the ocean and the beach, and as summarized is a function of several key parameters. These include the deepwater wave height ($H_o$ or $H_s$), peak spectral wave period ($T_p$), and the wave length ($L_o$) (specifically the wave steepness, $H_o/L_o$), and a surf similarity parameter called the Iribarren number,

$$\xi_o = \frac{\beta}{\sqrt{H_o/L_o}},$$

which accounts for the slope ($\beta$) of a beach or an engineering structure and the steepness of the wave.

**Figure 6-1. Conceptual model showing the components of wave runup associated with incident waves (modified from Hedges and Mase, 2004).**

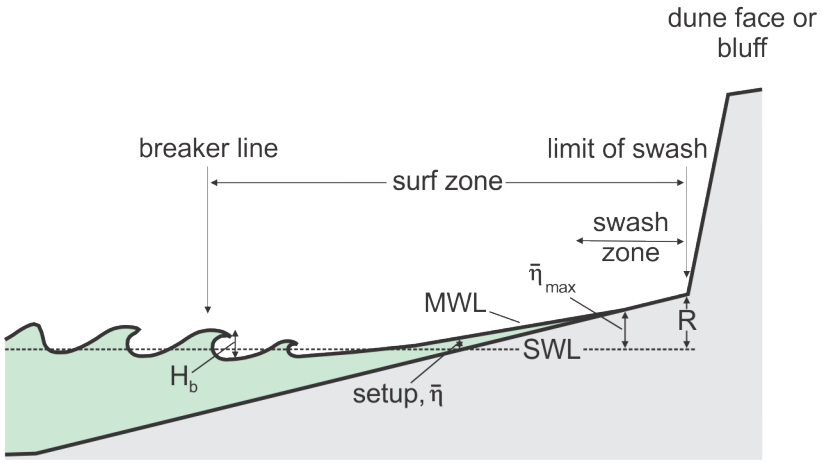


The total runup, *R*, produced by waves includes three main components:

- wave setup, $\overline{\eta}$;
- a dynamic component to the still water level, $\hat{\eta}$; and,
- incident wave swash, $S_{inc}$

$$R = \overline{\eta} + \hat{\eta} + S_{inc} \quad (6\text{-}1)$$

Along the Pacific Northwest coast (PNW) of Oregon and Washington, the dynamic component of still water level, $\hat{\eta}$, has been demonstrated to be a major component of the total wave runup due to relatively high contributions from infragravity energy (Ruggiero and others, 2004), allowing the swash to reach to much higher elevations at the shore.

A variety of models have been proposed for calculating wave runup on beaches (Ruggiero and others, 2001; Hedges and Mase, 2004; NHC, 2005; Stockdon and others, 2006). Here we explore two approaches available for runup calculations along Lane and Douglas County, Oregon: 1) the runup model developed by Stockdon and others (2006) and 2) the Direct Integration Method (DIM) described by NHC (2005).

## 6.1 Runup Models for Beaches

### 6.1.1 Stockdon runup model

For sandy beaches, Stockdon and others (2006) developed an empirical model based on analyses of 10 experimental runup datasets obtained from a wide variety of beach and wave conditions, including data from Oregon (Ruggiero and others, 2004), and by separately parameterizing the individual runup processes: setup and swash. Stockdon and others (2006) proposed the following general relationship for the elevation of the 2% exceedance elevation of swash maxima, $R_2$, for any data run:

$$R_2 = 1.1[\bar{\eta} + \frac{S}{2}] \tag{6-2}$$

where

$$S = \sqrt{(S_{inc})^2 + (\hat{\eta})^2} \tag{6-3}$$

and

$$\bar{\eta}, S_{inc}, \hat{\eta} = f(H_o, T_o, \beta_f)$$

where $\beta_f$ is the slope of the beach face, and $S$ reflects both the dynamic, $\hat{\eta}$, and incident swash, $S_{inc}$, components. The 1.1 coefficient value was determined because the swash level assumes a slightly non-Gaussian distribution. The final parameterized runup equation is

$$R_{2\%} = 1.1\left(0.35\tan\beta\,(H_oL_o)^{\frac{1}{2}} + \frac{[H_oL_o(0.563\tan\beta^2+0.004)]^{\frac{1}{2}}}{2}\right), \tag{6.4}$$

which may be applied to natural sandy beaches over a wide range of morphodynamic conditions. In developing equation 6.4, Stockdon and others (2006) defined the slope of the beach as the average slope over a region ±2σ around the wave setup, $\overline{\eta}$, where σ is the standard deviation of the continuous water level record, η(t). Simply put, the setup reflects the height of the mean-water level (MWL) excursion above the SWL, such that the slope is determined to span the region around this MWL. For Lane and Douglas County, the slope of the beach was determined by fitting a linear regression through those data points spanning the region located between 2 to 4 m.

Combining equation 6.4 with the measured water level at tide gauges produces the total water level (TWL) at the shore, important for determining the erosion or flood risk potential. Given that equation 6.4 has been derived from quantitative runup measurements spanning a range of beach slopes (beach slopes

ranged from 0.01 to 0.11 and Iribarren numbers (**ξ**), ranged from 0.1 (fully dissipative conditions) to ~2.2 (reflective conditions), Table 1 of Stockdon and others [2006]), the model is valid for the range of slopes and conditions observed along the Lane and Douglas County coastline and elsewhere on the Oregon coast.

### 6.1.2 Direct integration method—beaches

The FEMA coastal flood mapping guidelines (NHC, 2005) for the U.S. West Coast presents an alternative method for calculating runup. According to NHC (2005), the Direct Integration Method (DIM) approach allows for the wave and bathymetric characteristics to be taken into consideration; specifically, the spectral shape of the waves and the actual bathymetry can be represented. Here we review the parameterized set of runup equations that may be used to calculate runup on beaches. The equations are based on a parameterized JONSWAP spectra and uniform beach slopes.

Similar to equation 6.1, the runup of waves using DIM can be defined according to its three components: the wave setup, $\overline{\eta}$, a dynamic component, $\widehat{\eta}$, and the incident band swash, $S_{inc}$. Wave setup can be calculated using

$$\overline{\eta} = 4.0\, F_H F_T F_{Gamma} F_{slope}, \tag{6.5}$$

while the root mean square (rms) of the dynamic component, $\widehat{\eta}_{rms}$, may be estimated using

$$\widehat{\eta}_{rms} = 2.7\, G_H G_T G_{Gamma} G_{slope}, \tag{6.6}$$

where the units of $\overline{\eta}$ and $\widehat{\eta}_{rms}$ are in *feet* and the factors ($F$) are for the wave height ($F_H$ and $G_H$), wave period ($F_T$ and $G_T$), JONSWAP spectrum narrowness ($F_{Gamma}$ and $G_{Gamma}$), and the nearshore slope ($F_{slope}$ and $G_{slope}$). These factors are summarized as a series of simple equations in Table D.4.5-1 (NHC, 2005). For the purposes of defining an average slope, NHC recommended that the nearshore slope be based on the region between the runup limit and twice the wave breaking depth, $h_b$, where

$$h_b = H_b / k \tag{6.7}$$

and

$$H_b = 0.39 g^{0.2} \left(T_p H_o^2\right)^{0.4}, \tag{6.8}$$

where $H_b$ is the breaker height calculated using equation 6.8 (Komar, 1998), $g$ is acceleration due to gravity (9.81 m/s), and for the purposes here $k$ (breaker depth index) can be taken to be 0.78. Thus, one important distinction between the DIM and Stockdon methods for calculating runup is the method used to define the beach slope; the former accounts for a larger portion of the nearshore slope, while the latter is based on the slope calculated around the mid beach-face.

To derive the statistics of the oscillating wave setup and the incident swash components, the recommended approach is to base the calculations on the standard deviations (σ) of each component. The standard deviation of the incident wave oscillation ($\sigma_2$) on natural beaches may be calculated from

$$\sigma_2 = 0.3\xi_o H_o \tag{6.9}$$

Because the standard deviation of the wave setup fluctuations ($\sigma_1$) is proportional to equation 6.6, the total oscillating component of the dynamic portion of the wave runup can be derived from

$$\widehat{\eta_T} = 2.0\sqrt{\sigma_1^2 + \sigma_2^2} \tag{6.10}$$

Combining the results of equations 6.10 and 6.5 yields the 2% wave runup, and when combined with the tidal component results in the TWL.

### 6.1.3 Comparison of Stockdon and DIM runup calculations

Fundamentally, the wave runup model proposed by Stockdon and others (2006) and the DIM method described in NHC (2005) are similar, as both models account for the three components of runup described in equation 6.1. Here we examine the runup results derived from both models based on a range of conditions characteristic of the Clatsop shore (**Figure 6-2** and **Figure 6-3**).

**Figure 6-2. Calculated setup, swash, and runup using the Stockdon and DIM runup equations. In this example, slope values are defined similarly for both methods, at a mid-beach elevation range of 2–4 m (6.6–13 ft). A 6-m (19.7 ft) significant wave height, 12-s peak wave period, and 270 degree wave direction were used to drive the models. Due to the semi-empirical nature of the equations, only the magnitudes of the subplots outlined in magenta are directly comparable (the two panels showing swash results are not directly comparable). The total oscillating component compares the results from equation 6.3 ($S/2$) with equation 6.10.**

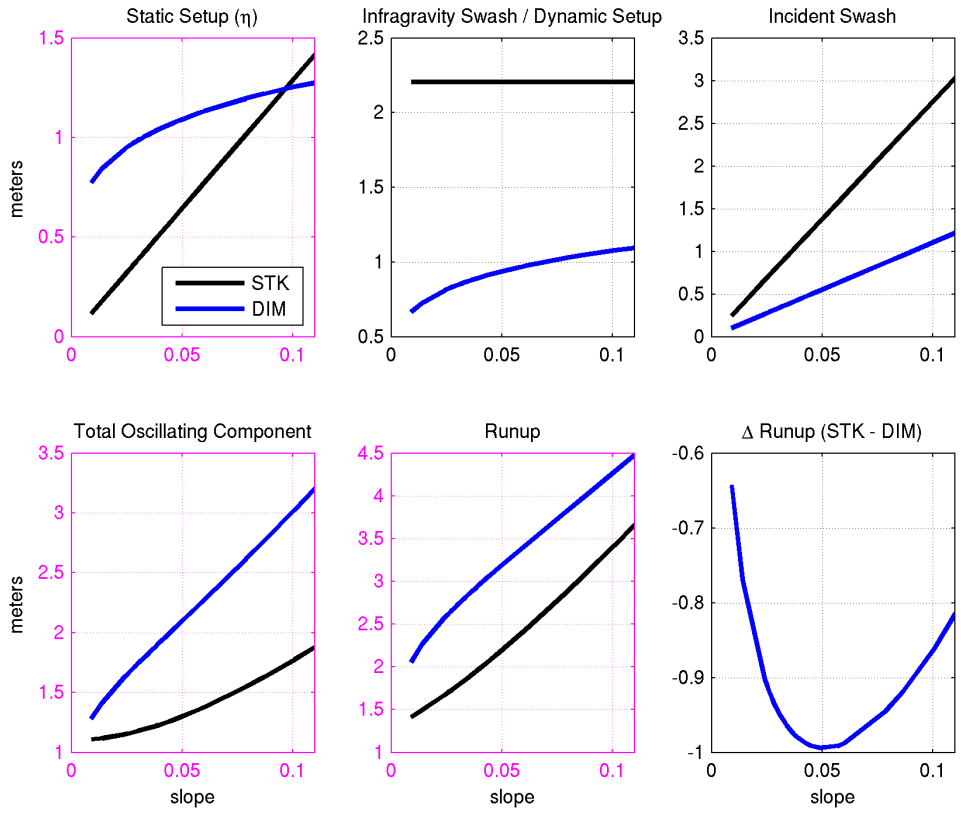


**Figure 6-2** provides a comparison of the various calculated parameters (setup, infragravity swash, incident swash, total oscillating component, and runup) determined using the Stockdon and DIM approaches. In this example, we use the same slope defined for the mid-beach region in order to provide a direct comparison between DIM and Stockdon. Upper estimates have been truncated to tan β = 0.11, which reflects the slope limit on which the Stockdon approach has been tested. In contrast, the range of slope conditions on which DIM may be applied is unclear as there is no quantitative field testing of this particular formulation. As can be seen in **Figure 6-2**, although there are notable differences in the various parameterizations, the derived runup (bottom, middle plot) is similar. Nevertheless, as can be seen from the ΔR plot (bottom right), the DIM approach tends to estimate a slightly higher runup when compared to Stockdon, which in this example reaches a maximum of ~1 m (3.3 ft) for a beach slope of 0.04 to 0.05. Thus, overall, we can conclude that the two approaches are performing in a similar fashion when tested using the same slope.

**Figure 6-3** presents a similar suite of comparisons under the same hydrodynamic conditions. Therefore, the Stockdon and others (2006) results are identical to **Figure 6-2** in all panels. However, in this example we now account for the appropriate nearshore slope in the DIM runup calculations as defined above in **SECTION 6.1.2**. This was originally done by computing the DIM runup components for this hydrodynamic condition using the full nearshore slope at 85 transects spread along the Clatsop County coast line (Allan and others, 2015c). The DIM values are, however, plotted against the foreshore beach slopes defined for all 85 transects in order to make the comparisons with Stockdon meaningful. As can be seen in **Figure 6-3**, application of the nearshore slope significantly changes the magnitudes of all the runup components, and in particular reduces the calculated runup when compared to Stockdon for most foreshore slopes. In general, at lower slopes ($\tan \beta < 0.05$) runup calculated by DIM is slightly higher than Stockdon, which reverses at steeper slopes ($\tan \beta > 0.05$). This pattern is consistent with analyses performed by Allan and others (2012b) in Coos County.

**Figure 6-3. Total water level calculations using the Stockdon (foreshore slope) and DIM runup equations (nearshore slope). A 6-m (19.7 ft) significant wave height, 12-s peak wave period, and 270 degree wave direction were used to drive the models. Due to the semi-empirical nature of these equations only the magnitudes of the subplots outlined in magenta are directly comparable. The results for DIM are sorted in ascending order as a function of foreshore beach slope.**

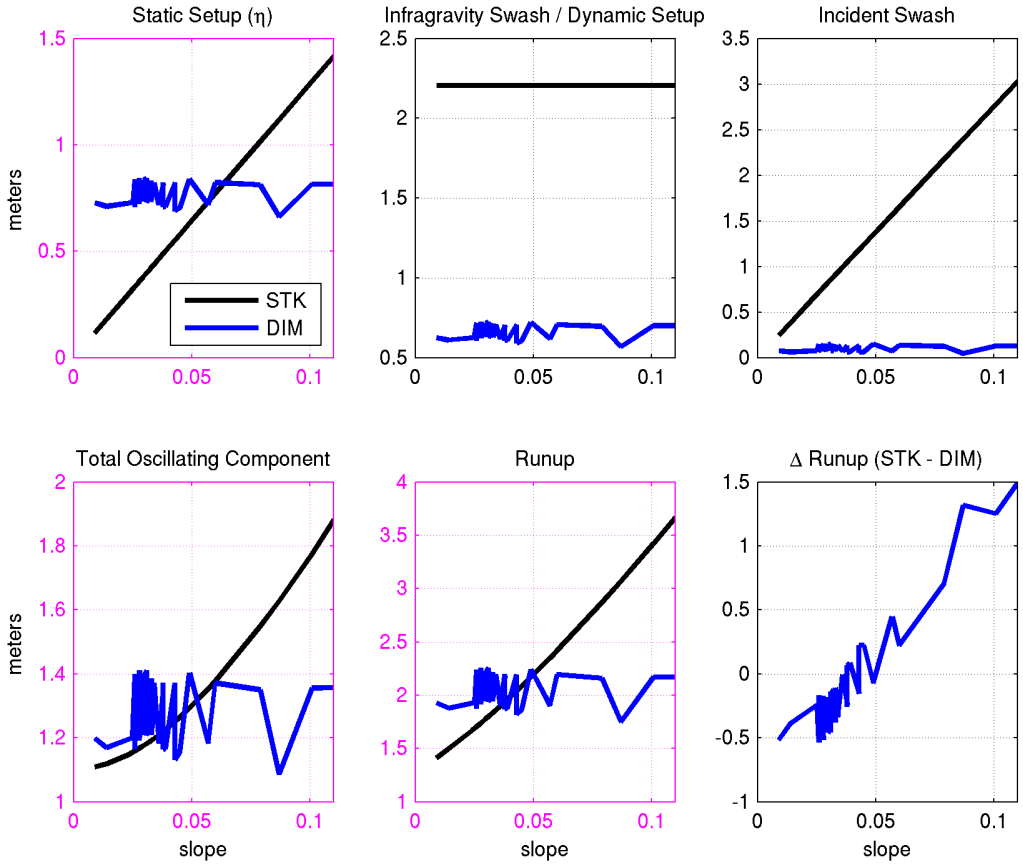

Most interesting in the comparisons shown in **Figure 6-3**, is that the DIM runup components actually do not vary as a function of the foreshore slope. The total runup (**Figure 6-3** bottom, middle plot) produced by DIM is relatively constant, oscillating between 1.7 and 2.3 m (5.6 and 7.5 ft). The oscillations are due primarily to the variability in the nearshore slopes, which are a function of wave height (equation 6.7-6.8). Because waves in the PNW are relatively large and upper shoreface slopes relatively shallow, the DIM runup values are controlled by the nearshore slope with little influence from the upper beach. This lack of dependence on the foreshore is in contrast to field measurements made in Oregon (Ruggiero and others, 2004) in which runup is clearly a function of the foreshore slope. Because the Stockdon model has been extensively validated against measured runup data, including measurements on the Oregon coast (e.g., Ruggiero and others, 2001; Ruggiero and others, 2004) together with qualitative observations of runup during storms by DOGAMI staff at multiple sites along the coast, 1% extreme values of $TWL_S$ calculated for sandy beaches along the Lane and Douglas County coast will be based primarily on the Stockdon and others (2006) model.

## 6.2 "Barrier" Runup Calculations

### 6.2.1 Introduction

According to NHC (2005), an alternate approach is recommended for use in calculating runup on steep barriers. By definition, *barriers include "steep dune features and coastal armoring structures such as revetments"* (NHC, 2005, p. D.4.5-10), although little guidance is offered in terms of the range of slopes to which this alternate approach would apply. Throughout this document we will use the generic term "barrier" to define the range of morphological and engineering conditions where barrier runup calculations may apply. In general, runup on barriers depends not only on the height and steepness of the incident wave defined through the Iribarren number or breaker parameter ($\xi_{m\text{-}1,0}$), but also on the geometry (e.g., the slope of the barrier and/or if a berm is present), design characteristics of the structure, and its permeability.

The recommended approach for calculating runup on barriers is to use the TAW (Technical Advisory Committee for Water Retaining Structures) method, which provides a mechanism for calculating the runup, adjusted for various reduction factors that include the surface roughness, the influence of a berm (if present), and effects associated with the angle of wave approach (van der Meer, 2002; NHC, 2005; EurOtop, 2016). According to NHC (2005) the TAW method is useful as it includes a wide range of conditions for calculating the wave runup (e.g., both smooth and rough slopes), and because it agrees well with both small- and large-scale experiments.

**Figure 6-4** is a conceptual model of the various components required to determine the extent of runup on barriers. Of importance is first determining the 2% Dynamic Water Level ($DWL_{2\%}$) at the barrier, which includes the combined effects of the measured still water level (SWL), the wave setup ($\overline{\eta}$), and the dynamic portion ($\widehat{\eta}$) of the runup (**Figure 6-4**), which is then used to establish the spectral significant wave height ($H_{mo}$) at the toe of the "barrier" (NHC, 2005).

**Figure 6-4. Wave runup on a beach backed by a structure or bluff (modified from NHC, 2005).**

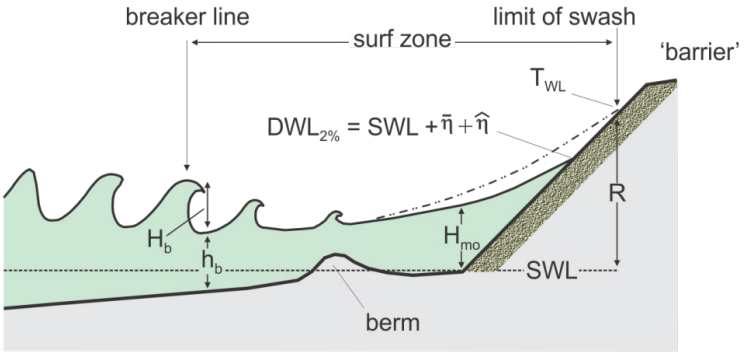


The general formula for calculating the 2% wave runup height on barriers is given in a non-dimensional form by equation 6.11:

$$\frac{R_{2\%}}{H_{mo}} = c_1 \cdot \gamma_b \cdot \gamma_f \cdot \gamma_\beta \cdot \xi_{m-1,0} \qquad (6.11)$$

with a maximum of

$$\frac{R_{2\%}}{H_{mo}} = \gamma_f . \gamma_\beta \left( c_2 - \frac{c_3}{\sqrt{\xi_{m-1,0}}} \right)$$

where

$R_{2\%}$ = wave runup height exceeded by 2% of the incoming waves,
$H_{mo}$ = spectral significant wave height at the structure toe,
$c_1$, $c_2$, and $c_3$ = empirical coefficients with:
$\gamma_b$ = influence factor for a berm (if present)
$\gamma_f$ = influence factor for roughness element of slope
$\gamma_\beta$ = influence factor for oblique wave attack,
$\xi_{m-1,0}$ = breaker parameter $\left(\tan\beta / \left(H_{mo}/L_{m-1,0}\right)^{0.5}\right)$,
$\tan\beta$ = slope of the "barrier",
$L_{m-1,0}$ = the deepwater wave length $\left(gT_{m-1,0}^2/2\pi\right)$, and
$T_{m-1,0}$ can be calculated from $T_p/1.1$, where $T_p$ is the peak spectral wave period.

Substituting the empirical coefficients derived from wave tank experiments and incorporating a 5% upper exceedance limit into the general equations of 6.11 (van der Meer, 2002; EurOtop, 2016), runup on barriers may be calculating by using:

$$R_{2\%} = H_{mo}\left(1.75 . \gamma_b . \gamma_f . \gamma_\beta . \xi_{m-1,0}\right), \text{where } 0 < \gamma_b . \xi_{m-1,0} < 1.8 \qquad (6.12)$$

with a maximum of:

$$R_{2\%} = H_{mo}\left(1.0 . \gamma_f . \gamma_\beta \left(4.3 - \frac{1.6}{\sqrt{\xi_{m-1,0}}}\right)\right), \text{where } \gamma_b . \xi_{m-1,0} \geq 1.8$$

There are, however, notable differences between equation 6.12 originally described by van der Meer (2002) and EurOtop (2016) from that presented in equation D.4.5-19 in the FEMA West Coast methodology (NHC, 2005). For example, equation D.4.5-19 in the NHC report contains a higher coefficient value (1.77), along with one additional reduction factor (porosity) for calculating runup when the breaker parameter is less than 1.8. Similarly, for conditions where the breaker parameter exceeds 1.8 and the maximum runup equation is used, equation D.4.5-19 in the NHC report contains two extra reduction factors (berm and porosity reduction factors) that are not included in the original solution; these potentially could have a very significant effect on the calculated runup. On the basis of these differences, we have used the original solution presented as equation 6.12 by van der Meer (2002) and EurOtop (2016).

### 6.2.2 Specific procedure for calculation of "barrier" runup

For those cases where the TAW method is used for determining runup on barriers (i.e., beaches backed by structures, cobble berms, and/or bluffs), we have followed the general approach laid out in section D.4.5.1.5.2 of NHC (2005), with the exception that we use Stockdon to define the $DWL_{2\%}$ (instead of DIM) at the structure toe, and TAW to calculate the incident swash on the barrier (i.e., equation 6-12). Because waves are depth limited at the barrier toe, $H_{mo}$ may be estimated from $DWL_{2\%}$ using a breaker index of 0.78 (i.e., $H_{mo} = DWL_{2\%} * 0.78$). In performing these various derivations, $DWL_{2\%}$ was first determined using equation 6.13:

$$\mathrm{DWL}_{2\%} = \mathrm{SWL} + 1.1 * \left(\overline{\eta} + \frac{\widehat{\eta}}{2}\right) - D_{low} \qquad (6.13)$$

where

SWL = measured tide,

$\overline{\eta} = 0.35 * \tan\beta\sqrt{H_s * L}$ (equation 10 of Stockdon and others [2006]),

$\widehat{\eta} = 0.06 * \sqrt{H_s * L}$ (equation 12 of Stockdon and others [2006]),

$D_{low}$ = the toe of the structure or bluff, and

$\tan\beta$ = the beach slope defined for the region between 2 and 4 m.

Having calculated $DWL_{2\%}$ and $H_{mo}$, the TAW runup calculation can be implemented. Equation 6.12 requires information on the slope of the barrier, used in the breaker parameter ($\xi_{m-1,0}$) calculation, which can be somewhat challenging to define. This is especially the case if the morphology of the barrier exhibits a composite morphology characterized by different slopes, such that errors in estimating the slope will translate to either significant underestimation or overestimation of the runup. According to van der Meer (2002) and EurOtop (2106), because the runup process is influenced by the change in slope from the breaking point to the maximum wave runup, the characteristic slope should be specified for this same region. On the Oregon coast, the most common composite slope example is the case where a broad, dissipative sand beach fronts a structure or bluff that is perched relatively high on the back of the beach (structure toe > ~4-5 m). In this example, the wave runup is first influenced by the sandy beach slope and finally by the slope of the structure itself. To address this type of situation, we define a "local barrier slope" as the portion of the barrier that ranges from the calculated storm TWL (calculated initially using equation 6.4) down to a lower limit defined by the wave setup plus the SWL [i.e., $(1.1 * \overline{\eta}) + SWL$]). In a few cases, the TWL was found to exceed the barrier crest; in these cases we used the structure crest as the upper limit for defining the local slope. This process is repeated for every storm condition. Having determined the barrier slope, the TAW runup is calculated using equation 6.12 and reduced based on the appropriate site specific reduction factors.

Under certain conditions, we identified events that generated extreme runup that made little physical sense. For these (rare) cases, we calculated the TAW runup using an iterative approach based on procedures outlined in the EurOtop (2016) manual. Because the maximum wave runup is the desired outcome and is unknown when initially defining the slope, the process is iterative and requires two steps. First, the breaking limit is defined as $1.5H_{mo}$ *below* the SWL, while $1.5H_{mo}$ *above* the SWL defines the upper limit of the first slope estimate (**Figure 6-5**). Having determined the first slope estimate, the TAW runup is calculated using equation 6.12 and reduced based on the appropriate reduction factors. A second slope

estimate is then performed based on the initial runup calculation, while a third iteration is not necessary based on our tests because this method converges quickly. The breaking limit is again defined as $1.5H_{mo}$ *below* the SWL, while $R_{2\%}$ *above* the SWL defines the upper limit, and the final barrier runup estimate is again calculated using equation 6.12 and reduced based on the appropriate reduction factors.

**Figure 6-5. Determination of an average slope based on an iterative approach. The first estimate is initially based on $1.5H_{mo}$ ± SWL, while the second estimate is based on $1.5H_{mo}$ below the SWL and the calculated $R_{2\%}$ above the SWL that is based on the first slope estimate.**

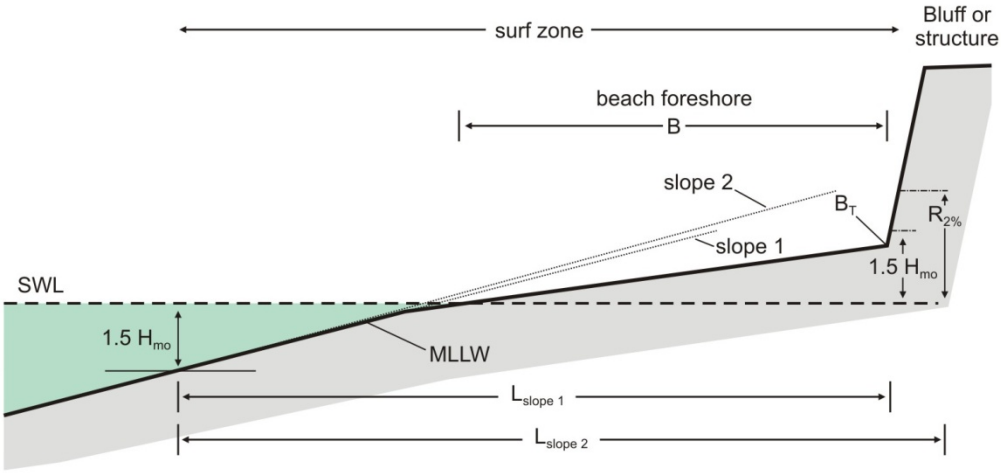


Finally, it is important to note that the runup estimates based on the "barrier" runup calculations are sensitive to the slope. Similar to our study in Coos and Clatsop Counties, we identified several sites (primarily beaches backed by bluffs) along the Lane County coast where the final $TWL_s$ calculated using TAW was unreasonably low. These few cases are entirely due to there being a very wide dissipative surf zone at these transect locations that results in very low slopes being defined. For these sites where the calculated $TWL_s$ seemed unreasonably low (relative to the morphology of the beach and observations of storm wave runup along this shore and elsewhere), we have defaulted to the $TWL_s$ calculated using the Stockdon and others model.

### 6.2.3 "Barrier" runup reduction factors

**Table 6-1** below presents information pertaining to the suite of parameters used to define wave runup ($R$) and ultimately the 1% $TWL_s$ along the Lane County coast. In the case of bluff roughness along Lane County, we used a value of 0.6 for those situations where a bluff face was highly vegetated. These bluffs are typically located at or near their stable angle of repose and are covered with salal (*Gaultheria shallon*), where it forms a deep, nearly impenetrable thicket. The decision to use 0.6 was based on discussions with Dr. W. G. McDougal (Coastal Engineer, OSU, and Technical Coordinator of the North Pacific FEMA West Coast Guidelines, pers. comm., April 2010). At the Lane County transects 25, 26, 28, 30–35, 37, 38, 40, 41, 44, 47, 49, 50, 52–54, and 56 (**Table 6-1**), the reduction factor was set to 1 due to the fact that these beaches were backed by a near vertical bluff face that was essentially akin to a seawall situation. For those beaches backed by a significant riprap structure, we used a reduction factor of 0.55. In other cases, this

was increased to 0.6 to 0.8, depending on whether the beach was backed by gravels/cobbles, a vegetated bluff face, or poor quality riprap. Wave direction ($\gamma_\beta$) reduction factors were determined based on the shoreline orientation at every transect site and the actual wave directions measured during each storm condition. The reduction factor was calculated using equation D.4.5-22 (NHC, 2005, p D.4.5-13). Finally, of the 57 primary transects established along the Lane County coast, 4 are characterized with having a broad rock (basalt) platform within the intertidal zone that is akin to a protective berm. For these sites, we calculated a berm reduction factor using equation D.4.5-21 (NHC, 2005, p. D.4.5-13).

**Table 6-1. Various parameters used to define runup (*R*) and total water levels (TWLs) on beaches backed by dunes, structures, and bluffs.** *(Table continued on next page.)*

| Reach | Transect (Lane) | $D_{HIGH}$ (m) | $D_{LOW}$ (m) | Beach Slope (tan $\beta$) | Wave Dir. ($\gamma_\beta$) | Rough-ness ($\gamma_r$) | Approach | Description |
|---|---|---|---|---|---|---|---|---|
| Heceta Beach | 1 | 5.726 | 3.618 | 0.034 | 283.7 | 1 | 3 | sand beach backed by dunes |
| | 2 | 8.491 | 5.387 | 0.053 | 284.8 | 1 | 3 | sand beach backed by dunes |
| | 3 | 8.549 | 5.578 | 0.051 | 283.0 | 1 | 3 | sand beach backed by dunes |
| | 4 | 9.081 | 5.154 | 0.044 | 283.6 | 1 | 3 | sand beach backed by dunes and bluff |
| | 5 | 12.038 | 4.041 | 0.043 | 277.5 | 0.70 | 3 | sand beach backed by riprap and bluff |
| | 6 | 8.643 | 4.100 | 0.038 | 283.0 | 0.70 | 1 | sand beach backed by riprap |
| | 7 | 7.106 | 5.181 | 0.038 | 279.5 | 0.70 | 3 | sand beach backed by riprap |
| | 8 | 6.852 | 5.471 | 0.032 | 278.1 | 1 | 3 | sand beach backed by dune ramp |
| | 9 | 9.730 | 4.908 | 0.039 | 282.4 | 0.70 | 3 | sand beach backed by riprap |
| | 10 | 9.034 | 4.953 | 0.038 | 281.6 | 1 | 3 | sand beach backed by dunes |
| | 11 | 14.080 | 4.229 | 0.043 | 280.7 | 0.70 | 1 | sand beach backed by riprap |
| | 12 | 8.948 | 4.666 | 0.047 | 280.7 | 0.70 | 1 | sand beach backed by riprap |
| | 13 | 7.768 | 4.634 | 0.045 | 282.0 | 0.70 | 1 | sand beach backed by riprap |
| | 14 | 10.151 | 4.476 | 0.044 | 280.8 | 0.70 | 1 | sand beach backed by riprap |
| | 15 | 9.572 | 3.771 | 0.050 | 280.5 | 0.70 | 3 | sand beach backed by riprap |
| | 16 | 9.097 | 3.439 | 0.033 | 280.4 | 0.55 | 1 | sand beach backed by riprap |
| | 17 | 10.822 | 3.474 | 0.023 | 279.0 | 1 | 3 | sand beach backed by dunes |
| | 18 | 7.585 | 4.778 | 0.057 | 277.3 | 1 | 3 | sand beach backed by dunes |
| | 19 | 9.449 | 4.924 | 0.052 | 278.0 | 1 | 3 | sand beach backed by dunes |
| | 20 | 15.475 | 6.005 | 0.055 | 277.7 | 1 | 3 | sand beach backed by dunes |
| | 21 | 18.978 | 4.759 | 0.051 | 277.2 | 1 | 3 | sand beach backed by dunes |
| | 22 | 19.185 | 5.617 | 0.057 | 277.9 | 1 | 3 | sand beach backed by dunes |
| | 23 | 5.730 | 3.065 | 0.019 | 277.1 | 1 | 3 | sand beach backed by dunes |
| | 24 | 22.259 | 5.495 | 0.045 | 275.3 | 1 | 3 | sand beach backed by dunes |
| Heceta Head | **25** | **24.190** | **3.765** | **0.081** | **274.8** | **0.95** | **1** | **basalt cliff** |
| | **26** | **23.581** | **5.238** | **0.090** | **274.0** | **0.95** | **1** | **sand beach backed by high bluff** |
| | 27 | 23.154 | −0.506 | 0.010 | 275.0 | 0.95 | 1 | basalt cliff |
| | **28** | **18.233** | **5.192** | **0.083** | **275.7** | **0.95** | **1** | **sand beach backed by high bluff** |
| | 29 | 6.490 | 3.820 | 0.047 | 252.5 | 1 | 3 | sand beach backed by high bluff |
| | **30** | **32.039** | **1.904** | **0.025** | **276.0** | **0.95** | **1** | **basalt cliff** |
| Muriel O'Ponsler | **31** | **22.957** | **4.097** | **0.040** | **279.1** | **0.95** | **1** | **sand beach backed by high bluff** |
| | **32** | **9.775** | **4.467** | **0.048** | **278.1** | **0.95** | **1** | **sand beach backed by low bluff** |
| | **33** | **8.982** | **4.273** | **0.041** | **278.4** | **0.95** | **1** | **sand beach backed by low bluff** |
| | **34** | **11.208** | **4.774** | **0.064** | **277.4** | **0.95** | **1** | **sand beach backed by low bluff** |
| | **35** | **20.565** | **4.759** | **0.063** | **276.0** | **0.95** | **1** | **sand beach backed by high bluff** |
| | 36 | 25.230 | 4.850 | 0.055 | 275.6 | 0.80 | 1 | moderately wide rock platform backed by high bluff |
| Stonefield | **37** | **21.045** | **5.183** | **0.057** | **275.1** | **0.95** | **1** | **sand beach backed by high bluff** |

| Reach | Transect (Lane) | $D_{HIGH}$ (m) | $D_{LOW}$ (m) | Beach Slope (tan $\beta$) | Wave Dir. ($\gamma_\beta$) | Rough-ness ($\gamma_r$) | Approach | Description |
|---|---|---|---|---|---|---|---|---|
| Beach | **38** | **18.245** | **5.670** | **0.093** | **275.3** | **0.95** | **1** | **moderately wide rock platform backed by high bluff** |
| | 39 | 11.970 | 5.003 | 0.100 | 273.5 | 0.95 | 3 | sand beach backed by high bluff |
| | **40** | **17.186** | **5.301** | **0.086** | **275.9** | **0.95** | **1** | **moderately wide rock platform backed by high bluff** |
| | **41** | **19.745** | **6.222** | **0.110** | **276.8** | **0.80** | **1** | **sand beach backed by high bluff** |
| | 42 | 6.331 | 6.301 | 0.078 | 275.3 | 0.95 | 3 | sand beach backed by dunes |
| | 43 | 6.693 | 3.624 | 0.020 | 276.2 | 0.80 | 1 | sand beach backed by low bluff |
| | **44** | **8.058** | **4.562** | **0.051** | **276.5** | **0.80** | **1** | **moderately wide rock platform backed by high bluff** |
| | 45 | 8.314 | 4.726 | 0.067 | 276.1 | 0.80 | 1 | sand beach backed by low bluff |
| | 46 | 7.542 | 4.919 | 0.067 | 276.8 | 0.80 | 1 | sand beach backed by low bluff |
| | **47** | **17.942** | **4.797** | **0.053** | **276.0** | **0.95** | **1** | **sand beach backed by high bluff** |
| | 48 | 29.229 | 3.201 | 0.053 | 273.9 | 0.95 | 1 | moderately wide rock platform backed by high bluff |
| | **49** | **28.958** | **6.552** | **0.110** | **273.9** | **0.80** | **1** | **moderately wide rock platform backed by high bluff** |
| | **50** | **15.647** | **5.408** | **0.098** | **271.3** | **0.80** | **1** | **moderately wide rock platform backed by high bluff** |
| | 51 | 8.330 | 4.894 | 0.080 | 252.7 | 0.80 | 1 | mixed sand and gravel beach backed by low bluff |
| Cummins Creek/ Cape Perpetua | **52** | **28.047** | **1.906** | **0.023** | **277.9** | **0.95** | **1** | **narrow rock platform backed by high bluff** |
| | **53** | **20.355** | **5.944** | **0.125** | **280.2** | **0.80** | **1** | **narrow rock platform backed by high bluff** |
| | **54** | **19.471** | **4.871** | **0.066** | **279.1** | **0.95** | **1** | **sand beach backed by high bluff** |
| | 55 | 34.099 | 3.709 | 0.021 | 277.8 | 0.95 | 1 | moderately wide rock platform backed by high bluff |
| | **56** | **12.687** | **3.535** | **0.020** | **274.8** | **0.95** | **1** | **sand beach backed by low bluff** |
| | 57 | 10.730 | 6.739 | 0.031 | 271.5 | 0.95 | 1 | narrow rock platform backed by low bluff |

Notes:

$D_{HIGH}$ denotes the crest of the dune, bluff, or structure;

$D_{LOW}$ denotes the toe of the dune (i.e., $E_j$), bluff, or structure;

Beach slope reflects the calculated slope spanning the region between 2- and 4-m elevation;

Wave direction denotes the shoreline orientation used to calculate the wave reduction ($\gamma_\beta$) factor used in TAW runup calculations;

Roughness ($\gamma_r$) defines the backshore roughness used in TAW runup calculations. **Boldface values** indicate sites where the local slope goes to 1 due to the presence of a vertical bluff; and

Approach defines the final runup approach used to calculate the wave runup, where 3 = Stockdon, 2 = nearshore slope and TAW, and 1 = the local barrier slope and TAW.

## 6.3 Lane and Douglas County Wave Runup and Total Water Level Calculations

The complete hourly combined time series is run through the lookup tables to derive alongshore varying transformed wave time series. By using the transformed wave conditions, and the measured alongshore varying beach and barrier slopes, initial TWL time series based on the Stockdon approach are developed at all transect locations. From these time series we identify the ~150 highest independent TWLs at each transect over the length of the record. Wave runup is then computed for each of these storm input conditions (about five events per year) at every profile site shown in **Figure 3-1** and **Figure 3-2** by using a combination of the Stockdon and others (2006) runup equation for dune-backed beaches (equation 6.4) and TAW (equation 6-12) for wave runup on a barrier. The specific approaches used in our calculations are defined above in **Table 6-1**. For both models, the calculated runup is combined with the SWL (measured tides) to develop the TWL conditions used to generate the 10-, 50-, and 100-year return level event as well as the 500-year return event. The input wave conditions from the SWAN modeling used in the various calculations were determined for each transect location by extending the shore perpendicular transects from the backshore to where they intersected the 20-m contour, or the seaward most location of $H_{mo}$/depth = 0.4, whichever was farther offshore (but almost always shallower than 30 m). This ensured that only minor dissipation due to wave breaking influenced the model results. These intersections are where wave statistics from the SWAN output were extracted.

Having calculated the storm-induced TWLs, we used the generalized extreme value (GEV) family of distributions (specifically the peak over threshold (POT) approach) to estimate the 100-year and 500-year total water levels for each of the beach profile sites. Specific information about the extreme value techniques used to estimate these $TWL_S$ is provided in **SECTION 4.6**. **Figure 6-6** gives an example of the extreme value (GPD-Poisson) model for the Lane 32 transect site in which the 100-year event is calculated to be 9.3 m (30.5 ft) and the 500-year event is estimated to be 9.69 m (31.8 ft). The results for all of the transects can be found in **Table 6-2**.

**Figure 6-6. Example peak over threshold (POT) extreme value theory results for the Lane 32 transect site (with 95% confidence levels) located near Muriel O'Ponsler State Park. Note the y-axis vertical datum is relative to the NAVD88 vertical datum.**

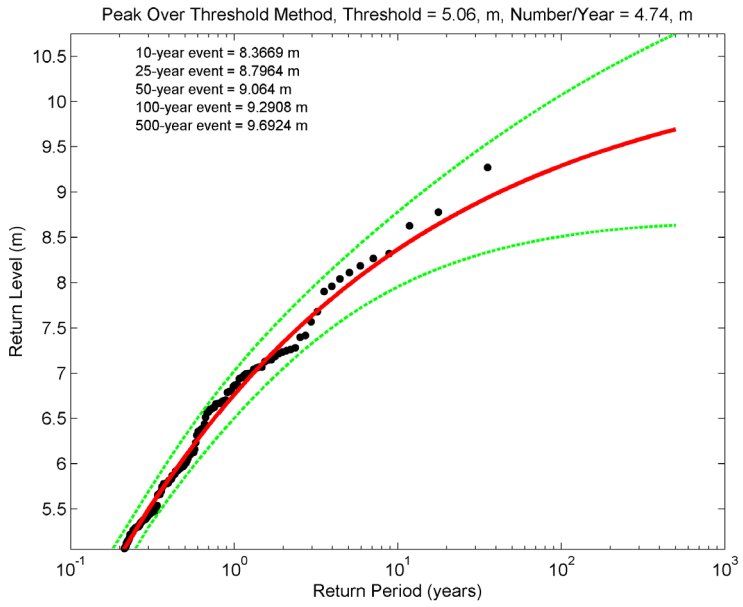

**Table 6-2. 100-year (1%) and 500-year (0.2%) total water levels (TWL) calculated for the Lane County transect sites.** *(Table continued on next page.)*

| Reach | Transect (Lane) | $D_{HIGH}$ (m) | $D_{LOW}$ (m) | 100-Year TWL (m) | 500-Year TWL (m) | Description |
|---|---|---|---|---|---|---|
| Heceta Beach | 1 | 5.726 | 3.618 | 5.90 | 5.99 | sand beach backed by dunes |
| | 2 | 8.491 | 5.387 | 6.86 | 6.97 | sand beach backed by dunes |
| | 3 | 8.549 | 5.578 | 6.70 | 6.82 | sand beach backed by dunes |
| | 4 | 9.081 | 5.154 | 6.39 | 6.48 | sand beach backed by dunes and bluff |
| | 5 | 12.038 | 4.041 | 6.31 | 6.41 | sand beach backed by riprap and bluff |
| | 6 | 8.643 | 4.100 | 6.37 | 6.54 | sand beach backed by riprap |
| | 7 | 7.106 | 5.181 | 6.16 | 6.25 | sand beach backed by riprap |
| | 8 | 6.852 | 5.471 | 5.95 | 6.03 | sand beach backed by dune ramp |
| | 9 | 9.730 | 4.908 | 6.15 | 6.23 | sand beach backed by riprap |
| | 10 | 9.034 | 4.953 | 6.12 | 6.20 | sand beach backed by dunes |
| | 11 | 14.080 | 4.229 | 7.04 | 7.50 | sand beach backed by riprap |
| | 12 | 8.948 | 4.666 | 6.50 | 6.60 | sand beach backed by riprap |
| | 13 | 7.768 | 4.634 | 6.38 | 6.51 | sand beach backed by riprap |
| | 14 | 10.151 | 4.476 | 6.55 | 6.76 | sand beach backed by riprap |
| | 15 | 9.572 | 3.771 | 6.58 | 6.67 | sand beach backed by riprap |
| | 16 | 9.097 | 3.439 | 7.41 | 7.57 | sand beach backed by riprap |
| | 17 | 10.822 | 3.474 | 5.79 | 5.86 | sand beach backed by dunes |
| | 18 | 7.585 | 4.778 | 7.18 | 7.39 | sand beach backed by dunes |
| | 19 | 9.449 | 4.924 | 6.65 | 6.73 | sand beach backed by dunes |
| | 20 | 15.475 | 6.005 | 6.86 | 6.99 | sand beach backed by dunes |
| | 21 | 18.978 | 4.759 | 6.68 | 6.77 | sand beach backed by dunes |
| | 22 | 19.185 | 5.617 | 7.03 | 7.14 | sand beach backed by dunes |
| | 23 | 5.730 | 3.065 | 5.61 | 5.68 | sand beach backed by dunes |
| | 24 | 22.259 | 5.495 | 6.57 | 6.67 | sand beach backed by dunes |
| Heceta Head | 25 | 24.190 | 3.765 | 14.04 | 14.41 | basalt cliff |
| | 26 | 23.581 | 5.238 | 11.76 | 12.34 | sand beach backed by high bluff |
| | 27 | 23.154 | −0.506 | 17.24 | 17.36 | basalt cliff |
| | 28 | 18.233 | 5.192 | 11.70 | 12.25 | sand beach backed by high bluff |
| | 29 | 6.490 | 3.820 | 6.84 | 6.96 | sand beach backed by high bluff |
| | 30 | 32.039 | 1.904 | 14.36 | 14.65 | basalt cliff |
| Muriel O'Ponsler | 31 | 22.957 | 4.097 | 9.78 | 10.19 | sand beach backed by high bluff |
| | 32 | 9.775 | 4.467 | 9.29 | 9.69 | sand beach backed by low bluff |
| | 33 | 8.982 | 4.273 | 9.30 | 9.58 | sand beach backed by low bluff |
| | 34 | 11.208 | 4.774 | 10.43 | 10.85 | sand beach backed by low bluff |
| | 35 | 20.565 | 4.759 | 10.69 | 11.37 | sand beach backed by high bluff |
| | 36 | 25.230 | 4.850 | 8.99 | 10.08 | moderately wide rock platform backed by high bluff |
| Stonefield Beach | 31 | 21.045 | 5.183 | 8.95 | 10.53 | sand beach backed by high bluff |
| | 38 | 18.245 | 5.670 | 11.50 | 13.33 | moderately wide rock platform backed by high bluff |
| | 39 | 11.970 | 5.003 | 9.87 | 10.19 | sand beach backed by high bluff |
| | 40 | 17.186 | 5.301 | 11.90 | 12.58 | moderately wide rock platform backed by high bluff |
| | 41 | 19.745 | 6.222 | 10.75 | 11.24 | sand beach backed by high bluff |
| | 42 | 6.331 | 6.301 | 8.93 | 9.52 | sand beach backed by dunes |
| | 43 | 6.693 | 3.624 | 8.43 | 8.82 | sand beach backed by low bluff |
| | 44 | 8.058 | 4.562 | 9.67 | 10.65 | moderately wide rock platform backed by high bluff |
| | 45 | 8.314 | 4.726 | 9.79 | 10.43 | sand beach backed by low bluff |
| | 46 | 7.542 | 4.919 | 9.45 | 10.43 | sand beach backed by low bluff |
| | 47 | 17.942 | 4.797 | 9.19 | 9.70 | sand beach backed by high bluff |
| | 48 | 29.229 | 3.201 | 10.50 | 13.70 | moderately wide rock platform backed by high bluff |

| Reach | Transect (Lane) | $D_{HIGH}$ (m) | $D_{LOW}$ (m) | 100-Year TWL (m) | 500-Year TWL (m) | Description |
|---|---|---|---|---|---|---|
| | 49 | 28.958 | 6.552 | 11.00 | 12.70 | moderately wide rock platform backed by high bluff |
| | 50 | 15.647 | 5.408 | 12.44 | 13.59 | moderately wide rock platform backed by high bluff |
| | 51 | 8.330 | 4.894 | 9.95 | 10.35 | mixed sand and gravel beach backed by low bluff |
| Cummins Creek/ Cape Perpetua | 52 | 28.047 | 1.906 | 14.04 | 14.34 | narrow rock platform backed by high bluff |
| | 53 | 20.355 | 5.944 | 12.83 | 13.58 | narrow rock platform backed by high bluff |
| | 54 | 19.471 | 4.871 | 10.47 | 11.03 | sand beach backed by high bluff |
| | 55 | 34.099 | 3.709 | 13.39 | 14.33 | moderately wide rock platform backed by high bluff |
| | 56 | 12.687 | 3.535 | 9.53 | 9.86 | sand beach backed by low bluff |
| | 57 | 10.730 | 6.739 | 7.19 | 7.91 | narrow rock platform backed by low bluff |
| Supple-mental Lines | 33_575 | 9.576 | 4.802 | 9.20 | 9.94 | sand beach backed by low bluff |
| | 33_577 | 5.946 | 3.854 | 8.27 | 8.72 | sand beach backed by gravel berm |
| | 34_523 | 16.465 | 3.370 | 10.24 | 10.56 | sand beach backed by low bluff |
| | 34_530 | 4.832 | 4.069 | 6.38 | 6.54 | sand beach backed by gravel berm |
| | 42_292 | 5.020 | 4.029 | 6.63 | 6.79 | sand beach backed by dunes |
| | 42_313 | 8.712 | 5.336 | 10.77 | 11.35 | sand beach backed by low bluff |
| | 51_179 | 7.587 | 4.061 | 6.94 | 7.02 | mixed sand and gravel beach |
| | 51_177 | 3.608 | 3.608 | 6.94 | 7.02 | mixed sand and gravel beach |
| | 56_49 | 3.788 | 2.953 | 6.16 | 6.27 | sand beach backed by gravel berm |
| | 56_54 | 8.097 | 3.303 | 9.66 | 9.79 | sand beach backed by low bluff |

Notes:

100-year and 500-year total water level (TWL) values relative to NAVD88 vertical datum.

$D_{HIGH}$ is the crest of the dune, bluff, or barrier determined for the eroded profile. *Red text denotes that the crest is overtopped*.

## 6.4 Overtopping Calculations

Overtopping of natural features such as foredunes, spits, and coastal engineering structures and barriers occurs when the wave runup superimposed on the tide exceeds the crest of the foredune or structure (**Figure 6-7**). Hazards associated with wave overtopping can be linked to a number of simple direct flow parameters including (EurOtop, 2016):

- mean overtopping discharge, $q$;
- overtopping velocities over the crest and further landward, $V$;
- landward extent of green water and splash overtopping $y_{G,\,outer}$; and,
- overtopping flow depth, $h$ at a distance $y$ landward of the foredune crest or "barrier."

NHC (2005) noted that there are three physical types of wave overtopping:

1. *Green water or bore overtopping* occurs when waves break onto or over the foredune or barrier and the overtopping volume is relatively continuous;
2. *Splash overtopping* occurs when the waves break seaward of the foredune or barrier, or where the foredune or barrier is high relative to the wave height and overtopping consists of a stream of droplets. Splash overtopping can be a function of its momentum due to the runup swashing up the barrier and/or may be enhanced due to onshore direct winds; and,
3. *Spray overtopping* is generated by the effects of wind blowing droplets and spray that are derived from the wave crests.

Mapping these respective flood inundation zones requires an estimate of the velocity, $V$, the overtopping discharge, $q$, of the water that is carried over the crest, the inland extent of green water and splash overtopping, and the envelope of the water surface that is defined by the water depth, $h$, landward of the barrier crest. According to NHC (2005) these hazard zones are ultimately defined based on the following two derivations:

- Base flood elevations (BFEs) are determined based on the water surface envelope landward of the barrier crest; and
- Hazard zones are determined based on the landward extent of green water and splash overtopping, and on the depth and flow velocity in any sheet flow areas beyond that, defined as $hV^2$ = 5.7 $m^3/s^2$ or 200 $ft^3/s^2$.

A distinction can be made between whether green water (or bore) or splash overtopping predominates at a particular location that is dependent on the ratio of the calculated wave runup height relative to the barrier crest elevation, $R/Z_c$. When $1 < R/Z_c < 2$, splash overtopping dominates; for $R/Z_c > 2$, bore propagation occurs. In both cases, $R$ and $Z_c$ are relative to the 2% Dynamic Water Level ($DWL_{2\%}$) at the barrier (Figure D.4.5-12 in NHC [2005, p. D.4.5-22]).

### 6.4.1 Mean overtopping rate at the "barrier" crest

Wave overtopping of dunes and barrier is a function of both hydraulic and barrier structure parameters whereby

$$q = f(H_{mo}, T_p, \beta, F_c, DWL_{2\%}, geometry) \tag{6.14}$$

where $q$ is the overtopping discharge (expressed as cubic meters per second per meter, $m^3/s/m$ [$ft^3/s/ft$]), $H_{mo}$ is the significant wave height at the toe of the structure, $T_p$ is the peak period, $\beta$ is the angle of wave attack, $F_c$ is the freeboard, and $DWL_{2\%}$ is 2% dynamic water level at the toe of the structure (**Figure 6-7**).

Prior to calculating the mean overtopping rate at the barrier crest it is necessary to first distinguish between four contrasting types of wave breaking situations that may impact a particular barrier or dune overtopping situation. There four conditions include *non-breaking* or *breaking* on a normally sloped barrier (where $0.067 < \tan\alpha < 0.67$), and *reflecting* or *impacting* on steeply sloping or vertical barriers (where $\tan\alpha \geq 0.67$). Of these, the breaking wave situation is the dominant condition in Lane and Douglas County, where the waves have already broken across the surf zone and are reforming as bores prior to swashing up the beach face or barrier.

For beaches and normally sloping barriers (where $0.067 < \tan\alpha < 0.67$), a distinction can be made between situations where waves break directly on the barrier versus those conditions where the waves have not yet broken. These conditions can be determined using the surf similarity parameter (Iribarren number) defined here in terms of the beach or structure slope ($\tan\alpha$), and the wave steepness ($S_{op} = H_{mo}/L_o$):

$$\xi_{op} = \frac{\tan\alpha}{\sqrt{\frac{H_{mo}}{L_o}}} = \frac{\tan\alpha}{\sqrt{S_{op}}} \tag{6.15}$$

Breaking on normally sloping surfaces generally occurs where the surf similarity number, $\xi_{op} \leq 1.8$, while non-breaking conditions occur when $\xi_{op} > 1.8$. As noted above, for the Lane and Douglas County coastline the identified Iribarren numbers almost always fell below the 1.8 criteria indicating that the incident waves are always broken prior to reaching the beach or the barrier face.

**Figure 6-7. Nomenclature of overtopping parameters available for mapping base flood elevations (BFEs) and flood hazard zones (after NHC, 2005).**

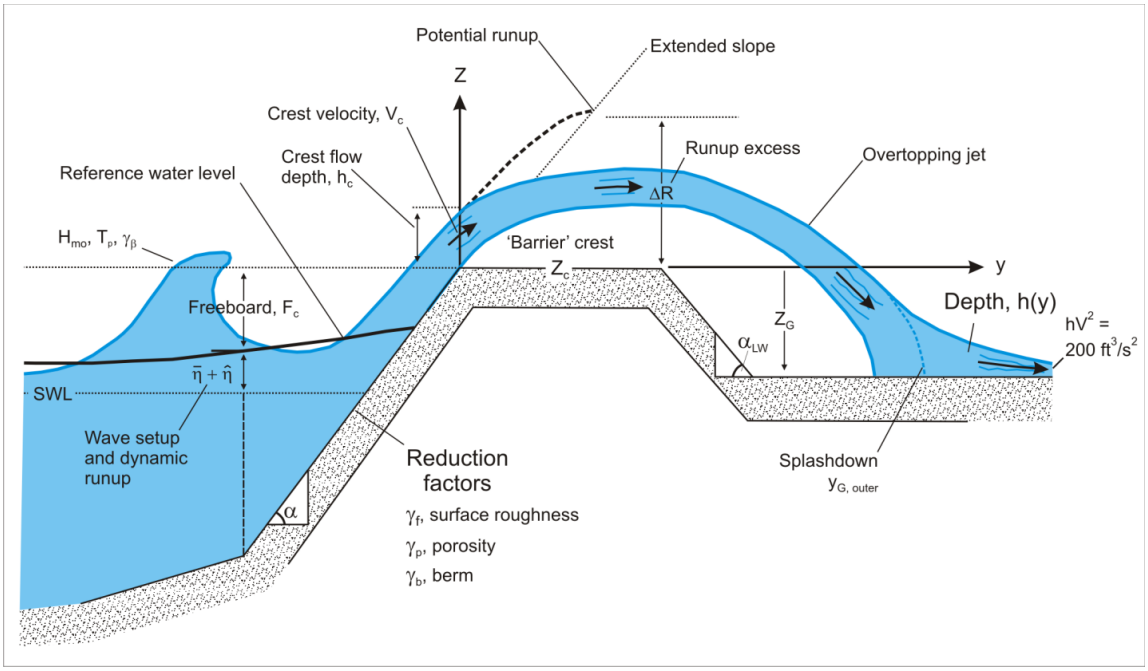


At the beach or barrier crest, the relative freeboard ($F_c/H_{mo}$), **Figure 6-7**, is a particularly important parameter because changing these two parameters controls the volume of water that flows over the barrier crest. For example, increasing the wave height or period increases the overtopping discharge, as does reducing the beach or barrier crest height or raising the water level.

A variety of prediction methods are available for calculating the overtopping discharge and are almost entirely based on laboratory experiments based on a range of structure slopes (slopes between 1:1 and 1:8, with occasional tests at slopes around 1:15 or lower). Factors that will serve to reduce the potential overtopping discharge include the barrier *surface roughness* ($\gamma_f$), the presence of a *berm* ($\gamma_b$), *wave approach directions* ($\gamma_\beta$), and the *porosity* of the barrier ($\gamma_p$) (**Figure 6-7**). In terms of porosity, increasing this variable effectively reduces the wave runup and overtopping discharge because more of the water can be taken up by the voids between clasts and particles. As noted by NHC (2005), the effect of the *porosity* factor makes it convenient to distinguish between impermeable and permeable structures. Methods for determining the various reduction factors are described in Table D.4.5-3 of NHC (2005, p. D.4.5-13), with one difference whereby the approach recommended for determining the wave approach ($\gamma_\beta$) reduction factor for wave overtopping calculations is based on the following equation:

$$\gamma_\beta = \begin{cases} 1 - 0.0033|\beta|, & (0 \le |\beta| \le 80°) \\ 1 - 0.0033|80|, & (|\beta| \ge 80°) \end{cases} \qquad (6.16)$$

Table D.4.5-3 of NHC (2005, p. D.4.5-13) identifies four general categories of overtopping applications: overtopping on a normally sloping barrier (e.g., riprap structure); steeply sloping or vertical barrier (e.g., seawall or bluff where some waves broken); steeply sloping or vertical barrier (all waves broken); and shallow foreshore slopes subject to large Iribarren numbers.

For a normally sloping barrier, where $0.05 < \tan\alpha < 0.67$ and the Iribarren number ($\xi_{op}$) $\leq 1.8$ (breaking wave condition), the following formulation can be used to determine the mean overtopping discharge (both dimensional ($q$) and non-dimensional ($Q$) forms) at the barrier crest:

$$q = Q\sqrt{\frac{gH_{mo}\tan\alpha}{S_{op}}} \tag{6.17}$$

where

$$Q = 0.06e^{-4.7F'}$$

and

$$F' = \frac{F_c}{H_{mo}}\frac{\sqrt{S_{op}}}{\tan\alpha}\frac{1}{\gamma_f\gamma_b\gamma_\beta\gamma_p}$$

For non-breaking conditions (Iribarren number ($\xi_{op}$) > 1.8):

$$q = Q\sqrt{gH_{mo}^3} \tag{6.18}$$

where

$$Q = 0.2e^{-2.3F'}$$

and

$$F' = \frac{F_c}{H_{mo}}\frac{1}{\gamma_f\gamma_\beta}$$

For steeply sloping or vertical barrier, where $\tan\alpha > 0.67$ and $h_* \geq 0.3$ (reflecting condition, where

$$h_* = \frac{h}{H_{mo}}\left(\frac{2\pi h}{gT_m^2}\right)$$

and $h$ is the water depth at the structure toe), the following formulation can be used:

$$q = Q\sqrt{gH_{mo}^3} \tag{6.19}$$

where

$$Q = 0.05e^{-2.78F_c/H_{mo}}$$

For impacting conditions ($h_* < 0.3$):

$$q = Q\sqrt{gh^3}\, h_*^2 \tag{6.20}$$

where

$$Q = 1.37 * 10^{-4}(F')^{-3.24}$$

and

$$F' = \frac{F_c}{H_{mo}}\, h_*$$

For steeply sloping or vertical barrier (all waves are broken) where the structure toe < $DWL_{2\%}$ water level and where $(F_c/H_{mo})^* h_* \leq 0.03$:

$$q = Q\sqrt{gh^3}\, h_*^2 \tag{6.21}$$

where

$$Q = 0.27 * 10^{-4} e^{-3.24\,(F_c/H_{mo})h_*}$$

For steeply sloping or vertical barrier (all waves are broken) where the structure toe > $DWL_{2\%}$ water level:

$$q = Q\sqrt{gh^3}\, h_*^2 \tag{6.22}$$

where

$$Q = 0.06 e^{-4.7\, F_c S_{op}^{-0.17}}$$

We have implemented two additional overtopping calculations following discussions with Dr. W. G. McDougal, which may be applied to beaches subject to gently sloping ($\tan\beta < 0.4$), dissipative foreshores:

$$q = Q\sqrt{gh^3}h_*^2 \tag{6.23}$$

where

$$Q = 0.21\sqrt{gH_{mo}^3}e^{-F'}$$

and

$$F' = \frac{F_c}{\gamma_f\gamma_\beta H_{mo}(0.33 + 0.022\xi_{op})}$$

and cases where there is negative freeboard. The latter occurs when the dynamic water level ($DWL_{2\%}$) is higher than the barrier crest, which produces a negative freeboard (i.e., $-F_c$). In this situation we apply the well-known weir type formula to define the volume of water that is overflowing the crest (EurOtop, 2016). The formulation used is:

$$q = Q_s + q_w \tag{6.24}$$

where

$$Q_s = 0.4583(-F_C)\sqrt{-F_C g}$$

and

$$Q_w = 0.21\sqrt{gH_{mo}^3}$$

and

$$q_w = Q_w\sqrt{gh^3}h_*^2$$

### 6.4.2 Overtopping limits and flood hazard zones landward of the "barrier" crest

Estimates of the landward limit of the splashdown distance associated with wave overtopping and the landward limit of the hazard zone require several calculation steps. These are:

1. Three initial parameters are first calculated:
   a. excess potential runup: $\Delta R = R - Z_c$;
   b. crest flow rate, $V_c \cos \alpha$ (where $V_c = 1.1\sqrt{g\Delta R}$ for cases where splash overtopping, and $V_c = 1.8\sqrt{g\Delta R}$ for bore overtopping); and,
   c. initial flow depth, $h_c$ (where $h_c = 0.38\Delta R$).
2. The associated onshore wind component, *Wy* is determined from available wind data. For the purposes of this study, we used *Wy* = 19.6 m/s (64.3 ft/s), which was determined from an analysis of winds (mean from a select number of storms) measured at the Cape Arago C-MAN station operated by the NDBC. In the absence of wind data, NHC (2005) recommends a wind speed of 13.4 m/s (44 ft/s).
3. The enhanced onshore water velocity component $(V_c \cos \alpha)'$ is then calculated using equation 6.25:

$$\begin{aligned} \text{For vertical bluffs and seawalls:} \quad & (V_c \cos \alpha)' = 0.3 * W_y \\ \text{All other cases:} \quad & (V_c \cos \alpha)' = V_c \cos \alpha + 0.3(W_y - V_c \cos \alpha) \end{aligned} \tag{6.25}$$

4. The effective angle, $\alpha_{eff}$, is calculated from: $\tan \alpha_{eff} = \frac{V_c \sin \alpha}{(V_c \cos \alpha)'}$.
5. With the above parameters, the outer limit of the splash region, $y_{G\ outer}$ is calculated using equation 6.26. Here we have used an algorithm developed by Dr. Bill McDougal (Coastal Engineer, OSU, and Technical Coordinator of the North Pacific FEMA West Coast Guidelines) of the form:

$$y_{G\ outer} = \frac{(V_c \cos \alpha)'}{g} * V_c \sin \alpha - mBackshore * (V_c \cos \alpha)' * \tag{6.26}$$

$$1 + \sqrt{1 - \frac{2g * bBackshore}{(V_c \sin \alpha - mBackshore * (V_c \cos \alpha)'^2)}}$$

and

$$Z_G = bBackshore + (mBackshore * y_{G\ outer}) \tag{6.27}$$

where *bBackshore* is the intercept for the backshore slope adjacent to the barrier crest and *mBackshore* is the slope of the backshore. Equation 6.26 is ultimately based on Figure D.4.5-15 of NHC (2005, p D.4.5-30).

6. The total energy, *E*, of the splashdown is calculated from $E = \Delta R - Z_G$.
7. Finally, the initial splashdown velocity, $V_o$ (where $V_o = 1.1\sqrt{gE}$), and depth, $h_o$ (where $h_o = 0.19E$) are calculated. In the case of green water or bore overtopping, the splashdown velocity, $V_o$, can be calculated from $V_o = 1.1\sqrt{g\Delta R}$, while the flow depth is determined as $h_o = 0.38E$.

Having determined the initial splashdown velocity, $V_o$, and flow depth, $h_o$, the landward extent of the overland flow is calculated using an approach modified from that originally proposed by (Cox and Machemehl, 1986). The version presented in NHC (2005) effectively calculates the flow depth, $h$, with distance, $y$, from the barrier crest, such that the flow depth decays asymptotically as y-distance increases away from the barrier crest, eventually approaching zero. The NHC (2005) equation is shown as equation 6.28:

$$h(y) = \left[\sqrt{h_o} - \frac{5(y - y_o)}{A\sqrt{gT^2}}\right]^2 \tag{6.28}$$

where $h_o$ is determined from step 7 above and for an initial approximation the non-dimensional $A$ parameter may be taken as unity. For sloping backshores, the $A$ parameter in equation 6.28 can be modified such that $A_m = A(1 - 2 * \tan \alpha_{LW})$, and the value in parentheses is limited to the range 0.5 to 2. According to NHC (2005), if the maximum distance of splash or bore propagation calculated using equation 6.28 does not appear reasonable or match field observations, the $A$ parameter can be adjusted in order to increase or decrease the landward wave propagation distance. In addition, for green water or bore propagation the $A$ parameter value is taken initially to be 1.8.

For the purposes of this study we have adopted a modified version of equation 6.28 developed by Dr. W. G. McDougal of the form:

$$h(y) = \left[h_o^{1/2} - \frac{y - y_o}{2\alpha(\alpha + 1)^{\frac{3}{2}}(1 - 2m)\, g^{0.5}T}\right]^2 \tag{6.29}$$

where $m$ is the slope of the backshore and α is a constant that can be varied in order to increase or decrease the landward wave propagation distance.

Finally, the landward limit of the hazard zone defined as $hV^2$ = 5.7 $m^3/s^2$ (or 200 $ft^3/s^2$) is determined, whereby $h$ is the water depth given by the modified Cox and Machemehl (1986) method (equation 6.29) and $V = V_o$ calculated from step 7 above.

### 6.4.3 Initial testing of the landward limit of wave overtopping

Our initial computations of the landward extent of wave overtopping using the steps outlined above yielded narrow hazard zones for our original coastal FIRM study in Coos County. In order to calibrate equation 6.29, we performed wave overtopping calculations and inundation for a site on the northern Oregon coast where there are field observations of wave overtopping. The site is Cape Lookout State Park in Tillamook County (Allan and others, 2006; Allan and Komar, 2002b; Komar and others, 2003). The southern portion of Cape Lookout State Park is characterized by a wide, gently sloping, dissipative sand beach, backed by a moderately steep gravel berm and ultimately by a low foredune that has undergone significant erosion since the early 1980s (Komar and others, 2000).

On March 2-3, 1999, the crest of the cobble berm/dune at Cape Lookout State Park was overtopped during a major storm; the significant wave heights reached 14.1 m (46.3 ft), while the peak periods were 14.3 s measured by a deepwater NDBC wave buoy (Allan and Komar, 2002a). Wave overtopping of the dune and flooding extended ~70 m (230 ft) into the park (Dr. P. Komar, Emeritus Professor, College of Oceanic and Atmospheric Sciences, oral comm., 2010), evidence for which included photos and field

evidence including pockmarks at the bases of the tree trunks located in the park. These pockmarks were caused by cobbles carried into the park from the beach by the overtopping waves, where the cobbles slammed into the trees as ballistics. Because the average beach slopes at Cape Lookout State Park are analogous to those observed along the Lane and Douglas County coastline and because large wave events associated with extratropical storms affect significant stretches (100s to 1,000 kilometers) of the coast at any single point in time, we believe these data provide a reasonable means by which to investigate a range of alpha ($\alpha$) values that may be used to determine the landward extent of wave inundation.

Using beach morphology data (slope ($\tan \beta$) = 0.089, barrier crest = 5.5 m [18 ft]) from Cape Lookout State Park and deepwater wave statistics from a nearby NDBC wave buoy (#46050), we experimented with a range of $\alpha$ values (**Figure 6-8**) in order to replicate the landward extent of the inundation. As can be seen in **Figure 6-8**, in order to emulate the landward extent of flooding observed at Cape Lookout our analyses yielded an $\alpha$ of 0.58. Using $\alpha$ = 0.58, we in turn calculated the extent of the hazard zone where $h(y)$ = 200 $ft^3/s^2$, which was found to be ~34 m from the crest of the cobble berm/dune, consistent with damage to facilities in the park.

**Figure 6-8. Calculations of bore height decay from wave overtopping at Cape Lookout State Park at the peak of the March 2-3, 1999, storm based on a range of alpha (α) values.**

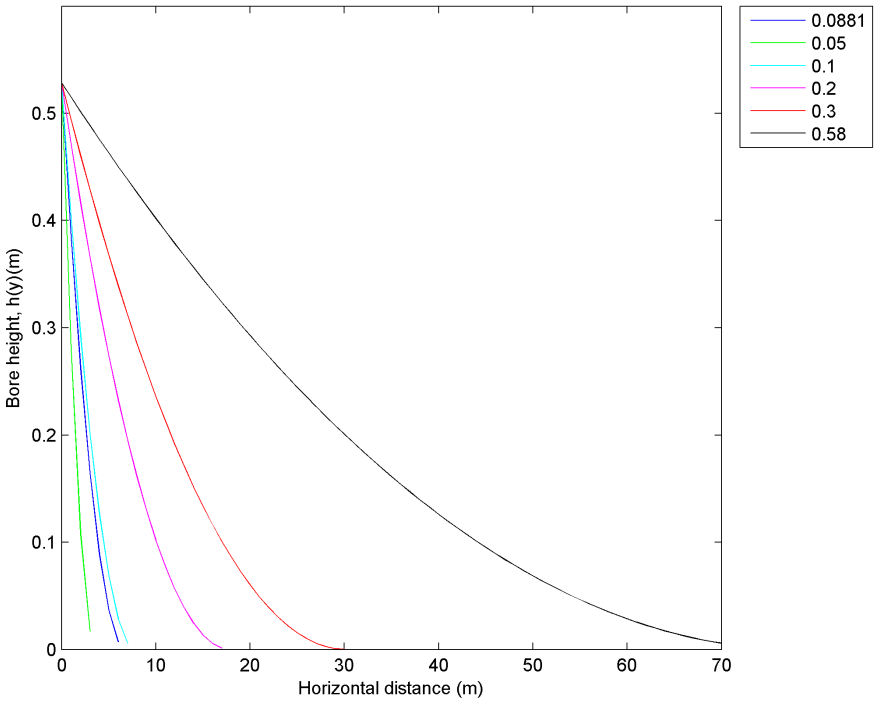

### 6.4.4 Wave overtopping and hazard zone limits calculated for Lane and Douglas counties

**Table 6-3** presents the results of the calculated splashdown distances ($y_{G\ outer}$) and the landward extent of the flow ($hV^2$) where the flows approach 5.7 $m^3/s^2$ (or 200 $ft^3/s^2$). **Table 6-3** includes a more conservative splashdown distance, based on an enhanced wind velocity of 19.6 m/s (64.3 ft/s); this contrasts with the default wind speed of 13.4 m/s (44 ft/s) suggested by NHC (2005). This enhanced wind velocity was determined from an analysis of wind speeds measured by the Cape Arago C-MAN[11] station located adjacent to the mouth of Coos Bay (Allan and others, 2012b). Essentially, Allan and others examined the wind speeds identified at Cape Arago for a range of storm events and identified a wide range of values, with a maximum mean wind speed of 19.6 m/s (64.3 ft/s). Because the measured wind speeds reflect a 2-minute average such that higher wind speeds have been measured throughout the entire record (e.g., the maximum 2-minute average wind speed is 29.3 m/s [96 ft/s], while the maximum 5-second wind gust reached 38.1 m/s [(125.0 ft/s]), we believe it is justified to use the more conservative enhanced wind velocity of 19.6 m/s (64.3 ft/s). Furthermore, comparisons by Allan and others (2012b) indicated that the relative difference between the value suggested by NHC (2005) and the enhanced wind used here differs by about 30%. As can be seen from the **Table 6-3**, the calculated splashdown distances ($y_{G\ outer}$) indicate splash distances that range from as little as 0.4 m (1.3 ft) to a maximum of 8.8 m (28.9 ft); the mean splash distance is 2.4 m (7.9 ft), while the standard deviation is 2.2 m (7.2 ft). Thus, adopting the reduced wind velocity would cause the zones to narrow by ~2.6 m (8.5 ft) for the highest splash distance and 0.1 m (0.33 ft) for the smallest. Overall, these differences are acceptable given the tremendous uncertainties in calculating splash and overtopping (NHC, 2005).

**Table 6-3. Splashdown and hazard zone limits calculated for Lane County detailed coastal sites. Values reported in the table reflect the maximum values derived from all the storm runup and overtopping calculations. Note: Dist_3, Dist_2, and Dist_1 reflect the landward extent at which the calculated bore height decreases from 0.9 m (3 ft), to 0.6 m (2 ft), and to 0.3 m (1 ft). In all cases, the hazard zones are ultimately defined relative to the location of the dune/structure crest.**

| Profiles | Transect (Lane) | Splashdown $y_{G\ outer}$ (m) | Bore Height (m) | Dist_3 (≥ 0.91 m) | Dist_2 (> 0.61 < 0.91 m) | Dist_1 (≤ 0.31 m) | $hV^2 > 5.7\ m^3/s^2$ (m) |
|---|---|---|---|---|---|---|---|
| Heceta Beach | 1 | 0.72 | 0.04 | | | | |
| Heceta Head | 29 | 0.83 | 0.08 | | | | |
| Muriel O'Ponsler | 33 | 1.98 | 0.09 | | | | |
| Stonefield Beach | 42 | 2.98 | 0.55 | | | 28.02 | 49.53 |
| | 43 | 4.46 | 0.40 | | | 11.08 | 21.65 |
| | 44 | 3.58 | 0.29 | | | | |
| | 45 | 1.98 | 0.28 | | | | |
| | 46 | 1.60 | 0.33 | | | 3.36 | 7.45 |
| | 51 | 2.16 | 0.32 | | | 2.11 | 5.36 |
| Supplemental Lines | 33_577 | 8.76 | 1.15 | 21.63 | 53.75 | 95.60 | 145.35 |
| | 34_530 | 0.36 | 0.44 | | | 19.62 | 36.98 |
| | 42_292 | 1.10 | 0.32 | | | 2.06 | 5.28 |
| | 42_313 | 4.05 | 0.37 | | | 8.89 | 18.05 |
| | 51_177 | 1.24 | 0.64 | | 2.94 | 43.88 | 75.09 |
| | 56_54 | 3.77 | 0.31 | | | 0.38 | 1.34 |
| | 56_49 | 0.75 | 0.45 | | | 16.21 | 30.32 |

[11] http://www.ndbc.noaa.gov/station_page.php?station=CARO3

Hazard zone calculations shown in **Table 6-3** indicate a similarly broad range of values that vary from negligible (i.e., effectively where the 1% TWL intersects with the backshore, plus the width of the splash zone where applicable) to as much as 145 m (475 ft) wide; the widest zones occur at creek mouths where overtopping significantly exceeds the barrier beach crest elevations. Qualitative field observations of past storm wave overtopping events at all sites subject to overtopping calculated in this study confirm that this is indeed the case. Hence, field-based observations appear to be consistent with the calibrated results identified in **Table 6-3**. The depth of flooding at each mapped overtopping zone is indicated in **Table 6-4**.

**Table 6-4. The depth of flooding at the overtopping zones landward of the structure crest. Note: Dist_3, Dist_2, and Dist_1 reflect the landward extent at which the calculated bore height decreases from 0.9 m (3 ft), to 0.6 m (2 ft), and to 0.3 m (1 ft).**

| Profiles | Transect (Lane) | Dist_3 (≥ 0.91 m) | Dist_2 (> 0.61 < 0.91 m) | Dist_1 (≤ 0.31 m) | $hV^2 > 5.7 m^3/s^2$ (m) | Comments |
|---|---|---|---|---|---|---|
| Heceta Beach | 1 | | | | | overtopping stops seaward of PFD |
| Heceta Head | 29 | | | | | VE zone mapped to $D_{high}$ |
| Muriel O'Ponsler | 33 | | | | | mapped to splashdown distance |
| Stonefield Beach | 42 | | | 0.31 | 0.31 | none |
| | 43 | | | 0.31 | 0.31 | narrow D1 added to HV2 |
| | 44 | | | | | mapped to splashdown distance |
| | 45 | | | | | mapped to splashdown distance |
| | 46 | | | 0.31 | 0.31 | narrow D1 added to HV2 |
| | 51 | | | 0.31 | 0.31 | very narrow D1 and HV2 added to main VE zone |
| Supplemental Lines | 33_577 | 0.91 | 0.61 | 0.31 | 0.31 | none |
| | 34_530 | | | 0.31 | 0.31 | none |
| | 42_313 | | | 0.31 | 0.31 | narrow D1 added to HV2 |
| | 42_292 | | | 0.31 | 0.31 | transect not used for mapping |
| | 51_177 | | 0.61 | 0.31 | 0.31 | narrow D2 added to D1 |
| | 56_54 | | | 0.31 | 0.31 | very narrow D1 and HV2 added to main VE zone |
| | 56_49 | | | 0.31 | 0.31 | none |

# 7.0 COASTAL EROSION

To estimate beach (or bluff) erosion and the resulting profile changes that occur during a particular storm, it is important to establish the profile conditions that existed prior to the storm. As outlined in **SECTION 3.2**, this initial profile morphology is represented by the most likely winter profile (MLWP), which forms the basis for determining profile changes that could eventuate from a particularly severe storm(s). After the MLWP is established for a site, the profile is modified according to the amount of erosion estimated to occur during a specified storm as a result of the increased water levels (tide + surge + ENSO) as well as from wave processes, specifically wave runup. This section explores two approaches described in the revised FEMA guidelines, which may be used to establish the eroded profiles along the Lane County coastline. The second half of the section describes the specific approach adopted for Lane and Douglas County and the results from our erosion analyses.

## 7.1 Models of Foredune Erosion

### 7.1.1 The Komar and others (1999) model

The erosion potential of sandy beaches and foredunes along the Pacific Northwest coast of Oregon and Washington is a function of the total water level produced by the combined effect of the wave runup plus the tidal elevation ($E_T$), exceeding some critical elevation of the fronting beach, typically the elevation of the beach-dune junction ($E_J$). This basic concept is depicted conceptually in **Figure 7-1**A based on the model developed by (Ruggiero and others, 1996), and in the case of the erosion of a foredune backing the beach the application of a geometric model (**Figure 7-1**B) formulated by Komar and others (1999). Clearly, the more extreme the total water level elevation, the greater the resulting erosion that occurs along both dunes and bluffs.

**Figure 7-1. A) The foredune erosion model. B) The geometric model used to assess the maximum potential beach erosion in response to an extreme storm (Komar and others, 1999).**

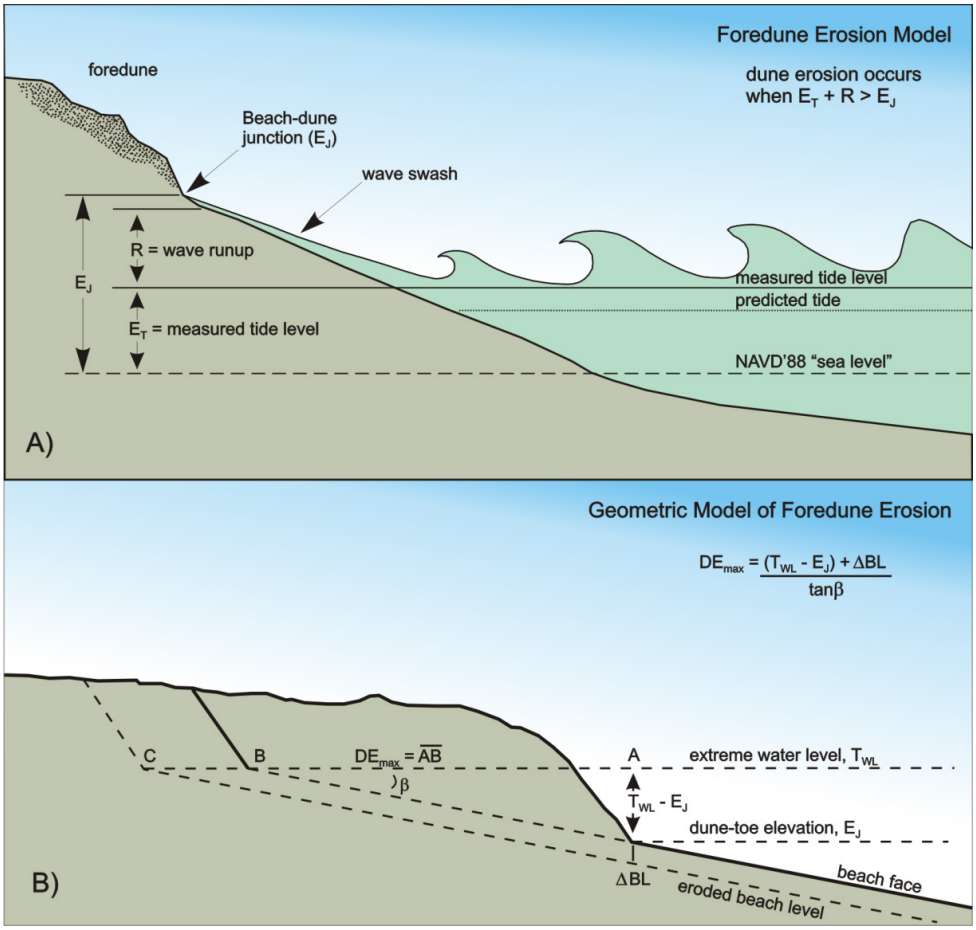


As can be seen from **Figure 7-1**B, estimating the maximum potential dune erosion ($DE_{MAX}$) is dependent on first determining the total water level (TWL) elevation diagrammed in **Figure 7-1**A, which includes the combined effects of extreme high tides plus storm surge plus wave runup, relative to the elevation of the beach-dune junction ($E_J$). Therefore, when the TWL > $E_J$ the foredune retreats landward by some distance, until a new beach-dune junction is established, whose elevation approximately equals the extreme water level. Because beaches along the high-energy Oregon coast are typically wide and have a nearly uniform slope (tan $\beta$), the model assumes that this slope is maintained, and the dunes are eroded landward until the dune face reaches point B in **Figure 7-1**B. As a result, the model is geometric in that it assumes an upward and landward shift of a triangle, one side of which corresponds to the elevated water levels, and then the upward and landward translation of that triangle and beach profile to account for the total possible retreat of the dune (Komar and others, 1999). An additional feature of the geometric model is its ability to accommodate further lowering of the beach face due to the presence of a rip current, which has been shown to be important to occurrences on the Oregon coast of localized "hot spot" erosion and property impacts (Komar, 1997). This feature of the model is represented by the beach-level change $\Delta BL$ shown in **Figure 7-1**B, which causes the dune to retreat some additional distance landward until it reaches point C. As can be seen from **Figure 7-1**B, the distance from point A to point C depicts the total retreat, $DE_{MAX}$, expected during a particularly severe storm event (or series of storms) that includes the

localized effect enhancement by a rip current. Critical then in applying the model to evaluate the susceptibility of coastal properties to erosion is an evaluation of the occurrence of extreme tides ($E_T$), the runup of waves, and the joint probabilities of these processes along the coast (Ruggiero and others, 2001), this having been the focus of **SECTION 6**.

The geometric model gives the maximum potential equilibrium cross-shore change in the shoreline position landward of the MLWP resulting from a storm. However, in reality it is unlikely that this extreme degree of response is ever fully realized, because of the assumptions that had been made in deriving the geometric model with the intent of evaluating the maximum potential dune erosion. As noted by Komar and others (1999), in the first instance the geometric model projects a mean linear beach slope. As a result, if the beach is more concave, it is probable that the amount of erosion would be less, though not by much. Perhaps of greater significance is that the geometric model assumes an instantaneous erosional response, with the dunes retreating landward as a result of direct wave attack. However, the reality of coastal change is that it is far more complex, there in fact being a lag in the erosional response behind the forcing processes. As noted by Komar and others (1999), extreme runup elevations typically occur for only a relatively short period of time (e.g., the period of time in which the high wave runup elevations coincide with high tides). Because the elevation of the tide varies with time (e.g., hourly), the amount of erosion can be expected to be much less when the water levels are lower. Thus, it is probable that several storms during a winter may be required to fully realize the degree of erosion estimated by the geometric model; this did occur for example during the winter of 1998-99, with the last in the series of five storms having been the most extreme and erosive (Allan and Komar, 2002). In addition, as beaches erode, the sediment is removed offshore (or farther along the shore) into the surf zone, where it accumulates in nearshore sand bars. This process helps to mitigate the incoming wave energy by causing the waves to break farther offshore, dissipating some of the wave energy, and forming the wide surf zones that are characteristic of the Oregon coast. In turn, this process helps to reduce the rate of beach erosion that occurs. In summary, the actual amount of beach erosion and dune recession is dependent on many factors, the most important of which include the incident wave conditions, the TWL, and the duration of the storm event(s).

### 7.1.2 The Kriebel and Dean (1993) model

Kriebel and Dean (1993), hereafter known as K&D, developed a dune erosion model that is broadly similar to the Komar and others (1999) geometric model. At its core is the assumption that the beach is in statistical equilibrium with respect to the prevailing wave climate and mean water levels (Bruun, 1962). As water levels increase, the beach profile is shifted upward by an amount equal to the change in water level ($S$) and landward by an amount $R_\infty$ until the volume of sand eroded from the subaerial beach matches the volume deposited offshore in deeper water (**Figure 7-2**); *note that $DE_{MAX}$ and $R_\infty$ are essentially synonymous with each other*. One important distinguishing feature in the K&D model relative to Bruun (1962) is that it relies on the equilibrium beach profile theory proposed by Dean (1977) to account for the erosion following an increase in the water level. The Dean model is a simplified equilibrium form for open-coast beach profiles expressed as a power-law curve of the form:

$$h = Ax^{2/3} \text{ or equivalently as } x = \left(\frac{h}{A}\right)^{3/2} \tag{7.1}$$

where $h$ is the water depth at a distance $x$ offshore from the still-water level and $A$ is a parameter that governs the overall steepness (and slope) of the profile and is a function of the beach grain size. Thus, incorporating the assumed components of Bruun (1962) and Dean (1977), the maximum erosion

potential, $R_\infty$, was determined by K&D to be a function of the increase in mean water level ($S$) caused by a storm, the breaking wave water depth ($h_b$), surf zone width ($W_b$), berm or dune height ($B$ or $D$), and the slope ($\beta_f$) of the upper foreshore beach face. The breaking wave depth ($h_b$) may be calculated from the wave breaker height (equation 6.8) multiplied by 0.78 (the breaker index).

**Figure 7-2. Maximum potential erosion ($R_\infty$) due to a change in water levels (after Kriebel and Dean, 1993).**

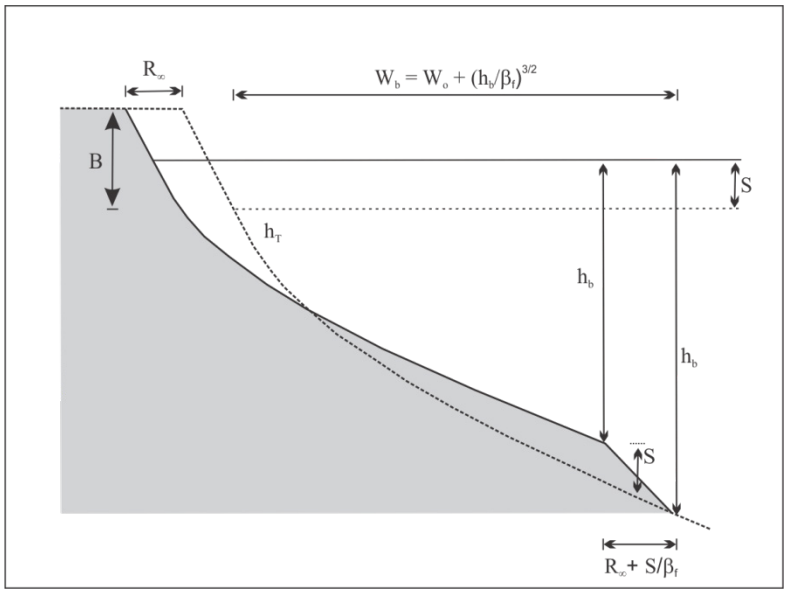


As a result of the above concepts, K&D developed two approaches for determining the maximum erosion potential. These are:

- A beach backed by a low sand berm

$$R_\infty = \frac{S\left(W_b - h_b/\beta_f\right)}{B + h_b - S/2} \tag{7.2}$$

- A beach backed by high sand dune

$$R_\infty = \frac{S\left(W_b - h_b/\beta_f\right)}{D + h_b - S/2} \tag{7.3}$$

Like the Komar and others (1999) model, the Kriebel and Dean (1993) dune erosion model estimates the maximum potential erosion ($DE_{MAX}$) associated with a major storm, and assume that a particular storm will last sufficiently long enough to fully erode the dune. In reality, $DE_{MAX}$ is almost never fully realized because storms rarely last long enough to fully erode the dune to the extent of the model predictions. Because the duration of a storm is a major factor controlling beach and dune erosion, K&D developed an approach to account for the duration effects of storms with respect to the response time scale required to

fully erode a beach profile. The time scale for the erosion of a dune to the extent *R* given by equation 7.2 can be estimated using equation 7.4:

$$T_S = C_1 \frac{H_b^{3/2}}{g^{1/2} A^3} \left(1 + \frac{h_b}{B} + \frac{\beta_f W_b}{h_b}\right)^{-1} \tag{7.4}$$

where $T_S$ is the time scale of response, $C_1$ is an empirical constant (320), $H_b$ is the breaker height, $h_b$ is the breaker depth, $g$ is acceleration due to gravity, $B$ is the berm elevation, $\beta_f$ is the slope of the foreshore, $W_b$ is the surf zone width, and $A$ is the beach profile parameter that defines an equilibrium profile. Using equation 7.4 yields typical response times for complete profile erosion that are on the order of 10 to 100 hours [NHC, 2005]. In general, as the surf zone width increases due to larger wave heights, smaller grain sizes, or gentler slopes, the response time increases. In addition, the response time will increase as the height of the berm increases.

The beach profile response is determined by a convolution integral. According to NHC (2005), the time dependency of the storm hydrograph may be approximated by

$$f(t) = \sin^2\left(\pi \frac{t}{T_D}\right) \text{ for } 0 < t < T_D \tag{7.5}$$

where $t$ is time from the start of the storm and $T_D$ is the storm duration. The convolution integral is

$$DE(t) = \frac{DE_{MAX}}{T_S} \int_0^t f(\tau) e^{-(t-\tau)/T_S} \, d\tau \tag{7.6}$$

which integrates to

$$\frac{DE(t)}{DE_{MAX}} = 0.5 \left\{1 - \frac{\beta^2}{1+\beta^2} \exp\left(-\frac{t}{T_S}\right) - \frac{1}{1+\beta^2}\left[\cos\left(\frac{2\pi t}{T_D}\right) + \beta \sin\left(\frac{2\pi t}{T_D}\right)\right]\right\} \tag{7.7}$$

where $\beta = 2\pi T_S / T_D$ and $DE_{MAX}$ is the maximum potential recession that would occur if the storm duration was infinite. Thus, if the storm duration, $T_D$, is long relative to the time scale of profile response, $T_S$, then a significant portion of the estimated erosion determined by the K&D or geometric model will occur. As the ratio of these two values decreases, the amount of erosion will also decrease. The time required for maximum beach and dune recession is determined by setting the derivative of equation 7.7 to zero and solving for time. This yields

$$\exp\left(-\frac{t_m}{T_D}\right) = \cos\left(\frac{2\pi t_m}{T_S}\right) - \frac{T_D}{2\pi T_S} \sin\left(\frac{2\pi t_m}{T_S}\right) \tag{7.8}$$

in which $t_m$ is the time that the maximum erosion occurs with respect to the beginning of the storm. Unfortunately, this equation can only be solved by approximation or numerically. Thus the maximum recession associated with a duration limited storm can be calculated by

$$\alpha = \frac{DE_m}{DE_{MAX}} = 0.5\left[1 - \cos\left(2\pi\frac{t_m}{T_D}\right)\right] \tag{7.9}$$

where $\alpha$ is the duration reduction factor and $DE_m$ is the maximum recession that occurs for a given storm duration that occurs at time $t_m$. As a result, the duration limited recession is

$$DE_m = \alpha DE_{MAX} \tag{7.10}$$

## 7.2 Erosion Modeling on Lane and Douglas County Beaches

In order to determine the duration reduction factor, α, the duration of each storm event must first be identified. The approach used here involved an analysis of the number of hours a specific TWL event was found to exceed a particular beach profile's beach-dune junction elevation, applying the Ruggiero and others (2001) analysis approach. **Figure 7-3** is an example of the approach we used in our Coos County study, which is based on a script developed in MATLAB. In essence, the blue line is the TWL time series for a particular profile, ±3 days from the event. The script moves backwards and forwards in time from the identified event until the TWL falls below the critical threshold shown as the black line in **Figure 7-3**, which reflects the beach-dune junction elevation. The duration of the storm was then determined as the period where the TWL exceeds the threshold and includes the shoulders of the event (i.e., when the TWL first falls below the critical threshold). This process was undertaken for every storm and for each of the profile sites. One limitation of this approach that was encountered is that it is possible for the duration to be underestimated if the TWL dips below the threshold for an hour or more and then rises again above the threshold, as seen in the example in **Figure 7-3**.

**Figure 7-3. Example plot of the approach used to define storm duration along the Coos County shoreline (Allan and others, 2012b). Note: The red asterisk denotes the location of the storm peak. The blue circles denote the hours when the event exceeded the critical beach-dune junction toe elevation (including the shoulders) that are used to define the "duration" of the event.**

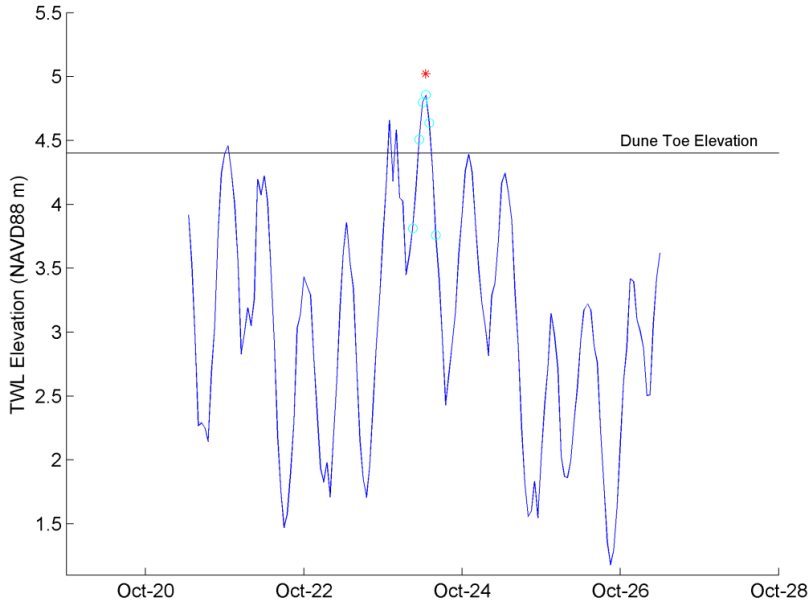

As described previously, the breaker height, $H_b$, was calculated by using equation 6.8, and the breaker depth, $h_b$, was calculated by using a breaker index of 0.78. The berm elevation was established at 3 m (typical for PNW beaches), while the surf zone width, $W_b$, was determined for each breaker depth value by interpolating along a profile line of interest (**Figure 7-4**). Although we have grain size information available that could have been used to define the $A$ parameter for Lane County, the approach we took was to iteritively determine an equilibrium $A$ value based on the actual beach profile data. Here we used the profile data seaward to the 8-m (26.3 ft) water depth, and a range of $A$ values were fit to the data until a value was found that best matched the profile morphology. This approach was adopted for all the profile sites. **Figure 7-5** presents the alongshore varying dune erosion parameters (beach slope, $A$, surf zone width, and breaker depth) calculated for each transect site and averaged over every storm. These data are also summarized in **Table 7-1**.

**Figure 7-4. Example transect from Coos County showing the locations of $h_b$, used to define the cross-shore width ($W_b$) of the surf zone.**

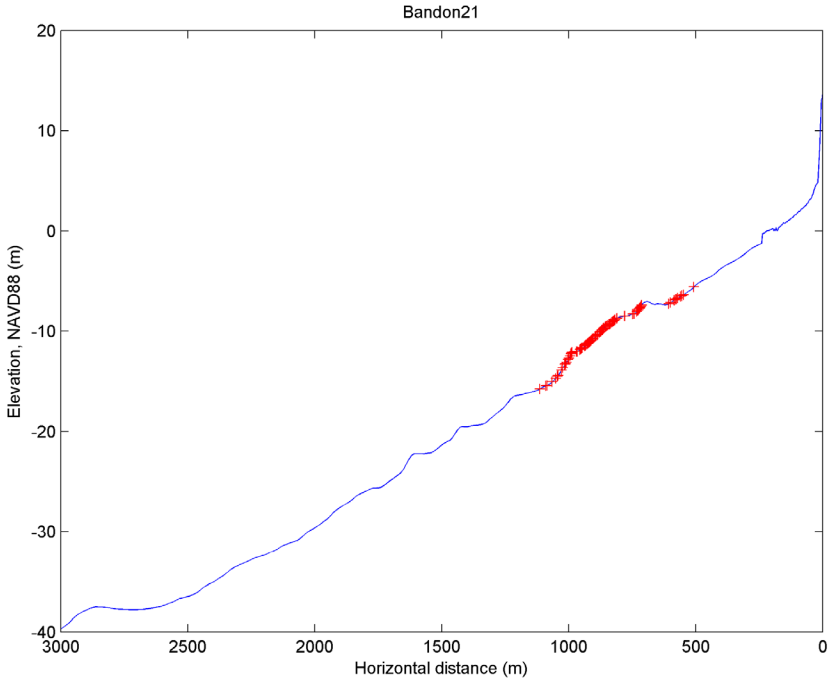


**Figure 7-6** presents the alongshore varying time scale for the erosion of a dune ($T_S$), storm duration ($T_D$), and duration reduction factor ($\alpha$) values determined for those transect sites characterized as "dune-backed" in Lane County. In all cases, we used the surf zone width, breaking depth, and water levels determined at the respective transect site (along with information pertaining to the site's beach-dune morphology) to calculate $T_S$ and $T_D$ for each storm, while the final parameter, $T_m$, was solved numerically using equation 7.8 in order to define the duration reduction factor ($\alpha$). These data have subsequently been averaged for each of the transect locations and are included in **Table 7-1** and presented in **Figure 7-5** and **Figure 7-6**.

**Figure 7-5. Plot showing the dune erosion parameters (tan $\beta$, $A$, $W_b$, and $h_b$) used to calculate the profile responses ($T_S$), storm durations ($T_D$), $\alpha$, and the storm-induced dune erosion. For $W_b$ and $h_b$ we show the mean value and ±1 standard deviation computed using all of the storms.**

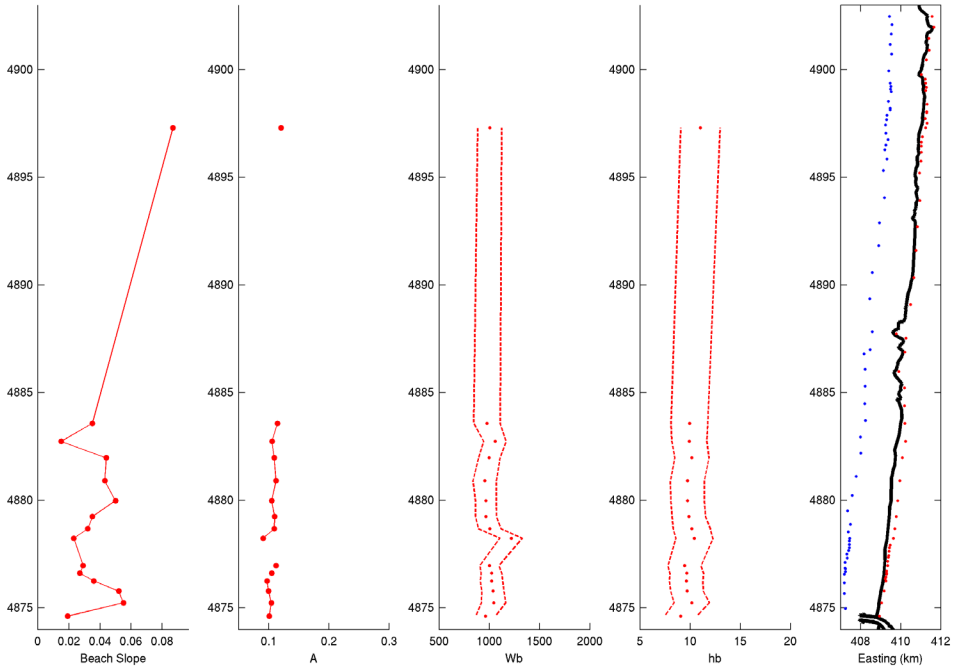


**Figure 7-6. Plot showing the storm duration hours ($T_D$), the calculated time scale of profile response hours ($T_S$), $\alpha$, and the storm-induced K&D and geometric model erosion adjusted using equation 7.10 for the dune-backed profiles along the Lane County shore.**

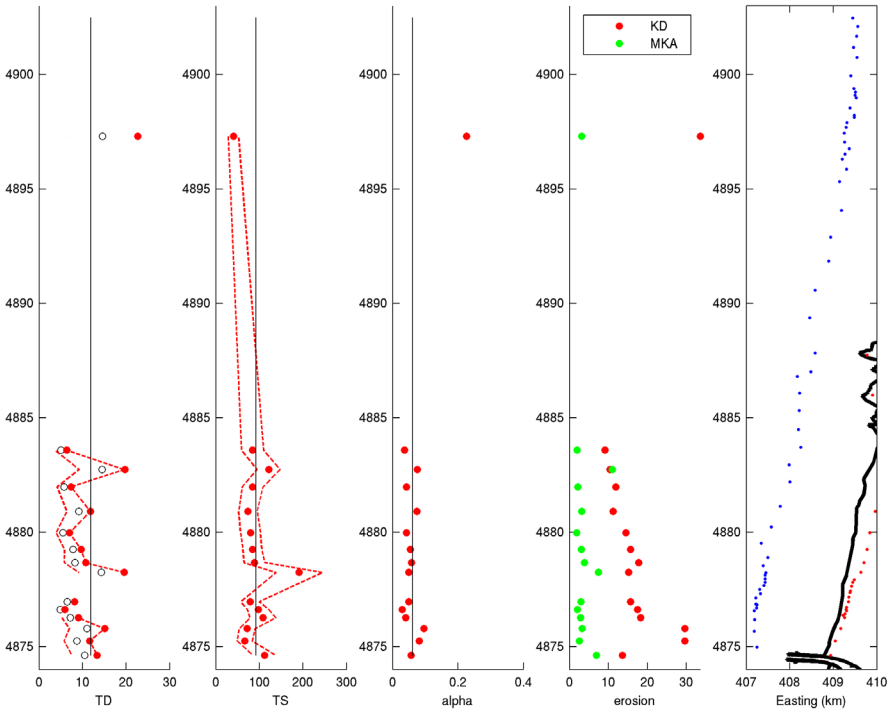

Having defined the duration reduction factor ($\alpha$) for each transect location, the storm-induced erosion was calculated using equation 7.10. As can be seen in **Table 7-1**, calculations of the maximum potential dune erosion ($DE_{MAX}$) using the Komar and others (1999) geometric model yielded results that are considerably smaller than those derived using the Kriebel and Dean (1993) approach. These differences are largely due to the effect of the surf zone width parameter and the low nearshore slopes used in the K&D calculations. Our calculations of storm-induced erosion based on the K&D approach indicated a couple of sites with large estimates of dune erosion (>20 m [65.6 ft]), while the majority of the sites agree well with field-based observations. In contrast, storm-induced erosion estimates based on the duration-reduced maximum potential dune erosion ($DE_{MAX}$) calculated using the geometric model produced negligible erosion responses that made little physical sense. As a result, our final calculation of the storm-induced erosion ($DE_m$) is based on the K&D approach. To reduce the large erosion responses observed at several of the transect sites, we ultimately defined an alongshore averaged duration reduction factor ($\alpha$) of 0.048 (**Table 7-1**), which was used to calculate the storm-induced erosion ($DE_m$) at each of the dune-backed transect sites present along Lane and Douglas County. As can be seen from **Table 7-1**, this resulted in erosion responses that range from a minimum of 9.1 m (30 ft) to as much as 29.5 m (96.8 ft), while the mean storm-induced erosion response is calculated to be 17.5 m (57.4 ft). These results are entirely consistent with actual field observations derived from both GPS beach surveys and from previous analyses of topographic change data measured using lidar (Allan and Harris, 2012; Allan and Stimely, 2013).

**Table 7-1. Calculated storm-induced erosion parameters for dune-backed beaches in Lane and Douglas counties. Note: MKA denotes the geometric model and K&D is the Kriebel and Dean (1993) model.**

| Profiles | Transect (Lane) | *A* | $W_b$ (m) | $T_D$ (hours) | $T_S$ (hours) | $\alpha$ | K&D ($DE_{MAX}$) | MKA ($DE_{MAX}$) | K&D ($DE_m$) | MKA ($DE_m$) |
|---|---|---|---|---|---|---|---|---|---|---|
| Heceta | 1 | 0.101 | 962.457 | 13.333 | 111.730 | 0.057 | 223.709 | 114.315 | 13.597 | 6.948 |
| Beach | 2 | 0.104 | 1,042.379 | 11.623 | 66.697 | 0.081 | 485.673 | 42.404 | 29.520 | 2.577 |
| | 3 | 0.100 | 1,034.940 | 15.069 | 71.866 | 0.096 | 485.472 | 52.392 | 29.508 | 3.184 |
| | 4 | 0.097 | 1,021.822 | 9.039 | 108.431 | 0.040 | 300.032 | 47.295 | 18.236 | 2.875 |
| | 8 | 0.105 | 1,020.799 | 5.918 | 97.134 | 0.030 | 287.139 | 32.811 | 17.453 | 1.994 |
| | 10 | 0.112 | 1,001.313 | 8.173 | 78.606 | 0.050 | 257.662 | 48.958 | 15.661 | 2.976 |
| | 17 | 0.091 | 1,216.568 | 19.540 | 191.372 | 0.049 | 249.736 | 121.098 | 15.179 | 7.361 |
| | 18 | 0.109 | 1,004.686 | 10.718 | 88.655 | 0.057 | 291.561 | 62.781 | 17.722 | 3.816 |
| | 19 | 0.110 | 966.325 | 9.637 | 83.996 | 0.054 | 258.065 | 50.187 | 15.686 | 3.050 |
| | 20 | 0.105 | 965.506 | 7.003 | 79.381 | 0.042 | 238.204 | 29.464 | 14.478 | 1.791 |
| | 21 | 0.112 | 953.405 | 11.783 | 73.824 | 0.074 | 184.549 | 50.900 | 11.217 | 3.094 |
| | 22 | 0.109 | 998.746 | 7.369 | 84.438 | 0.042 | 194.668 | 34.367 | 11.832 | 2.089 |
| | 23 | 0.105 | 1,056.026 | 19.675 | 121.111 | 0.076 | 170.860 | 179.797 | 10.385 | 10.928 |
| | 24 | 0.114 | 976.431 | 6.376 | 84.354 | 0.037 | 150.234 | 32.087 | 9.131 | 1.950 |
| Stonefield | 42 | 0.121 | 1,003.279 | 22.654 | 40.400 | 0.226 | 550.807 | 51.908 | 33.479 | 3.155 |
| Beach | 42_309 | 0.121 | 1,003.279 | 22.654 | 40.400 | 0.226 | 550.807 | 51.908 | 33.479 | 3.155 |
| Summary | | 0.106 | 1,014.979 | 11.861 | 92.133 | 0.061 | 288.558 | 63.384 | 17.539 | 3.853 |

*A* is the beach profile parameter that defines an equilibrium profile; $W_b$ is the surf zone width; $T_D$ is the storm duration; $T_S$ is duration of the response; $\alpha$ is the alongshore averaged duration reduction factor; $DE_{MAX}$ is the maximum potential dune erosion; $DE_m$ is the duration limited erosion.

**Figure 7-7** and **Figure 7-8** provide two examples where the most eroded winter profile is eroded to reflect the storm-induced erosion values identified in **Table 7-1**. The first example is the LD 10 profile site (located at Heceta Beach) where the beach is backed by a prominent foredune. In this example, the calculated duration reduced recession is ~15.7 m (51.5 ft). The location of the beach-dune junction is depicted in **Figure 7-7** by the magenta dot, while the most eroded winter profile is shown as the solid black line. Because the underlying principle of the K&D and geometric models is for the slope to remain constant, the dune is eroded landward by shifting the location of the beach-dune junction landward by 15.7 m (51.5 ft) and upward to its new location where it forms an erosion scarp (**Figure 7-7**). Due to the high dune crest, overtopping does not occur at this location. Furthermore, this site is backed by a marine terrace that provides resistance to erosion once the dune is fully removed. **Figure 7-8** provides an example where dune breaching and overtopping occurs in response to the calculated 1% TWL for the LD 42 profile site located at Stonefield Beach. The calculated dune erosion for LD 42 is ~33.5 m (110 ft). The original location of the beach-dune junction is located at an elevation of ~4.8 m (15.7 ft), **Figure 7-8**, and is shifted upward and landward to its new location depicted by the magenta dot; the most eroded winter profile is shown as the solid black line. As noted by NHC (2005), when dunes are subject to major overtopping events, breaching of the dune typically results in significant lowering of the dune morphology and the development of an overwash fan on the lee side of the dune. Because the present methodologies are unable to account for such responses, NHC recommends that the dune profile is adjusted by extending the most likely winter profile slope to the backside of the dune. This type of adjustment is demonstrated in **Figure 7-8** where the entire foredune is assumed to be eroded and removed as a result of a major storm.

Unfortunately, there are no measured examples of the type of response depicted in **Figure 7-8** for the Lane County area against which to make comparisons. However, monitoring of beaches by DOGAMI on the Oregon coast provides some suggestion that this approach is probably reasonable. **Figure 7-9** is an example of beach profile changes measured along a barrier beach adjacent to Garrison Lake, Port Orford, located south of Bandon. In this example, the barrier beach, which has a crest elevation of 8-9 m NAVD88 (26–29 ft), is known to have been overtopped during several major storms in February-March 1999 (**Figure 7-10**) (Allan and others, 2003). Analyses of the mean shoreline position at this site indicate that changes in the morphology of the beach are controlled primarily by the occurrence of these major storms as well as by El Niño climate events that result in hotspot erosion. Examination of the beach profile changes along the Garrison Lake shore indicate that during major events characterized by overtopping, the crest of the barrier beach is lowered, with some of the eroded sand carried landward where the sand forms washover fans, while the bulk is removed seaward to form sand bars. Ultimately, though, any dune located at the back of the profile is removed entirely, as the barrier rolls landward, consistent with the response depicted in **Figure 7-8**.

**Figure 7-7. Application of the duration reduced erosion estimate to the Most Likely Winter Profile (MLWP) at the LD 10 transect. The location of the beach-dune junction is depicted by the magenta dot, while the most eroded winter profile is shown as the solid black line. TWL is the calculated total water level, MLLW is mean lower low water, and MHHW is mean higher high water.**

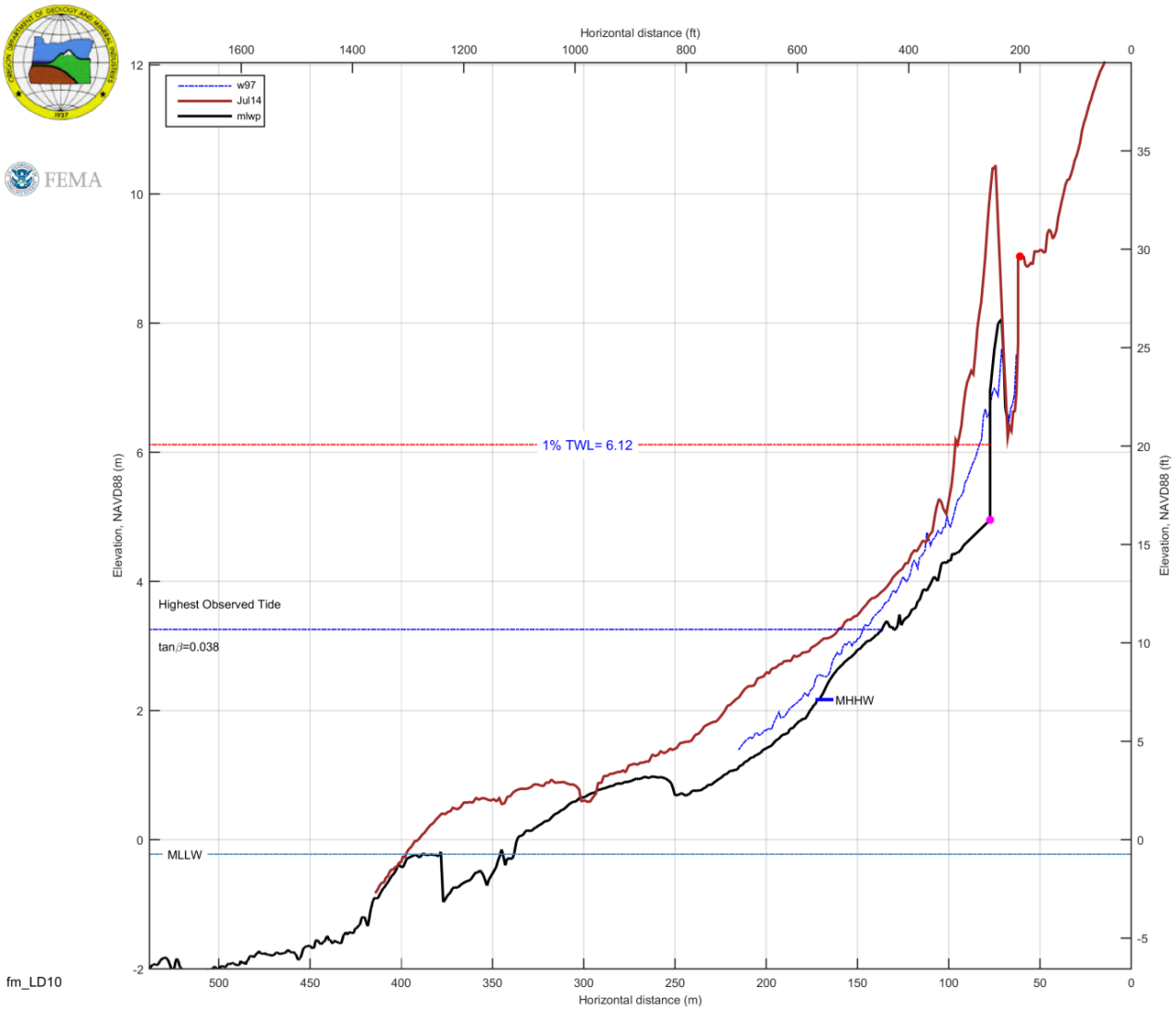

**Figure 7-8. Application of the duration reduced erosion estimate to the Most Likely Winter Profile (MLWP) at LD 42 where overtopping and breaching occurs. The location of the beach-dune junction is depicted by the magenta dot; the most eroded winter profile is shown as the solid black line. TWL is the calculated total water level, MLLW is mean lower low water, and MHHW is mean higher high water.**

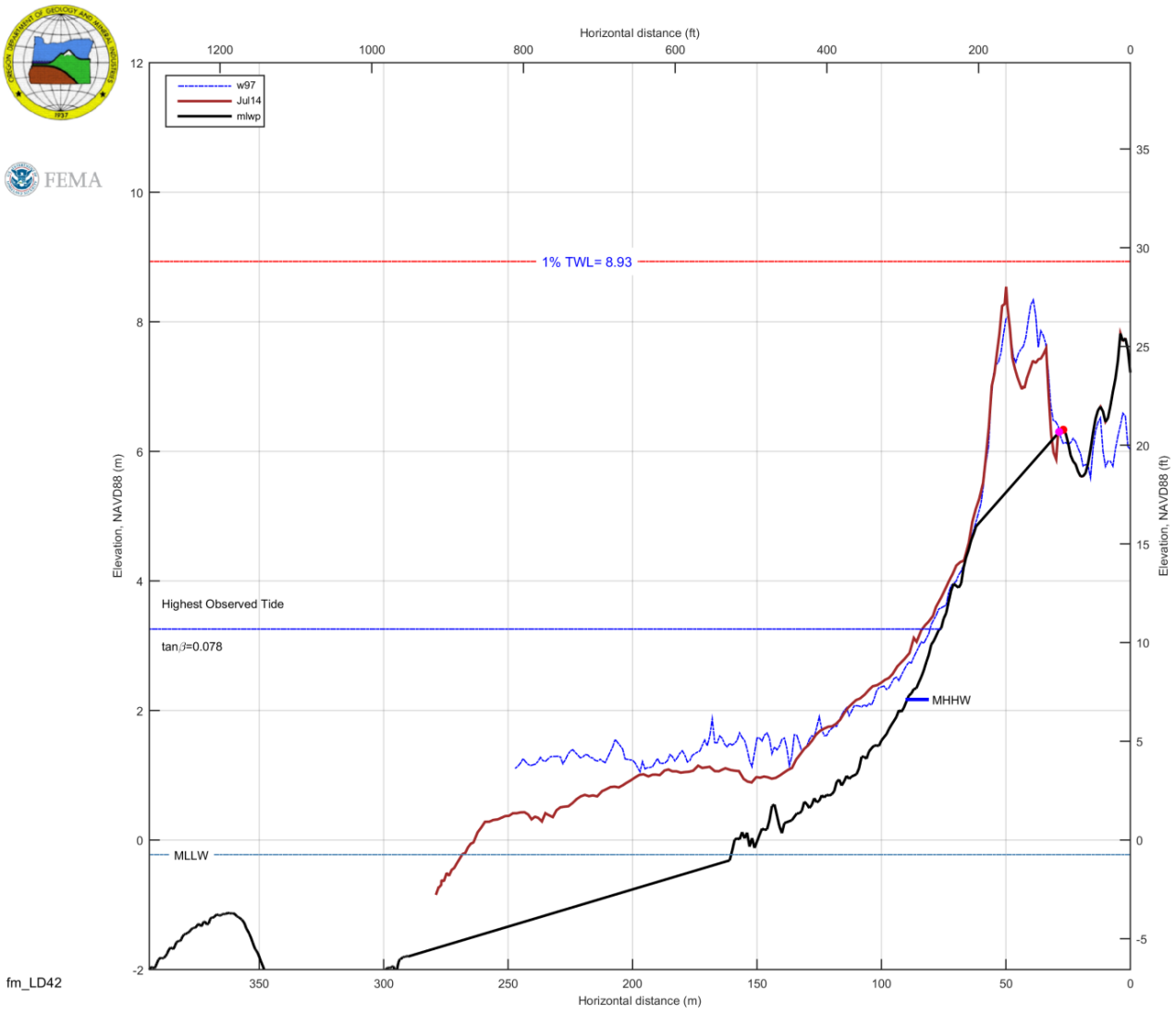

**Figure 7-9. Example profile where a barrier beach is overtopped and eroded. This example is based on measured beach profile changes at Garrison Lake, Port Orford on the southern Oregon coast. The 1967 morphology was derived from Oregon Department of Transportation surveys of the beach on September 25, 1967, used to define the Oregon statutory vegetation line.**

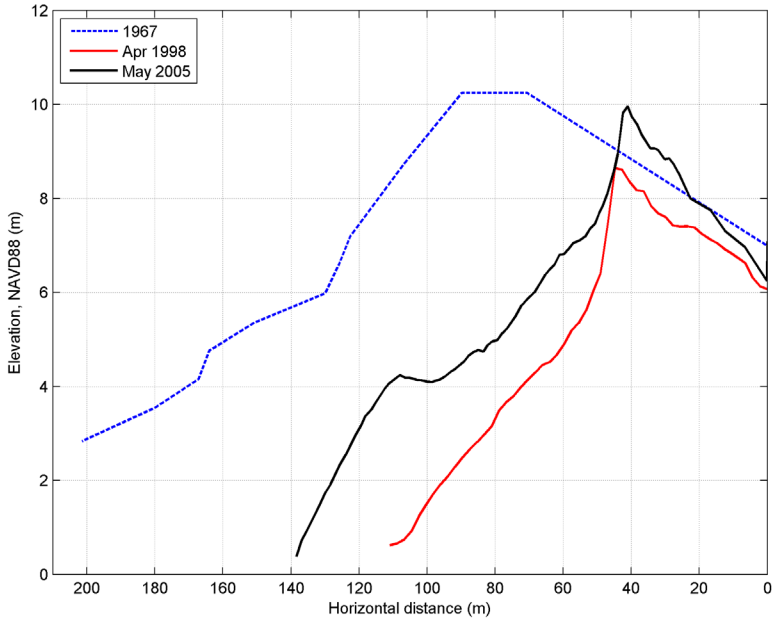


**Figure 7-10. Overtopping of the barrier beach adjacent to Garrison Lake during a major storm on February 16, 1999 (photo courtesy of a resident at Port Orford).**

# 8.0 FLOOD MAPPING

## 8.1 Detailed Coastal Zone VE Flood Zone Mapping

Detailed mapping of the 1% chance flood event within selected areas of Lane and Douglas County was performed using two contrasting approaches, controlled ultimately by the geomorphology of the beach and backshore. In all cases we followed the methods described in section D.4.9 in the final draft guidelines of the Coastal Flood Hazard Analysis and Mapping for the Pacific Coast of the United States (NHC, 2005). Due to the complexities of each mapping approach for the 0.1% chance flood event, it was not possible to reasonably map the 0.2% chance event. The reasons for this are described in more detail in the following sections.

### 8.1.1 Bluff-backed beaches

For bluff-backed beaches the total water level (TWL) values calculated in **SECTION 6.3** were extended into the bluff. The first step involved identifying specific contours of interest, which were extracted from the 1-m resolution bare-earth lidar grid DEM (surveyed in 2009). For the bluff-backed beaches the landward extent of the coastal Zone VE is defined by the contour representing the TWL elevation calculated for each of the represented detailed surveyed transects (e.g., **Figure 8-1** and **Table 6-2**). FEMA Operating Guidance 9-13 (2013) dictates that areas near the landward extent of Zone VE, where the difference between the TWL and ground elevation are less than 3 feet, be designated as Zone AE. However, due to the steepness of the shoreline along bluff-backed beaches such areas are too thin in Lane and Douglas County to be visible at the prescribed map scale; therefore Zone AE was not designated in these environments.

To define the velocity zones between transects, we used professional judgment to establish appropriate zone breaks between the transects. For example, along-shore geomorphic barriers were identified within which the transect TWL value is valid (**Figure 8-2**). Slope and hillshade derivatives of the lidar DEM, as well as 1-m orthophotos (acquired in 2009), provided the base reference. An effort was made to orient zone breaks perpendicular to the beach at the location of the geomorphic barrier. The seaward extent for the majority of Zone VE were inherited from the preliminary DFIRM (2011). In some cases adopting the effective extent produced inconsistent zone widths (too thin) and the boundaries were subsequently extended seaward.

**Figure 8-1. Example of a bluff-backed beach (LD 35) where the calculated total water level (TWL) and defined velocity (VE) zone extends into the bluff. The location of the beach-dune junction is depicted by the magenta dot; the most eroded winter profile is shown as the solid black line. MLLW is mean lower low water, MHHW is mean higher high water.**

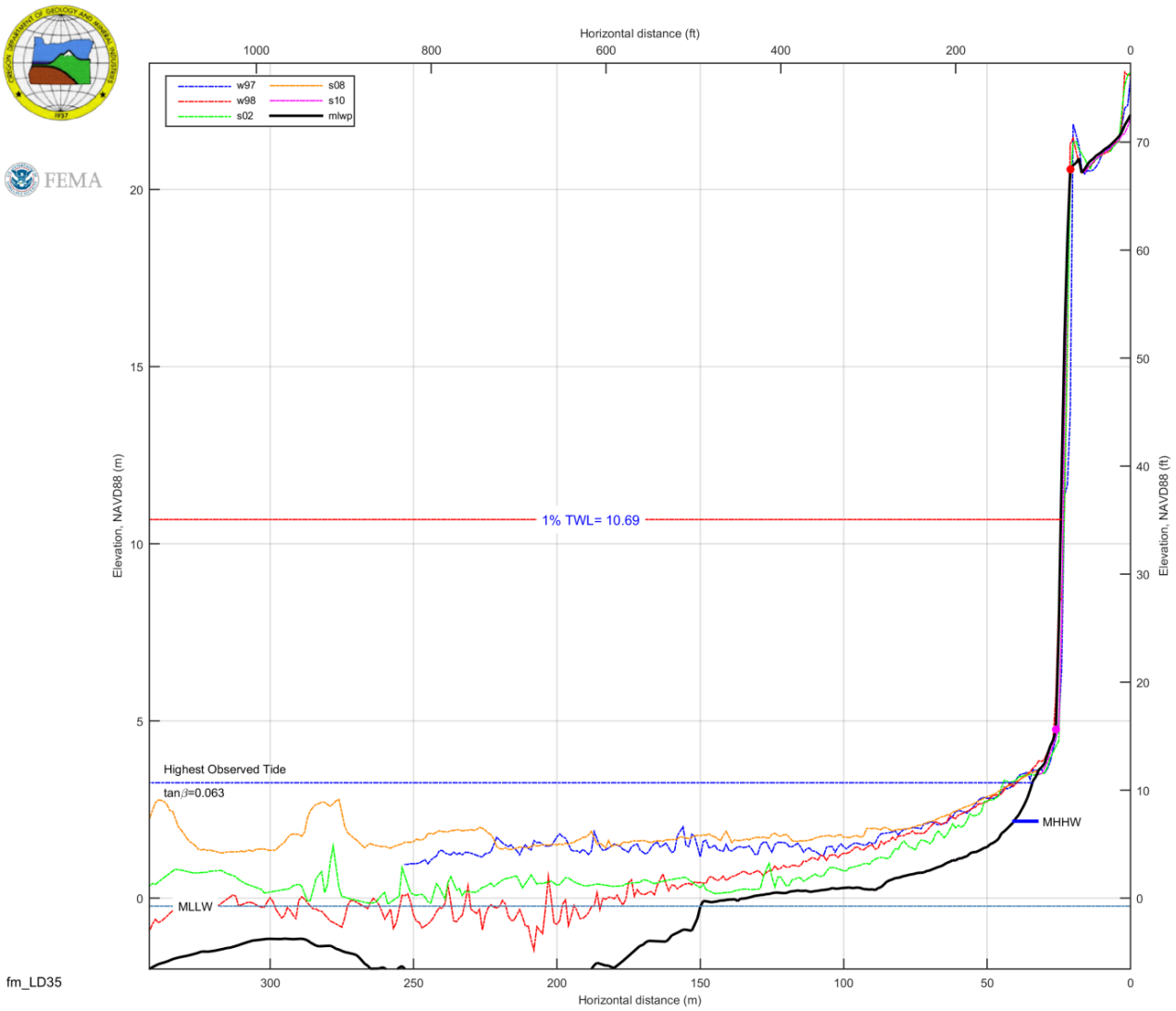

**Figure 8-2. Example of along-shore zone breaks and their relationship to geomorphic barriers and surveyed transects near Cummins Creek, Lane County, Oregon. Surveyed transects are symbolized as yellow lines; zone breaks are solid black lines.**

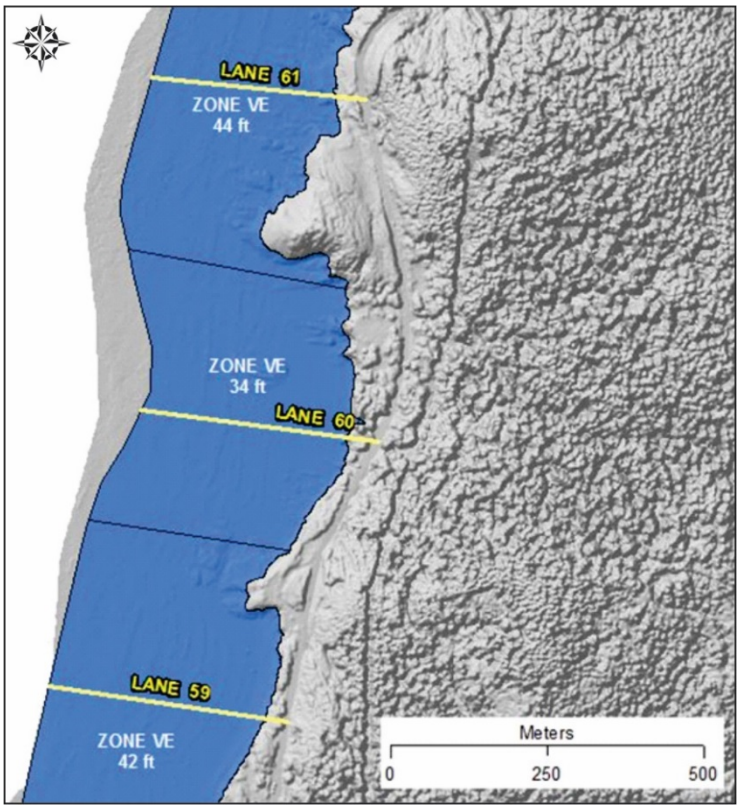


### 8.1.2 Dune-backed beaches

For dune-backed beaches, the VE flood zone was determined according to one or more criteria specified in the NHC (2005) guidelines. These are:

1. The ***wave runup zone***, which occurs where the TWL exceeds the (eroded) ground profile by ≥ 0.91 m (3 ft);
2. The ***wave overtopping splash zone*** is the area landward of the dune/bluff/structure crest where splashover occurs. The landward limit of the splash zone is only mapped in cases where the wave runup exceeds the crest elevation by ≥ 0.91 m (3 ft);
3. The ***high-velocity flow zone*** occurs landward of the overtopping splash zone, where the product of flow times the flow velocity squared ($hV^2$) is ≥ 5.7 $m^3/s^2$ (or 200 $ft^3/s^2$);
4. The ***breaking wave height zone*** occurs where wave heights ≥ 0.91 m (3 ft) could occur and is mapped when the wave crest profile is 0.64 m (2.1 ft) or more above the static water elevation; and,
5. The ***primary frontal dune (PFD) zone*** as defined in Part 44 of the U.S. Code of Federal Regulations, Section 59.1; FEMA Coastal Hazard Bulletin, No. 15.

**Table 6-3** lists the overtopping calculations for those transects where overtopping occurs, including the calculated splashdown distances ($Y_{G\ outer}$), bore height associated with wave overtopping ($h_o$), and the landward extent of the high-velocity flow ($hV^2$) where the flows approach 5.7 $m^3/s^2$ (or 200 $ft^3/s^2$). As noted above, $hV^2$ reflects the farthest point landward of the dune/bluff/structure crest that experiences coastal flooding due to overtopping and is ultimately controlled by the extent of the landward flow where it approaches 5.7 $m^3/s^2$ (or 200 $ft^3/s^2$); values greater than 5.7 $m^3/s^2$ (or 200 $ft^3/s^2$) are located within the high-velocity flow (VE) zone, while lower values are located within the passive overland flooding (AE) zone. Included in **Table 6-3** are the transition zones in which the calculated bore decreases in height, which have been defined accordingly:

- Dist_3 identifies the landward extent of flood zones where the bore height ($h_o$) was determined to be ≥ 0.91 m (3 ft) and were ultimately rounded up to the nearest whole foot (i.e., having an elevation of 0.91 m (3 ft) above the land surface);
- Dist_2 identifies the landward extent of flood zones where the bore height ($h_o$) was determined to be between 0.61 and 0.91 m (2 and 3 ft high) and were ultimately rounded up to the nearest whole foot above the ground surface; and,
- "Dist_1" marks the seaward extent of flood zones where the bore height falls below 0.3 m (1 ft) above the ground surface; these values were ultimately rounded up to the nearest whole foot.

Areas where flood zones exhibited bore height elevations of 0.61 m (2 ft) above the land surface were inferred as existing in the area between the two previously described regions (i.e., between "Distance from "x" Where Bore > 2 < 3 ft" and "Distance from "x" Where Bore < 1").

As for bluff-backed beaches, professional judgment was used to establish appropriate zone breaks between the detailed transects. This was achieved through a combination of having detailed topographic information of the backshore and from knowledge of the local geomorphology. Some interpretation was required to produce flood zones appropriate for the printed map scale. Elevations were identified from the 1-m resolution bare earth lidar DEM to aid in establishing zone breaks due to changes in flood depth landward of the dune crest (**Figure 8-3**). Slope and hillshade derivatives of the lidar DEM, as well as 1-m orthophotos, provided base reference.

In overtopping splash situations, the flood zone was determined by adding the splashdown distances ($Y_{G\ outer}$) to the $D_{high}$ distance. For all overtopping splash situations on the Lane County coast, the splash distance was very short and not distinguishable at a mapping scale. Therefore, it was added to the VE zone extent (**Figure 8-4**).

For flood zones seaward of the dune crest, the calculated TWL values were used. As with the bluff-backed beaches, along-shore geomorphic barriers were identified within which the transect TWL value is valid. In all cases, an effort was made to orient zone breaks perpendicular to the beach at the location of the geomorphic barrier. The seaward extent of the flood zones were inherited from the preliminary DFIRM (2011).

The PFD is defined (FEMA, 2006) as "a continuous or nearly continuous mound or ridge of sand with relatively steep seaward and landward slopes immediately landward and adjacent to the beach and subject to erosion and overtopping from high tides and waves during major coastal storms. The inland limit of the primary frontal dune [also known as the toe or heel of the dune] occurs at a point where there is a distinct change from a relatively steep slope to a relatively mild slope." The PFD toe represents the landward extension of the Zone VE coastal high hazard velocity zone (Part 44 of the U.S. Code of Federal Regulations, Section 59.1; FEMA Coastal Hazard Bulletin 15).

**Figure 8-3. Overtopping along the LANE 34 transect (at Big Creek), where *Dhigh* is the area seaward of $D_{high}$ distance, Splash is the splashdown distance, D3 is depth > 3 ft, D2 is depth > 2 < 3 ft, D1 is depth ≤ 0.31 m, and $HV^2$ is flow < 5.7 $m^3/s^2$ (or 200 $ft^3/s^2$). Zone breaks are solid black lines. Dark blue flood zones are VE zones; light blue zone is the AE zone.**

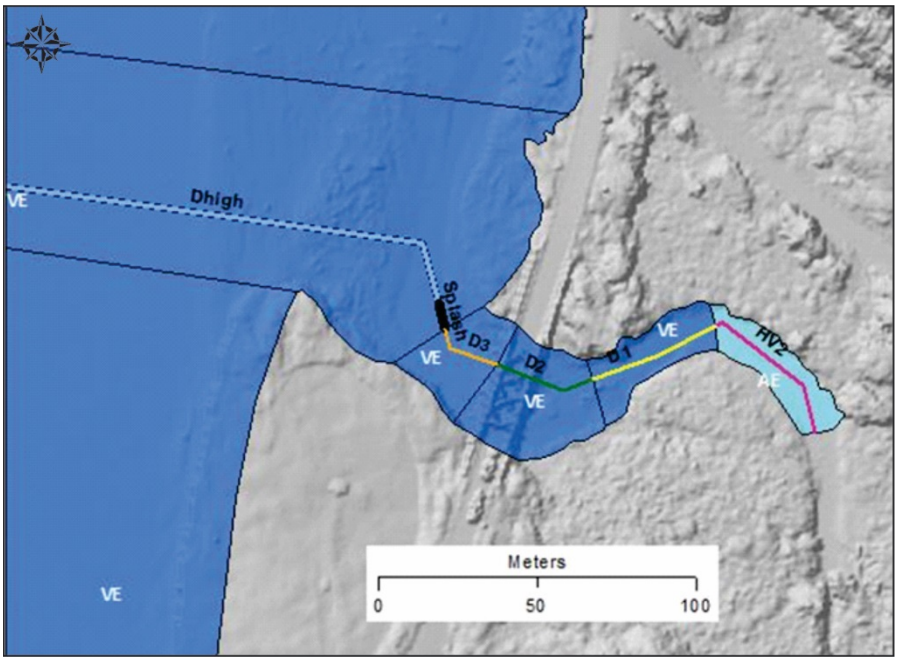


**Figure 8-4. LANE 48 transect at Stonefield Beach with overtopping Splash zone. The short splash zone distance (black) was added to the extent of Zone VE.**

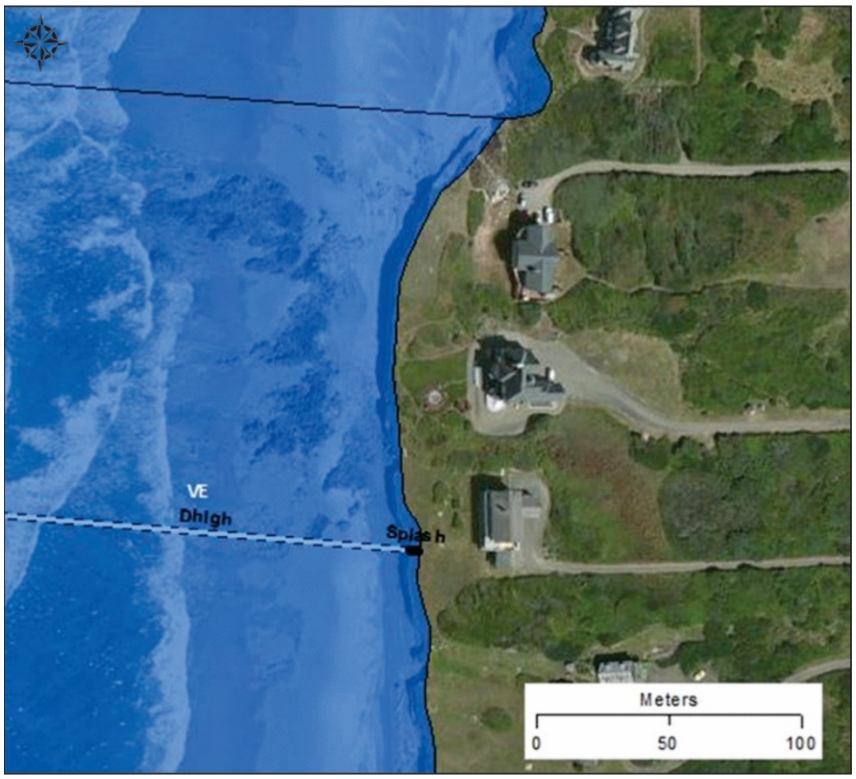

The approach developed by DOGAMI to define the morphology of the beach and dune system, including the location of the PFD, followed procedures developed in our Coos Bay study (Allan and others, 2012b) and was based on detailed analyses of lidar data measured by the USGS/NASA/NOAA in 1997, 1998, and 2002; by DOGAMI in 2009; and by the USACE in 1010. However, because the lidar data acquired by the USGS/NASA/NOAA and USACE are of relatively poor resolution (~1 point/$m^2$) and reflect a single return (i.e., vegetation included where present), whereas the lidar data acquired by DOGAMI have a higher resolution (8 points/$m^2$) and were characterized by multiple returns, enabling the development of a bare-earth DEM, determination of the PFD was based entirely on analysis of the 2009 lidar data.

Lidar data flown in 1997, 1998, 2002, and 2010 were downloaded from NOAA's Coastal Service Center[12], and gridded in ArcGIS using a triangulated irregular network (TIN) algorithm (Allan and Harris, 2012). Transects spaced 20 m apart were cast for the full length of the county coastline using the Digital Shoreline Analysis System (DSAS) developed by the USGS (Thieler and others, 2009); this process yielded 3,453 individual transects throughout Lane and Douglas County. For each transect, *xyz* values for the 1997, 1998, 2002, 2009, and 2010 lidar data were extracted at 1-m intervals along each transect line and were saved as a text file using a customized ArcGIS script.

Processing of the lidar data was undertaken in MATLAB using a beach profile analysis script developed by DOGAMI. This script requires the user to interactively define various morphological features including the dune/bluff/structure crest/top, bluff/structure slope, landward edge of the PFD(s), beach-dune junction elevations for various years, and the slopes of the beach foreshore (Allan and Harris, 2012). Although we evaluated all 3,453 transects, not all morphological features were applicable and therefore the PFD could be defined for only a subset of transects. **Figure 8-5** provides an example from Lane County #1044 located at the north end of Heceta Beach (adjacent to Heceta Head). In this example, the dune crest in 2009 is located at 18.4 m (60.5 ft); the dune crest has grown vertically ~2 m (6 ft) since 1997. As can be seen from the figure, the seaward face of the dune has accreted ~6.5 m (21.3 ft) since 1997; shoreline change (erosion/accretion) was determined based on the change in position of the 6 m (19.7 ft) contour elevation, which is an excellent proxy for determining the effects of storm erosion (Allan and others, 2003). **Figure 3-9** to **Figure 3-11** show changes in the position of the 6-m (19.6 ft) contour along the length of the Lane and Douglas County shoreline. As can be seen from the figures, erosion hazards are confined primarily to southern Lane and Douglas County (**Figure 3-11**). In contrast, accretion dominates the area on both sides of the mouth of the Siuslaw River and along Heceta Beach to the north.

[12] http://www.csc.noaa.gov/digitalcoast/data/coastallidar/index.html

**Figure 8-5. Example beach profile (#1044) located at the north end of Heceta Beach (adjacent to Heceta Head) and derived from 1997, 1998, 2002, 2009, and 2010 lidar data. $E_j$ is the dune-dune junction characterized by the colored circles seaward of the dune; S is the beach slope.**

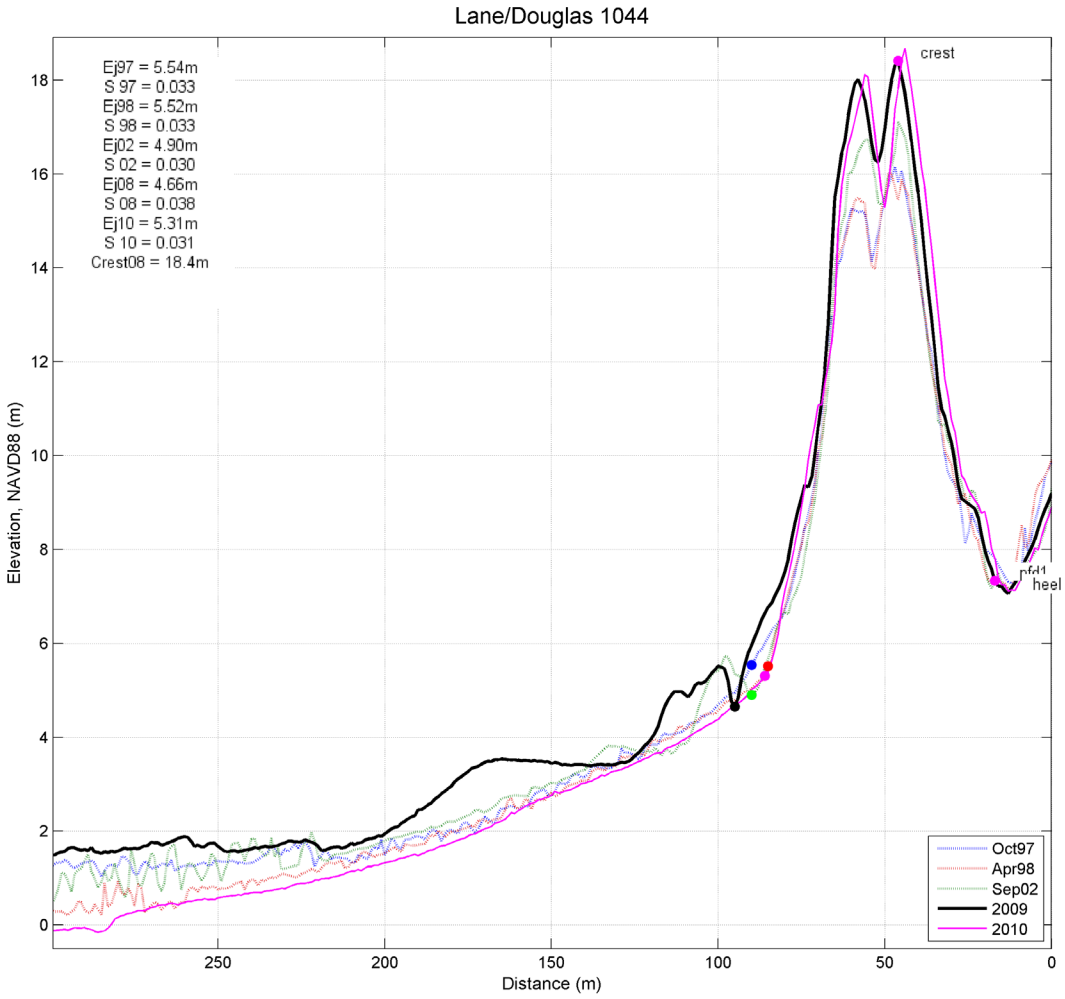


Having interpolated the lidar transect data in order to define the morphological parameters, the actual locations of the PFDs[13] were subsequently plotted in ArcGIS and overlaid on both current and historical aerial photos of the county and on shaded relief derived from the 2009 lidar. In a number of locations the PFD was found to be located either farther landward or seaward relative to adjacent PFD locations. This response is entirely a function of the degree to which the morphology of foredunes varies along a coast, and, further, of the ambiguity of the FEMA's PFD definition (see above). Our observations of the PFD approach highlighted a number of uncertainties, including:

1) There were numerous examples of smaller dune features that have begun to develop in front of a main dune (or are the product of erosion of the dune). These features may yet attain dimensions and volumes where they would be considered established dunes, or the features may erode and disappear entirely. However, the PFD approach does not adequately account for such features. In this example, the smaller dunes are almost certainly subject to erosion and periodic overtopping

[13] In many cases, multiple PFD locations were defined along a single transect.

and have morphologies that resemble the FEMA PFD definition. However, because they are subject to short-term erosion responses, they are more ephemeral in nature and thus it is debatable whether they should be defined as PFDs. Furthermore, over the life of a typical map (~10 years) these dunes could be eroded and removed entirely, leaving a "gap" between the original polygon boundary and the eroding dune. For example, from repeated observations of beach profile transects on the northern Oregon coast, single storm events have been documented to remove as much as 9 to 25 m (30–82 ft) of the dune (Allan and Hart, 2007, 2008);

2) The PFD does not adequately account for a large established foredune, where the dune may have attained heights of 10 to 15 m (33–49 ft), with cross-shore dimensions on the order of 100 to 200 m (328–656 ft) wide due to prolonged aggradation and progradation of the beach. In this example, although there may be a clear landward heel located well inland away from the beach (e.g., profile #840 in **Figure 8-6**, which was derived from our Clatsop County study), the PFD is clearly not subject to "frequent" wave overtopping due to its height and erosion (because of its large volume of sand). Defining the PFD at the location of the heel is consistent within the definition provided by FEMA but would almost certainly generate a very conservative V-zone.
3) Although numerous transects exhibited clear examples of single PFD locations, many others were characterized by more than one PFD. Profile #1120 (**Figure 8-7**) is an example where multiple potential PFDs could be defined.

To account for these variations and uncertainties, the PFD shown on the profile plots (e.g., **Figure 8-5** to **Figure 8-7**) were re-examined and adjustments were made where necessary in order to define a single PFD line. For example, in a few locations along the Lane and Douglas County coastline, the PFD extent for a particular transect was physically moved so that it was more in keeping with the adjacent PFD locations to its immediate north and south, and the overall terrain derived from the lidar data. **Figure 8-8** presents the final PFD designation for a small section of coast, immediately south of the Siuslaw River. As can be seen from the figure, the final designation was invariably based on the clearest dune morphology signal determined from all available data and adhering best to the FEMA definition.

The PFD was defined at a number of locations where significant human modification has occurred on the dune. In these areas, the natural dune system has been severely impacted and the PFD line does not represent a natural dune system.

**Figure 8-6. Example profile from the Clatsop Plains where considerable aggradation and progradation of the dune has occurred. In this example, the primary frontal dune (PFD) could conceivably be drawn at a variety of locations and meet the FEMA definition.**

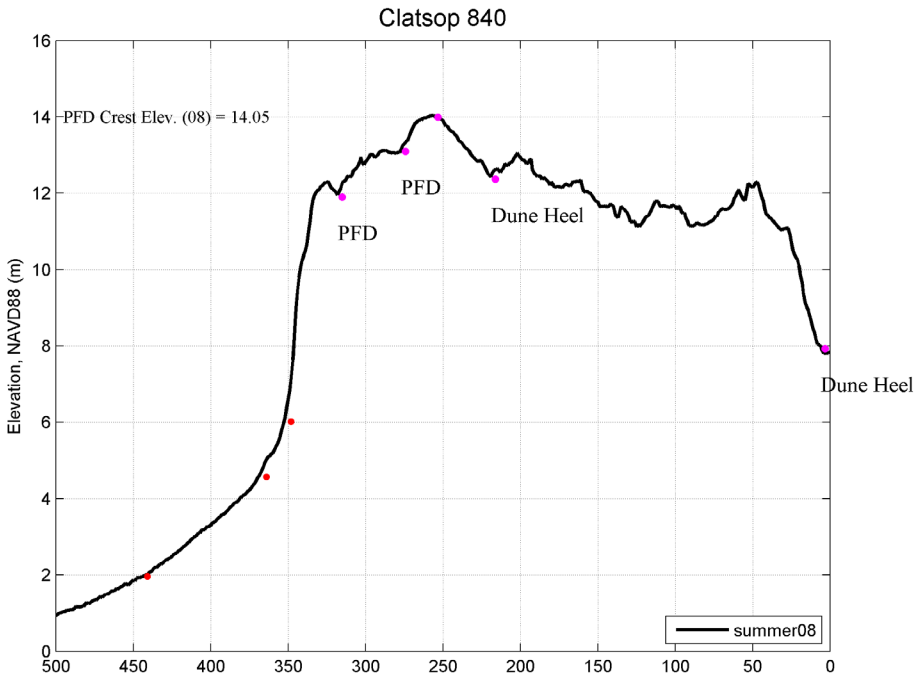

**Figure 8-7. Example profile (#1120) from Heceta Beach showing the presence of at least two primary frontal dune (PFD) locations (pdf1 and pdf2). $E_j$ is the dune-dune junction characterized by the colored circles seaward of the dune; S is the beach slope.**

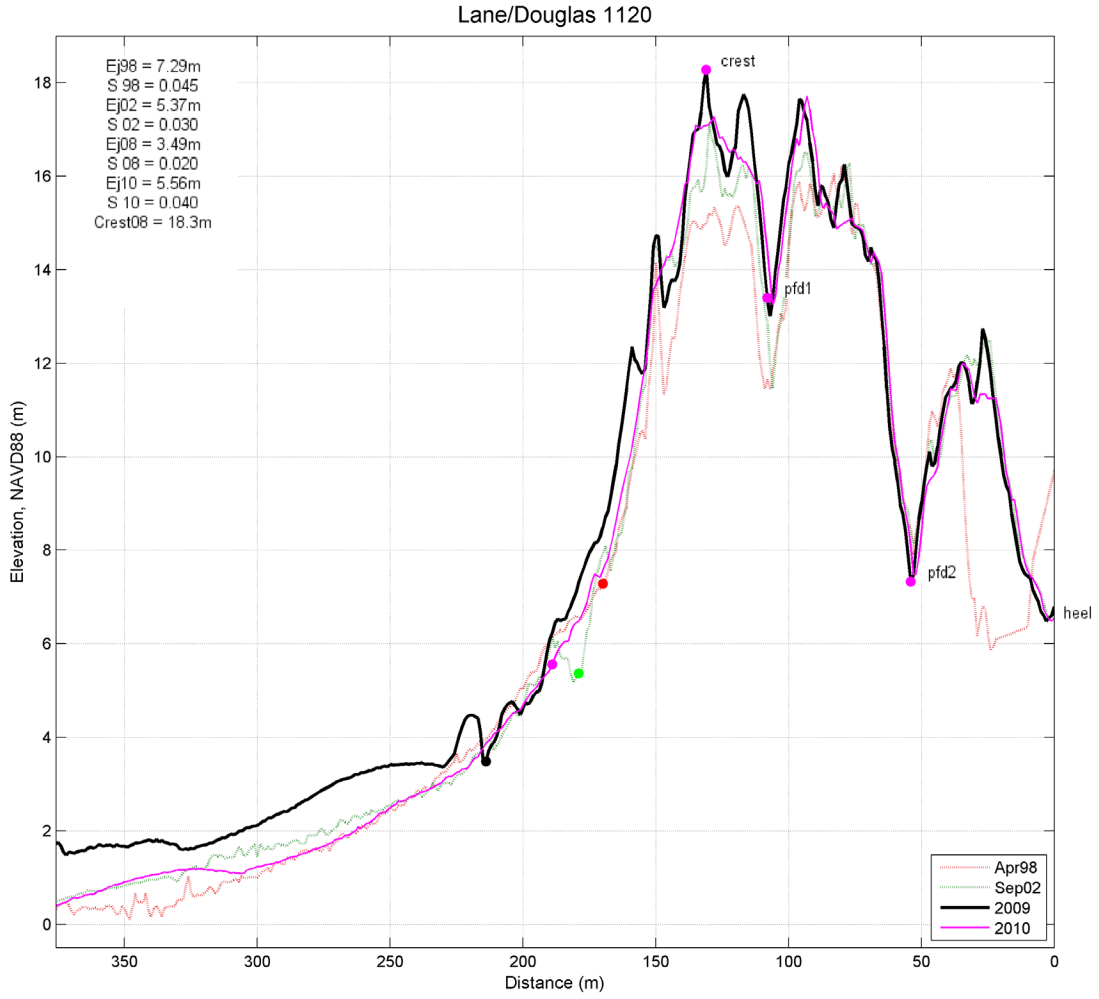

**Figure 8-8. Plot for a small section of Oregon coast, immediately south of the Siuslaw River, Lane County, Oregon, showing identified primary frontal dune (PFD) locations (yellow dots) along each transect, landward most dune heel (pink line), and derived PFD line (dashed black/white line). Red zone depicts the VE zone having accounted for all possible criteria. Gray lines depict the locations of the lidar transects, which were spaced 20 m (65.6 ft) apart.**

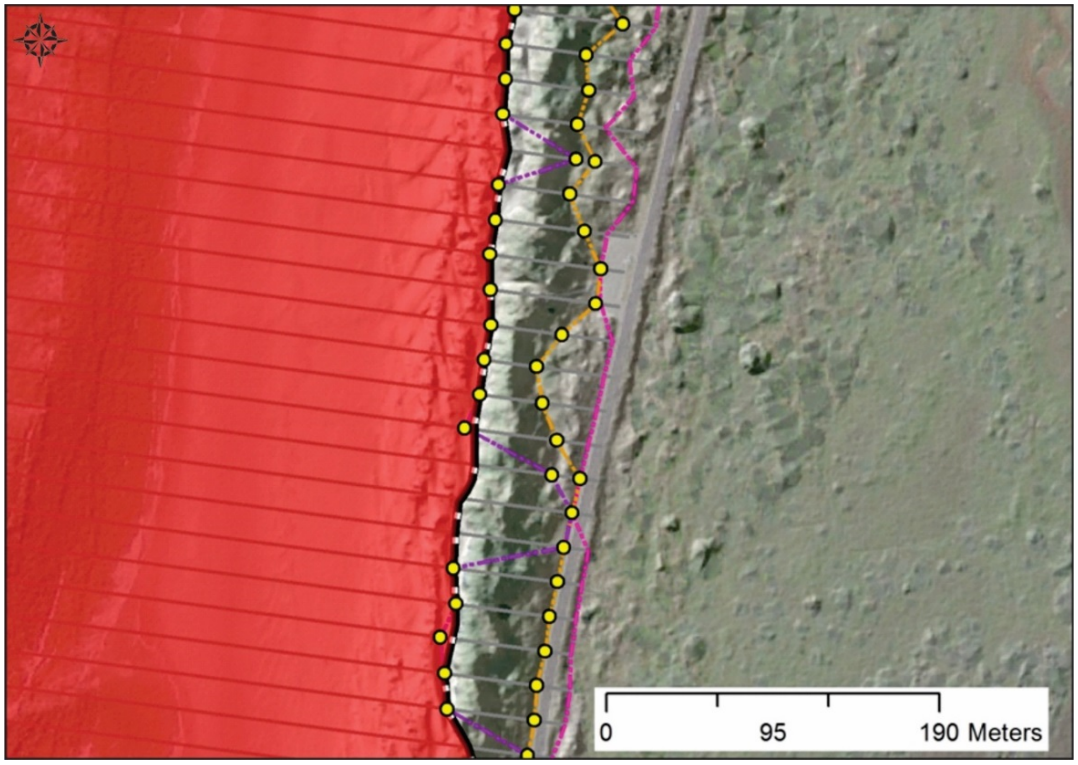

### 8.1.3 Mapping of estuarine flooding

Lane and Douglas counties include several estuarine features. They were mapped using the still water level (SWL) or redelineated from the effective BFE.

Due to its complexity, the Siuslaw River mouth in Lane County was redelineated using the previously effective BFE (**Figure 8-9**). No new study was performed at this location, and the adjacent open coast detailed coastal analysis could not reasonably be used for mapping this estuary.

At the Umpqua River mouth in Douglas County we used the SWL to map the coastal backwater effect of the 1% and 0.2% flood events. The Umpqua River mouth is a complex estuary. However, mapping the SWL was considered to be the best option because it was only 0.1 ft different from the effective BFE. Procedures for developing the SWL are described in **SECTION 4.6**. The 1% SWL value for Lane and Douglas County is 3.47 m (11.4 ft, NAVD88) and the 0.2% SWL is estimated to be 3.67m (11.7ft NAVD88).

The mouths of the Siltcoos River and Tahkenitch Creek had not previously been subjected to detailed coastal or riverine analyses. These particular estuaries are periodically influenced by coastal backwater flooding due to extreme coastal water levels, and so they were also mapped using the SWL (**Figure 8-10**).

**Figure 8-9. Detailed redelineation on the lower Siuslaw River.**

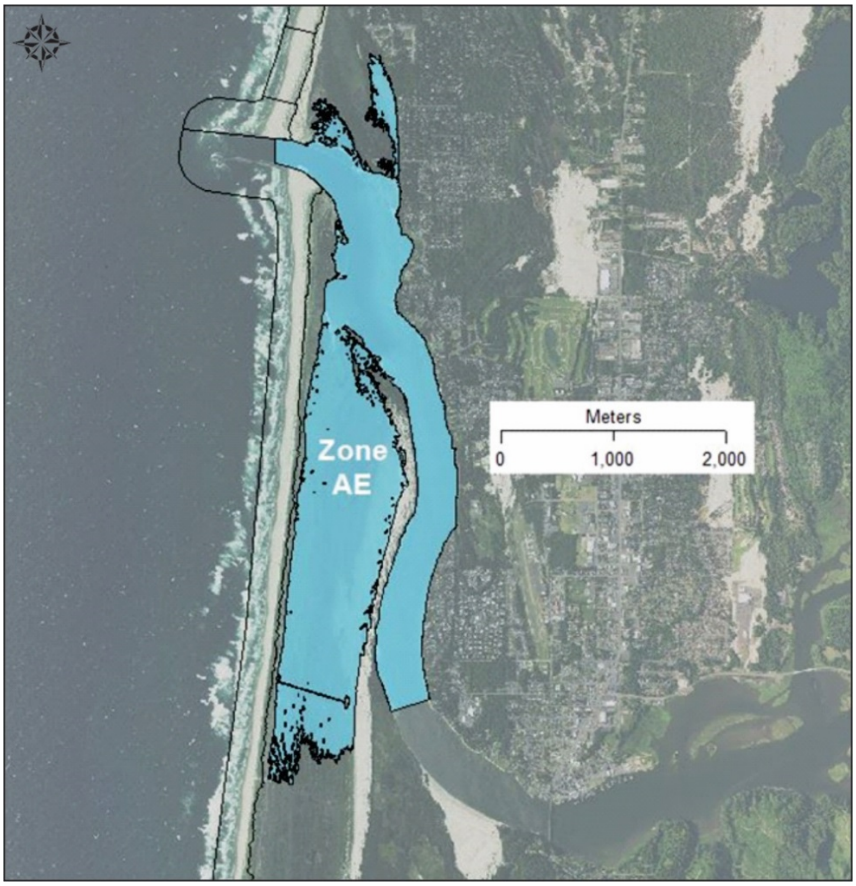

**Figure 8-10. Coastal backwater flooding mapped from still water levels (SWLs) for the Siltcoos River. The 0.2% chance flooding is visible in green at the upstream end of the reach.**

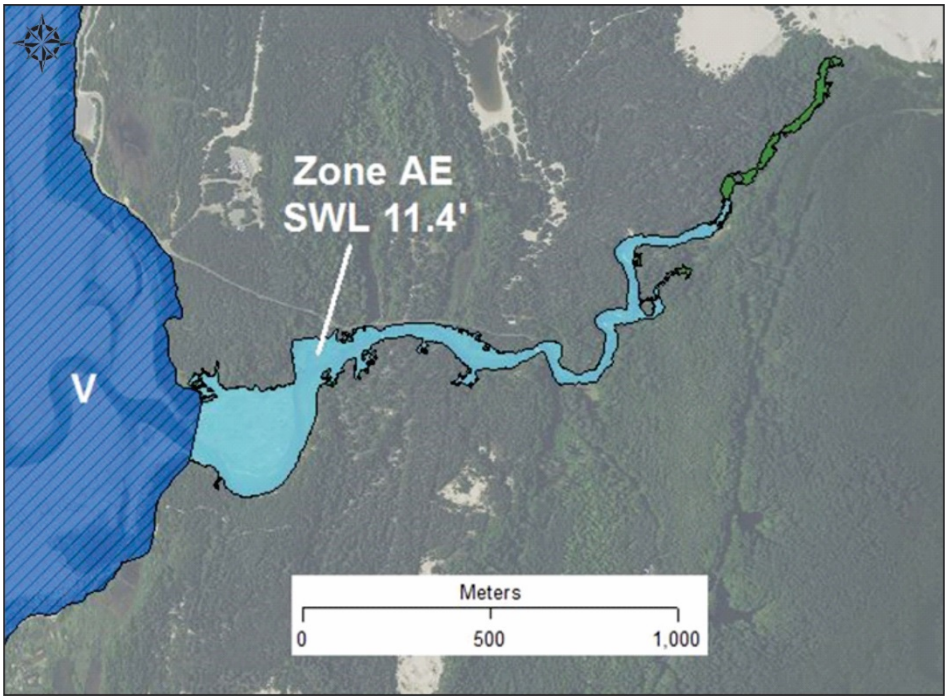


## 8.2 Coastal V-Zone Mapping along the Lane and Douglas County Shoreline

### 8.2.1 Dune-backed beaches

The FEMA guidelines provide little direct guidance for mapping approximate coastal velocity zones (Zone V) in areas where no detailed studies have occurred, other than by defining the location of the PFD, using the methodology described above. In the case of Lane and Douglas County, we have endeavored to undertake detailed mapping in all areas backed by dunes.

### 8.2.2 V-Zone mapping on coastal bluffs and headlands

Several sections of the Lane County coastline are characterized by coastal bluffs and cliffs of varying heights. For these areas, the approach adopted by DOGAMI was to calculate the 1% TWLs using the approaches described in **SECTIONS 3** to **6**.

# 9.0 ACKNOWLEDGMENTS

Funding for this study was provided by the Federal Emergency Management Agency as part of the Flood Map Modernization program under Cooperating Technical Partner award EMS-2011-GR-0013. We are grateful to Dr. Bill McDougal for his technical advice throughout this project. We would especially like to acknowledge Dr. Paul Komar and Mr. Bob Houston for their thoughtful review and comments on the report.

# 10.0 REFERENCES


Aguilar-Tunon, N.A., and Komar, P.D., 1978, The annual cycle of profile changes of two Oregon beaches: Ore Bin, v. 40, no. 2, p. 25–39. http://www.oregongeology.org/pubs/og/OBv40n02.pdf

Allan, J.C., and Harris, E.L., 2012, An "expanded" geospatial database of beach and bluff morphology determined from lidar data collected on the northern Oregon coast; Tillamook to Clatsop County: Oregon Department of Geology and Mineral Industries Open-File Report O-12-08, 23 p., geodatabase. http://www.oregongeology.org/pubs/ofr/p-O-12-08.htm

Allan, J.C., and Hart, R., 2007, Assessing the temporal and spatial variability of coastal change in the Neskowin littoral cell: Developing a comprehensive monitoring program for Oregon beaches Oregon Department of Geology and Mineral Industries Open-File Report O-07-01, 27 p. http://www.oregongeology.org/pubs/ofr/O-07-01.pdf

Allan, J.C., and Hart, R., 2008, Oregon beach and shoreline mapping and analysis program: 2007-2008 beach monitoring report: Oregon Department of Geology and Mineral Industries Open-File Report O-08-15, 60 p. http://www.oregongeology.org/pubs/ofr/O-08-15.pdf

Allan, J.C., and Komar, P.D., 2002a, Extreme storms on the Pacific Northwest Coast during the 1997-98 El Niño and 1998-99 La Niña: Journal of Coastal Research, v. 18, no. 1, p. 175–193. http://www.jstor.org/stable/4299063

Allan, J. C., and Komar, P. D., 2002b, A dynamic revetment and artificial dune for shore protection, *in* Proceedings of the 28th Conference on Coastal Engineering, Cardiff, Wales, vol. 2: American Society of Civil Engineers, p. 2044–2056.

Allan, J.C., and Komar, P.D., 2006, Climate controls on U.S. West Coast erosion processes: Journal of Coastal Research, v. 22, no. 3, p. 511–529. https://doi.org/10.2112/03-0108.1

Allan, J.C., and Stimely, L.L., 2013, Oregon Beach Shoreline Mapping and Analysis Program: Quantifying short- to long-term beach and shoreline changes in the Gold Beach, Nesika Beach, and Netarts littoral cells, Curry and Tillamook Counties: Oregon Department of Geology and Mineral Industries Open-File Report O-2013-07, 47 p. http://www.oregongeology.org/pubs/ofr/p-O-13-07.htm

Allan, J.C., Komar, P.D., and Priest, G.R., 2003, Shoreline variability on the high-energy Oregon coast and its usefulness in erosion-hazard assessments, *in* Byrnes, M.R., Crowell, M., and Fowler, C., eds., Shoreline mapping and change analysis: Technical considerations and management implications: Journal of Coastal Research Special Issue 38, p. 83–105. http://www.jstor.org/stable/25736601

Allan, J. C., Hart, R., and Tranquilli, V., 2006, The use of passive integrated transponder tags (pit-tags) to trace cobble transport in a mixed sand-and-gravel beach on the high-energy Oregon coast, USA: Marine Geology, v. 232, no. 1-2, 63–86.

Allan, J.C., Witter, R.C., Ruggiero, P., and Hawkes, A.D., 2009, Coastal geomorphology, hazards, and management issues along the Pacific Northwest coast of Oregon and Washington, *in* O'Connor, J.E., Dorsey, R.J., and Madin, I.P., eds., Volcanoes to vineyards: Geologic field trips through the dynamic landscape of the Pacific Northwest: Geological Society of America Field Guide 15, p. 495–519.

Allan, J.C., Komar, P.D., and Ruggiero, P., 2011, Storm surge magnitudes and frequencies on the central Oregon coast, *in* Solutions to Coastal Disasters 2011, June 25-29, 2011, Anchorage, Alaska, American Society of Civil Engineers. https://doi.org/10.1061/41185(417)6

Allan, J.C., Komar, P.D., Ruggiero, P., and Witter, R.C., 2012a, The March 2011 Tōhoku tsunami and its impacts along the U.S. West Coast: Journal of Coastal Research, v. 28, no. 5, p. 1142–1153. https://doi.org/10.2112/JCOASTRES-D-11-00115.1

Allan, J.C., Ruggiero, P., and Roberts, J.T., 2012b, Coastal flood insurance study, Coos County, Oregon: Oregon Department of Geology and Mineral Industries Special Paper 44, 132 p. http://www.oregongeology.org/pubs/sp/SP-44.pdf

Allan, J.C., Ruggiero, P., Garcia, G., O'Brien, F.E., Stimely, L.L., and Roberts, J.T., 2015a, Coastal flood hazard study, Tillamook County, Oregon: Oregon Department of Geology and Mineral Industries Special Paper 47, 274 p.

Allan, J.C., Ruggiero, P., Cohn, N., Garcia, G., O'Brien, F.E., Serafin, K., Stimely, L.L., and Roberts, J.T., 2015b, Coastal flood hazard study, Lincoln County, Oregon: Oregon Department of Geology and Mineral Industries Open-File Report O-15-06, 351 p.

Allan, J.C., Ruggiero, P., Garcia, G., Harris, E.L., Roberts, J.T., and Stimely, L., 2015c, Coastal flood hazard study, Clatsop County, Oregon: Oregon Department of Geology and Mineral Industries Open-File Report O-15-05, 210 p. http://www.oregongeology.org/pubs/ofr/O-15-05.pdf

Amante, C., and Eakins, B.W., 2009, ETOPO1 1 Arc-Minute Global Relief Model: Procedures, data sources and analysis: Boulder, Colo., National Geophysical Data Center, Marine Geology and Geophysics Division, NOAA Technical Memorandum NESDIS NGDC-24. https://docs.lib.noaa.gov/noaa_documents/NESDIS/NGDC/TM/NOAA_TM_NESDIS_NGDC_24.pdf

Atwater, B.F., Satoko, M.-R., Satake, K., Yoshinobu, T., Kazue, U., and Yamaguchi, D.K., 2005, The orphan tsunami of 1700—Japanese clues to a parent earthquake in North America: U.S. Geological Survey Professional Paper 1707, 144 p. https://doi.org/10.3133/pp1707

Beaulieu, J.D., 1973, Environmental geology of inland Tillamook and Clatsop Counties, Oregon: Oregon Department of Geology and Mineral Industries Bulletin 79, 65 p. http://www.oregongeology.org/pubs/B/B-079.pdf

Bernstein, D.J., Freeman, C., Forte, M.F., Park, J.-Y., Gayes, P.T., and Mitasova, H., 2003, Survey design analysis for three-dimensional mapping of beach and nearshore morphology, *in* Davis, R. A., Sallenger, A., and Howd, P. (eds.), Coastal sediments '03: "Crossing disciplinary boundaries." Proceedings of the Fifth International Symposium on Coastal Engineering and Science of Coastal Sediment Processes, May 18–23, 2003, Clearwater Beach, Fla., American Society of Civil Engineers.

Booij, N., Ris, R.C., and Holthuijsen, L.H., 1999, A third-generation wave model for coastal regions, Part 1: Model description and validation: Journal of Geophysical Research, v. 104, no. C4, p. 7649–7666. http://dx.doi.org/10.1029/98JC02622

Boon, J.D., 2004, Secrets of the tide: Tide and tidal current analysis and predictions, storm surges and sea level trends: Sawston, England, Woodhead Publishing, 224 p.

Bruun, P., 1962, Sea-level rise as a cause of shore erosion: Journal of the Waterways and Harbors Division, v. 88, no. 1, p. 117–130.

Burgette, R.J., Weldon, R.E., III, and Schmidt, D.A., 2009, Interseismic uplift rates for western Oregon and along-strike variation in locking on the Cascadia subduction zone: Journal of Geophysical Research, v. 114, no. B01408, p. 24. http://dx.doi.org/10.1029/2008JB005679

Carignan, K.S., Taylor, L.A., Eakins, B.W., Warnken, R.R., Lim, E., and Grothe, P.R., 2009a, Digital elevation model of central Oregon coast: procedures, data sources and analysis: Boulder, Colo., National Geophysical Data Center, Marine Geology and Geophysics Division, NOAA Technical Memorandum NESDIS NGDC-25, 38 p. https://docs.lib.noaa.gov/noaa_documents/NESDIS/NGDC/TM/NOAA_TM_NESDIS_NGDC_25.pdf

Carignan, K.S., Taylor, L.A., Eakins, B.W., Warnken, R.R., Sazonova, T., and Schoolcraft, D.C., 2009b, Digital elevation model of Port Orford, Oregon: Procedures, data sources and anlysis: Boulder, Colo., National Geophysical Data Center, Marine Geology and Geophysics Division, NOAA Technical Memorandum NESDIS NGDC-21, 38 p. https://docs.lib.noaa.gov/noaa_documents/NESDIS/NGDC/TM/NOAA_TM_NESDIS_NGDC_21.pdf

Clemens, K.E., and Komar, P.D., 1988, Oregon beach-sand compositions produced by the mixing of sediments under a transgressing sea: Journal of Sedimentary Research, v. 58, no. 3, p. 519–529. https://doi.org/10.1306/212F8DDC-2B24-11D7-8648000102C1865D

Coles, S., 2001, An introduction to statistical modeling of extreme values: London, Springer-Verlag, 208 p.

Cooper, W.S. (ed.), 1958, Coastal sand dunes of Oregon and Washington: Charleston, Oreg., Oregon Institute of Marine Biology, Geological Society of America Memoir 72, 169 p. https://dx.doi.org/10.1130/MEM72

Cox, J. C., and Machemehl, J., 1986, Overload bore propagation due to an overtopping wave: Journal of Waterway, Port, Coastal and Ocean Engineering, v. 112, no. 1, 161–163. https://doi.org/10.1061/(ASCE)0733-950X(1986)112:1(161)

Darienzo, M. E., Peterson, C. D., and Clough, C., 1994, Stratigraphic evidence for great subduction-zone earthquakes at four estuaries in northern Oregon, U.S.A.: Journal of Coastal Research, v. 10, p. 850–876.

Davis, R.E., and Dolan, R., 1993, Nor'easters: American Scientist, v. 81, no. 5, p. 428–439. http://www.jstor.org/stable/29775010

Dean, R.G., 1977, Equilibrium beach profiles: U.S. Atlantic and Gulf Coasts: Newark, University of Delaware, Department of Civil Engineering, Ocean Engineering Report No. 12, 45 p.

EurOtop, 2016, Manual on wave overtopping of sea defences and related structures. An overtopping manual largely based on European research, but for worldwide application. Van der Meer, J.W., Allsop, N.W.H., Bruce, T., De Rouck, J., Kortenhaus, A., Pullen, T., Schüttrumpf, H., Troch, P. and Zanuttigh, B., www.overtopping-manual.com

FEMA, 2006, 44 CFR Section 59.1 of the National Flood Insurance Program (NFIP) Regulations: Definitions of NFIP Terms (44CFR59.1), p. 235–243. https://www.fema.gov/media-library/assets/documents/12437

Goldfinger, C., 2009, Paleoseismically derived probabilities for Cascadia great earthquakes [abs.], Geological Society of America Abstracts with Programs, v. 41, no. 7, p. 520.

Goldfinger, C., Nelson, C.H., and Johnson, J.E., 2003, Holocene earthquake records from the Cascadia subduction zone and northern San Andreas fault based on precise dating of offshore turbidites: Annual Review of Earth and Planetary Sciences, v. 31, no. 1, p. 555–577. https://doi.org/10.1146/annurev.earth.31.100901.141246

Goldfinger, C., Nelson, C.H., Morey, A.E., Johnson, J.E., Patton, J.R., Karabanov, E., Gutiérrez-Pastor, J., Eriksson, A.T., Gràcia, E., Dunhill, G., Enkin, R.J., Dallimore, A., and Vallier, T., 2012, Turbidite event history—Methods and implications for Holocene paleoseismicity of the Cascadia subduction zone: U.S. Geological Survey Professional Paper 1661-F, 170 p. https://pubs.usgs.gov/pp/pp1661f/

Harris, E.L., 2011, Assessing physical vulnerability of the coast in light of a changing climate: An integrated, multi-hazard, multi-timescale approach: Corvallis, Oreg., Oregon State University, Master's thesis, 82 p.

Hedges, T.S., and Mase, H., 2004, Modified Hunt's Equation incorporating wave setup: Journal of Waterway, Port, Coastal and Ocean Engineering, v. 130, no. 3, p. 109–113. https://doi.org/10.1061/(ASCE)0733-950X(2004)130:3(109)

Jennings, R., and Shulmeister, J., 2002, A field based classification scheme for gravel beaches: Marine Geology, v. 186, p. 211–228. https://doi.org/10.1016/S0025-3227(02)00314-6

Kelsey, H.M., Nelson, A.R., Hemphill-Haley, E., and Witter, R.C., 2005, Tsunami history of an Oregon coastal lake reveals a 4600 yr record of great earthquakes on the Cascadia subduction zone: Geological Society of America Bulletin, v. 117, no. 7/8, p. 1009–1032. http://dx.doi.org/10.1130/B25452.1

Komar, P.D., 1997, The Pacific Northwest coast: Living with the shores of Oregon and Washington: Durham and London, Duke University Press, 195 p.

Komar, P.D., 1998, Beach processes and sedimentation (2nd ed.): Englewood Cliffs, N.J., Prentice Hall, 544 p.

Komar, P.D., McManus, J., and Styllas, M., 2004, Sediment accumulation in Tillamook Bay, Oregon: Natural processes versus human impacts: Journal of Geology, v. 112, p. 455–469.

Komar, P.D., Torstenson, R.T., and Shih, S.-M., 1991, Bandon, Oregon: Coastal development and the potential for extreme ocean hazards: Shore & Beach, v. 59, no. 4, p. 14–22.

Komar, P.D., McDougal, W.G., Marra, J.J., and Ruggiero, P., 1999, The rational analysis of setback distances: Applications to the Oregon coast: Shore & Beach, v. 67, no. 1, p. 41–49.

Komar, P. D., Allan, J. C., Diaz-Mendez, G. M., Marra, J.J., and Ruggiero, P., 2000, El Niño and La Niña—erosion processes and impacts: American Society of Civil Engineers, Proceedings of the 27th International Conference on Coastal Engineering, Sydney, Australia, July 16–21, 2000, p. 2414–2427.

Komar, P.D., Allan, J.C., and Winz, R., 2003, Cobble beaches — the "design with nature" approach for shore protection: Coastal Sediments' 03, 5th International Symposium on Coastal Engineering and Science of Coastal Sediment Processes, Clearwater Beach, Fla., May 18–23, 2003.

Komar, P.D., McManus, J., and Styllas, M., 2004, Sediment accumulation in Tillamook Bay, Oregon: Natural processes versus human impacts: Journal of Geology, v. 112, no. 4, p. 455–469. https://doi.org/10.1086/421074

Komar, P.D., Allan, J.C., and Ruggiero, P., 2011, Sea level variations along the U.S. Pacific Northwest coast: Tectonic and climate controls: Journal of Coastal Research, v. 27, no. 5, p. 808–823. https://doi.org/10.2112/JCOASTRES-D-10-00116.1

Kriebel, D. L., and Dean, R. G., 1993, Convolution method for time-dependent beach-profile response: Journal of Waterway, Port, Coastal and Ocean Engineering, v. 119, no. 2, 206–226. https://doi.org/10.1061/(ASCE)0733-950X(1993)119:2(204)

Leonard, L.J., Hyndman, R.D., and Mazzotti, S., 2004, Coseismic subsidence in the 1700 great Cascadia earthquake: Coastal estimates versus elastic dislocation models: Geological Society of America Bulletin, v. 116, no. 5-6, p. 655–670. https://doi.org/10.1130/B25369.1

Lizarraga-Arciniega, J.R., and Komar, P.D., 1975, Shoreline changes due to jetty construction on the Oregon coast: Oregon State University Sea Grant College Program Publication No. ORESU-T-75-004, 90 p. http://nsgl.gso.uri.edu/oresu/oresut75004.pdf

Moore, L.J., 2000, Shoreline mapping techniques: Journal of Coastal Research, v. 16, p. 111–124. http://www.jstor.org/stable/4300016

Mori, N., Takahashi, T., Yasuda, T., and Yanagisawa, H., 2011, Survey of 2011 Tohoku earthquake tsunami inundation and run-up: Geophysical Research Letters, v. 38, no. L00G14, p. 6. https://doi.org/10.1029/2011GL049210

Morton, R.A., Leach, M.P., Paine, J.G., and Cardoza, M.A., 1993, Monitoring beach changes using GPS surveying techniques: Journal of Coastal Research, v. 9, no. 3, p. 702–720.

Nelson, A.R., Atwater, B.F., Bobrowsky, P.T., Bradley, L., Clague, J.J., Carver, G.A., Darienzo, M.E., Grant, W.C., Krueger, H.W., Sparkes, R., Stafford, T.W., Jr., and Stuiver, M., 1995, Radiocarbon evidence for extensive plate-boundary rupture about 300 years ago at the Cascadia subduction zone: Nature, v. 378, no. 23, p. 371–374.

NHC, 2005, Final draft guidelines for coastal flood hazard analysis and mapping for the Pacific Coast of the United States: West Sacramento, Calif., Northwest Hydraulics Consultants, 334 p.

Oceanweather, 2010, Global Reanalysis of Ocean Waves Fine Northeast Pacific Hindcast (GROW-FINE NEPAC): Oceanweather Inc., 39 p.

Peterson, C., Scheidegger, K., Komar, P.D., and Niem, W., 1984, Sediment composition and hydrography in six high-gradient estuaries of the northwestern United States: Journal of Sedimentary Research, v. 54, no. 1, p. 86–97. http://jsedres.geoscienceworld.org/content/54/1/86

Peterson, C.D., Darienzo, M.E., Hamilton, D., Pettit, D.J., Yeager, R.K., Jackson, P.L., Rosenfeld, C.L., and Terich, T.A., 1994, Beach-shoreline data base, Pacific Northwest region, USA: Oregon Department of Geology and Mineral Industries Open-File Report O-94-2, 29 p. http://www.oregongeology.org/pubs/ofr/O-94-04.zip

Priest, G.R., Goldfinger, C., Wang, K., Witter, R.C., Zhang, Y., and Baptista, A.M., 2009, Confidence levels for tsunami-inundation limits in northern Oregon inferred from a 10,000-year history of great earthquakes at the Cascadia subduction zone: Natural Hazards, first online September 21, 2009. https://doi.org/10.1007/s11069-009-9453-5

Ris, R.C., Holthuijsen, L.H., and Booij, N., 1999, A third-generation wave model for coastal regions, Part 2: Verification: Journal of Geophysical Research, v. 104, no. C4, p. 7667–7681. http://dx.doi.org/10.1029/1998JC900123

Ruggiero, P., and Voigt, B., 2000, Beach monitoring in the Columbia River littoral cell, 1997–2000: Olympia, Wash., Coastal Monitoring & Analysis Program, Washington Department of Ecology Publication 00-06-26, 113 p.

Ruggiero, P., Komar, P.D., McDougal, W.G., and Beach, R.A., 1996, Extreme water levels, wave runup and coastal erosion, *in* Proceedings of the 25th Conference on Coastal Engineering, September 2–6, 1996, Orlando, Fla., American Society of Civil Engineers, p. 2793–2805. https://doi.org/10.1061/9780784402429.216

Ruggiero, P., Komar, P.D., McDougal, W.G., Marra, J.J., and Beach, R.A., 2001, Wave runup, extreme water levels and the erosion of properties backing beaches: Journal of Coastal Research, v. 17, no. 2, p. 407–419. http://www.jstor.org/stable/4300192

Ruggiero, P., Kaminsky, G.M., and Gelfenbaum, G., 2003, Linking proxy-based and datum-based shorelines on a high-energy coastline: Implications for shoreline change analyses: Journal of Coastal Research, no. SI 38, p. 57–82.

Ruggiero, P., Holman, R.A., and Beach, R.A., 2004, Wave run-up on a high-energy dissipative beach: Journal of Geophysical Research, v. 109, p. C06025. http://dx.doi.org/10.1029/2003JC002160

Ruggiero, P., Kaminsky, G.M., Gelfenbaum, G., and Voight, B., 2005, Seasonal to interannual morphodynamics along a high-energy dissipative littoral cell: Journal of Coastal Research, v. 21, no. 3, p. 553–578. https://doi.org/10.2112/03-0029.1

Ruggiero, P., Buijsman, M.C., Kaminsky, G.M., and Gelfenbaum, G., 2010a, Modeling the effects of wave climate and sediment supply variability on large-scale shoreline change: Marine Geology, v. 273, no. 1–4, p. 127–140. https://doi.org/10.1016/j.margeo.2010.02.008

Ruggiero, P., Komar, P.D., and Allan, J.C., 2010b, Increasing wave heights and extreme value projections: The wave climate of the U.S. Pacific Northwest: Coastal Engineering, v. 57, no. 5, p. 539–552. https://doi.org/10.1016/j.coastaleng.2009.12.005

Ruggiero, P., Kratzmann, M.G., Himmelstoss, E.A., Reid, D., Allan, J., and Kaminsky, G., 2013, National Assessment of Shoreline Change: Historical Shoreline Change along the Pacific Northwest coast (Oregon and Washington): U.S. Geological Survey Open-File Report 2012–1007. https://doi.org/10.3133/ofr20121007

Satake, K., Shemazaki, K., Yoshinobu, T., and Ueda, K., 1996, Time and size of a giant earthquake in Cascadia inferred from Japanese tsunami records of January 1700: Nature, v. 379, no. 6562, p. 246–249. https://doi.org/10.1038/379246a0

Schlicker, H.G., Deacon, R.J., Newcomb, R.C., and Jackson, R.L., 1974, Environmental geology of coastal Lane County, Oregon: Oregon Department of Geology and Mineral Industries Bulletin 85, 125 p. http://www.oregongeology.org/pubs/B/B-085.pdf

Smith, J.M., Sherlock, A.R., and Resio, D.T., 2001, STWAVE: Steady-state spectral wave model user's manual for STWAVE, Version 3.0: Coastal and Hydraulics Laboratory, U.S. Army Engineer Research and Development Center Technical Report ERDC/CHL SR-01-1, 81 p. http://citeseerx.ist.psu.edu/viewdoc/download?doi=10.1.1.916.2457&rep=rep1&type=pdf

Soler, T., Weston, N.D., and Foote, R.H., 2011, The "Online Positioning User Service" suite (OPUS-S, OPUS-RS, OPUS-DB), Chapter 3 *in* Soler, T., ed., CORS and OPUS for engineers: Tools for surveying and mapping applications: Reston, Va., American Society of Civil Engineers, p. 17–26. https://doi.org/10.1061/9780784411643.ch03

Stockdon, H.F., Holman, R.A., Howd, P.A., and Sallenger, A.H., Jr., 2006, Empirical parameterization of setup, swash, and runup: Coastal Engineering, v. 53, no. 7, p. 573–588. https://doi.org/10.1016/j.coastaleng.2005.12.005

Suppasri, A., Muhari, A., Futami, T., Imamura, F., and Shuto, N., 2014, Loss functions for small marine vessels based on survey data and numerical simulation of the 2011 Great East Japan tsunami: Journal of Waterway, Port, Coastal, and Ocean Engineering, v. 140, no. 5. https://ascelibrary.org/doi/full/10.1061/(ASCE)WW.1943-5460.0000244

Thieler, E.R., Himmelstoss, E.A., Zichichi, J.L., and Ergul, Ayhan, 2009, Digital Shoreline Analysis System (DSAS) version 4.0—An ArcGIS extension for calculating shoreline change (ver. 4, July 2009): U.S. Geological Survey Open-File Report 2008-1278. https://woodshole.er.usgs.gov/project-pages/DSAS/version4/index.html

Tillotson, K., and Komar, P.D., 1997, The wave climate of the Pacific Northwest (Oregon and Washington): A comparison of data sources: Journal of Coastal Research, v. 13, no. 2, p. 440–452. http://www.jstor.org/stable/4298639

Trimble, 2005, Trimble 5700 GPS system datasheet: Trimble Navigation Limited, 2 p.

Tuba Özkan-Haller, H., Allan, J.C., Barth, J.A., Haller, M.C., Holman, R.A., and Ruggiero, P., 2009, Baseline observations and modeling for the Reedsport Wave Energy Site: Corvallis, Oreg., Oregon State University, and Portland, Oreg., Oregon Department of Geology and Mineral Industries, 35 p.

van der Meer, J.W., 2002, Technical report: Wave run-up and wave overtopping at dikes: Technical Advisory Committee on Flood Defence, 50 p.

W.F. Baird and Associates, 2005, Pacific Ocean wave information study validation of wave model: Results against satellite altimeter data: Vicksburg, Miss., prepared for U.S. Army Corps of Engineers Engineering Research and Development Center, 13 p.

Wilson, R.I., Admire, A.R., Borrero, J.C., Dengler, L.A., Legg, M.R., Lynett, P., McCrink, T.P., Miller, K.M., Ritchie, A., and Sterling, K., 2013, Observations and impacts from the 2010 Chilean and 2011 Japanese tsunamis in California (USA): Pure and Applied Geophysics, v. 170, no. 6–8, p. 1127–1147.

Witter, R.C., 2008, Prehistoric Cascadia tsunami inundation and runup at Cannon Beach, Clatsop County, Oregon: Oregon Department of Geology and Mineral Industries Open-File Report O-08-12.

Witter, R.C., Kelsey, H.M., and Hemphill-Haley, E., 2003, Great Cascadia earthquakes and tsunamis of the past 6700 years, Coquille River estuary, southern coastal Oregon: Geological Society of America Bulletin, v. 115, p. 1289–1306. https://doi.org/10.1130/B25189.1

Witter, R.C., Zhang, Y., Goldfinger, C., Priest, G.R., and Wang, K., 2010, Validating numerical tsunami simulations in southern Oregon using late Holocene records of great Cascadia earthquakes and tsunamis, *in* Seismological Society of America 2010 Annual Meeting, Portland, Oreg., p. 290.

Yamamoto, M., 2011, IOC/UNESCO Bulletin No. 13 (March 30, 2011)—Tōhoku Tsunami March 11, 2011. http://itic.ioc-unesco.org/images/docs/no_13_ioc_unesco_bulletin_30_mar.doc

Zhang, K., Douglas, B.C., and Leatherman, S., 2001, Beach erosion potential for severe nor'easters: Journal of Coastal Research, v. 17, no. 2, p. 309–321.

# 11.0 APPENDICES

- Appendix A: Ground Survey Accuracy Assessment Protocols
- Appendix B: Lane County DFIRM/DOGAMI Naming Convention
- Appendix C: Lane County Beach and Bluff Profiles
- Appendix D: Supplemental Transect Overtopping Table

## 11.1 Appendix A: Ground Survey Accuracy Assessment Protocols

See report by Watershed Sciences, Inc., dated December 21, 2009.

## 11.2 Appendix B: Lane and Douglas County DFIRM/DOGAMI Naming Convention

| Reach | Trans Order | DFIRM Transect | DOGAMI Transect | Transect Type | Lidar Transect | Description |
|---|---|---|---|---|---|---|
| **Heceta** | 1 | 1 | 1 | Main | | sand beach backed by dunes |
| **Beach** | 2 | 2 | 2 | Main | | sand beach backed by dunes |
| | 3 | 3 | 3 | Main | | sand beach backed by dunes |
| | 4 | 4 | 4 | Main | | sand beach backed by dunes & bluff |
| | 5 | 5 | 5 | Main | | sand beach backed by riprap & bluff |
| | 6 | 6 | 6 | Main | | sand beach backed by riprap |
| | 7 | 7 | 7 | Main | | sand beach backed by riprap |
| | 8 | 8 | 8 | Main | | sand beach backed by dune ramp |
| | 9 | 9 | 9 | Main | | sand beach backed by riprap |
| | 10 | 10 | 10 | Main | | sand beach backed by dunes |
| | 11 | 11 | 11 | Main | | sand beach backed by riprap |
| | 12 | 12 | 12 | Main | | sand beach backed by riprap |
| | 13 | 13 | 13 | Main | | sand beach backed by riprap |
| | 14 | 14 | 14 | Main | | sand beach backed by riprap |
| | 15 | 15 | 15 | Main | | sand beach backed by riprap |
| | 16 | 16 | 16 | Main | | sand beach backed by riprap |
| | 17 | 17 | 17 | Main | | sand beach backed by dunes |
| | 18 | 18 | 18 | Main | | sand beach backed by dunes |
| | 19 | 19 | 19 | Main | | sand beach backed by dunes |
| | 20 | 20 | 20 | Main | | sand beach backed by dunes |
| | 21 | 21 | 21 | Main | | sand beach backed by dunes |
| | 22 | 22 | 22 | Main | | sand beach backed by dunes |
| | 23 | 23 | 23 | Main | | sand beach backed by dunes |
| | 24 | 24 | 24 | Main | | sand beach backed by dunes |
| | 25 | 25 | 25 | Main | | basalt cliff |
| | 26 | 26 | 26 | Main | | sand beach backed by high bluff |
| | 27 | 27 | 27 | Main | | basalt cliff |
| | 28 | 28 | 28 | Main | | sand beach backed by high bluff |
| | 29 | | | lidar | 29_1 | |
| | 30 | 29 | 29 | Main | | sand beach backed by high bluff |
| | 31 | 30 | 30 | Main | | basalt cliff |
| **Muriel** | 32 | 31 | 31 | Main | | sand beach backed by high bluff |
| **O'Ponsler** | 33 | 32 | 32 | Main | | sand beach backed by low bluff |
| | 34 | 33 | 33 | Main | | sand beach backed by low bluff |
| | 35 | 34 | | lidar | 33_577 | |
| | 36 | 35 | | lidar | 33_575 | |
| | 37 | 36 | 34 | Main | | sand beach backed by low bluff |
| | 38 | 37 | | lidar | 34_530 | |
| | 39 | 38 | | lidar | 34_523 | |
| | 40 | 39 | 35 | Main | | sand beach backed by high bluff |
| | 41 | 40 | 36 | Main | | rock platform backed by high bluff |
| **Stonefield** | 42 | 41 | 37 | Main | | sand beach backed by high bluff |
| **Beach** | 43 | 42 | 38 | Main | | rock platform backed by high bluff |
| | 44 | 43 | 39 | Main | | sand beach backed by high bluff |

| Reach | Trans Order | DFIRM Transect | DOGAMI Transect | Transect Type | Lidar Transect | Description |
|---|---|---|---|---|---|---|
| | 45 | 44 | 40 | Main | | rock platform backed by high bluff |
| | 46 | 45 | 41 | Main | | sand beach backed by high bluff |
| | 47 | | | lidar | 42_312 | |
| | 48 | | | lidar | 42_309 | |
| | 49 | 46 | 42 | Main | | sand beach backed by dunes |
| | 50 | | | lidar | 42_292 | |
| | 51 | 47 | 43 | Main | | sand beach backed by low bluff |
| | 52 | 48 | 44 | Main | | rock platform backed by high bluff |
| | 53 | 49 | 45 | Main | | sand beach backed by low bluff |
| | 54 | 50 | 46 | Main | | sand beach backed by low bluff |
| | 55 | 51 | 47 | Main | | sand beach backed by high bluff |
| | 56 | 52 | 48 | Main | | rock platform backed by high bluff |
| | 57 | 53 | 49 | Main | | rock platform backed by high bluff |
| | 58 | 54 | 50 | Main | | rock platform backed by high bluff |
| | 59 | 55 | 51 | Main | | mixed sand and gravel beach backed by low bluff |
| | 60 | 56 | | lidar | 51_179 | |
| | 61 | 57 | | lidar | 51_177 | |
| **Cummins** | 62 | 58 | 52 | Main | | rock platform backed by high bluff |
| **Creek** | 63 | 59 | 53 | Main | | rock platform backed by high bluff |
| | 64 | 60 | 54 | Main | | sand beach backed by high bluff |
| | 65 | 61 | 55 | Main | | rock platform backed by high bluff |
| | 66 | 62 | 56 | Main | | sand beach backed by low bluff |
| | 67 | 63 | | lidar | 56_49 | |
| | 68 | 64 | | lidar | 56_54 | |
| | 69 | 65 | 57 | Main | | rock platform backed by low bluff |

## 11.3 Appendix C: Lane and Douglas County Beach and Bluff Profiles

### 11.3.1 Heceta Beach

fm_LD 1

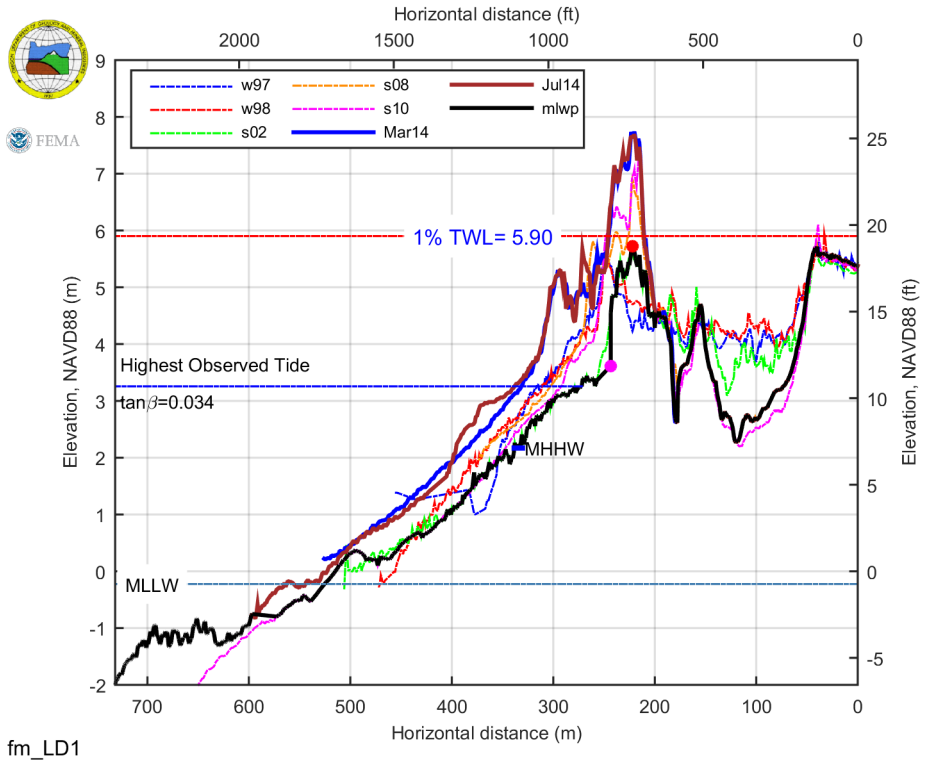


fm_LD1

fm_LD 2

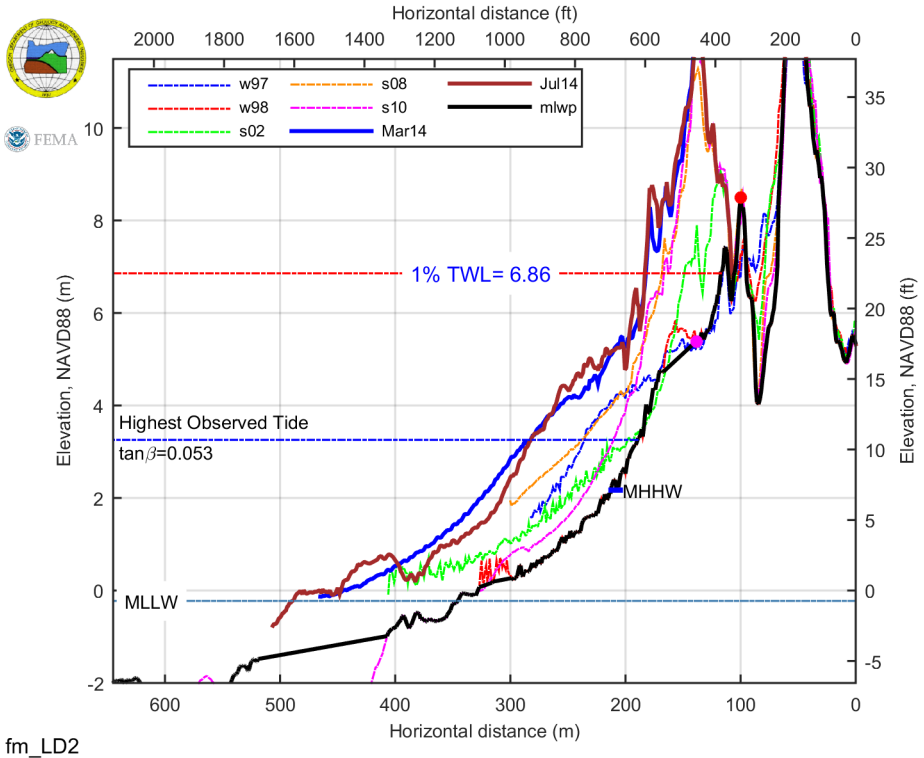


fm_LD2

fm_LD 3

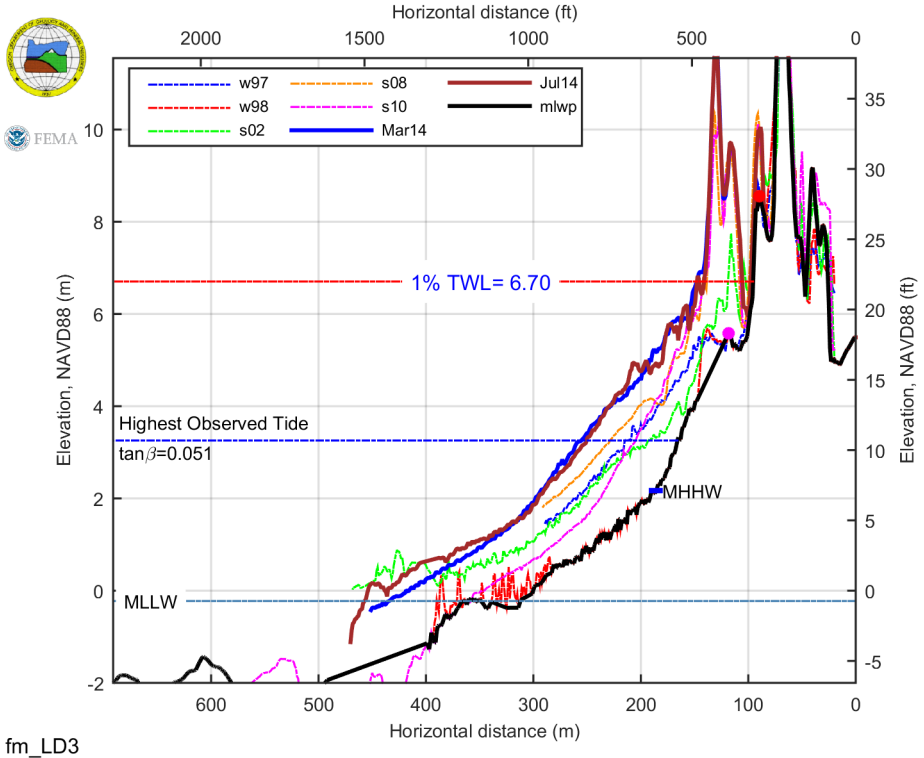


fm_LD3

fm_LD 4

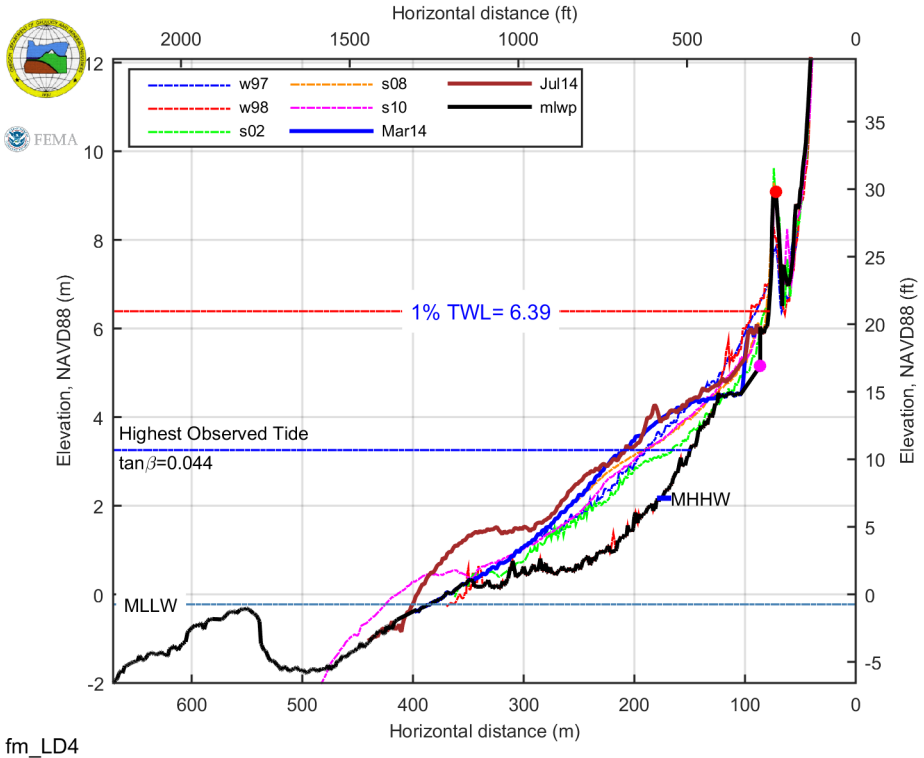


fm_LD4

fm_LD 5

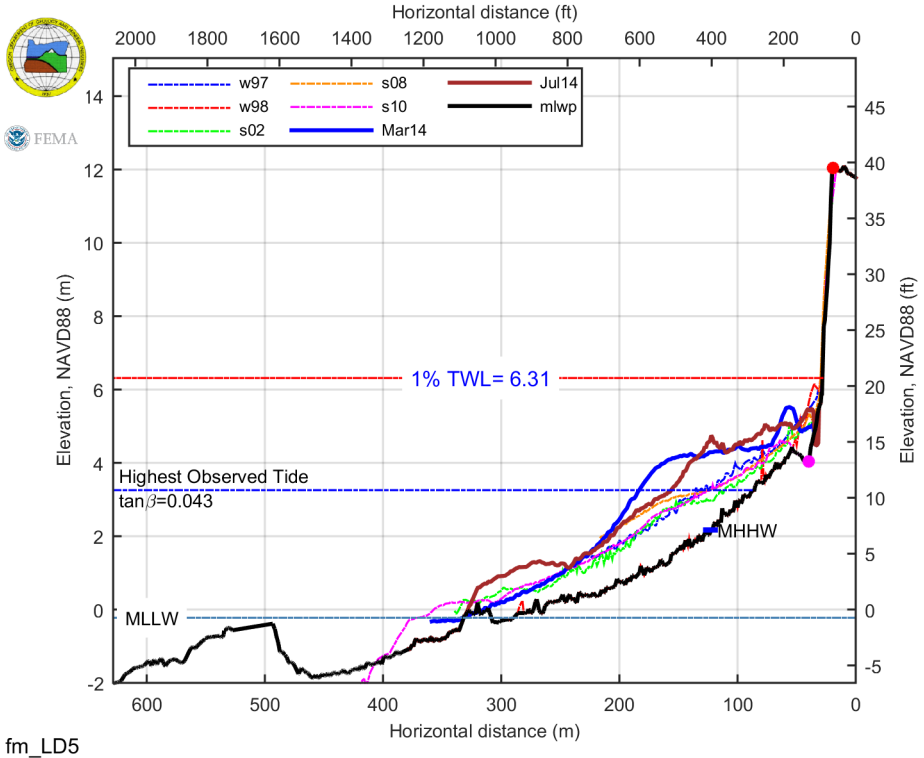


fm_LD5

fm_LD 6

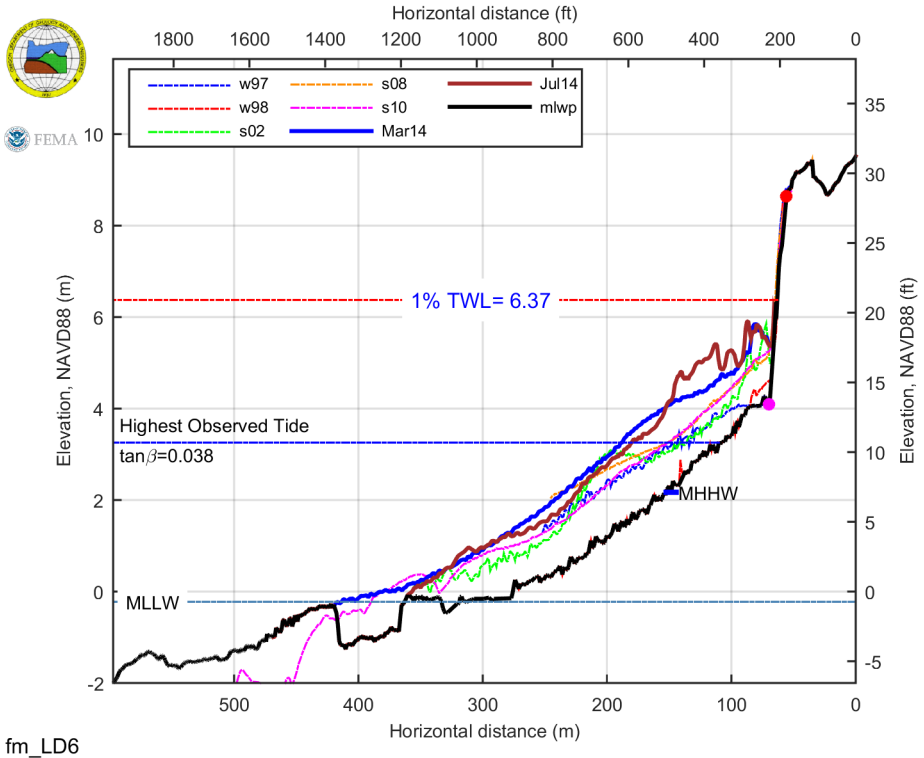


fm_LD6

fm_LD 7

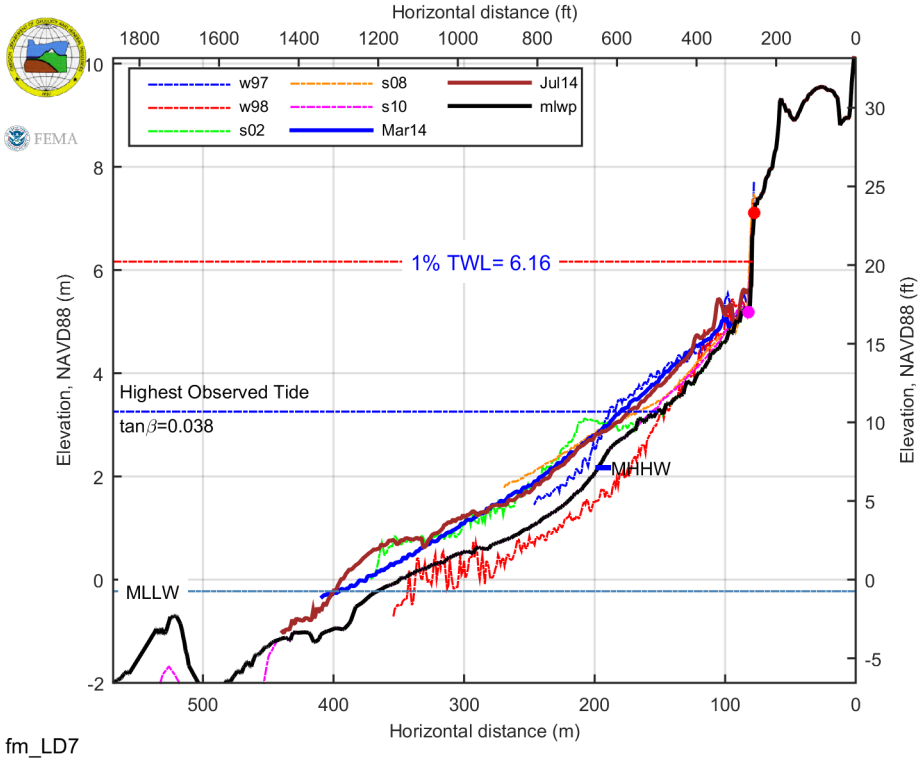


fm_LD7

fm_LD 8

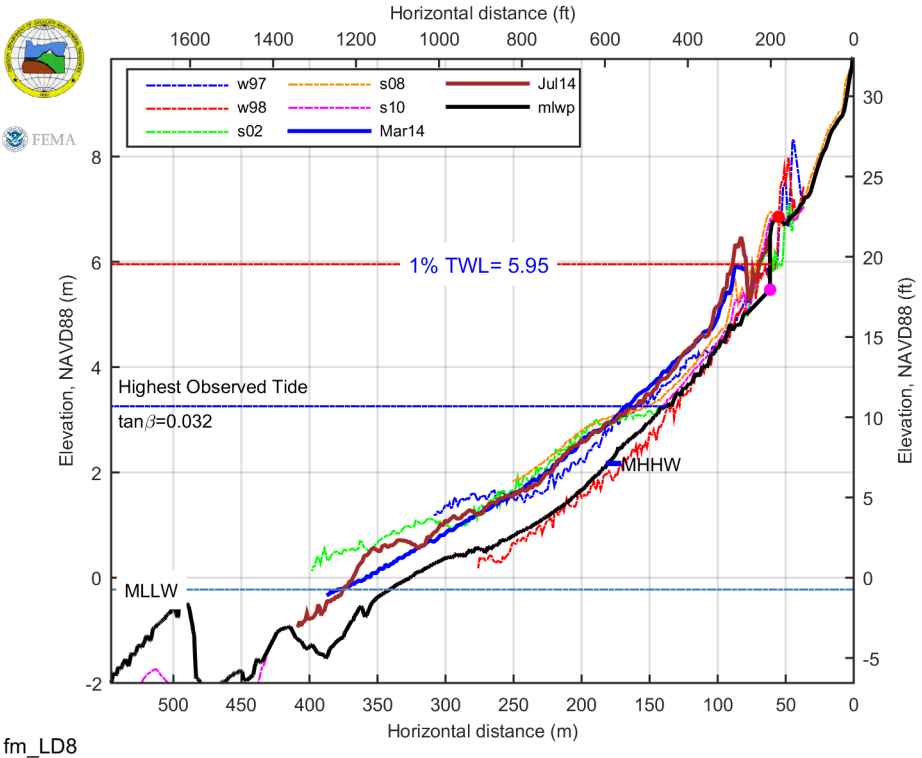


fm_LD8

fm_LD 9

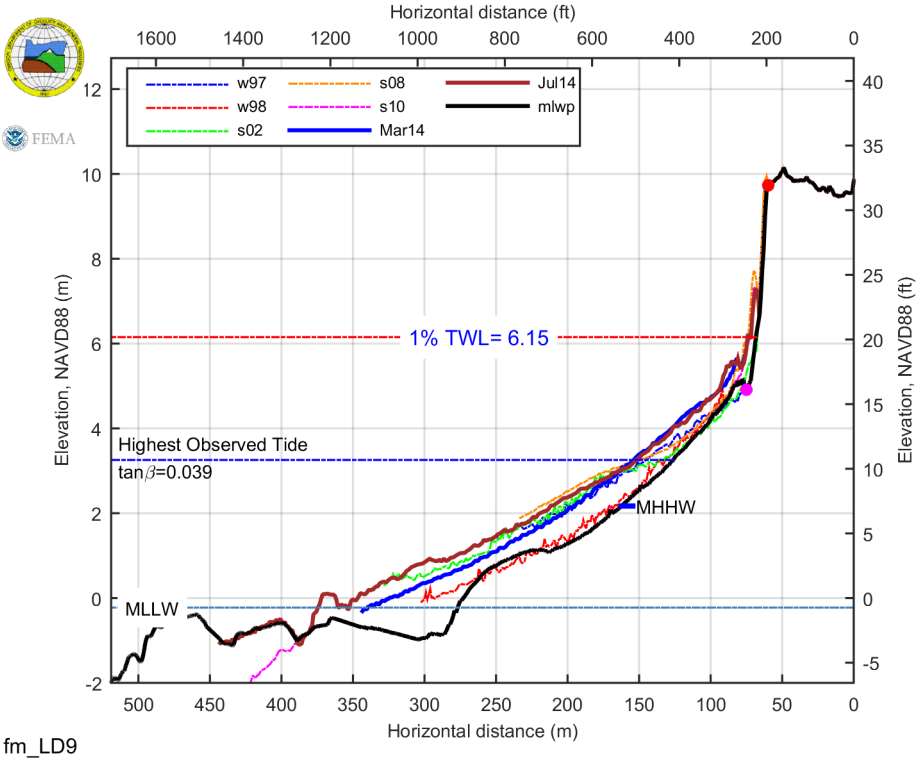


fm_LD9

fm_LD 10

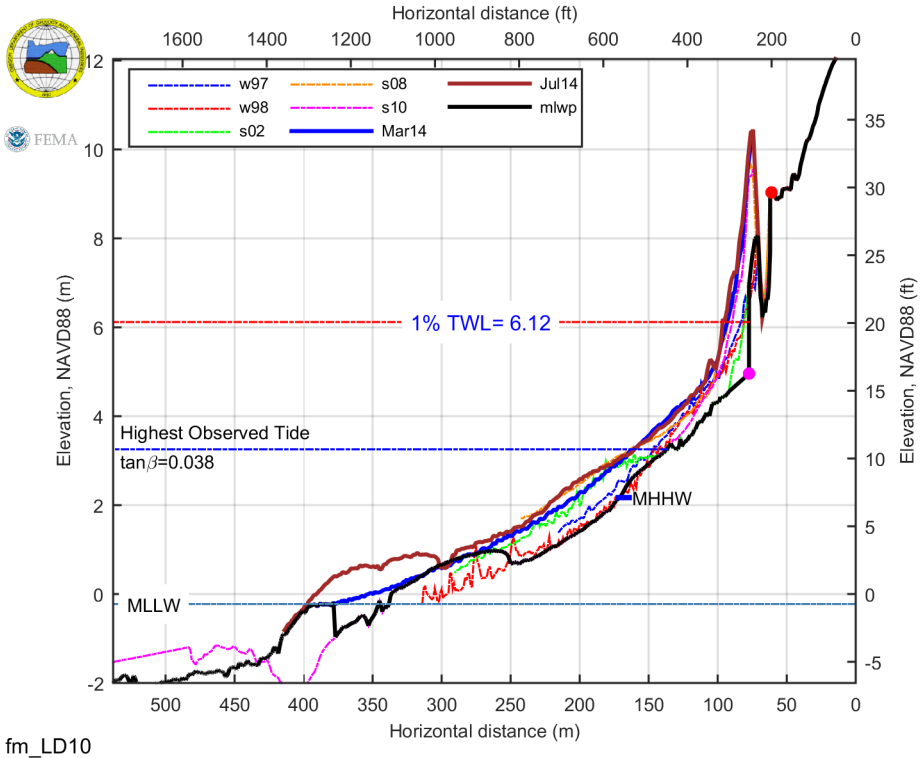


fm_LD10

fm_LD 11

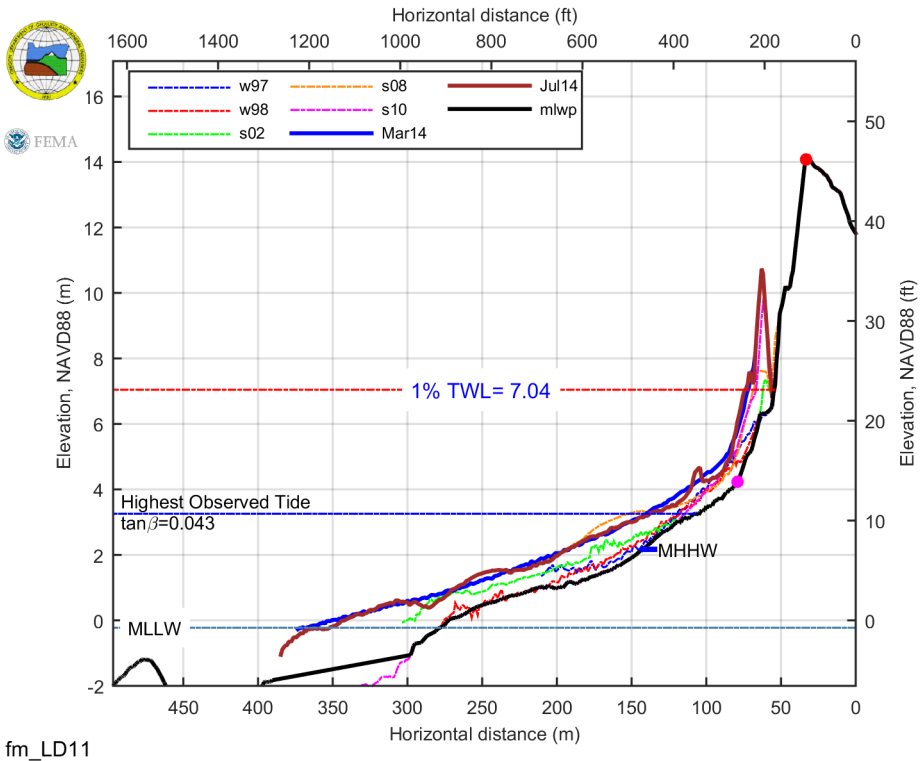


fm_LD11

fm_LD 12

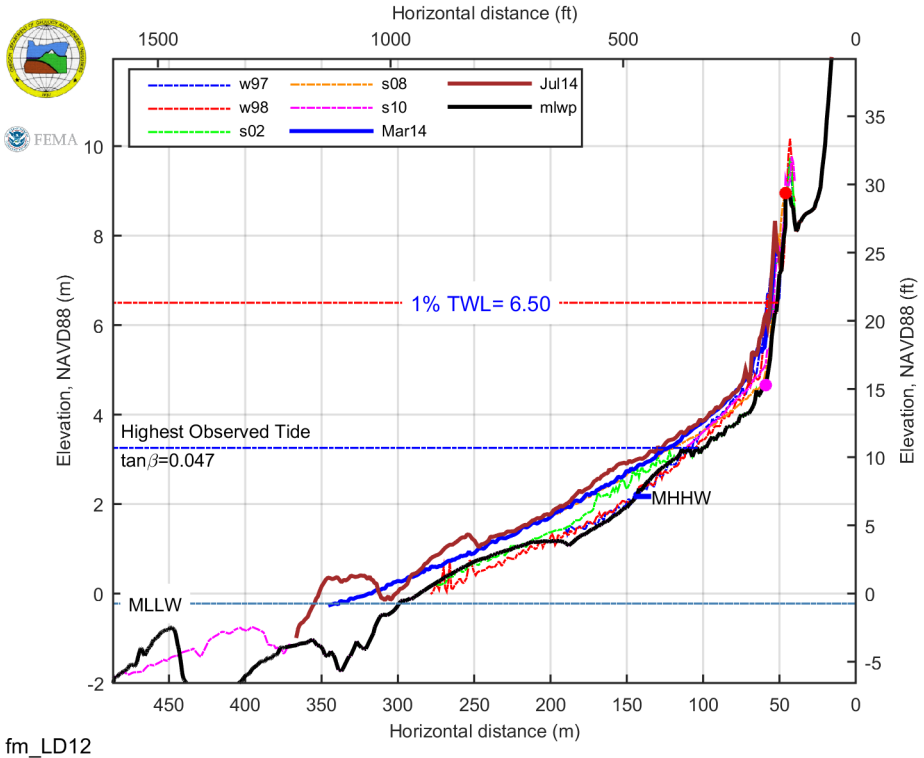


fm_LD12

fm_LD 13

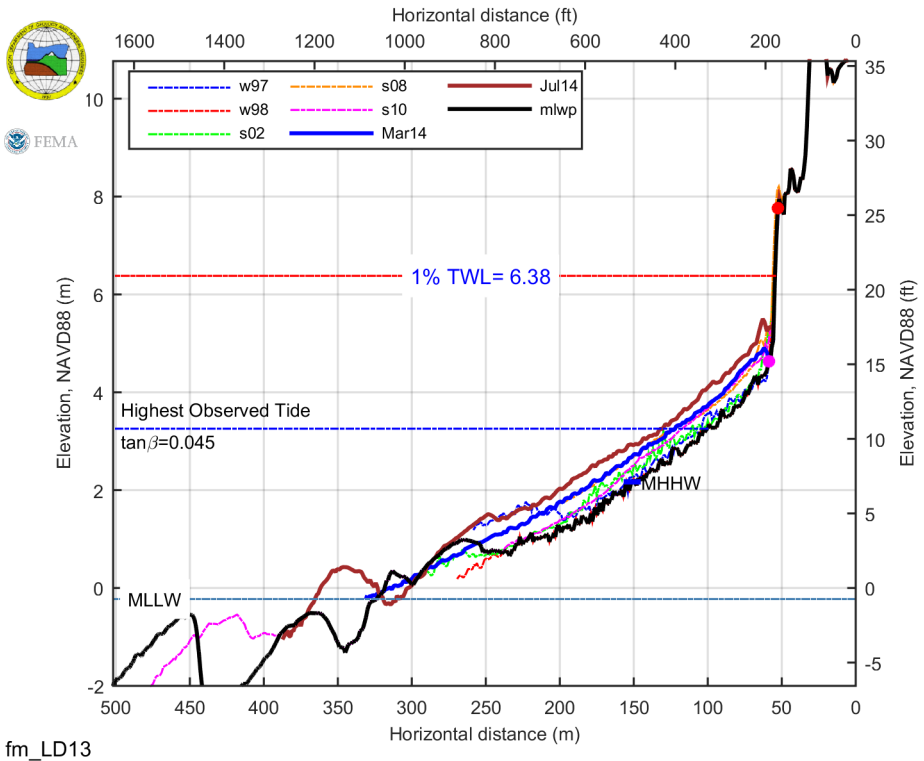


fm_LD13

fm_LD 14

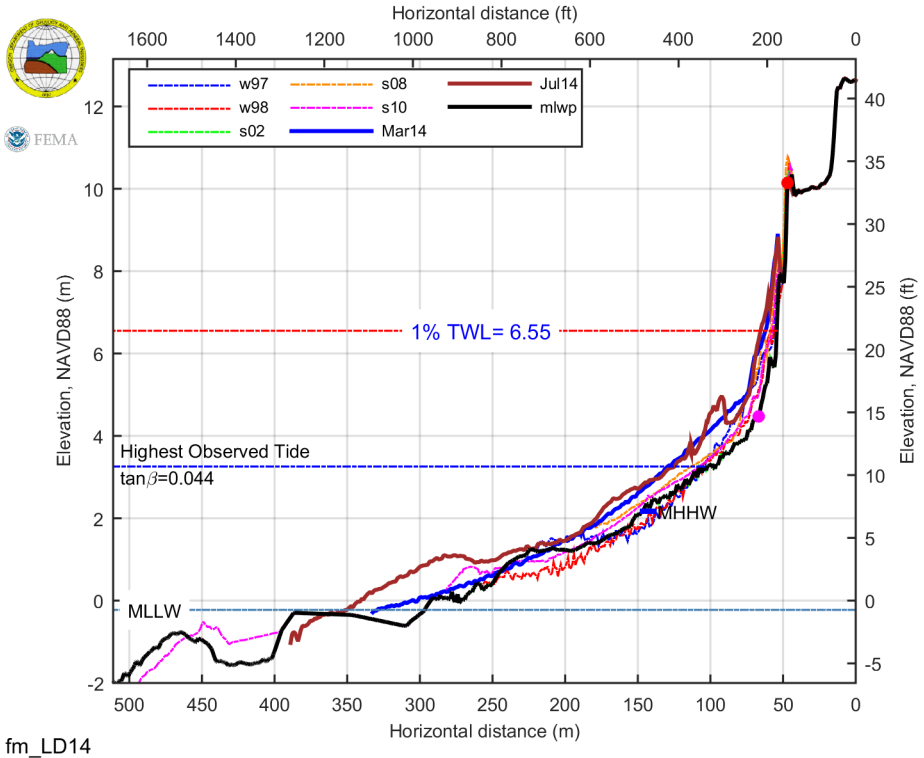


fm_LD14

fm_LD 15

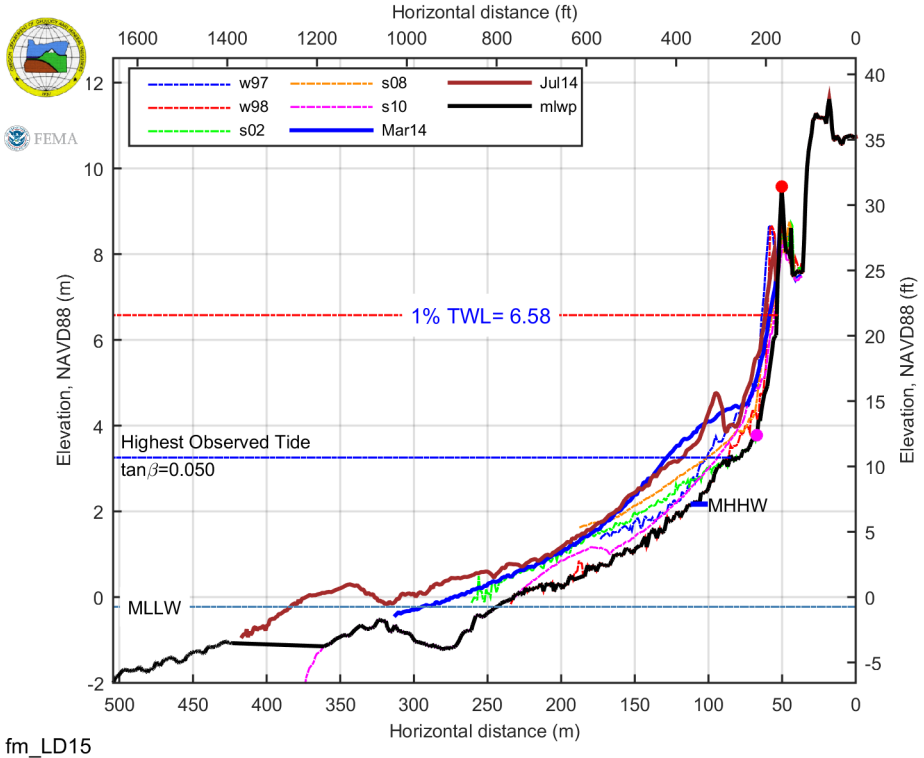


fm_LD15

fm_LD 16

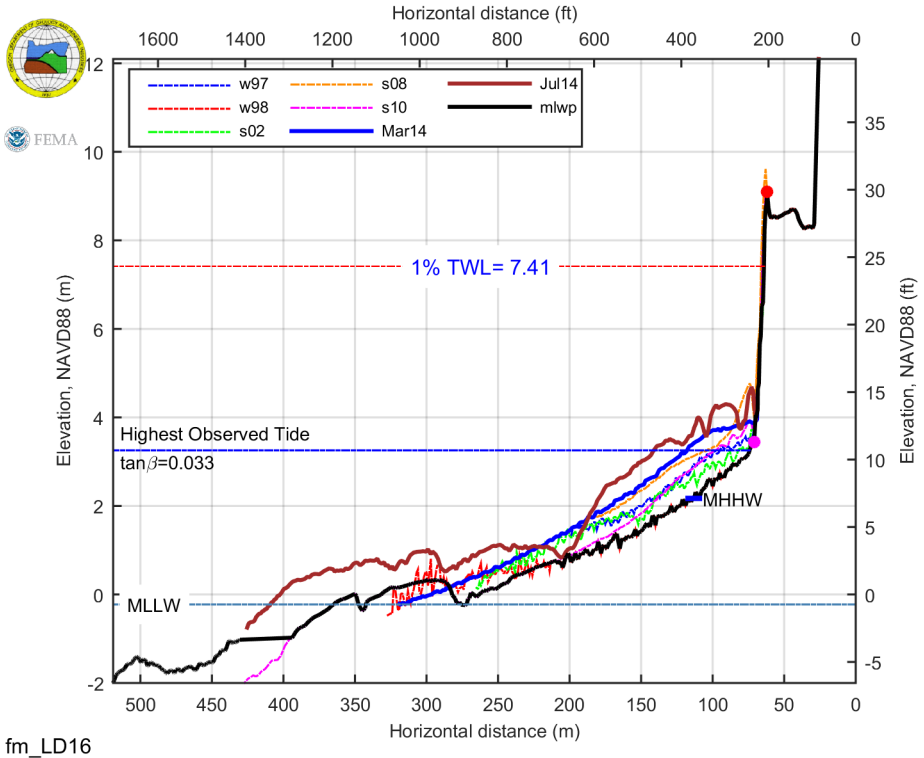


fm_LD16

fm_LD 17

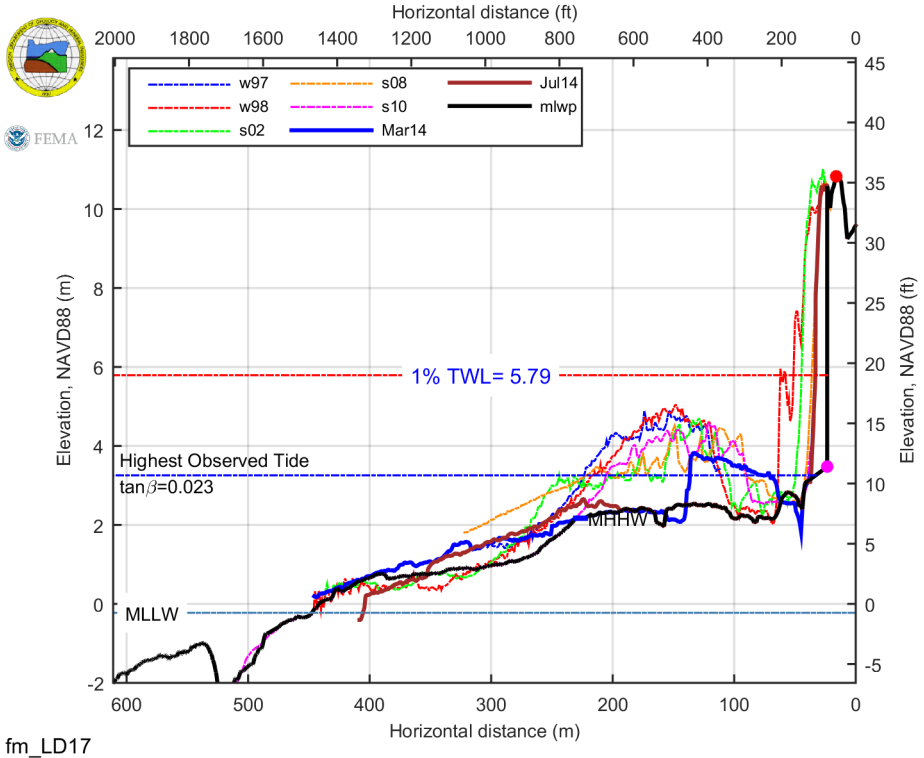


fm_LD17

fm_LD 18

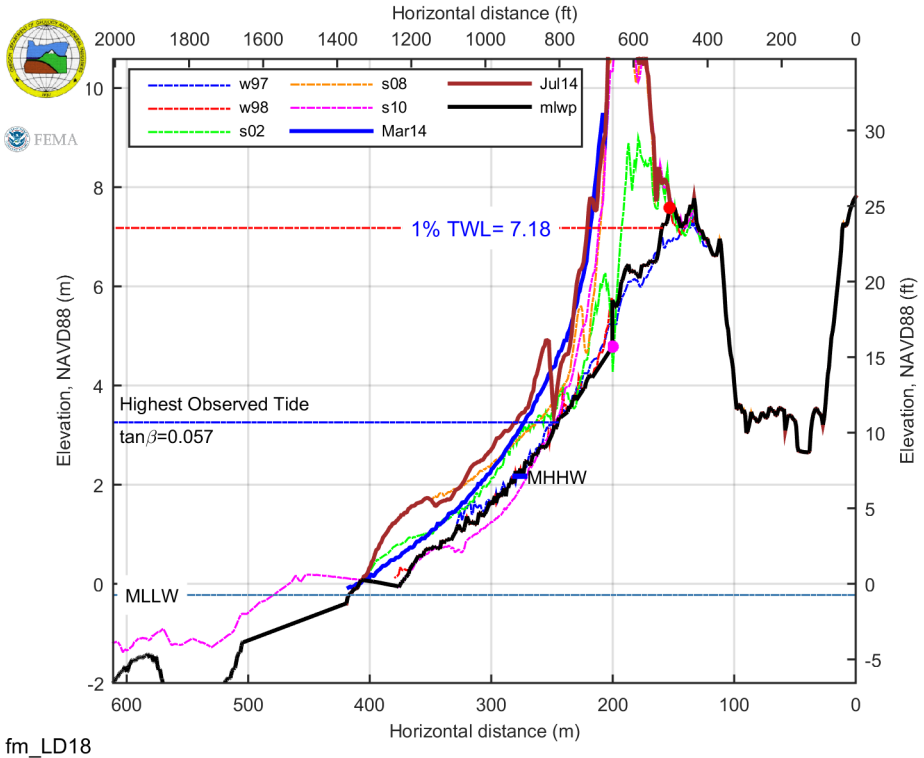


fm_LD18

fm_LD 19

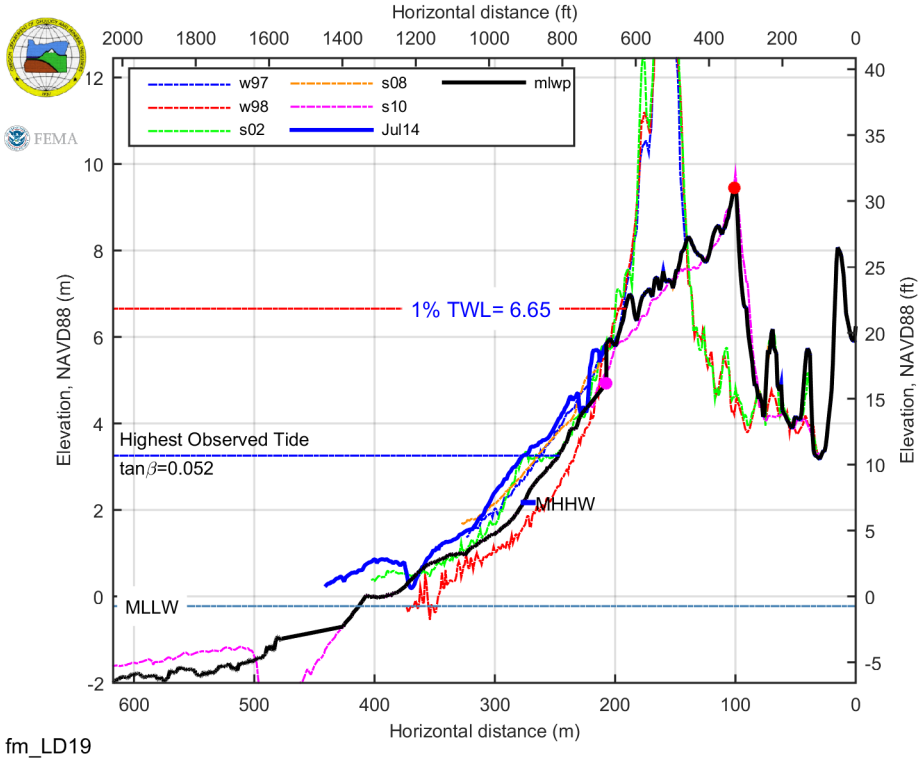


fm_LD19

fm_LD 20

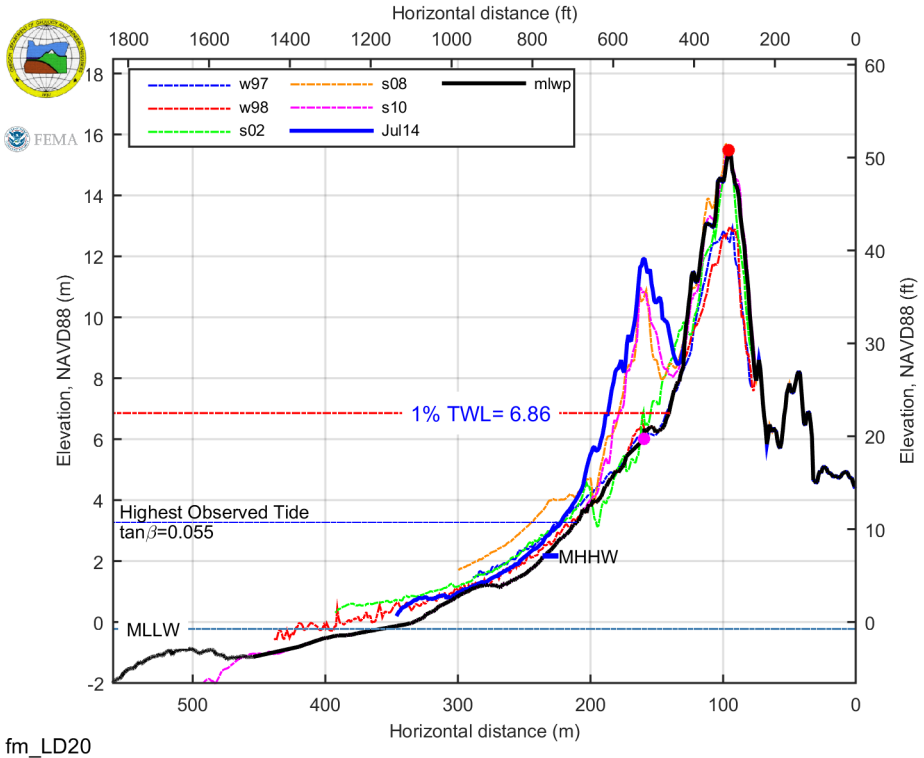


fm_LD20

fm_LD 21

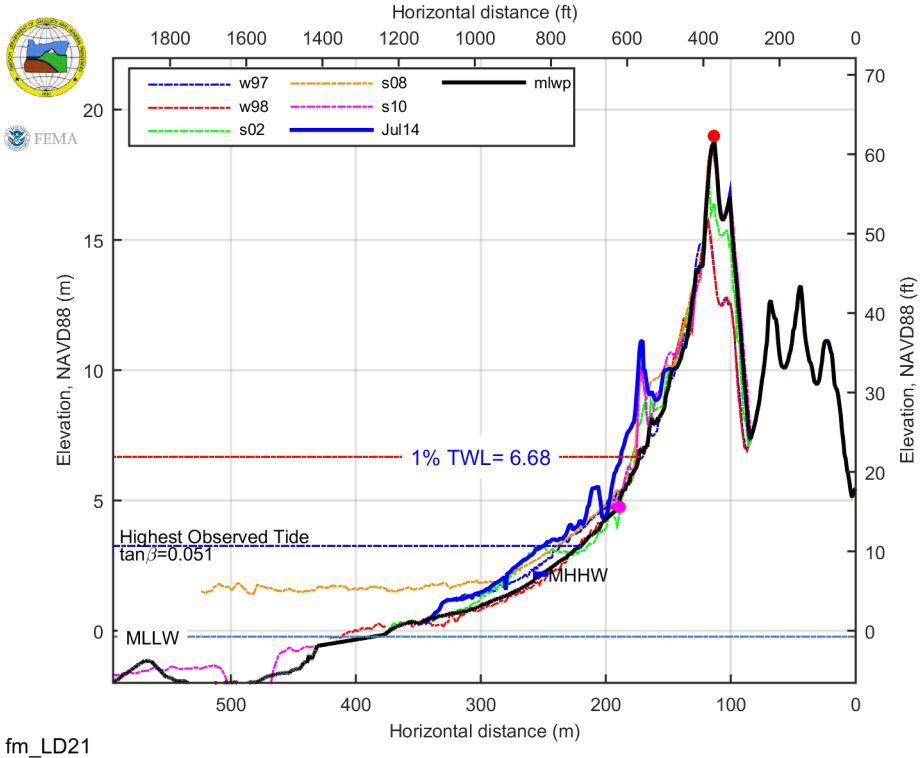


fm_LD21

fm_LD 22

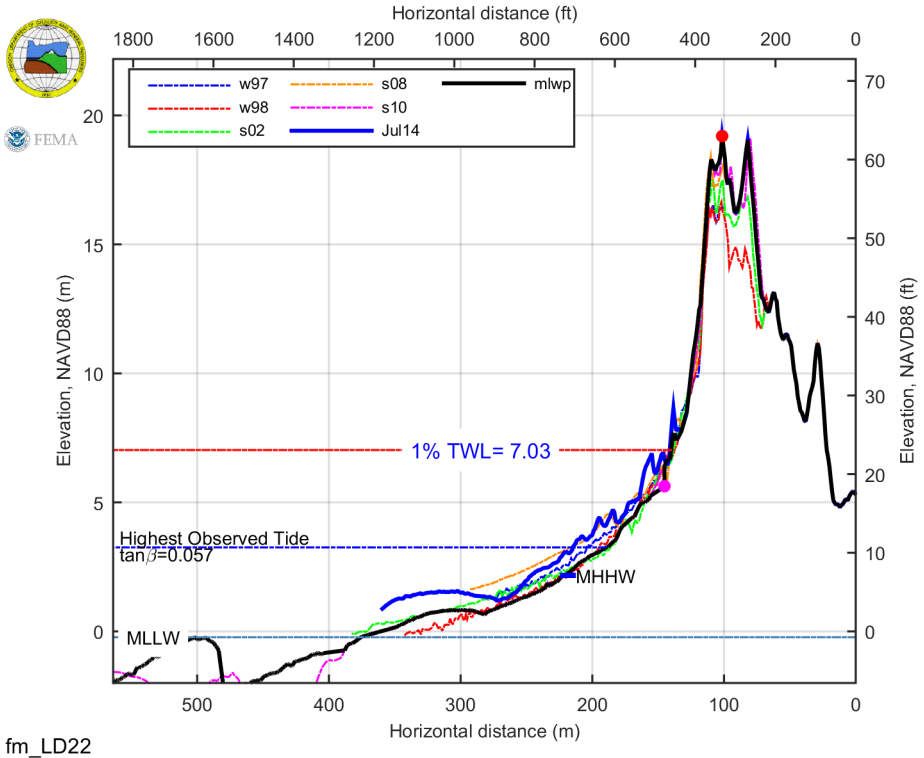


fm_LD22

fm_LD 23

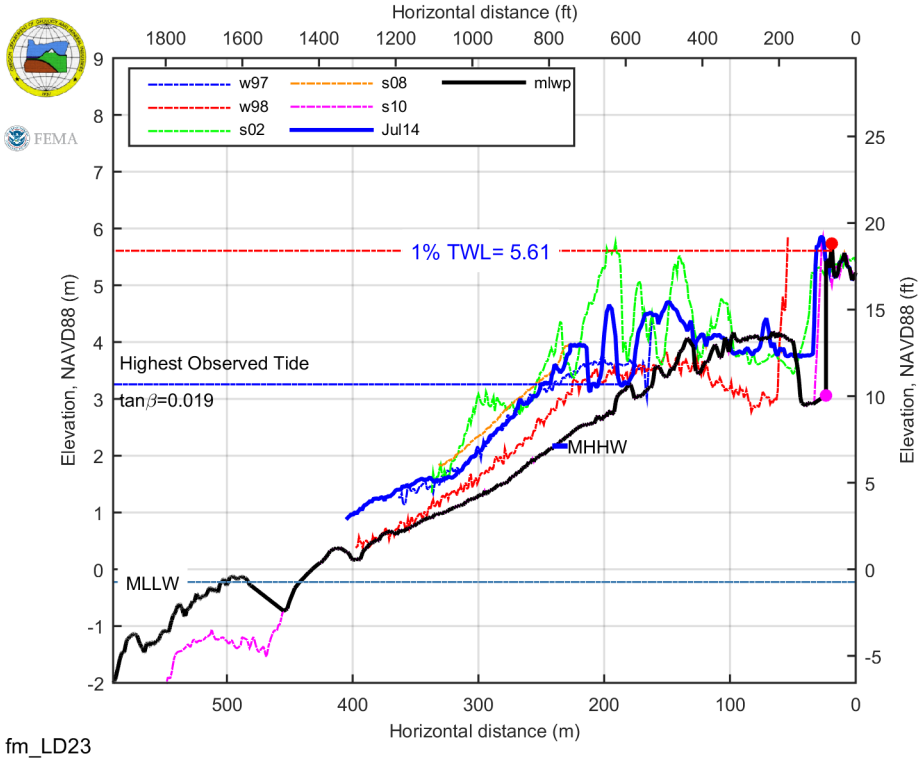


fm_LD23

fm_LD 24

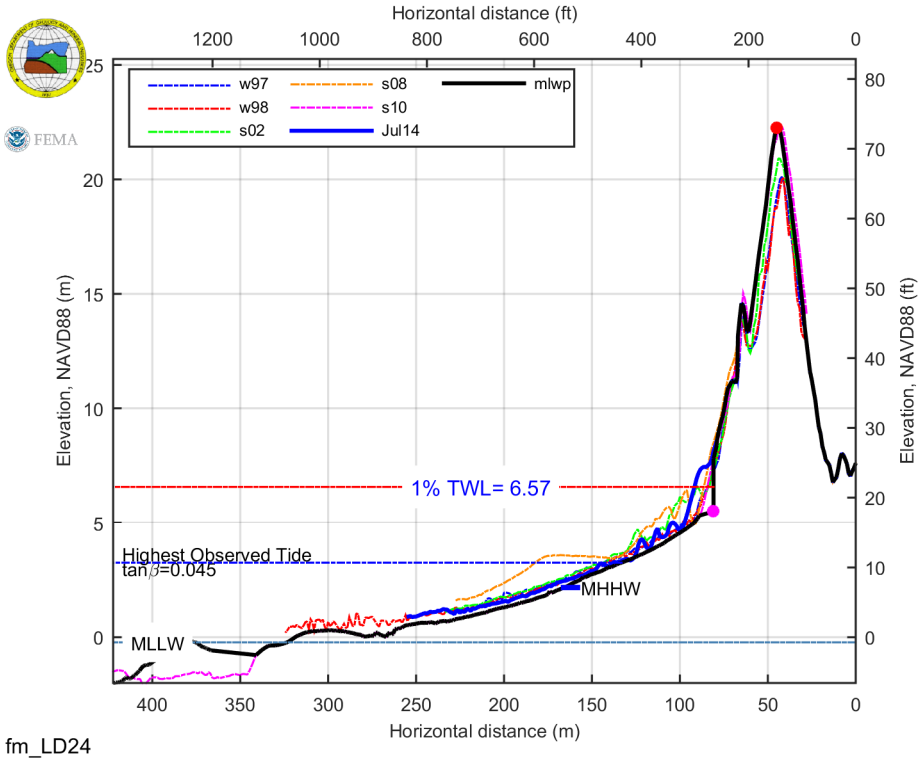


fm_LD24

## 11.3.2 Heceta Head

fm_LD 25

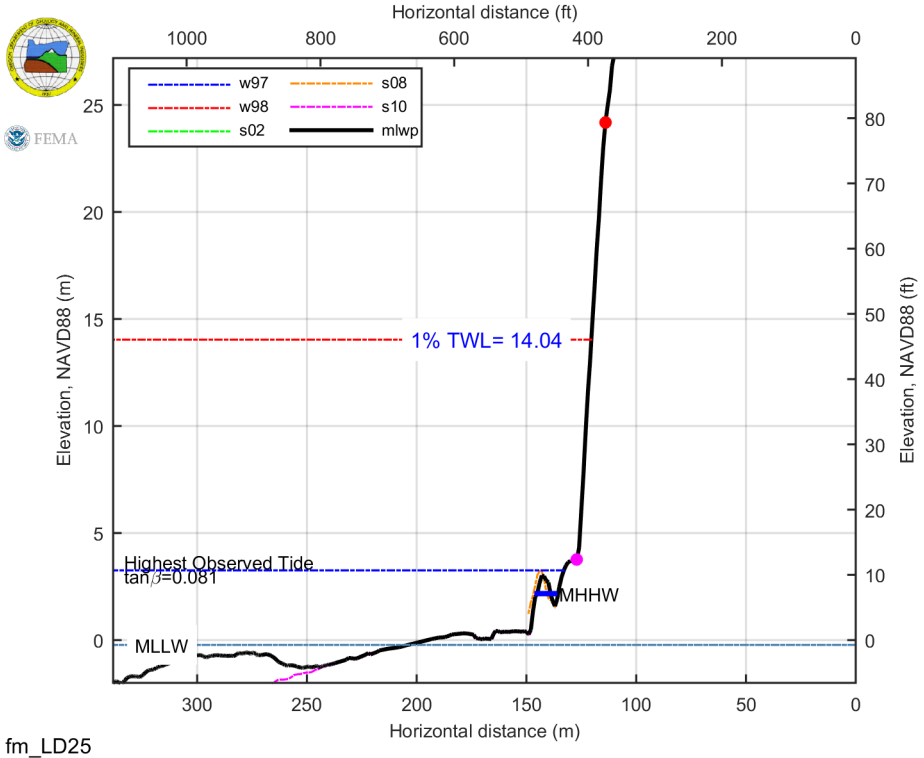


fm_LD25

fm_LD 26

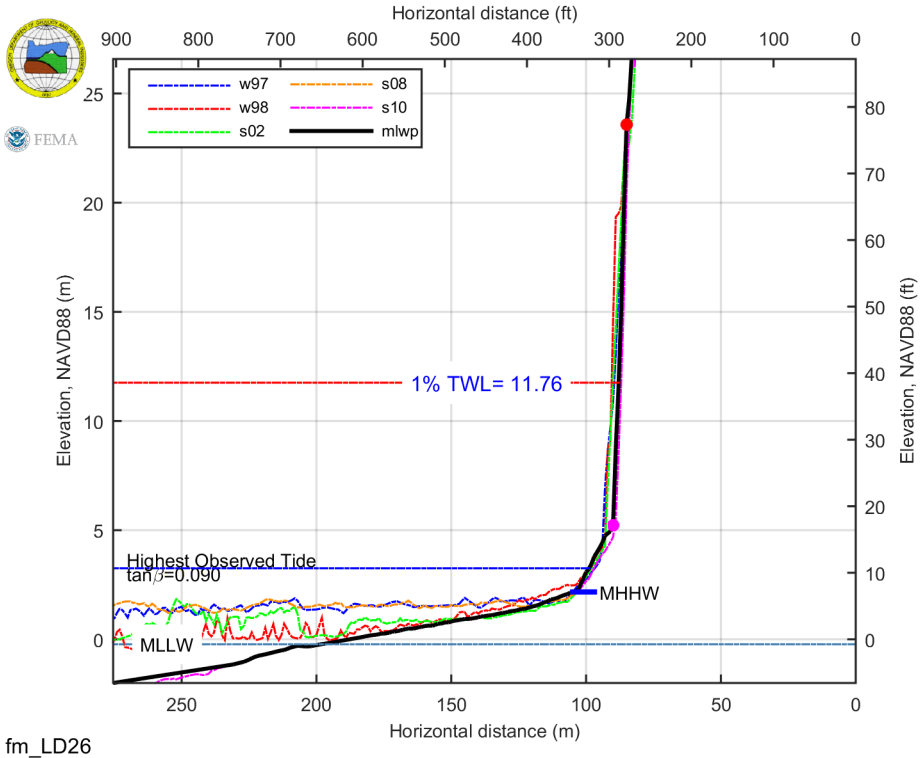


fm_LD26

fm_LD 27

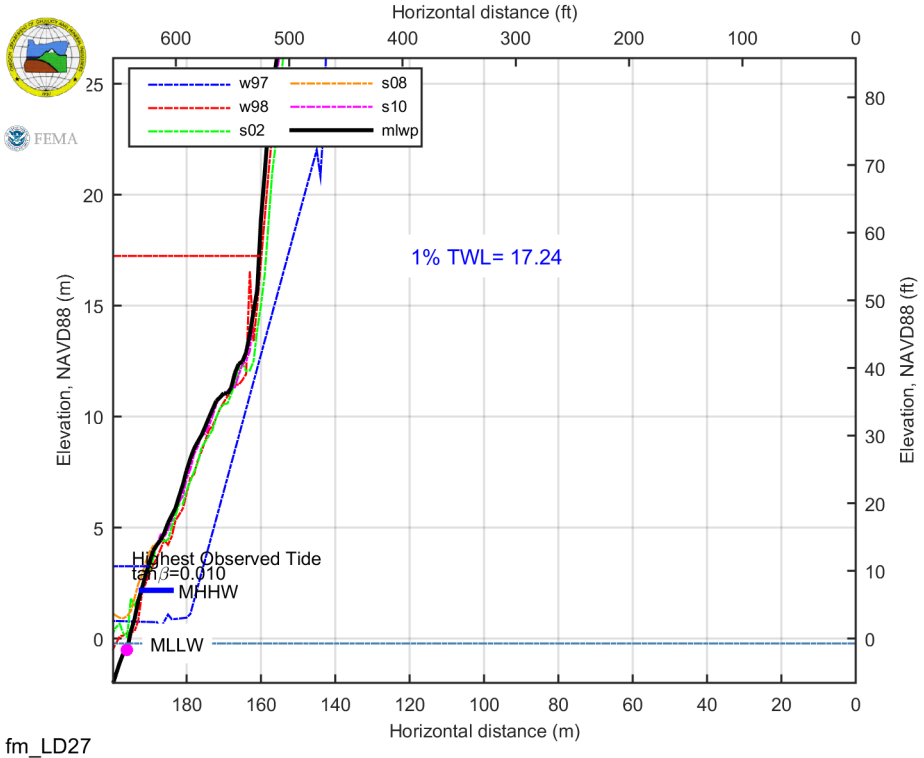


fm_LD27

fm_LD 28

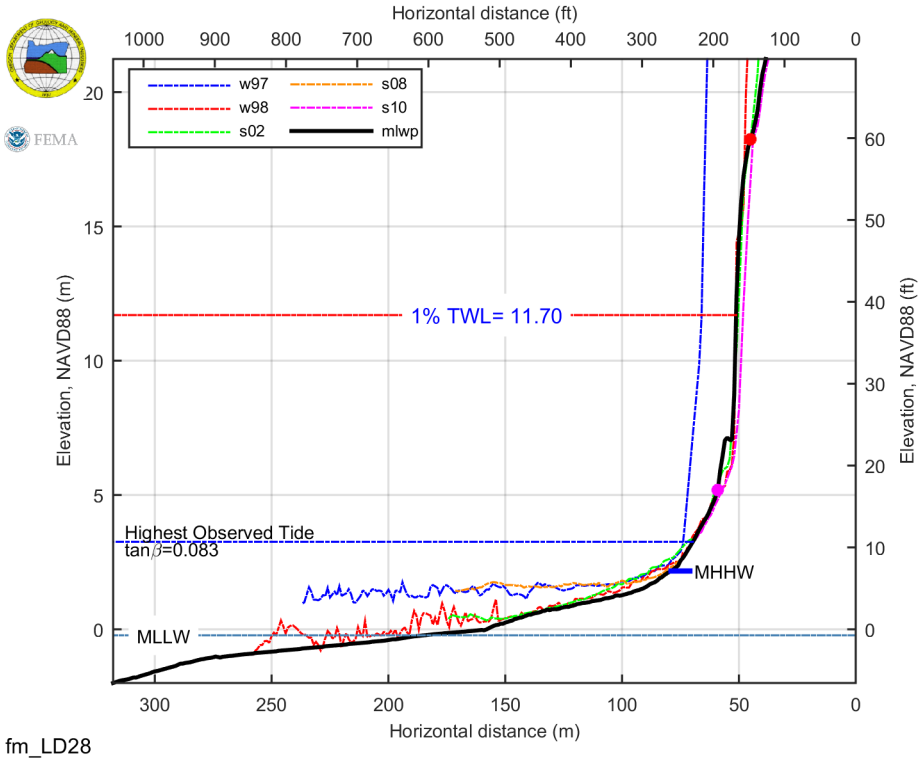


fm_LD28

fm_LD 29

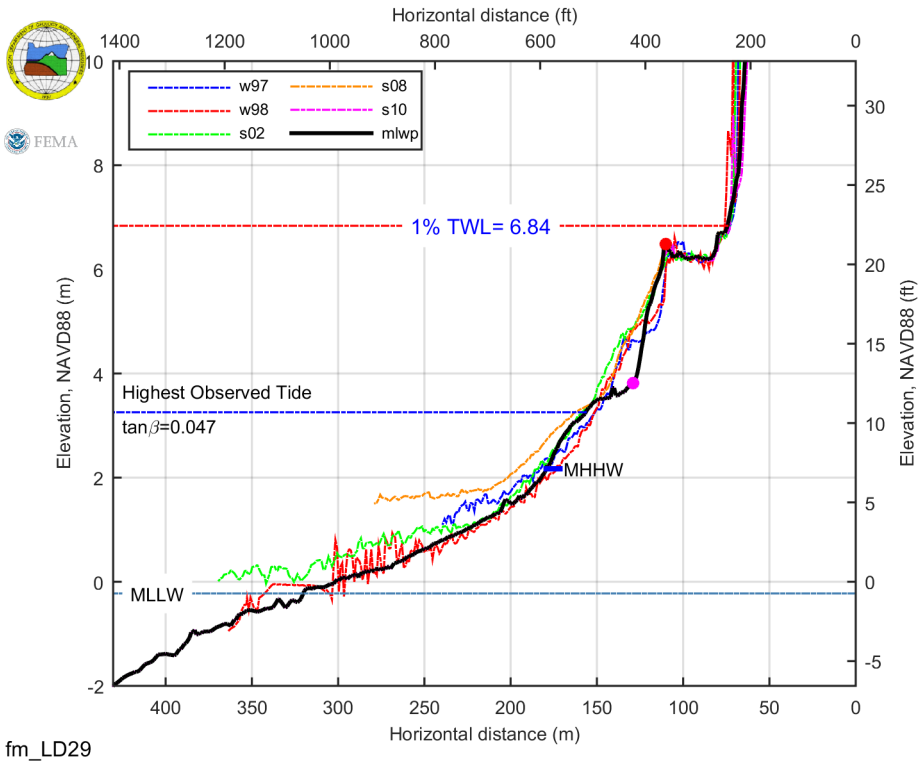


fm_LD29

fm_LD 30

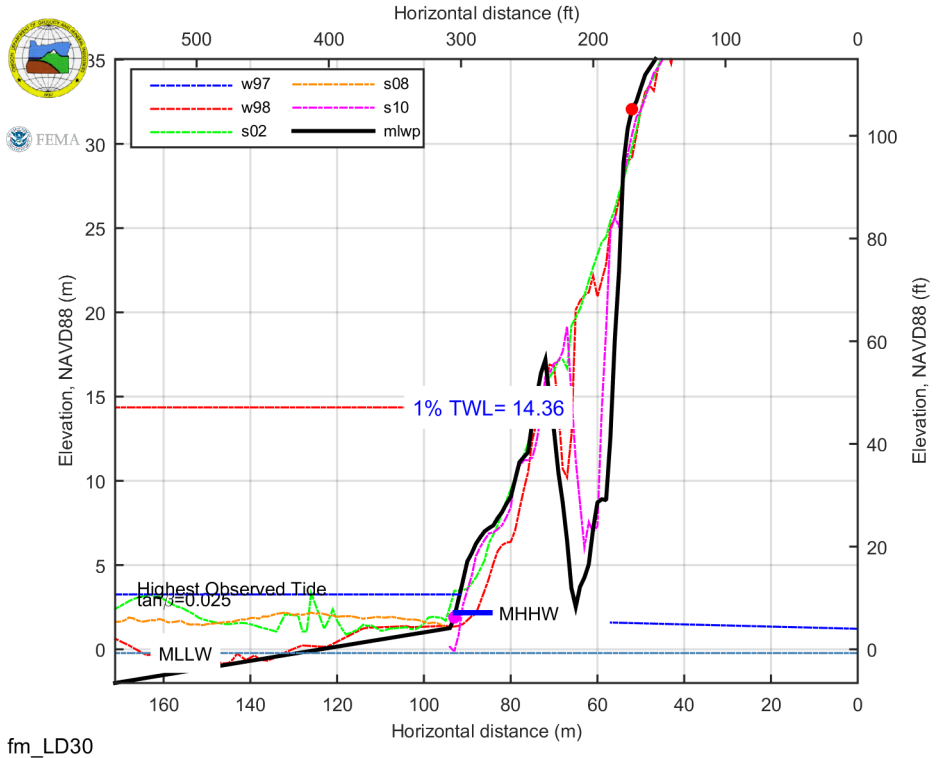


fm_LD30

### 11.3.3 Roosevelt Beach

fm_LD 31

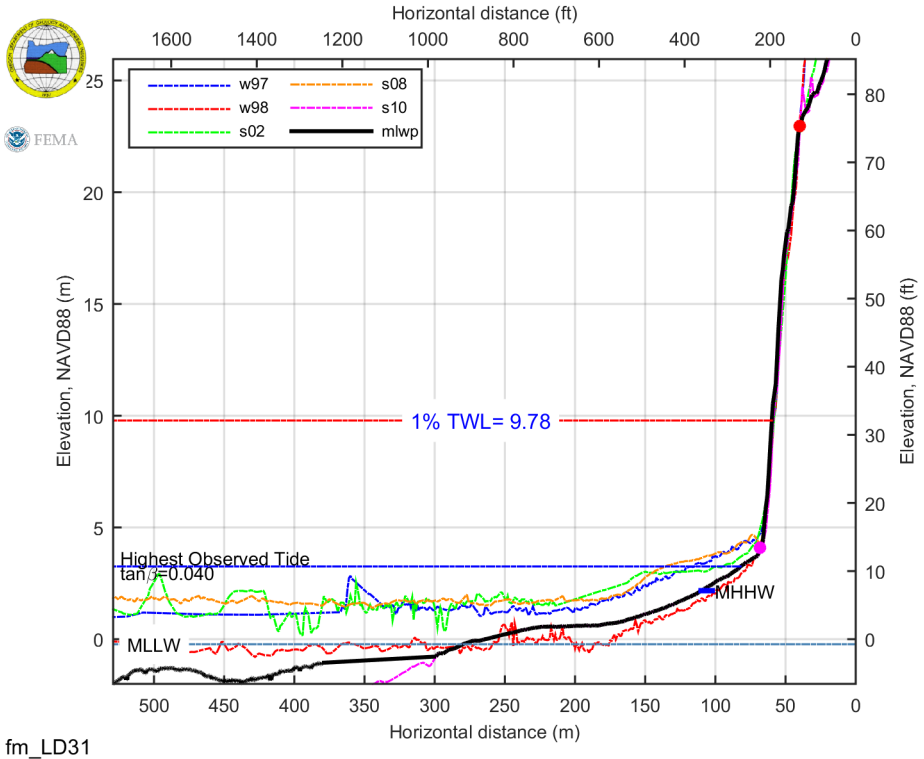


fm_LD31

fm_LD 32

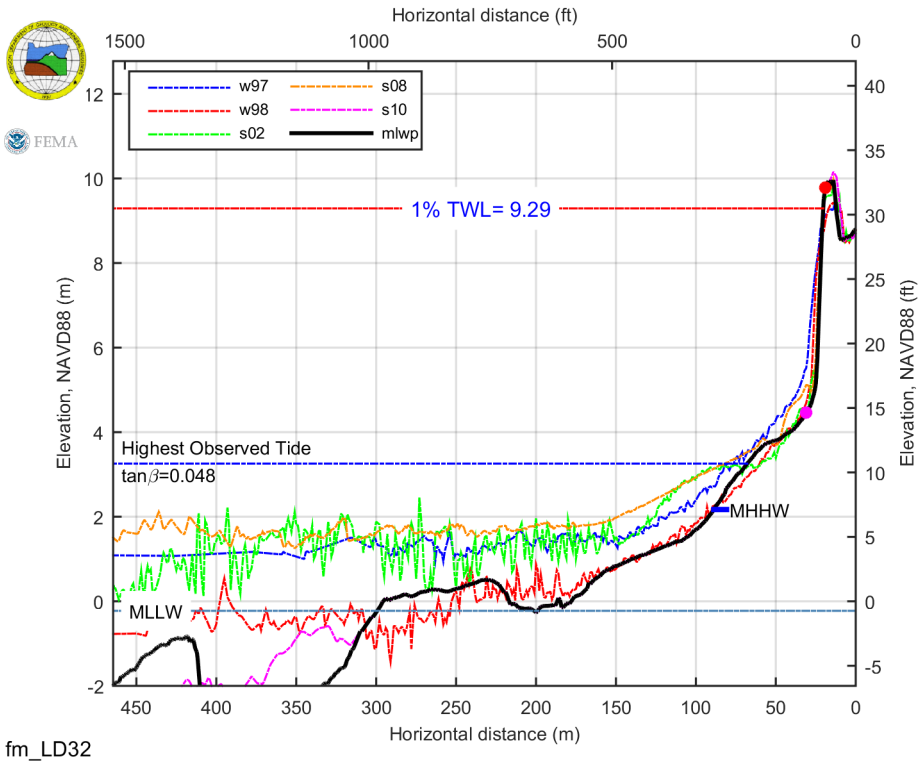


fm_LD32

fm_LD 33

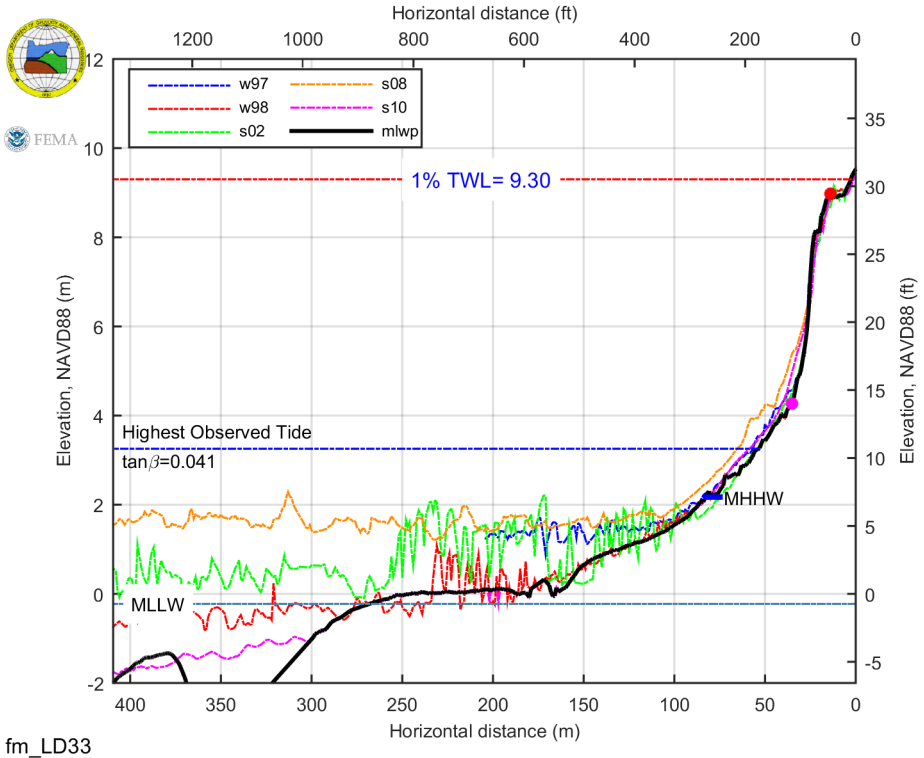


fm_LD33

fm_LD 34

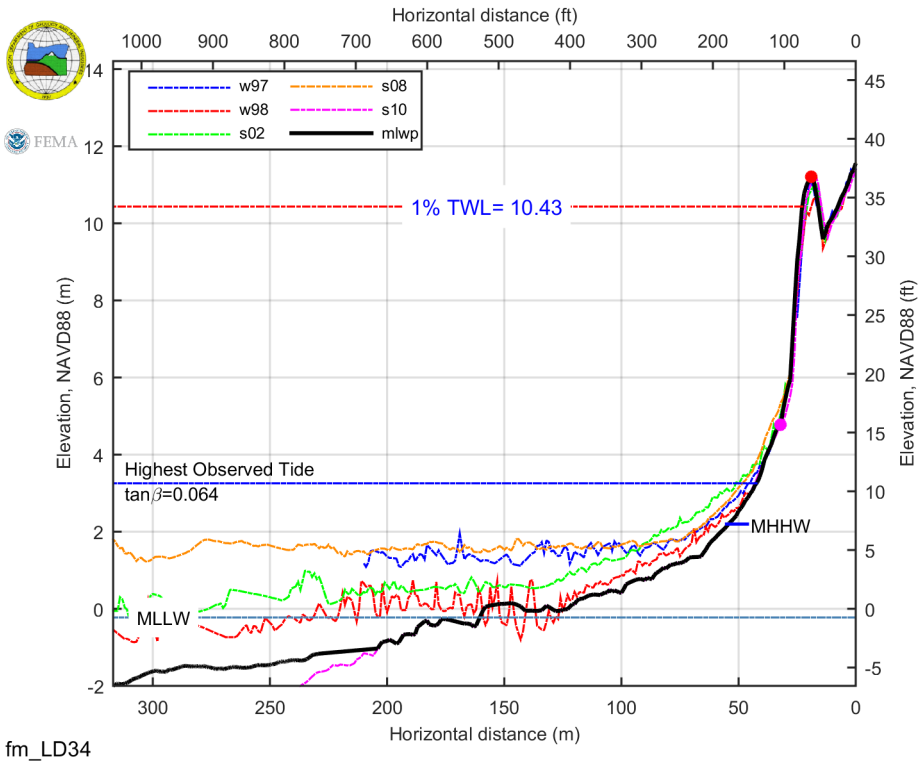


fm_LD34

fm_LD 35

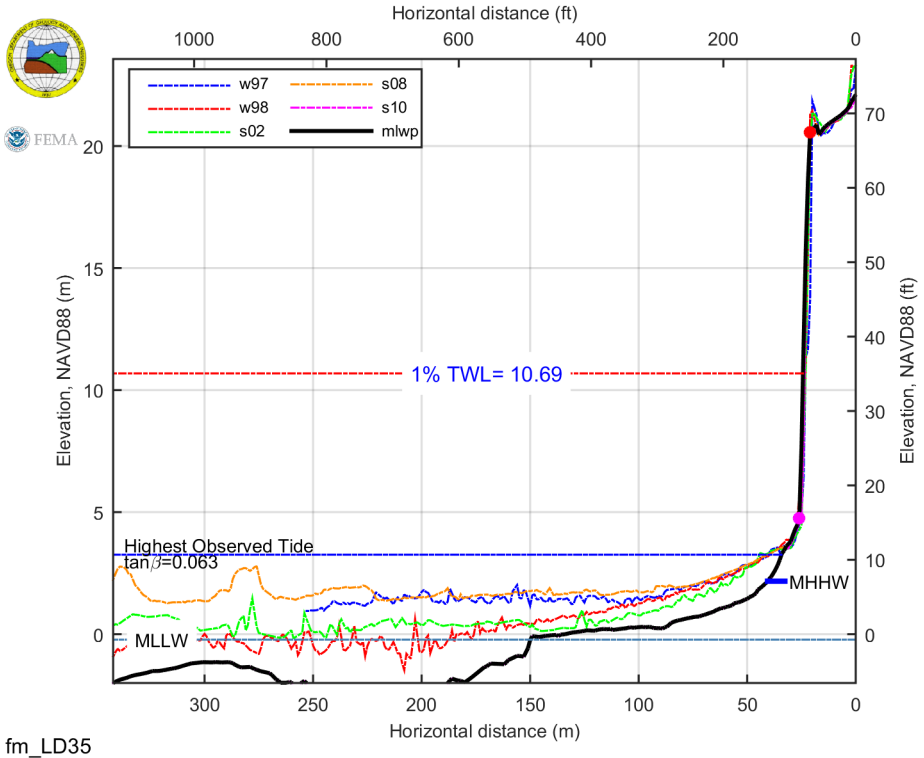


fm_LD35

fm_LD 36

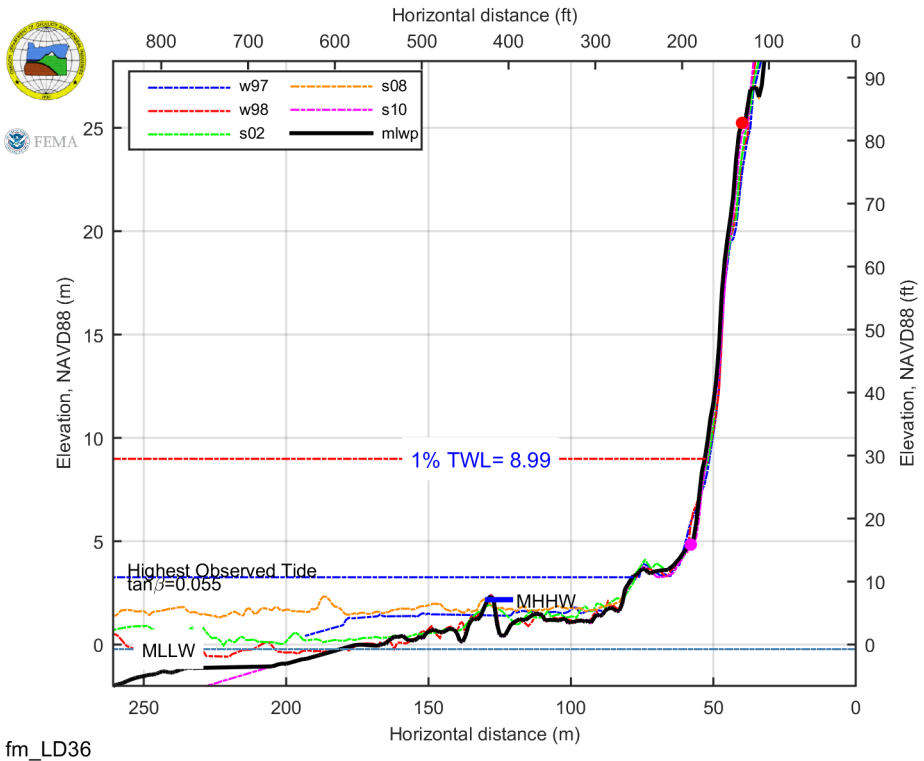


fm_LD36

### 11.3.4 Stonefield Beach

fm_LD 37

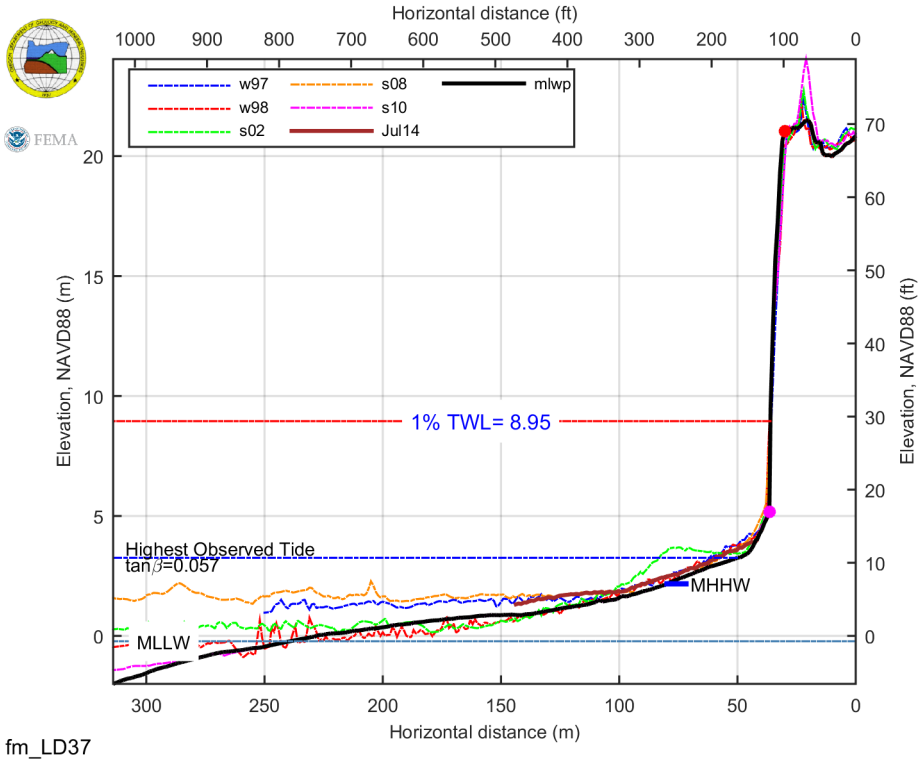


fm_LD37

fm_LD 38

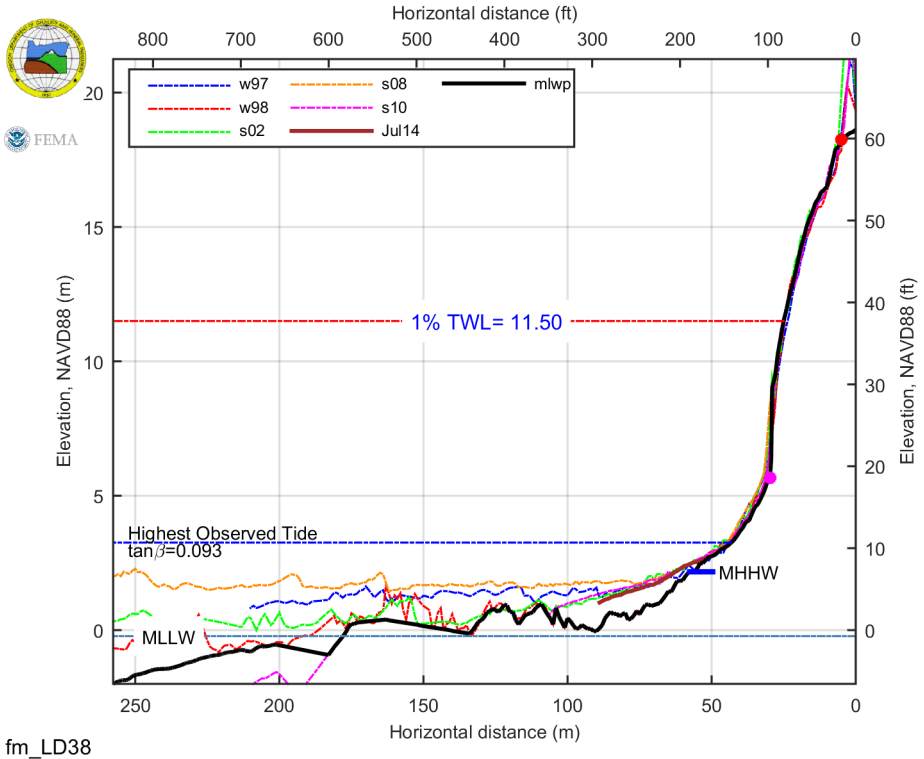


fm_LD38

fm_LD 39

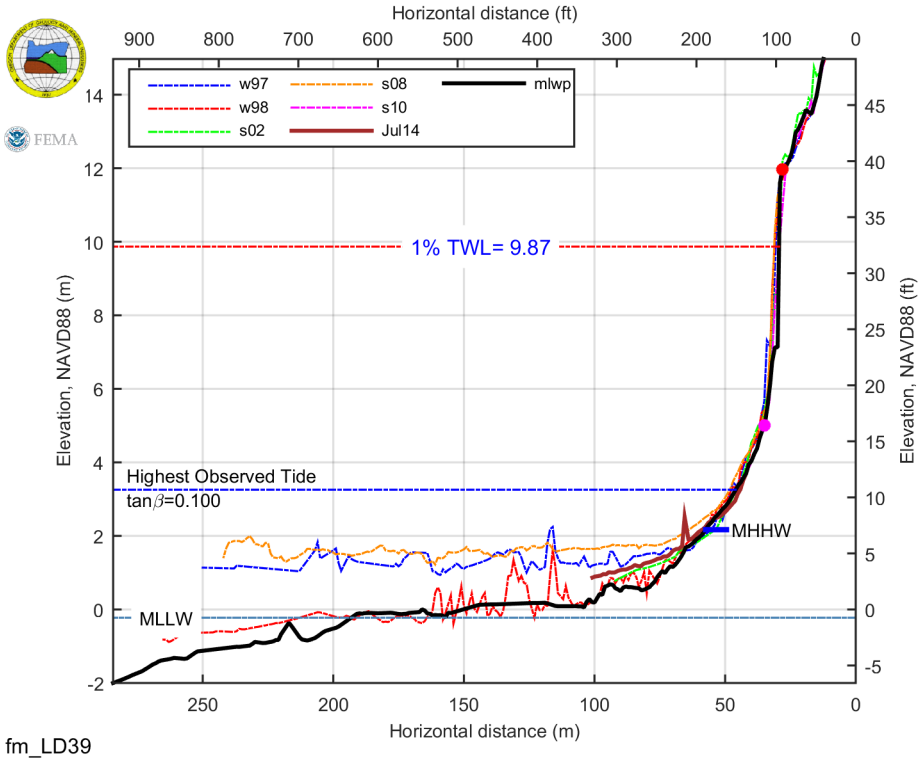


fm_LD39

fm_LD 40

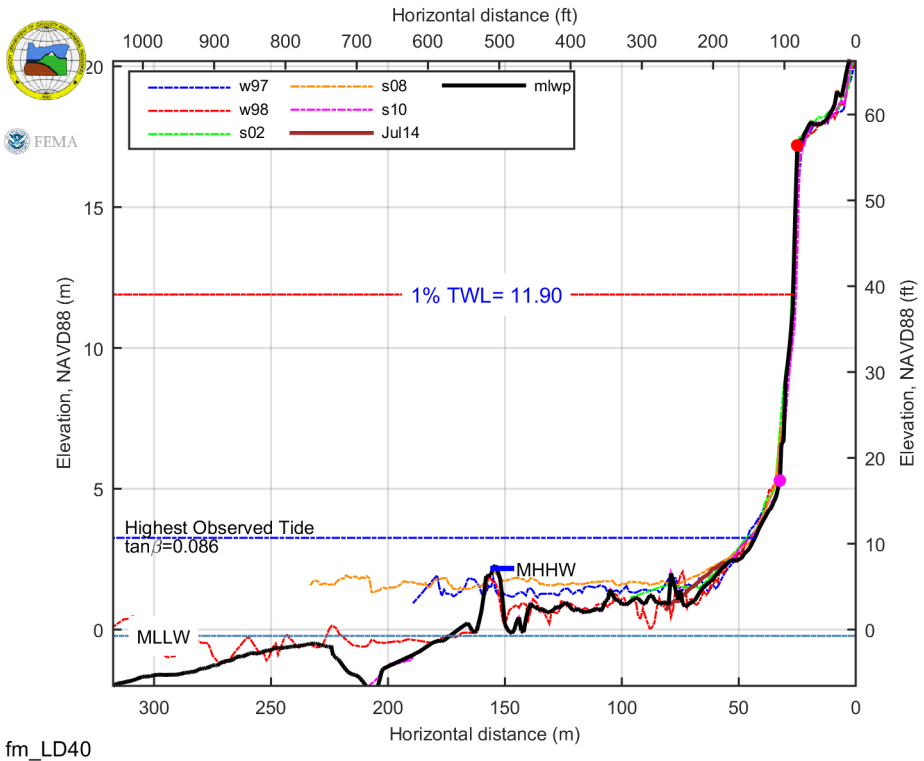


fm_LD40

fm_LD 41

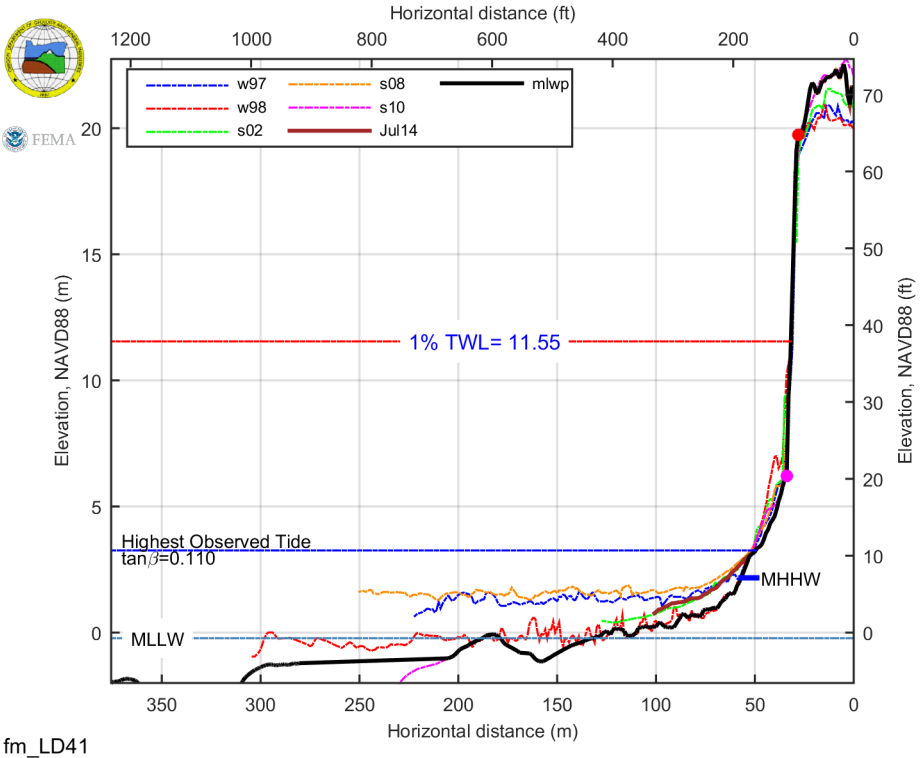


fm_LD41

fm_LD 42

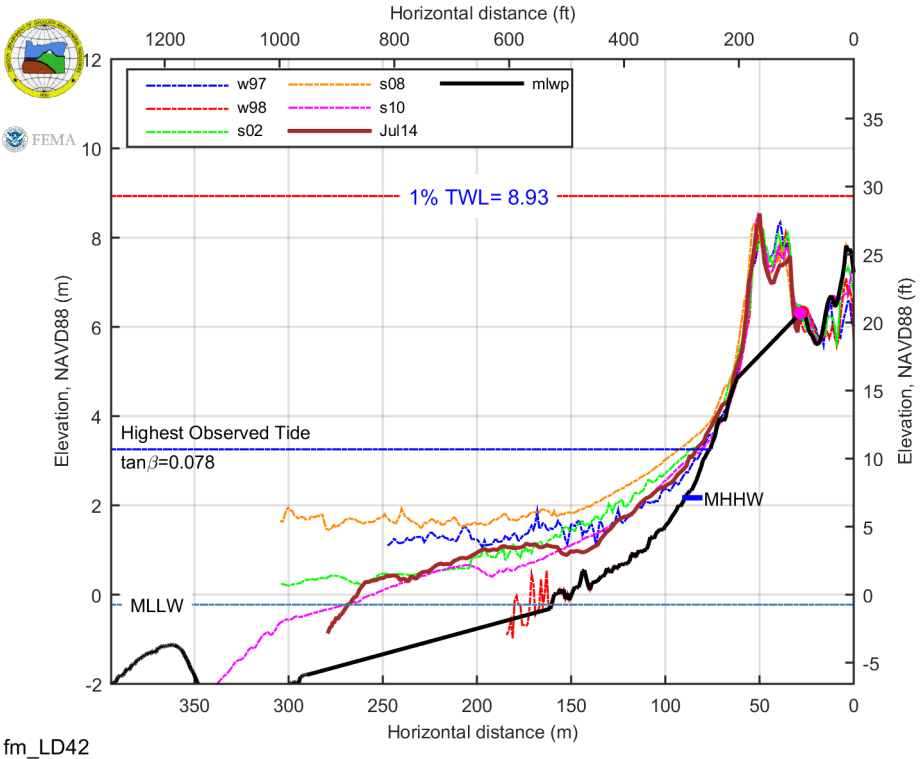


fm_LD42

fm_LD 43

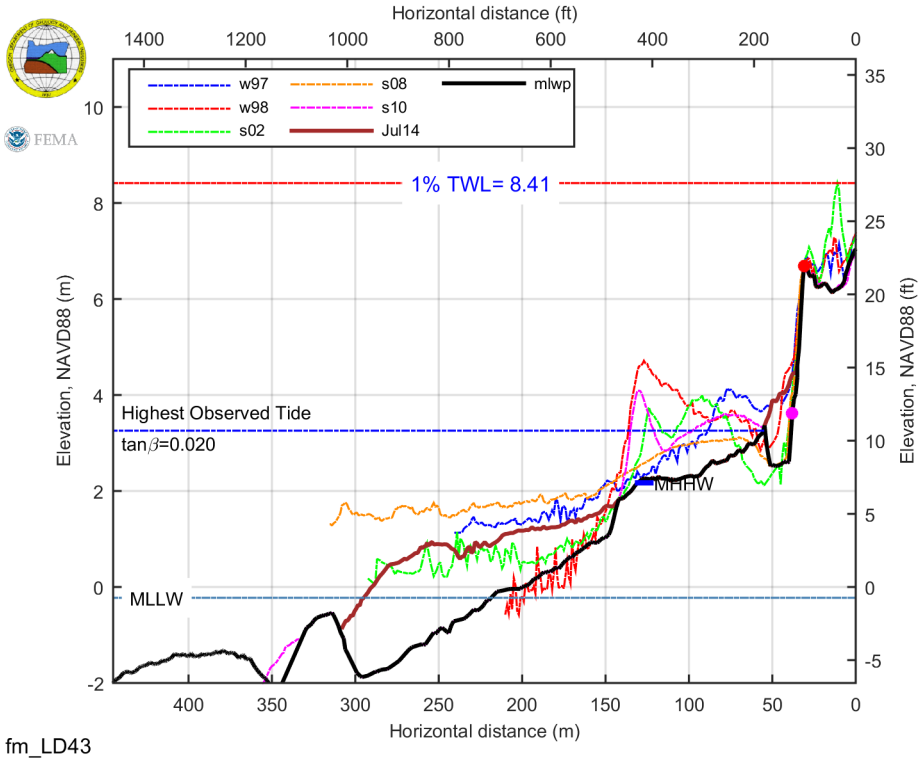


fm_LD43

fm_LD 44

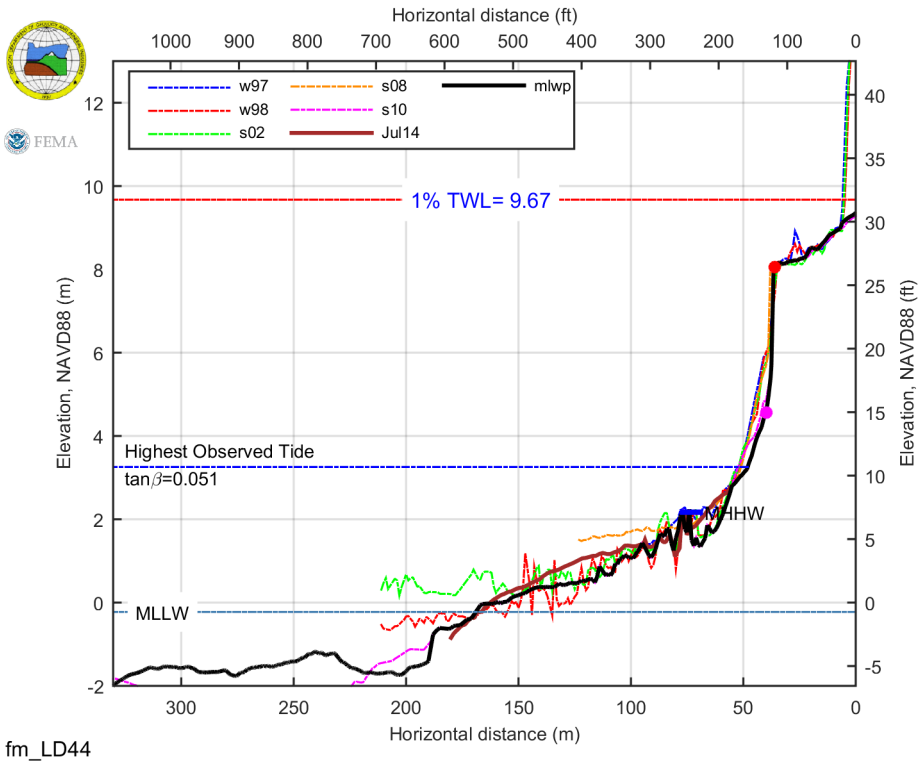


fm_LD44

fm_LD 45

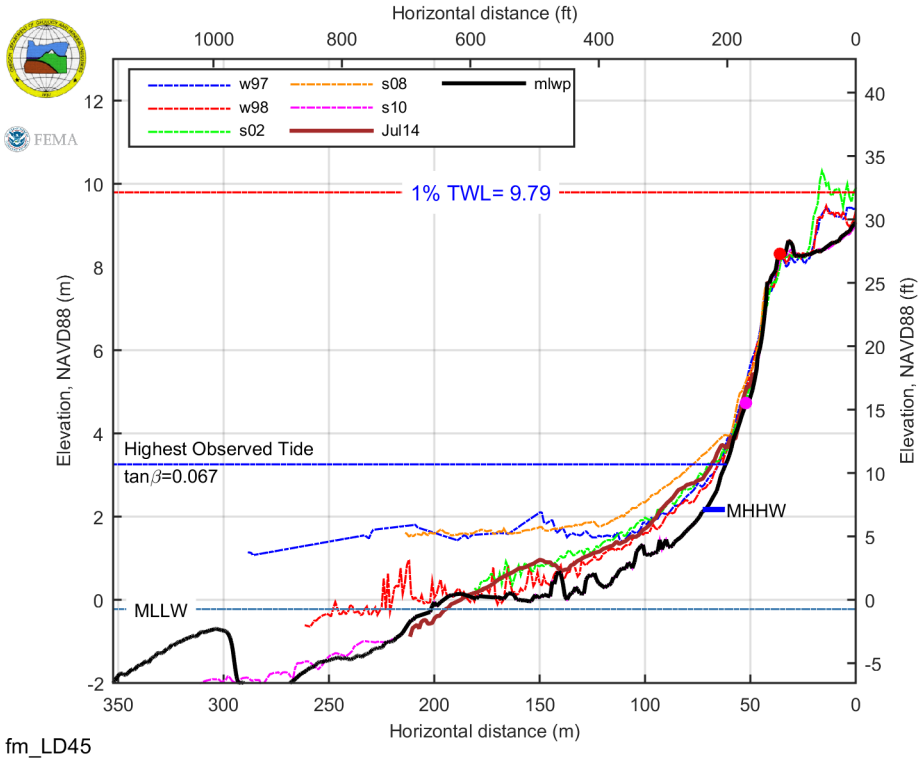


fm_LD45

fm_LD 46

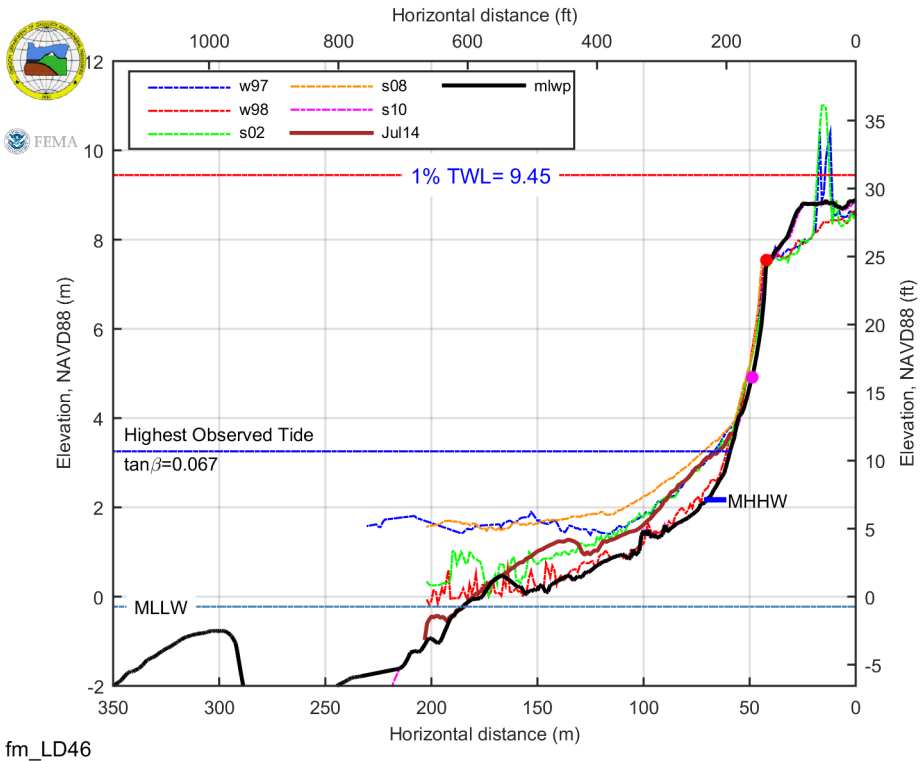


fm_LD46

fm_LD 47

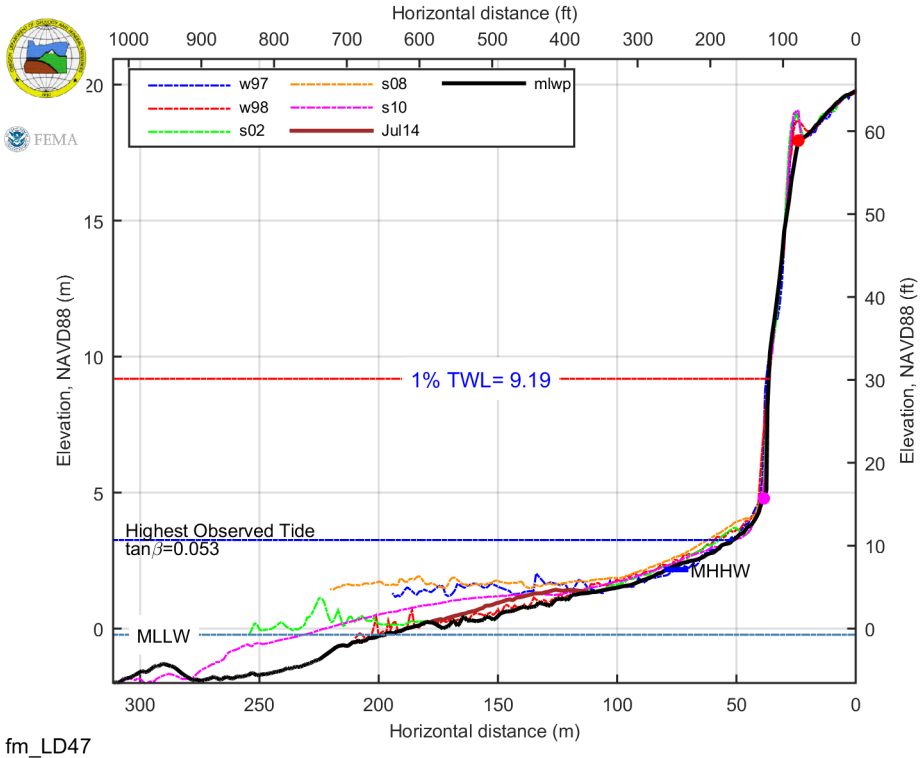


fm_LD47

fm_LD 48

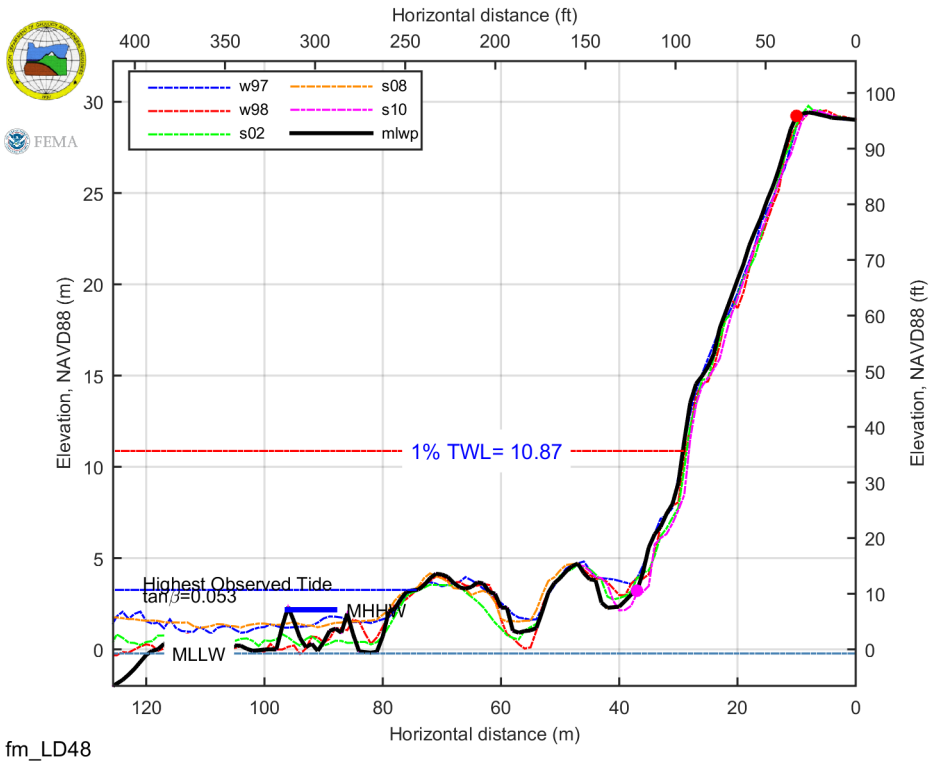


fm_LD48

fm_LD 49

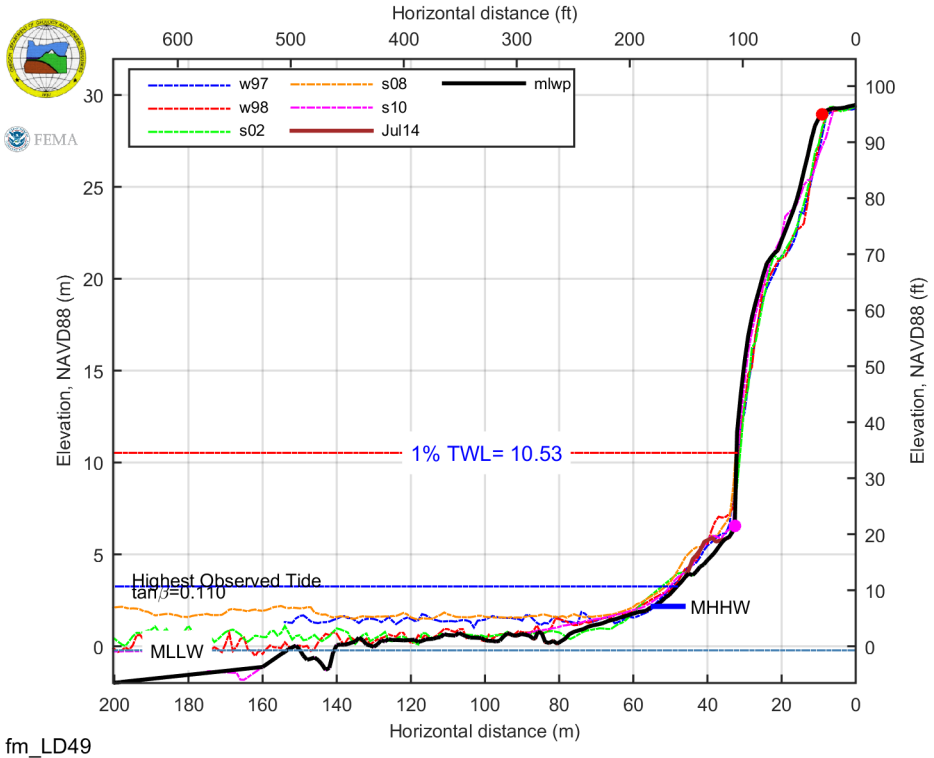


fm_LD49

fm_LD 50

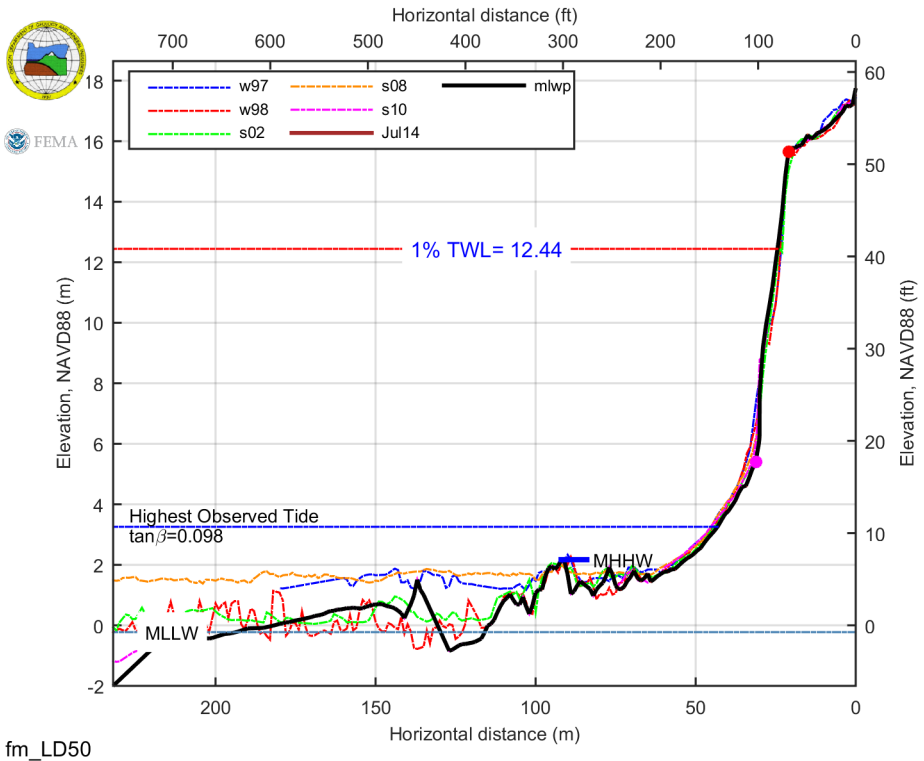


fm_LD50

fm_LD 51

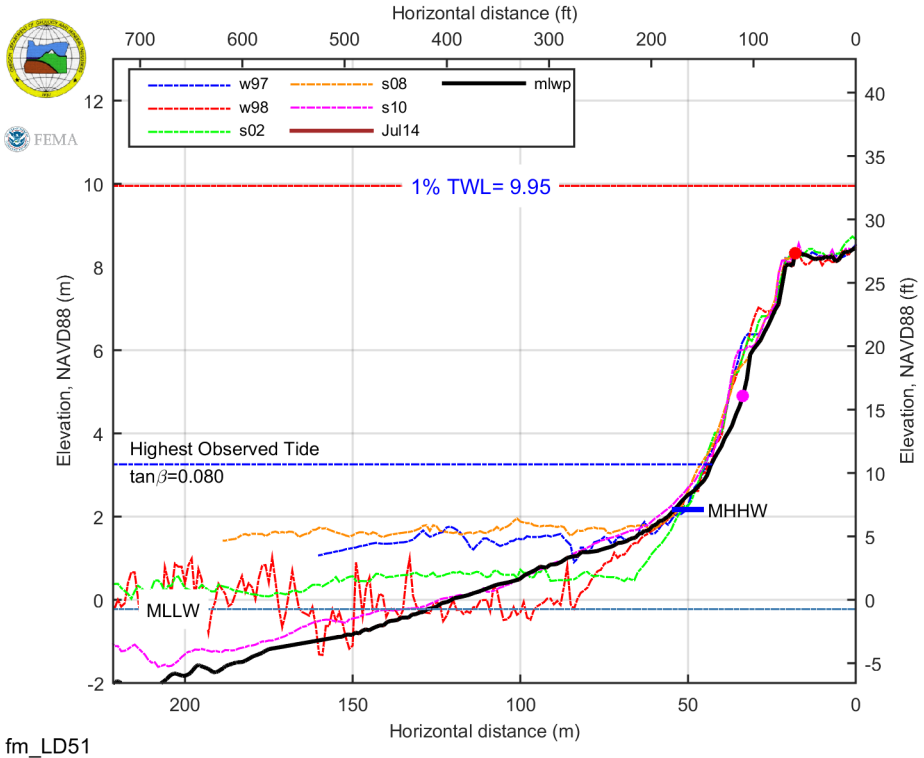


fm_LD51

fm_LD 52

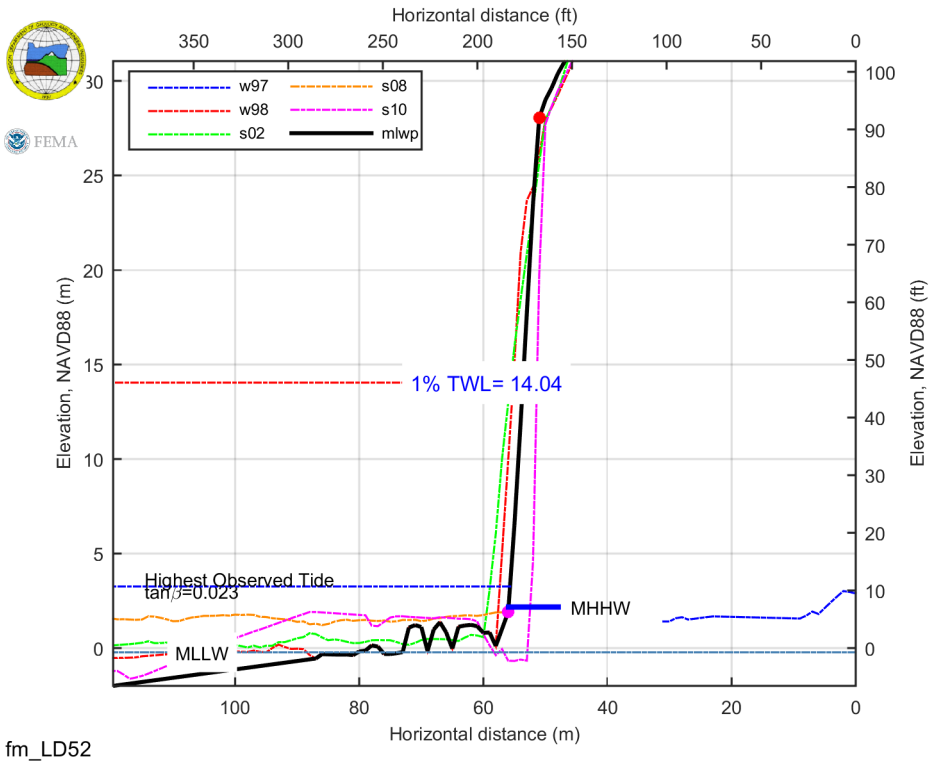


fm_LD52

fm_LD 53

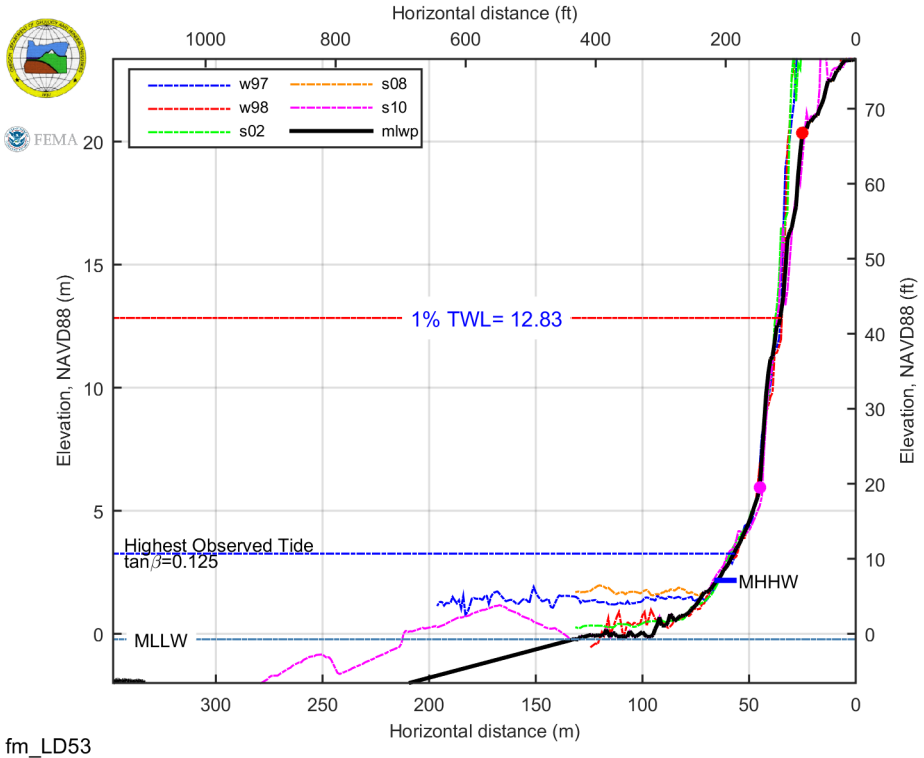


fm_LD53

fm_LD 54

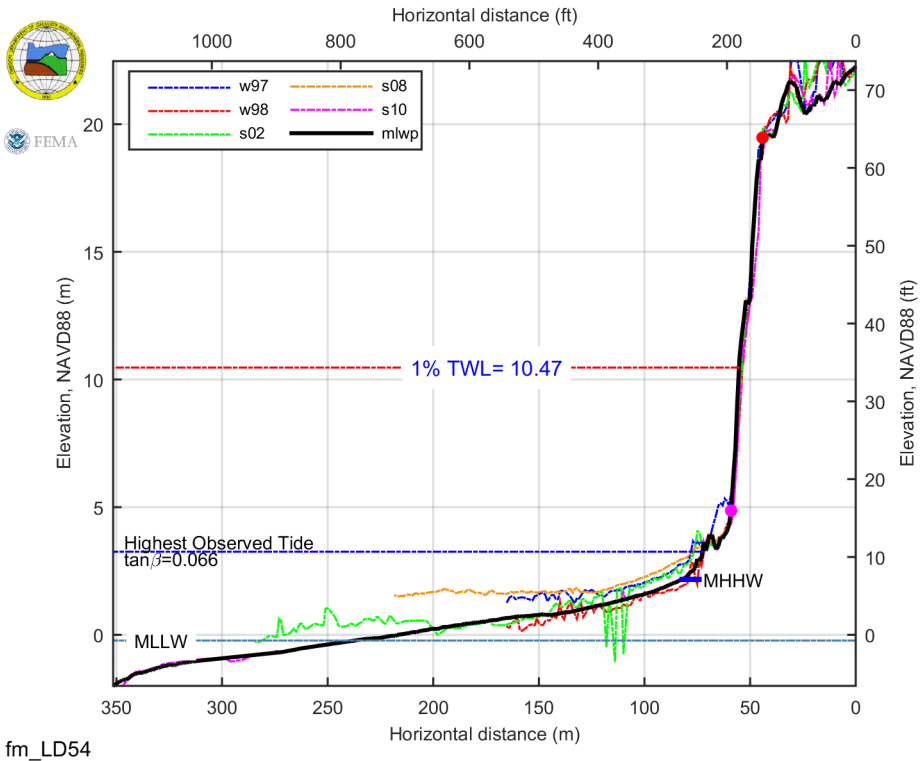


fm_LD54

fm_LD 55

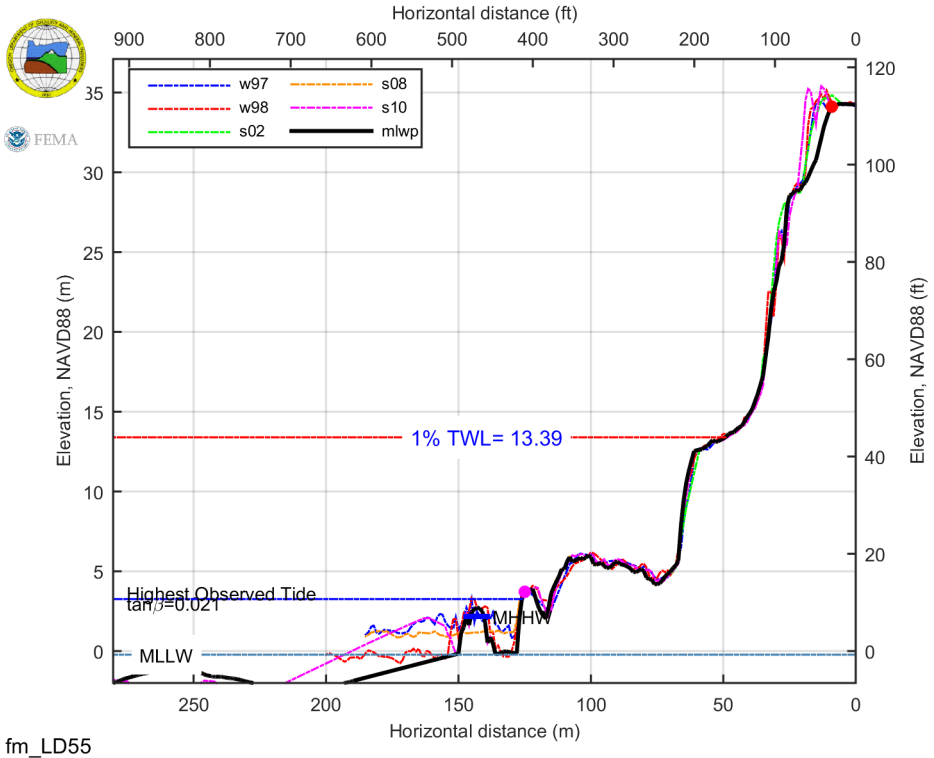


fm_LD55

fm_LD 56

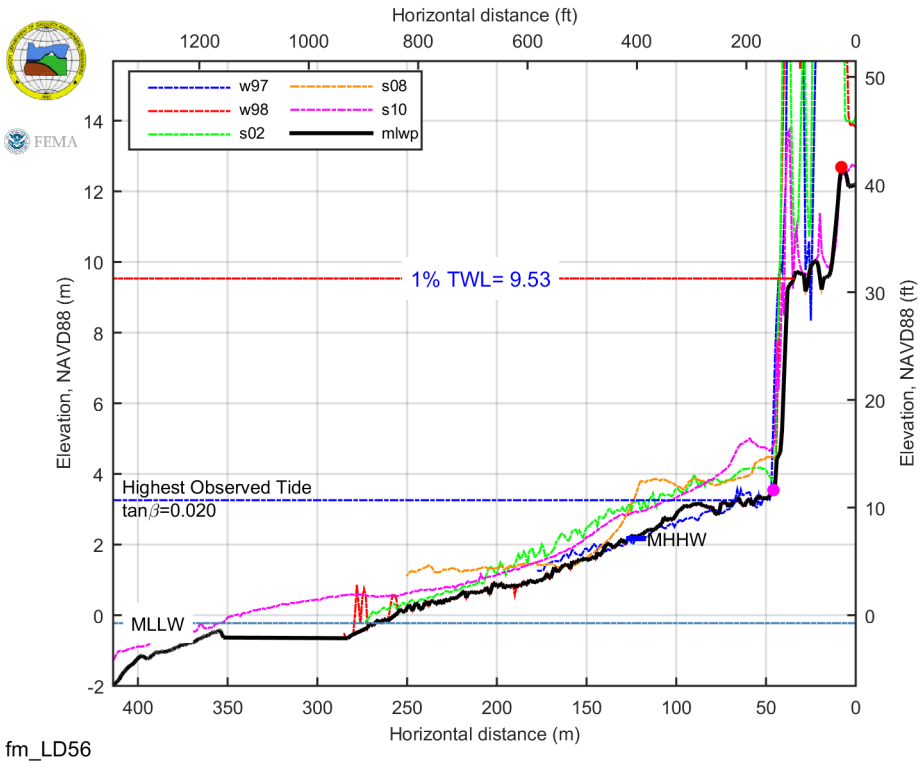


fm_LD56

fm_LD 57

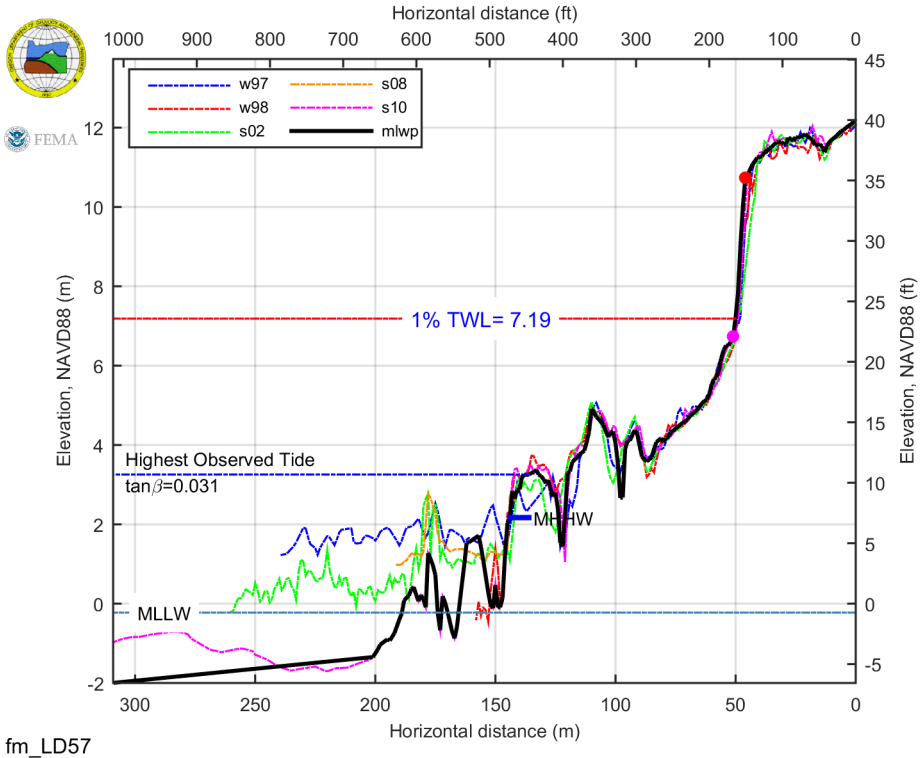


fm_LD57

### 11.3.5 Supplemental Lines

fm_LD 33_575

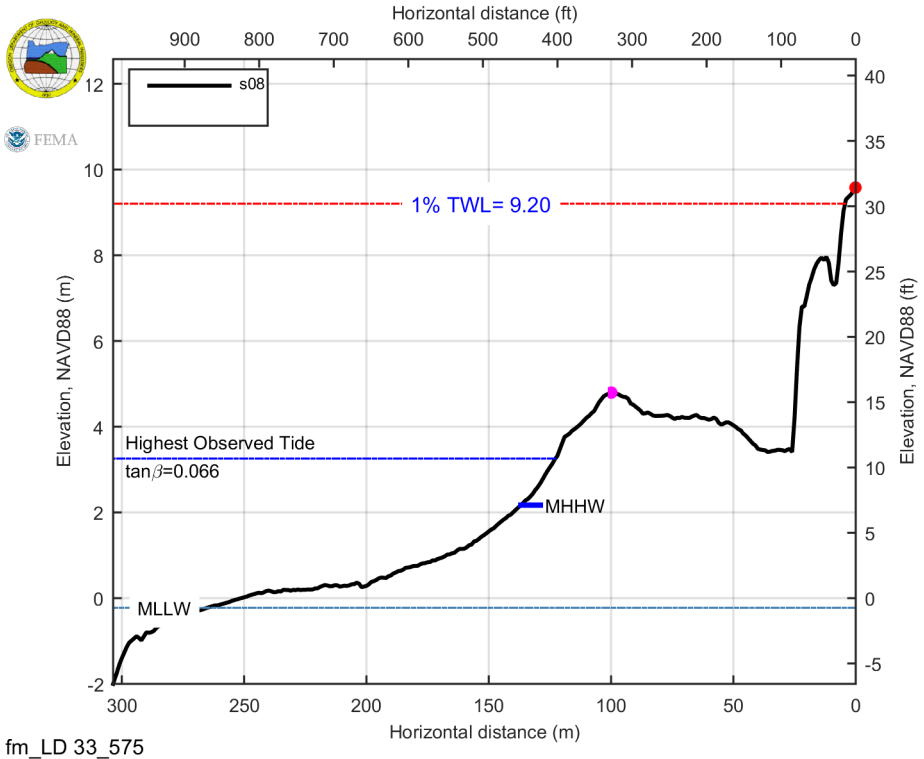


fm_LD 33_575

fm_LD 33_577

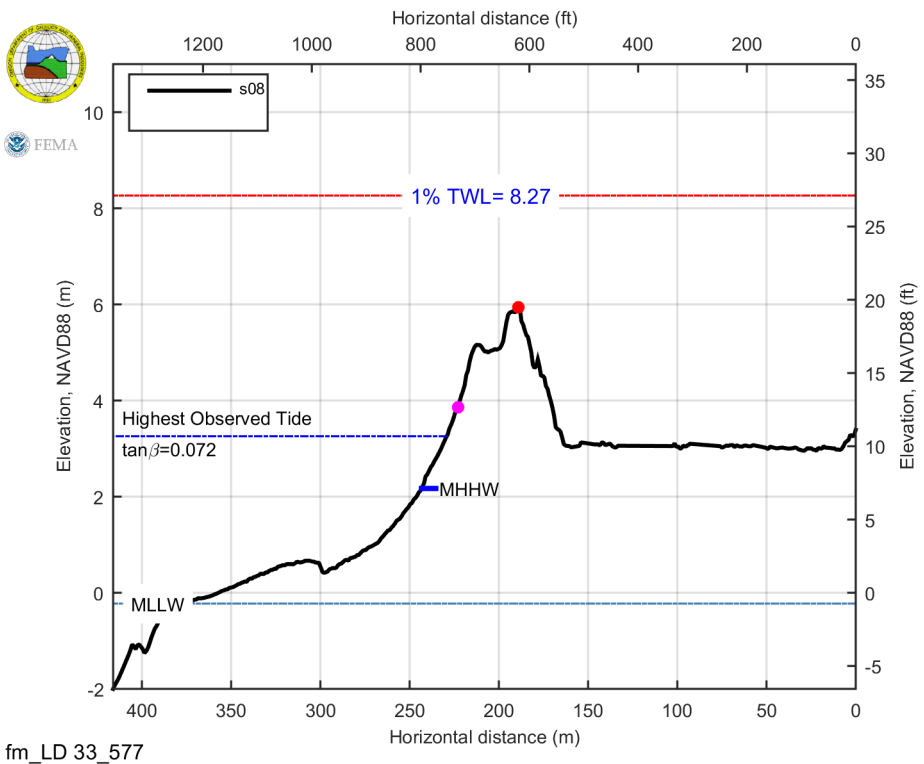


fm_LD 33_577

fm_LD 34_523

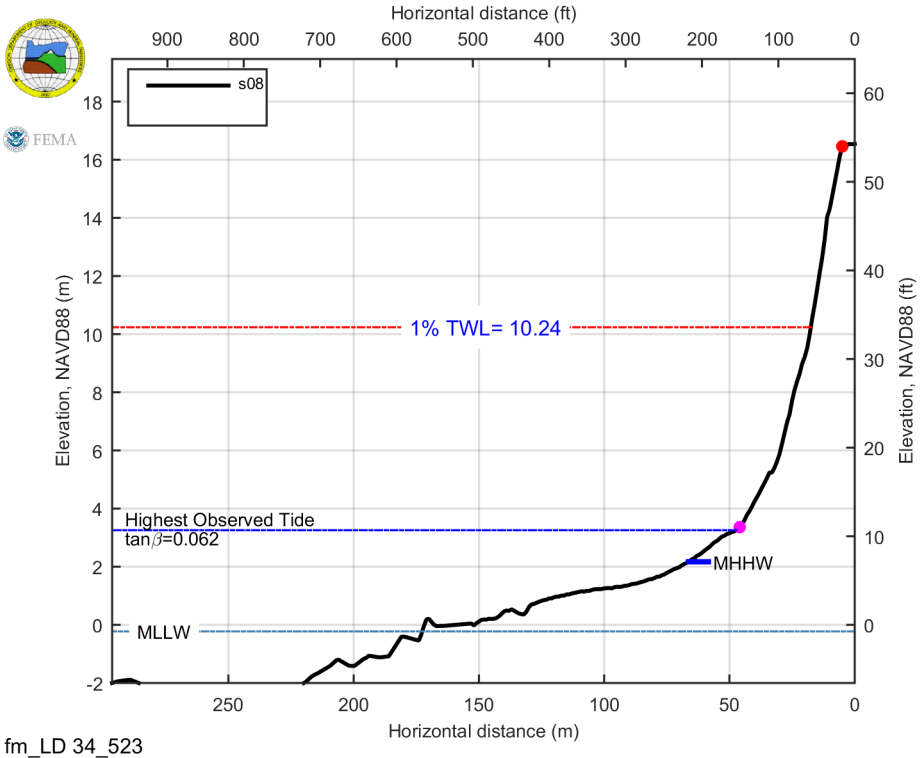


fm_LD 34_523

fm_LD 34_530

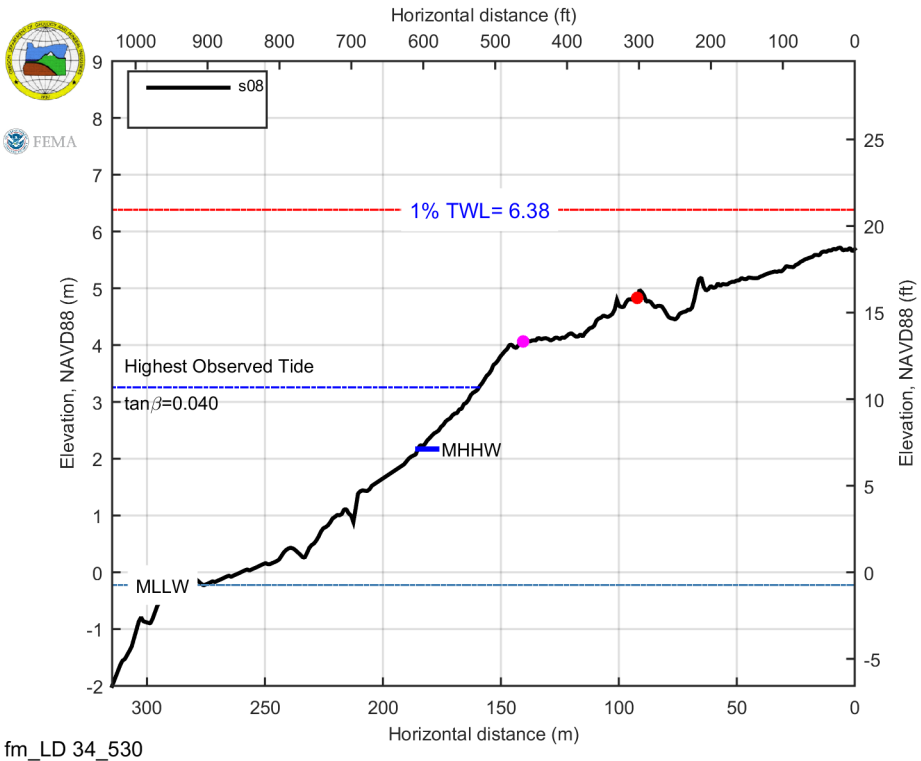


fm_LD 34_530

fm_LD 42_292

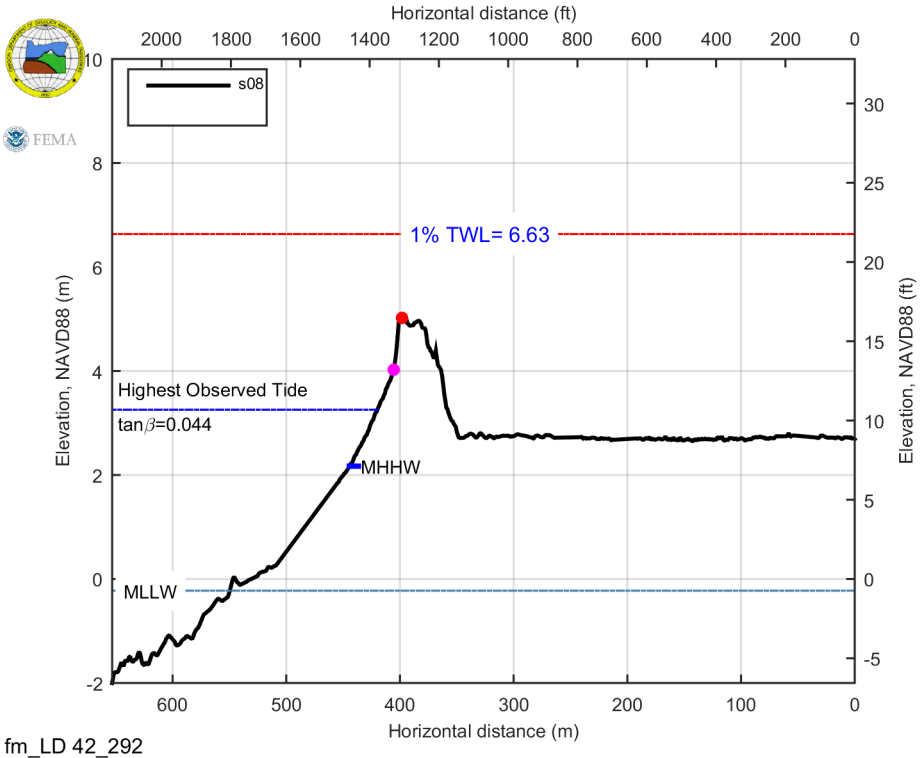


fm_LD 42_292

fm_LD 51_179

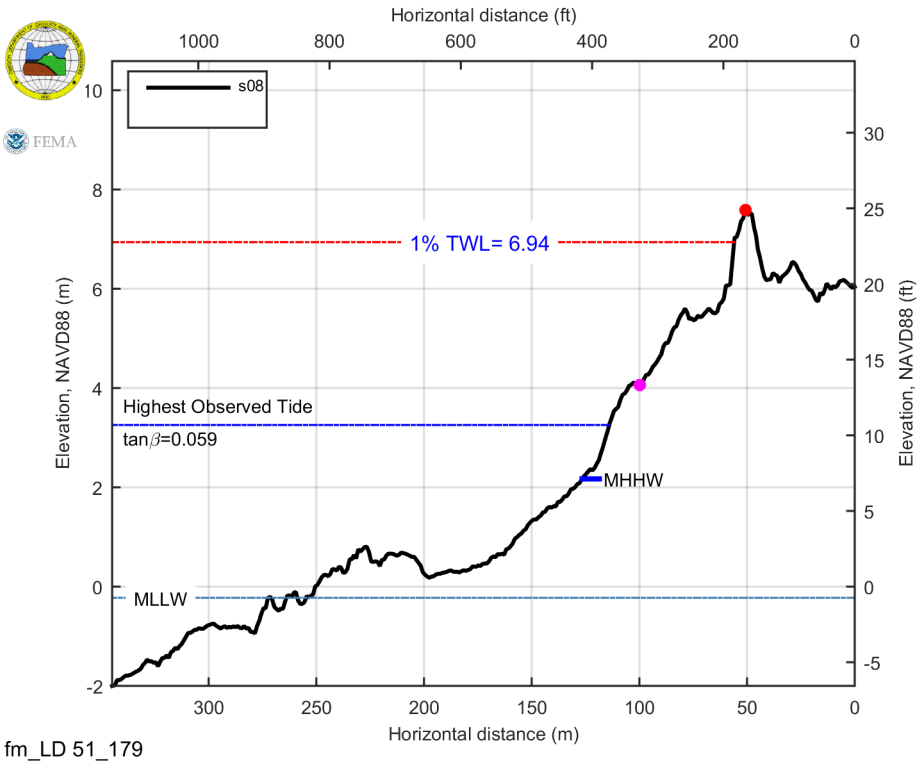


fm_LD 51_179

fm_LD 51_177

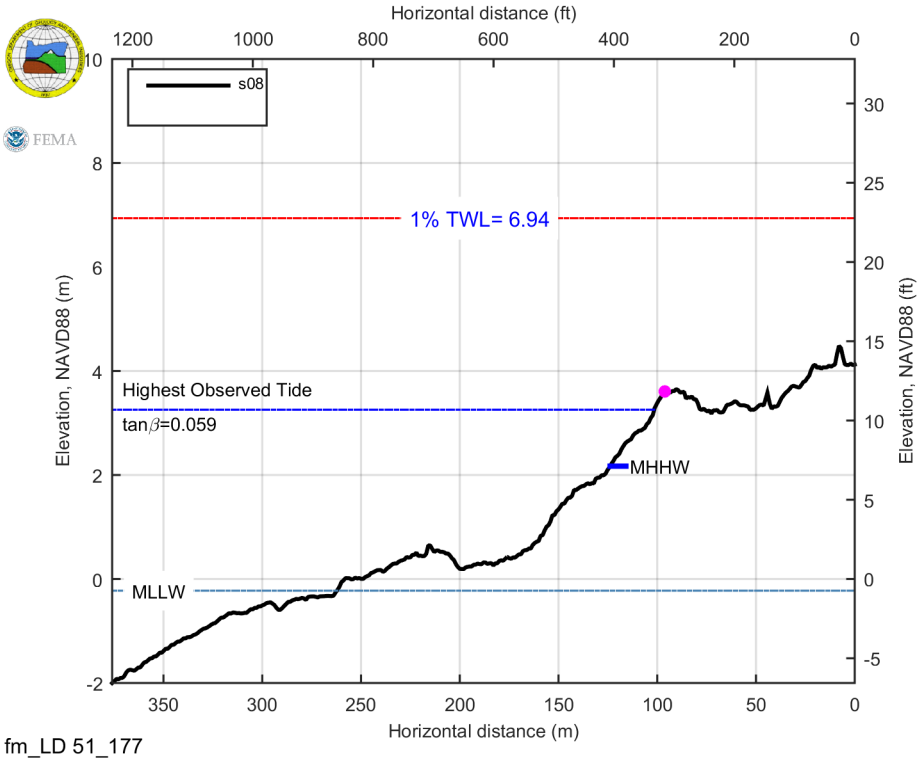


fm_LD 51_177

fm_LD 56_49

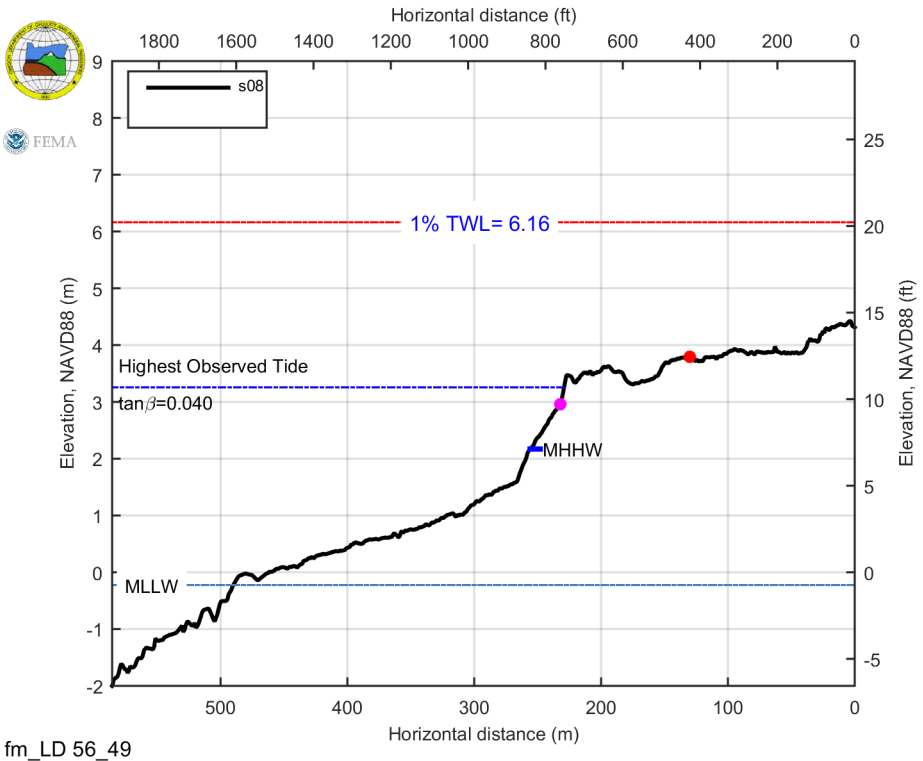


fm_LD 56_49

fm_LD 56_54

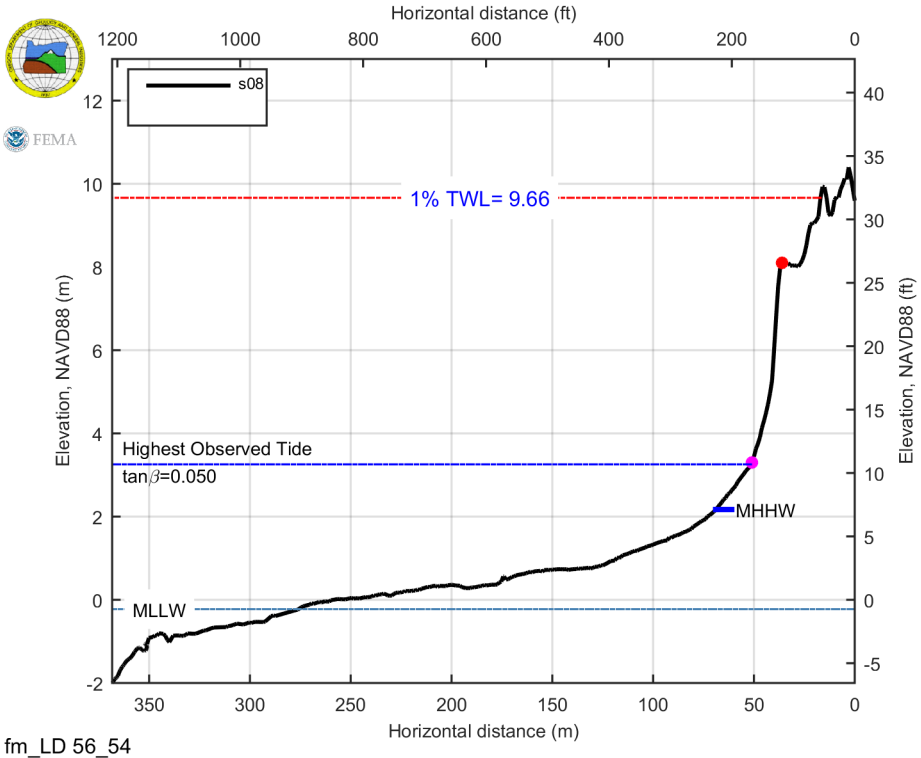


fm_LD 56_54

fm_LD 29_1

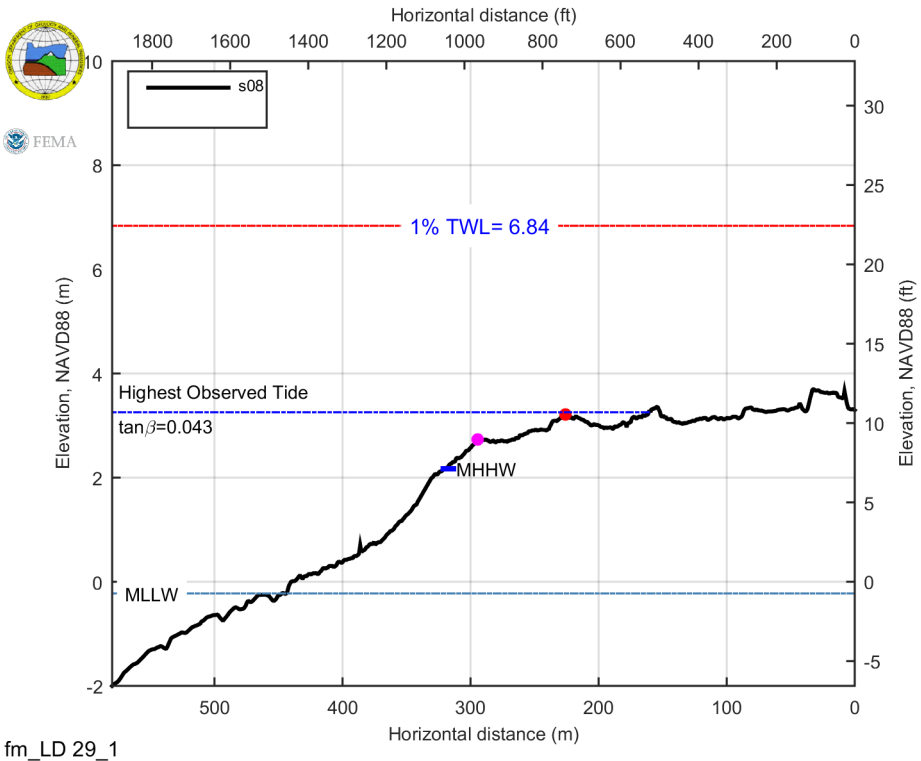


fm_LD 29_1

fm_LD 42_312

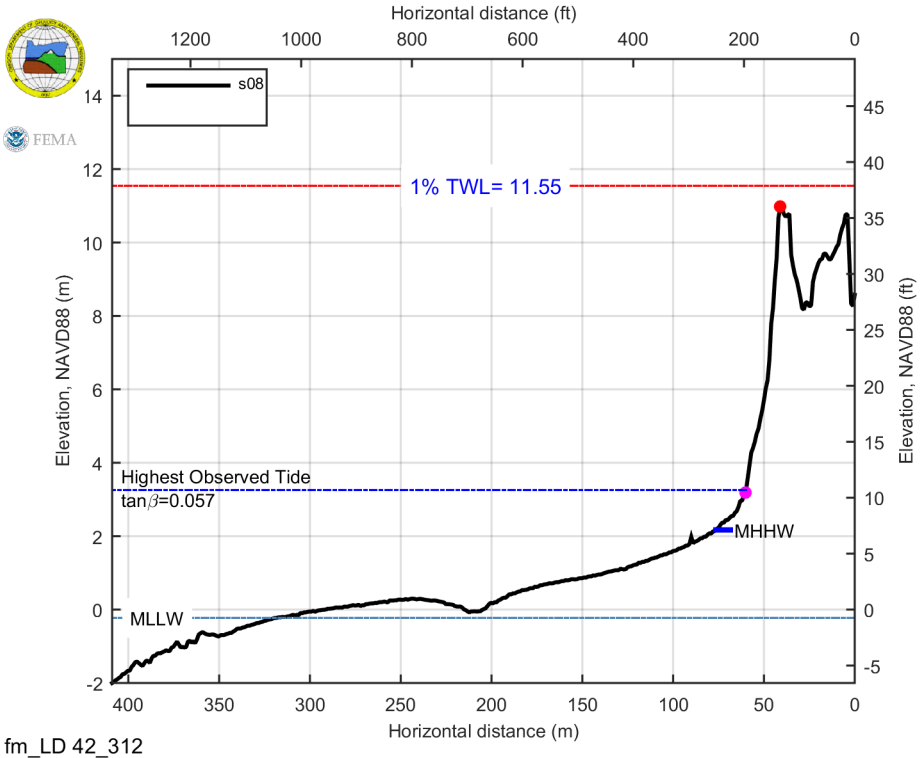


fm_LD 42_312

fm_LD 42_309

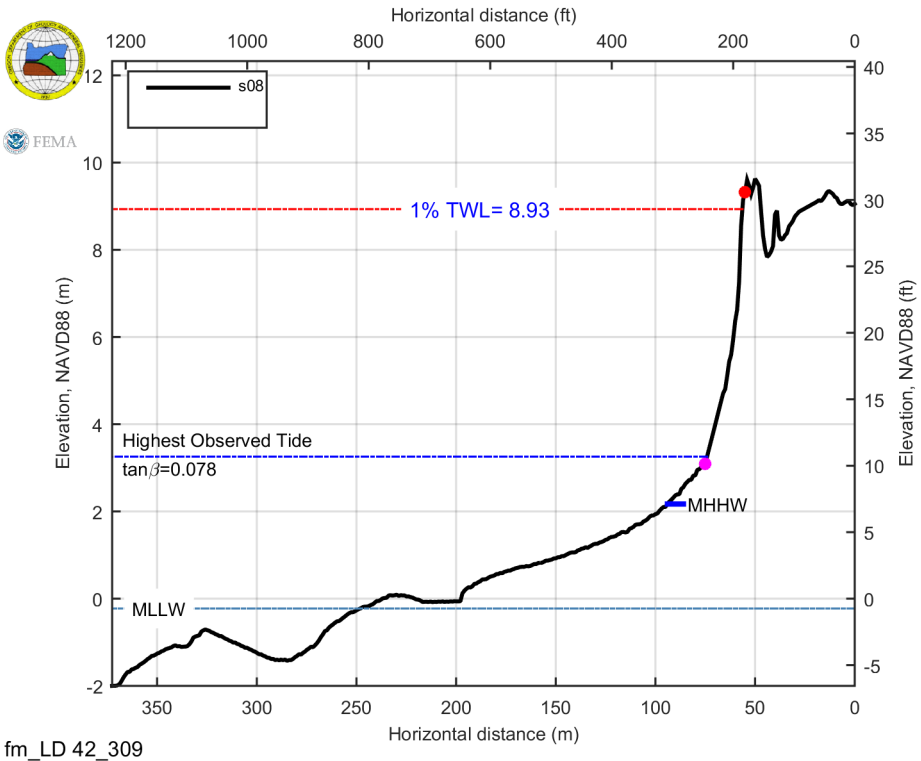


fm_LD 42_309

## 11.4 Appendix D: Supplemental Transect Overtopping Table

| Profiles | Transect | Dist_3 (≥ 0.91 m) | Dist_2 (> 0.61 < 0.91 m) | Dist_1 (≤ 0.31 m) | $hV^2 > 5.7$ $m^3/s^2$ (m) | Comment |
|---|---|---|---|---|---|---|
| **Heceta Head** | LANE 29_1 | 39.14 | 71.15 | 112.86 | 147.22 | none |
| **Stonefield** | LANE 42_312 | | | | | mapped to $D_{high}$ |
| **Beach** | LANE 42_309 | | | | | mapped to PFD |